UNIVERSIDADE FEDERAL DE JUIZ DE FORA

FACULDADE DE ENGENHARIA

PROGRAMA DE PÓS-GRADUAÇÃO EM ENGENHARIA ELÉTRICA

João Pedro Peters Barbosa

Using sigmoid functions for representing limits of generators and static Var compensators and their impact on the voltage stability study

Juiz de Fora

2023

João Pedro Peters Barbosa

Using sigmoid functions for representing limits of generators and static Var compensators and their impact on the voltage stability study

Dissertação apresentada ao Programa de Pós-Graduação em Engenharia Elétrica da Universidade Federal de Juiz de Fora como requisito parcial à obtenção do título de Mestre em Engenharia Elétrica. Área: Sistemas de Energia.

Orientador: Prof. João Alberto Passos Filho, D.Sc.

Juiz de Fora

2023

João Pedro Peters Barbosa

Using sigmoid functions for representing limits of generators and static var compensators and their impact on the voltage stability study

Thesis submitted to the Graduate Program in Electrical Engineering of the Federal University of Juiz de Fora as a partial requirement for obtaining a Master's degree in Electrical Engineering. Concentration area: Electric Power System.

Approved on 16 of May of 2023.

EXAMINING BOARD

Prof. Dr João Alberto Passos Filho – Academic Advisor
Federal University of Juiz de Fora

Prof. Dr. Igor Delgado de Melo
Federal University of Juiz de Fora

Prof. Dr. Luís Fernando Costa Alberto
University of São Paulo - São Carlos

Juiz de Fora, 04/27/2023.

To my parents, my brother and my love.

ACKNOWLEDGMENTS

Agradeço a Deus pelos desafios e oportunidades que colocou em minha vida, pois eles me ensinaram a sempre me empenhar com qualidade e sabedoria.

Ao meu orientador, Prof. João Alberto Passos Filho, pela oportunidade, confiança, paciência e apoio durante a elaboração deste trabalho.

Aos meus pais, Ana e Pedro, pelas orientações e referências. Ao meu irmão, Pedro Henrique, pelo incondicional companheirismo e carinho. Aos meus tios, Stela, José e Cristina, e minha segunda mãe, Rosângela, por sempre me motivarem e me apoiarem. Aos meus amigos de longa data e aos que fiz durante o período da faculdade, pela amizade. À minha namorada, Júlia, pela paciência, incentivo e amor.

Aos colegas de grupos de pesquisa e laboratórios que frequentei, em especial NAEP e NUPESP, por todos os momentos compartilhados.

À Dra. Rosa Célia e sua instituição Pró-Criança Cardíaca, promovendo melhoria na vida de crianças, assim como fez com a minha há mais de 20 anos.

Agradeço aos membros da banca avaliadora, pela disponibilidade de participar e pelas contribuições dadas neste texto.

À Universidade Federal de Juiz de Fora, à Faculdade de Engenharia e ao Programa de Pós-Graduação em Engenharia Elétrica pelo suporte educacional, por ampliar minha visão de mundo e por prover a infraestrutura fundamental para o desenvolvimento deste trabalho. Por último, o autor também gostaria de agradecer o apoio financeiro em parte da Coordenação de Aperfeiçoamento de Pessoal de Nível Superior (CAPES), e do Instituto Nacional de Energia Elétrica (INERGE) pela bolsa de estudos concedida.

"Two roads diverged in a yellow wood (...), and I—
I took the one less traveled by,
And that has made all the difference."

Robert Frost

ABSTRACT

This work presents new equipment's representation methodologies in the steady-state power flow analysis and their impacts on the voltage stability of electrical power systems. With special focus on system's voltage collapse scenario, characterized by a stability to instability transition, the traditional power flow method is reformulated with the introduction of smooth functions. As an option to introduce the desired smoothness, it is opted to incorporate the sigmoid function into the power flow formulation. The sigmoid function can be implemented within the traditional Newton-Raphson power flow formulation in the modeling of various control equipments. For the purpose of this work, it will be proposed new modelings for generators and Static VAr Compensators (SVCs). On account of being able to actively participate in voltage regulation, by means of controling reactive power injection, absorption and flow, these equipments received an exceptional attention. In order to analyze the condition of voltage collapse, power systems are stressed with gradual increases in generation and load. The continuous power flow tool is, therefore, applied, considering equipment's limits and saturation characteristics under study. On a general point of view, the voltage collapse is considered as a power system's point of maximum loadability, on the threshold of voltage stability. In a mathematical point of view, however, the voltage collapse is characterized as a point where a bifurcation occurs. Since power flow solves a system of nonlinear equations, and the continuous power flow determines a sequence of nonlinear equations solutions, bifurcations can be present throughout power flow analysis and simulations. Hence, several types of bifurcations can be observed, being characterized by different mathematical conditions. The use of sigmoid function in the modeling of control equipment proposes a new condition of voltage stability for electrical systems. The bifurcations found within the system, that once may have had different characteristics, now have the same common characteristic. This condition is translated as an advantage for voltage stability of electrical power systems in terms of easily identification of critical scenarios, which are responsible for admitting collapse. All propositions were tested by means of several simulations on different test-systems. A Python-based program was developed and the result simulations were validated by CEPEL's (Electric Energy Research Center) production-grade academic version software.

Keywords: Voltage Stability. Bifurcation. Control Devices. Newton Method. Sigmoid Function.

RESUMO

Este trabalho apresenta novas metodologias de representação de equipamentos na análise de fluxo de potência em regime permanente e seus impactos na estabilidade de tensão de sistemas elétricos de potência. Com foco especial no cenário de colapso de tensão do sistema, caracterizado por uma transição de estabilidade para instabilidade, o método tradicional de fluxo de potência é reformulado com a introdução de funções suaves. Como opção para introduzir a desejada suavidade, optou-se por incorporar a função sigmoide na formulação do fluxo de potência. A função sigmoide pode ser implementada dentro da formulação tradicional de fluxo de potência de Newton-Raphson na modelagem de vários equipamentos de controle. Para o propósito deste trabalho, serão propostas novas modelagens para geradores e Compensadores Estáticos de Potência Reativa (CERs). Por poderem participar ativamente da regulação de tensão, por meio do controle de injeção, absorção e fluxo de potência reativa, esses equipamentos receberam uma atenção excepcional. Para analisar a condição de colapso de tensão, os sistemas de potência são estressados com aumentos graduais em geração e demanda. A ferramenta de fluxo de potência continuado é, portanto, aplicada, considerando as características de limite e saturação dos equipamentos em estudo. De um ponto de vista geral, o colapso de tensão é considerado como um ponto de carga máxima do sistema de potência, no limiar da estabilidade de tensão. Do ponto de vista matemático, porém, o colapso de tensão é caracterizado como um ponto onde ocorre uma bifurcação. Como o fluxo de potência resolve um sistema de equações não lineares, e o fluxo de potência contínuo determina uma sequência de soluções de equações não lineares, as bifurcações podem estar presentes em análises e simulações de fluxo de potência. Assim, vários tipos de bifurcações podem ser observados, sendo caracterizadas por diferentes condições matemáticas. A utilização da função sigmoide na modelagem de equipamentos de controle propõe uma nova condição de estabilidade de tensão para sistemas elétricos. As bifurcações encontradas dentro do sistema, que antes poderiam ter características diferentes, agora têm uma mesma característica comum. Esta condição se traduz como uma vantagem para a estabilidade de tensão dos sistemas elétricos de potência em termos de facilidade na identificação de cenários críticos, responsáveis por admitir o colapso. Todas as proposições foram testadas por meio de várias simulações em diferentes sistemas-teste. Um programa em Python foi desenvolvido e as simulações dos resultados foram validadas pela versão acadêmica do software do CEPEL (Centro de Pesquisas em Energia Elétrica).

Palavras-chave: Estabilidade de Tensão. Bifurcação. Equipamentos de Controle. Método de Newton. Função Sigmoide.

LIST OF FIGURES

LIST OF TABLES

LIST OF ABBREVIATIONS AND ACRONYMS

AVR   Automatic Voltage Regulator

BP   Bifurcation Point

CEPEL   Electric Energy Research Center

CIG   Converter Interfaced Generation

CPF   Continuation Power Flow

CVIB   Constraint Violation Induced Bifurcation

EPS   Electric Power System

FACTS   Flexible AC Transmission System

FC-TCR   Fixed-Capacitor Thyristor-Controlled Reactor

HB   Hopf Bifurcation

IEEE   *Institute of Electric and Electronic Engineers*

LIB   Limit-Induced Bifurcation

MLP   Maximum Loadability Point

PF   Newton-Raphson's Power Flow

SNB   Saddle-Node Bifurcation

SPF   Smooth Power Flow

SVC   Static VAr Compensator

TP   Transition Point

VSA   Voltage Stability Assessment

VSM   Voltage Stability Margin

GENERAL NOTATION RULES

Notation conventions adopted in this work are displayed below, in accordance to Cutsem and Vournas (2007) and Milano (2010):

- Phasors: capital italic letter with an overline (e.g. $\overline{V}$, $\overline{S}$);

- Phasors magnitude and scalars: capital italic letter without an overline (e.g. V, P, Q, θ);

    – Greek letters are also treated as scalars (e.g. θ, α, λ, ε, γ);

- Vectors: lowercase bold-italic letter. Column oriented as default, while superscript ^{T} denotes transpose, or row oriented vectors (e.g. $\boldsymbol{x}$, $\boldsymbol{x^{T}}$);

- Phasors in a vector: capital bold-italic letter with an overline (e.g. $\overline{\boldsymbol{V}}$, $\overline{\boldsymbol{S}}$);

- Phasors magnitude vector and scalars vector: capital bold-italic letter without an overline (e.g. $\boldsymbol{V}$, $\boldsymbol{P}$, $\boldsymbol{Q}$, $\boldsymbol{\theta}$);

    – Greek letters vector (e.g. $\boldsymbol{\theta}$, $\boldsymbol{\alpha}$, $\boldsymbol{\lambda}$, $\boldsymbol{\varepsilon}$, $\boldsymbol{\gamma}$);

- Vector functions: lowercase bold-italic letter (e.g. $\boldsymbol{f}$);

- Scalar functions or functions parameters/variables: lowercase italic letter (e.g. f, tol, lim);

- Matrices: capital bold letter (e.g. $\mathbf{J}$);

- Submatrices: bold letter with bold subscript indicating the differentiable variable. A special notation is set for the Jacobian matrix, with bold subscripts indicating the state equation and the state variable, respectively.

$$\boldsymbol{f_x} = \left[\frac{\partial f_i}{\partial x_j}\right] \qquad\qquad \mathbf{J}_{\boldsymbol{P\theta}} = \left[\frac{\partial P_i}{\partial \theta_j}\right]$$

All notations are susceptible to the adoption of supscripts and/or subscripts.

LIST OF SYMBOLS

Functions and Equations

$\boldsymbol{f}$	Power flow system of nonlinear equations
$\boldsymbol{f^{sch}}$	Power flow system of nonlinear equations scheduled values
$\boldsymbol{g}$	Power flow system of inequations constraints
b_{eq}	SVC equivalent susceptance
x_{eq}	SVC equivalent reactance
$sw1$	SPF-Generator reactive power generation superior sigmoid function switch
$sw2$	SPF-Generator reactive power generation inferior sigmoid function switch
$sw3$	SPF-Generator voltage magnitude superior sigmoid function switch
$sw4$	SPF-Generator voltage magnitude inferior sigmoid function switch
$sw5$	SPF-SVC reactive power injection methodology superior $V_{m,svc}$ sigmoid function switch
$sw6$	SPF-SVC reactive power injection methodology inferior $V_{m,svc}$ sigmoid function switch
$sw7$	SPF-SVC current injection methodology superior $V_{m,svc}$ sigmoid function switch
$sw8$	SPF-SVC current injection methodology inferior $V_{m,svc}$ sigmoid function switch
$sw9$	SPF-SVC thyristor firing-angle methodology superior $\alpha_{k,svc}$ sigmoid function switch
$sw10$	SPF-SVC thyristor firing-angle methodology inferior $\alpha_{k,svc}$ sigmoid function switch
$sw11$	SPF-SVC thyristor firing-angle methodology superior $V_{m,svc}$ sigmoid function switch
$sw12$	SPF-SVC thyristor firing-angle methodology inferior $V_{m,svc}$ sigmoid function switch

Parameters

Ω_k	Set of all equipments connected to bus k
N_{BUS}	Total number of buses in an electric power system
N_{GEN}	Total number of generators in an electric power system
N_{SVC}	Total number of static var compensators in an electric power system
N_{PV}	Total number of PV buses in an electric power system
N_{PQ}	Total number of PQ buses in an electric power system
α_{svc}^0	SVC thyristor firing-angle equal to null equivalent susceptance
h	Newton-Raphson Power Flow solution iteration counting variable
ε_P	Newton-Raphson active power convergence tolerance

ε_Q	Newton-Raphson reactive power convergence tolerance
ε_Y	Newton-Raphson control equations convergence tolerance
ε_λ	CPF loading parameter convergence tolerance
slp	Sigmoid function slope
tol_α	Sigmoid function thyristor firing-angle tolerance
tol_q	Sigmoid function reactive power tolerance
tol_v	Sigmoid function voltage magnitude tolerance
$Q_{G_k,gen}$	Generator reactive power generation at bus k
$Q_{G_k,gen}^{max}$	Generator maximum reactive power generation at bus k
$Q_{G_k,gen}^{min}$	Generator minimum reactive power generation at bus k
$V_{k,gen}^{ref}$	Generator voltage magnitude reference value at bus k
$V_{k,gen}$	Generator voltage magnitude at bus k
$B_{svc}^{cap}, B_{svc}^{max}$	SVC capacitive susceptance or maximum susceptance
$B_{svc}^{ind}, B_{svc}^{min}$	SVC inductive susceptance or minimum susceptance
$I_{k,svc}$	SVC current generated at bus k
$Q_{G_k,svc}$	SVC reactive power generated at bus k
$Q_{G_k,svc}^{max}$	SVC maximum reactive power generated at bus k
$Q_{G_k,svc}^{min}$	SVC minimum reactive power generated at bus k
$V_{k,svc}$	SVC bus voltage magnitude at bus k
$V_{m,svc}^{ref}$	SVC voltage magnitude reference value of controlled bus m
$V_{m,svc}$	SVC voltage magnitude of controlled bus m
X_C	SVC capacitive reactance
X_L	SVC inductive reactance
λ	Loading parameter
λ^{step}	Loading parameter step variation
λ^{crit}	Critical loading parameter
$\tilde{\lambda}^{crit}$	Arbitrarily close critical loading parameter
$\Delta\lambda$	Loading parameter variation
λ^{eig}	Eigenvalue
θ_k	Power factor angle of load change at bus k
γ_k	Multiplier to designate the rate of load change at bus k as λ changes
β_k	Active generation variation rate at bus k
S_B	Apparent power to provide appropriate scaling of λ
$P_{G_k}^0$	Active generation initial value at bus k
$P_{L_k}^0$	Active load initial value at bus k
$Q_{L_k}^0$	Reactive load initial value at bus k
$\Delta P_{L,\lambda}^{sys}$	Power system's total active load variation per increment
a_{kj}	Element in the kth row and jth column of a matrix

Variables

$\alpha_{k,svc}$	SVC connected at bus k thyristor firing-angle
lim	Sigmoid function transition point

lim_α^{sup}	Sigmoid function superior thyristor firing-angle transition point
lim_α^{inf}	Sigmoid function inferior thyristor firing-angle transition point
lim_q^{sup}	Sigmoid function superior reactive power transition point
lim_q^{inf}	Sigmoid function inferior reactive power transition point
lim_v^{sup}	Sigmoid function superior voltage magnitude transition point
lim_v^{inf}	Sigmoid function inferior voltage magnitude transition point

Vectors and Matrices

$\mathbf{J}$	Jacobian matrix
$\mathbf{J_R}$	Reduced Jacobian matrix
$\mathbf{J_{P\theta}}$	Jacobian active power per phase angle submatrix
$\mathbf{J_{PV}}$	Jacobian active power per voltage magnitude submatrix
$\mathbf{J_{Q\theta}}$	Jacobian reactive power per phase angle submatrix
$\mathbf{J_{QV}}$	Jacobian reactive power per voltage magnitude submatrix
$\mathbf{J_{Y\theta}}$	Jacobian control equation per phase angle submatrix
$\mathbf{J_{YV}}$	Jacobian control equation per voltage magnitude submatrix
$\mathbf{J_{P\lambda}}$	Jacobian active power per loading parameter submatrix
$\mathbf{J_{Q\lambda}}$	Jacobian reactive power per loading parameter submatrix
$\mathbf{J_{Y\lambda}}$	Jacobian control equation per loading parameter submatrix
$\mathbf{J_{YX}}$	Jacobian control equation per control state variable submatrix
$\boldsymbol{\theta}$	Vector of buses phase angle
$\boldsymbol{V}$	Vector of buses voltage magnitude
$\boldsymbol{X}$	Vector of state variables θ and V
$\boldsymbol{P}$	Vector of buses active power injection
$\boldsymbol{Q}$	Vector of buses reactive power injection
$\boldsymbol{P_L^0}$	Vector of buses active loads on base case
$\boldsymbol{Q_L^0}$	Vector of buses reactive loads on base case
$\boldsymbol{I}$	Identity matrix
$\boldsymbol{A}$	Generic matrix
$\boldsymbol{\Lambda}$	Diagonal eigenvalue matrix
$\boldsymbol{\phi}$	Right eigenvector matrix
$\boldsymbol{\psi}$	Left eigenvector matrix
$\boldsymbol{\phi_k}$	Right eigenvector k
$\boldsymbol{\psi_k}$	Left eigenvector k
$\boldsymbol{P}$	Participation factor matrix
$\boldsymbol{p_k}$	Participation factor vector

SUMMARY

1 INTRODUCTION

Electric Power Systems (EPSs) consist of a complex network of multiple individual components that includes generators, loads, switching devices, transformers and many more, which are interconnected by transmission lines. Each of these components possesses unique operational characteristics that limit their functionality. Therefore, a series of control options are adopted in order to contribute for a satisfactory operation of the power system.

To analyze the operational behavior of a power system, at a given operating point, the Newton-Raphson's Power Flow (PF) tool is used. This tool is the most frequently used one in studies related to electrical power systems. From the results it returns, it is possible to infer about the operating conditions of the system in relation to stability, security, reliability, robustness and quality.

Power systems stability is defined, according to Kundur *et al.* (2004), as:

> the ability of an electric power system, for a given initial operating condition, to regain a state of operating equilibrium after being subjected to a physical disturbance, with most system variables bounded so that practically the entire system remains intact.

This definition ensures that an electrical power system is classified as stable once it can withstand a variety of disturbances without resulting in an operational collapse, failure or interruption. The definition presented in Kundur *et al.* (2004) is extended into three fields of study, which are *angle stability*, *frequency stability* and *voltage stability*. In Hatziargyriou *et al.* (2020), the definition is further extended to two more fields of study, named *resonance stability* and *converter-driven stability*, due to the recent and significant integration of Converter Interfaced Generations (CIGs) technologies.

On account of voltage stability, it is a major concern for EPS planning and operation. It is commonly related to power systems as the ability to maintain equilibrium (voltage at all buses at a specific interval level) given load disturbances. One of the main sources of equilibrium for this problem comes from EPSs ability to meet its own reactive power demand. This condition can be attained by means of generators, Static VAr Compensators (SVCs) and other electric devices actively operating in the EPS.

Once the disturbances are no longer compensated by reactive power generation, for example, a progressive decrease or increase in bus voltage values occurs. Although it is normally classified as a local phenomenon, voltage instability consequences may impact the EPS as whole. Voltage collapse, therefore, configures a condition where a series of voltage instability events leads to a significant low-voltage profile for a majority of buses in the EPS.

A classical example of the voltage stability phenomenon is given in Kundur (1994) and Taylor (1994). It consists in evaluating the voltage magnitude profile for the radial system illustrated in Figure 1, given a constant voltage source ability to meet a variable demand. Although this power system presents a simple topology, important information are obtained regarding the relationships between voltage magnitude (V), active power generation (P) and reactive power generation (Q). This information is crucial for a deeper understanding of (voltage) stability of EPSs.

Figure 1 – Radial power system to analyze voltage stability phenomenon.
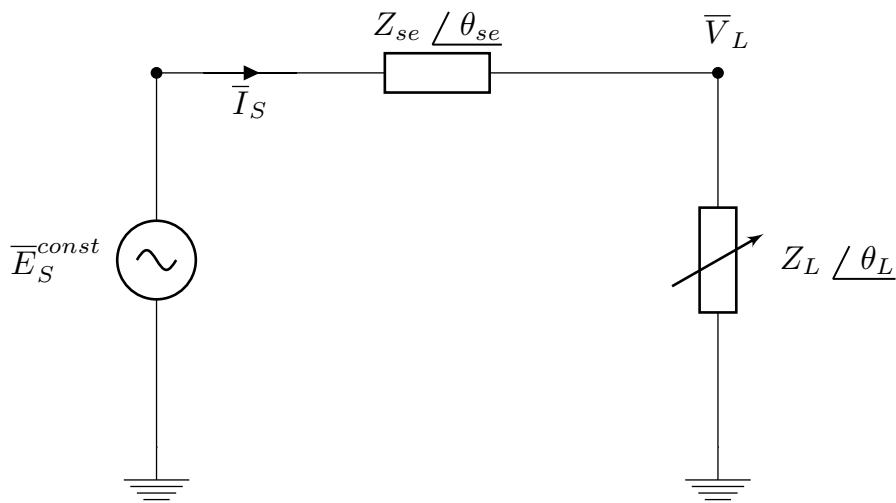
Source: Adapted from Kundur (1994), Taylor (1994).

However, for EPSs with higher complexity network containing multiple electric devices operating simultaneously, the same aforementioned relationships can be obtained via the adoption of the Continuation Power Flow (CPF) tool. This tool, developed by Ajjarapu and Christy (1992), consists of a series of PF analysis considering a gradual increment in load demand of the system, which is analogous to a controlled disturbance. Based on the implementation of this tool, it is possible to evaluate and define stable and unstable operational regions for EPSs, as well as predict the Maximum Loadability Point (MLP) that is identifiable in the transition between both regions.

All things considered, this work deals with voltage stability and, specifically, the indentification and classification of voltage collapse in EPS.

1.1 PROBLEM IDENTIFICATION

On a general point of view, voltage collapse is related to a power system's point of maximum loadability, on the threshold of voltage stability (this analysis is valid only if the constant power load models are adopted in the power flow problem). As mentioned previously, voltage collapse is characterized by a series of voltage instability events, and therefore, there are many conditions that lead up to this event in EPSs. In (KUNDUR

et al., 2004), the causes for voltage collapse are classified into two subcategories that are *large-disturbances*: systems faults, loss of generation or circuit contingencies; and *small-disturbances*: variations of loads, of continuous controls or of discrete controls.

In a mathematical point of view, however, voltage collapse is characterized as a point where bifurcation occurs. The bifurcation point is basically defined as a limit point in parameter space for which occurs a significant change on the qualitative structure that models EPS in the PF problem, resulting in the birth or death of (power flow) solution points (NEVES, 2022; CUTSEM; VOURNAS, 2007). Depending on the cause of voltage collapse, as mentioned previously, bifurcations can also be classified into other subcategories, such as Saddle-Node Bifurcation (SNB), Limit-Induced Bifurcation (LIB), Constraint Violation Induced Bifurcation (CVIB), Hopf Bifurcation (HB) and many others. Each bifurcation classification has particular mathematical properties that define them.

This comparison between general and mathematical points of view is correlated due to the nonlinearity characteristic of power systems. In the PF analysis, EPSs are translated into a system of nonlinear equations that are linearized in the Newton-Raphson method for solution finding. The control options adopted for the electric devices actively operating in EPSs are also incorporated in the system of nonlinear equations in order to approximate simulated solutions with real operating conditions. As PF analysis presents infinite possible solutions, depending on EPSs topology, generation and load scenarios, equally possible are the conditions that lead these same EPSs to voltage collapse.

In this work, a special emphasis is given to analyzing the events that lead up to voltage collapse which are mathematically classified as SNBs and LIBs. The former is a bifurcation point associated with the lose of equilibrium by the power system, whereas the latter occurs when two equilibrium points (power flow solutions) coalesce and disappear (CUTSEM; VOURNAS, 2007). Examples for these events are sustained load buildup, generators reaching reactive power limits and also SVCs alternating operational modes.

SNB and LIB bifurcations classifications are differed by a particular mathematical property that is the nonlinear system of equations singularity at the MLP. Although these events have mathematical characteristics that distinct themselves from each other, it is pratically difficult to analyze and indentify real causes for voltage collapse in EPSs.

1.2 MOTIVATION

In recent works available in power flow literature, a new PF formulation is proposed and entitled Smooth Power Flow (SPF) (NEVES; ALBERTO; CHIANG, 2022b; NEVES, 2022). This new formulation introduces a smoothness to the traditional power flow formulation, enhancing the simulated solutions and analysis of EPSs.

One of the ameliorations that comes with the introduction of smoothness within

the SPF formulation is precisely related to the multiple bifurcations classification. As mathematically proved and detailed in Neves (2022), with the implementation of SPF all static bifurcations are transformed into SNBs. This means that the events of sustained load buildup, generators reaching reactive power limits and also SVCs alternating operational modes, for example, are now all classified as SNB.

At first, this condition may not be interpreted as an improvement, or advantage, since it does not prevent EPSs from having voltage collapse. However, the improvement consists on how easily the events that lead up to voltage collapse in EPSs can now be indentified. It will not be necessary to accumulate concern when analyzing and classifying the voltage collapse numerical condition as well as identifying the causes for the same problem. This identification is simplified by implementing modal analysis on simulated SNB results, for example, as was done in this work.

The investigation of these different conditions motivated the development of this work.

1.3 CONTRIBUTIONS

From this work, mathematical steady-state models were developed to represent the SVCs in the power flow problem. The mathematical models incorporate sigmoid function based switches to alternate between the control equations that best represent the operating state of the control equipment. The sigmoid function is responsible for introducing smoothness to the traditional PF formulation, as proposed by the SPF.

The Jacobian matrix, which represents the linearization of the nonlinear equations that model an EPS, is resized considering the incorporation of the control equations that model each SVC active in the network analyzed. This approach is known as *full* Newton.

Regarding the proposed SVCs methodologies, a contribution is made to the traditional thyristor firing-angle methodology proposed by Ambriz-Perez, Acha and Fuerte-Esquivel (2000). This contribution, as it is detailed in Chapter 5, consists on the adoption of a variable to represent the characteristic *droop* of the linear operational region of the control device. The *droop* implementation was proposed once that, in the traditional methodology, the bus voltage magnitude is ideally controlled around a scheduled value.

An additional contribution is related to the numerical demonstration and indentification of SNBs in the SPF formulation. By means of the implemented sigmoid functions based switches in the generator's reactive power generation limits methodology and SVCs methodologies, it was able to numerically demonstrate the mathematical theorem developed in Neves (2022).

1.3.1 **Published Papers**

A conference paper was accepted and published:

- BARBOSA, J. P. P.; PASSOS FILHO, J. A. Avaliação e aprimoramento de metodologias para representação de CER no problema de fluxo de potência. **Simpósio Brasileiro de Sistemas Elétricos-SBSE**, v. 2, n. 1, 2022.

  - This paper was awarded the "SBSE 2022 Best Paper" prize in the Master's category.

Other papers are currently being developed regarding the content of this work.

1.4 DOCUMENT STRUCTURE

Regarding the structure of this document, it is organized in eight chapters, including this introductory Chapter 1, following:

- Chapter 2 describes the traditional power flow formulation and the operation conditions of generators and SVCs in an electrical power system.

- Chapter 3 presents an implementation overview of the proposed methodology into the traditional power flow formulation.

- Chapter 4 introduces the methodology to represent steady-state modeling of generators in the power flow formulation based on Chapter 3. This methodology was first introduced in the literature by Pontes, Passos Filho and La Gatta (2018), Pontes (2018).

- Chapter 5 proposes new methodologies to represent SVC in the power flow formulation based on Chapter 3. A total of three steady-state traditional models are reformulated for this control device.

- Chapter 6 proposes a new premise for voltage stability analysis, specially on the voltage collapse scenario. A new consideration upon electrical power systems and bifurcations is proposed based on the impacts of the SPF formulation.

- Chapter 7 introduces the computer simulations conducted on test systems along with carried out analysis, presentation and validation of results.

- Chapter 8 presents the research conclusions and contributions of this work.

In addition, Appendices A, B and C details mathematical information on the proposed SPF methodologies, the CPF methodology and the eigenproperties of the Jacobian matrix, respectively.

2 TRADITIONAL POWER FLOW FORMULATION

In this chapter, a brief review of the current and traditional literature on the steady-state PF formulation and modeling is made. A set of nonlinear equations is considered in order to propose a mathematical representation and, consequently, simulation of power systems.

A special focus on the traditional modeling of generators and SVCs will be held in the following sections. In view of Voltage Stability Assessment (VSA), these equipments actively participate in voltage regulation by means of controling reactive power injection, absorption and flow.

In addition, this work assumes the analysis of balanced three-phase electric power systems, which allows a single-phase equivalent model representation (KUNDUR, 1994). On account of loads representations, the constant power model was considered.

2.1 INITIAL CONSIDERATIONS

The Newton-Raphson method is a widespread numerical-computational technique applied in the analysis of EPS, first introduced in the literature by Tinney and Hart (1967). It is based on the power equations that model an EPS, which are deduced from Kirchhoff's Circuit Laws as given by (2.1) and (2.2). In general, these equations do not consider equipment controls or operational limits.

$$\sum_{m \in \Omega_k} \overline{I}_m = 0 \tag{2.1}$$

$$\overline{V}_k \cdot \sum_{m \in \Omega_k} \overline{I}_m^* = \sum_{m \in \Omega_k} S_k = 0 \tag{2.2}$$

where Ω_k is the set of all equipments connected to bus k, I_m is the current injected by a device m at bus k and S_m is the apparent power that device m injects at bus k.

From (2.1), Equations (2.3) and (2.4) determines "the relationship between node current $\overline{I}_k$ and node-to-datum voltage $\overline{V}_k$ in a network" as well as the complex power at a generic node k (TINNEY; HART, 1967), respectively.

$$\overline{I}_k = \sum_{m \in \Omega_k} Y_{km} \cdot \overline{V}_m \tag{2.3}$$

$$S_k = P_k + jQ_k = \overline{V}_k \cdot \overline{I}_k^* = \overline{V}_k \cdot \left(\sum_{m \in \Omega_k} Y_{km} \cdot \overline{V}_m \right)^* \tag{2.4}$$

$$Y_{km} = G_{km} + jB_{km}. \tag{2.5}$$

where Y_{km} is an element of the admittance matrix corresponding to the Ω_k-set of m buses connected to bus k, and G_{km} and B_{km} are its corresponding conductance and susceptance, respectively.

Note that, traditionally, the power flow formulation considers polar variables and its equations are modeled in terms of power. Therefore, from (2.4) it can be determined the active and reactive power injection equations, as follows:

$$P_k = V_k \cdot \sum_{m \in \Omega_k} V_m \cdot (G_{km} \cdot \cos\theta_{km} + B_{km} \cdot \sin\theta_{km}) \tag{2.6}$$

$$Q_k = V_k \cdot \sum_{m \in \Omega_k} V_m \cdot (G_{km} \cdot \sin\theta_{km} - B_{km} \cdot \cos\theta_{km}) \tag{2.7}$$

where θ_{km} is the difference between bus k and m voltage phase angles ($\theta_{km} = \theta_k - \theta_m$).

These are the canonical algebraic equations of the power flow formulation in polar coordinates. These equations represent the behavior of power flow in EPSs as illustrated in Figure 2. In addition, it is based in these equations that, by applying the numerical Newton-Raphson method, the power flow solution can be obtained.

Figure 2 – Power injection at a generic bus k.
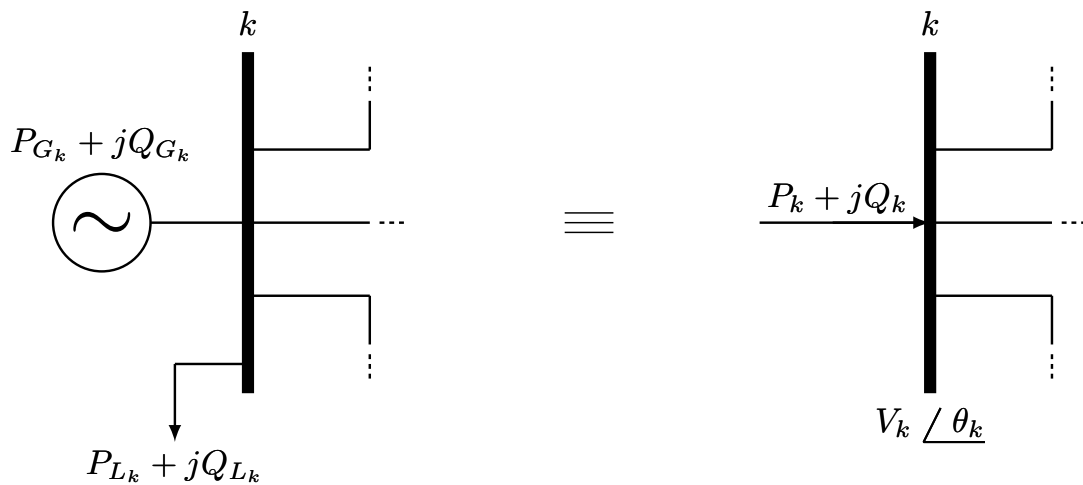
Source: Adapted from Pontes (2018).

As it can be observed, associated with each bus there are four variables: active power P, reactive power Q, voltage magnitude V and phase angle θ (STOTT, 1974; KUNDUR, 1994). The power equations (2.6) and (2.7) are equivalent to the difference

between power generated and power demanded by loads, as detailed in (2.8) and (2.9) respectively.

$$P_k = P_{G_k} - P_{L_k} \tag{2.8}$$

$$Q_k = Q_{G_k} - Q_{L_k} \tag{2.9}$$

Since only two state equations exist for four variables, a bus-type classification is specified for the Newton-Raphson method implementation. This specification is needed in order to prevail the power balance in the EPS, as stated in (2.1). According to Kundur (1994), the classifications are:

- PV bus: specification of active power P and voltage magnitude V variables. Typically, these are buses with generators, synchronous condensers, or static VAr compensators connected at them, where the voltage magnitude value is controlled. Reactive power Q and phase angle θ are treated as free variables. However, if reactive power limits are considered in the analysis, the reactive power variable must respect the imposed limits.

- PQ bus: specification of active power P and reactive power Q variables. Typically, these are buses that do not have voltage magnitude control and with only loads connected at them. Voltage magnitude V and phase angle θ are treated as free variables.

- Swing bus: specification of voltage magnitude V and phase angle θ variables. Typically, this bus has an active generation device connected at it which is responsible for suppling the remaining active power to balance the EPS nodal analysis (2.1). It is a mathematical workaround once EPS power losses are not known *a priori*. Active power P and reactive power Q are treated as free variables.

Based on the bus-type classification and the variables specification, the power equations that model an EPS can be synthesized by the following equation (STOTT, 1974):

$$\boldsymbol{f}\left(\boldsymbol{\theta}, \boldsymbol{V}\right) = \boldsymbol{0} \tag{2.10}$$

where $\boldsymbol{f}$ represents the vector of nonlinear equations that model an EPS. This vector dimension depends directly on the number of buses of the analyzed EPS.

In the implementation of the Newton-Raphson method, an initial estimation must be set for the state variables θ and V. This initial estimation has great influence on the iterative solution proposed by the method. In addition, Taylor's theorem is applied in order to expand the nonlinear equations in (2.10) in a resulting linear set of equations, as detailed in (2.11). Taylor's higher powers expansion can be neglected, leaving out only the first order expansion denoted by the subscript '0'.

$$\boldsymbol{f_{\theta,V}}\left(\boldsymbol{\theta^0} + \boldsymbol{\Delta\theta}, \boldsymbol{V^0} + \boldsymbol{\Delta V}\right) = \boldsymbol{f}\left(\boldsymbol{\theta^0}, \boldsymbol{V^0}\right) + \left[\frac{\partial \boldsymbol{f}}{\partial \boldsymbol{\theta}}\right]_0 \cdot \boldsymbol{\Delta\theta} + \left[\frac{\partial \boldsymbol{f}}{\partial \boldsymbol{V}}\right]_0 \cdot \boldsymbol{\Delta V} \qquad (2.11)$$

The Taylor expansion Equation (2.11) can also be formulated in the matrix form:

$$\left[\begin{array}{c} \boldsymbol{f^{sch}} - \boldsymbol{f}\left(\boldsymbol{\theta^0}, \boldsymbol{V^0}\right) \end{array}\right] = \left[\begin{array}{cc} \left[\frac{\partial \boldsymbol{f}}{\partial \boldsymbol{\theta}}\right]_0 & \left[\frac{\partial \boldsymbol{f}}{\partial \boldsymbol{V}}\right]_0 \end{array}\right] \cdot \left[\begin{array}{c} \boldsymbol{\Delta\theta} \\ \boldsymbol{\Delta V} \end{array}\right] \qquad (2.12)$$

which in turn is simplied by the following equation:

$$\boldsymbol{\Delta f} = \mathbf{J} \cdot \boldsymbol{\Delta X} \qquad (2.13)$$

where $\boldsymbol{\Delta f}$ is the vector of state equations variation, $\mathbf{J}$ is referred to as the Jacobian matrix and $\boldsymbol{\Delta X}$ is the vector of state variables (θ and V) variation.

If the initial estimation of $\boldsymbol{\theta^0}$ and $\boldsymbol{V^0}$ is exact, then $\boldsymbol{\Delta f}$ and $\boldsymbol{\Delta X}$ would be zero, as defined in (2.10) (KUNDUR, 1994). In contrast, the vector of state variables can be determined by (2.12) in order update the state variables values:

$$\boldsymbol{\theta^{h+1}} = \boldsymbol{\theta^h} + \boldsymbol{\Delta\theta} \qquad (2.14)$$

$$\boldsymbol{V^{h+1}} = \boldsymbol{V^h} + \boldsymbol{\Delta V} \qquad (2.15)$$

This process is repeated until the errors for the state equations are lower than a specified tolerance ε. During the Newton-Raphson iterative process, the Jacobian needs to be recalculated at each step h. In addition, the obtained results accuracy depends mainly on the tolerance determined for the calculation errors of the solution. The adopted tolerance value also has influence on the number of iterations needed to obtain a precise solution, which tends to be small and independent of the size of the EPS under study.

It is important to note that the initial estimation conveys an crucial condition for the simulation convergence. That is, the initial values of $\boldsymbol{\theta^0}$ and $\boldsymbol{V^0}$ must be sufficiently

reasonable in order to reliably simulate the EPS operational behavior. Otherwise, the initial values will lead up to convergence errors and the simulation will mistakenly return undesired results.

As mentioned before, the power equations that model an EPS do not consider equipments controls or operational limits. However, for an analysis of EPSs closer to realistic operation, controls and limits must be considered in the power flow formulation problem. In order to do so, a set of inequations must be defined and incorporated together with (2.10).

The inequations that model electric devices operational limits in an EPS can be synthesized by (2.16). This vector dimension depends directly on the number of controls adopted in the power flow formulation.

$$g\left(\boldsymbol{\theta}, \boldsymbol{V}\right) \geq \mathbf{0}. \tag{2.16}$$

In the following sections, the traditional modeling of generators and SVCs will be presented in detail. These equipments received a special focus in this work by reason of being able to actively impact voltage stability in an EPS.

2.1.1 Generators

Generators are one of the most important electric devices to be actively operating by reason of being the major source of electric power generation in EPSs. In steady-state analysis, generator buses are generally modeled as PV buses due to their ability to control the bus voltage magnitude at a specified value by means of actuation on the field current using an Automatic Voltage Regulator (AVR) (NEVES, 2022). Quoting Cutsem and Vournas (2007), "*Synchronous generators are a primary source of reactive power and are to a great extent responsible for maintaining a good voltage profile across a power system*".

In contrast, they are also one of the most complex electric devices to be actively operating in EPSs. Due to its constructive characteristics and operational limits, generators' reactive power generation capability is limited and, consequently, responsible for voltage instability incidents (TAYLOR, 1994). A generator capability curve[1] is defined and assembled by a series of operational limit curves, as illustrated by Figure 3 and exemplified in Kundur (1994), Taylor (1994), Monticelli and Garcia (1999), Cutsem and Vournas (2007).

The roman algarisms in Figure 3 reffer to the following generator's limits (PONTES, 2018):

---

[1] Capability curves can differ from generators to generators, depending mainly on the constructive characteristics of the equipment.

Figure 3 – Generator capability curve.
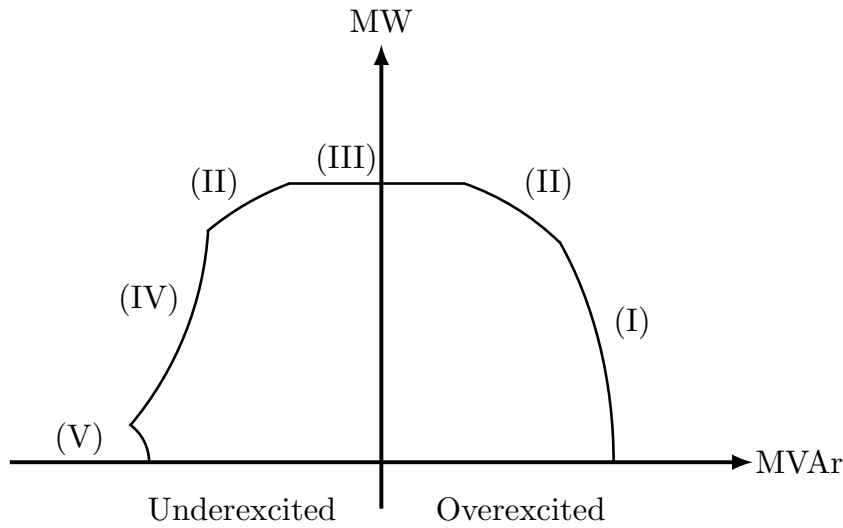
Source: Adapted from Monticelli and Garcia (1999).

(I) Field current maximum limit;

(II) Armature current maximum limit;

(III) Mechanical power limit;

(IV) Angular stability limit;

(V) Excitation current minimum limit.

Field current and armature current maximum limits are associated with generators heating problems, that can lead to a shortening service life. The mechanical power limit corresponds to the maximum mechanical power a generator can be tied up in his prime mover. The maximum power factor angle also limits generator's reactive power generation, and is referred to as angular stability limit. It is a theoretical limit and directly depends on the heating produced by the armature current. In conclusion, the excitation current minimum limit corresponds to the minimum current needed to keep generator's magnetic field energized. The overexcited and underexcited regions corresponds to the generator ability of reactive power injection or absorption in an EPS, respectively.

Nevertheless, as it is complex to determine generator's capability curve, a simplified approach, illustrated by Figure 4, is implemented for the steady-state analysis of EPSs.

From the following simplified approach, one can define the inequation that model upper and lower boundaries for reactive power generation in the power flow problem:

$$Q_{gen}^{min} \leq Q_{gen} \leq Q_{gen}^{max} \tag{2.17}$$

Figure 4 – Generator simplified capability curve.
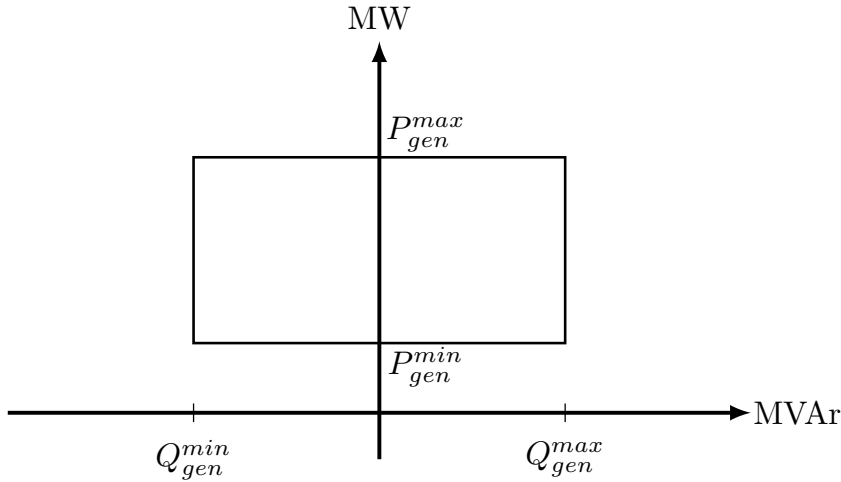
Source: Elaborated by the author (2023).

Since generators are able to regulate the voltage magnitude by means of reactive power generation, which is given by (2.7), a set of control inequations are proposed based on the generator's operational behavior detailed by (2.17), as follows:

$$
\begin{cases}
V_{gen} > V_{gen}^{ref} & \text{if } Q_{gen} = Q_{gen}^{min}, \\
V_{gen} = V_{gen}^{ref} & \text{if } Q_{gen}^{min} < Q_{gen} < Q_{gen}^{max}, \\
V_{gen} < V_{gen}^{ref} & \text{if } Q_{gen} = Q_{gen}^{max},
\end{cases}
\tag{2.18}
$$

where V_{gen} is the voltage magnitude of the generator's own bus, or of an controlled bus in the network, and V_{gen}^{ref} is its respective reference value.

As mentioned before, controls are not considered in the PF traditional formulation. For generators or PV buses, the linearized reactive power equations responsible for updating its voltage magnitude variable are disregarded and, therefore, the Jacobian matrix dimension is defined as $2\text{N}_{\text{PQ}} + \text{N}_{\text{PV}}$ (KUNDUR, 1994; MONTICELLI, 1983). However, in the scenario where the generator reactive power generation reach a limit, being it maximum or minimum, they become unable to control bus voltage magnitude at reference value. For that reason, reactive power equations must then be considered in the PF formulation.

For modeling reactive power generation limits in the PF problem, the following analysis must be considered (assume that the generator is connected at bus k, controlling its own bus voltage magnitude $V_{k,gen}$ and $Q_{G_k,gen}$ is the reactive power generation variable) (MONTICELLI, 1983; STOTT, 1974):

1. Normal operation: At each iteration h of Newton-Raphson's numerical method, Jacobian matrix dimension is $2N_{PQ} + N_{PV}$, generator's reactive power generation is

within limits ($Q_{G_k,gen}^{min} < Q_{G_k,gen} < Q_{G_k,gen}^{max}$) and the bus voltage magnitude value is at reference value ($V_{k,gen} = V_{k,gen}^{ref}$).

2. Bus type modification routine (PV → PQ): A verification on $Q_{G_k,gen}$ must be made at each iteration h of Newton-Raphson's numerical method. If $Q_{G_k,gen} \geq Q_{G_k,gen}^{max}$, then the bus type must convert to PQ and $Q_{G_k,gen} = Q_{G_k,gen}^{max}$. Else, if $Q_{G_k,gen} \leq Q_{G_k,gen}^{min}$, then the bus type must also convert to PQ and $Q_{G_k,gen} = Q_{G_k,gen}^{min}$. For both cases, the Jacobian matrix dimensions must be redefined considering now the reactive power equations in order to update generator's bus voltage magnitude value.

3. *Backoff* routine (PQ → PV): If condition 2 is true, a verification on $Q_{G_k,gen}$ must be made at each iteration $h + 1$ of Newton-Raphson's numerical method. If $Q_{G_k} = Q_{G_k,gen}^{max}$ and $V_{k,gen} < V_{k,gen}^{ref}$, then generator's bus type remains as PQ. The same stands if $Q_{G_k,gen} = Q_{G_k,gen}^{min}$ and $V_{k,gen} > V_{k,gen}^{ref}$. In contrast, if $Q_{G_k,gen} = Q_{G_k,gen}^{max}$ and $V_{k,gen} \geq V_{k,gen}^{ref}$, the generator's bus type is reconfigured to PV, its voltage magnitude is equal to the reference value, and the Jacobian matrix dimension must be reconfigured. The same is valid for $Q_{G_k,gen} = Q_{G_k,gen}^{min}$ and $V_{k,gen} \leq V_{k,gen}^{ref}$.

Note that the *Backoff* routine should be considered only after Newton-Raphson's first iteration, in order to avoid convergence problems.

2.1.2 Static VAr Compensators

With the rising in the field of power electronics and the emergence of Flexible AC Transmission System (FACTS) devices during the 1990s, the operation of EPSs became more reliable and efficient (TAYLOR; SCOTT; HAMMAD, 1994; MATHUR; VARMA, 2002). SVC is one of the multiple control equipments that integrates FACTS's devices family and, of the multiple benefits it can provide to EPS, voltage stability enhancement and stability margin increment can be highlighted (PEREZ; MESSINA; FUERTE-ESQUIVEL, 2000; MILLER *et al.*, 1982). It is an electric equipment with fast control response, capable of injecting or absorbing reactive power in an EPS in order to control its own bus k, or a controlled bus m, voltage magnitude at a reference value (PEREZ; MESSINA; FUERTE-ESQUIVEL, 2000; TAYLOR; SCOTT; HAMMAD, 1994; ERINMEZ, 1986).

Different constructive topologies have been proposed for SVCs. One of the most commonly adopted in researches and real-life operations is the Fixed-Capacitor Thyristor-Controlled Reactor (FC-TCR) (KUNDUR, 1994; TAYLOR; SCOTT; HAMMAD, 1994), as illustrated by Figure 5. As it can be observed from this illustration, the term "static" that makes up the SVC name indicates that this control device has no moving or rotating components (MILLER *et al.*, 1982; KUNDUR, 1994). Instead, it is basically consisted of thyristors, reactors and capacitors, that are power electronics components.

Figure 5 – Static VAr Compensator FC-TCR topology.
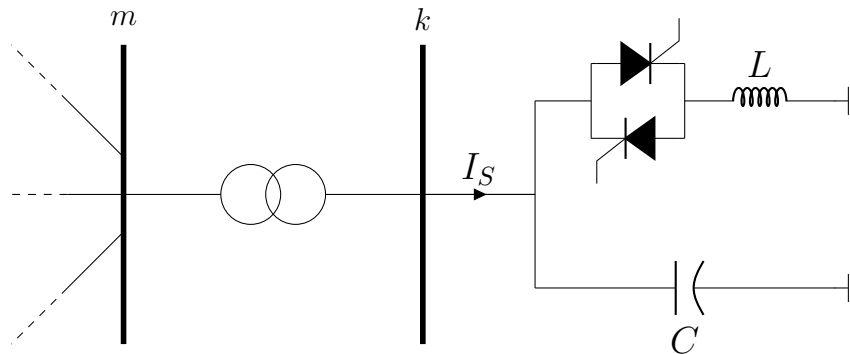
Source: Elaborated by the author (2023).

Initially, in Newton-Raphson's Power Flow (PF) formulation problem, SVCs were modeled as generators operating as Synchronous Condensers (TAYLOR; SCOTT; HAMMAD, 1994; ERINMEZ, 1986). Additionally, the SVC's connection bus is traditionally represented as PV type, applying the reactive power generation equation (2.7) to model its behavior. However, this modeling is only acceptable when the control device is operating within reactive power generation limits, otherwise a series of errors are identified (ALVARADO; DEMARCO, 1995). For that reason, other steady-state models were proposed in order to proper adjust simulation results to the SVC realistic operational behavior.

In this work, the methodologies proposed by Passos Filho (2000) and Ambriz-Perez, Acha and Fuerte-Esquivel (2000) will be detailed in the following sections and implemented in the following chapters. Besides these proposed methodologies, other SVC steady-state representation models are found in the literature, as in Cutsem and Vournas (2007, p.34).

2.1.2.1 *SVC reactive power injection methodology*

The SVC reactive power injection methodology proposed by Passos Filho (2000) is based on the control device steady-state VQ characteristic curve, as illustrated by Figure 6. This curve details the relationship between SVC's controlled bus m voltage magnitude ($V_{m,svc}$) and its reactive power generation ($Q_{G_k,svc}$) at bus k. It is considered a SVC connected at bus k, controlling the voltage magnitude of bus m. From Figure 6, three regions define the SVC operative behavior, nominated as: capacitive, linear and inductive.

First, the capacitive operational region is superiorly delimited by the controlled bus minimum voltage magnitude ($V_{m,svc}^{min}$). Likewise, the inductive operational region is delimited by the controlled bus maximum voltage magnitude ($V_{m,svc}^{max}$). SVC's linear operational region is inferiorly delimited by the capacitive region and superiorly delimited by the inductive region. The inequations that model SVC's operational regions are detailed below:

Figure 6 – Static VAr Compensator voltage magnitude per reactive power generation characteristic.
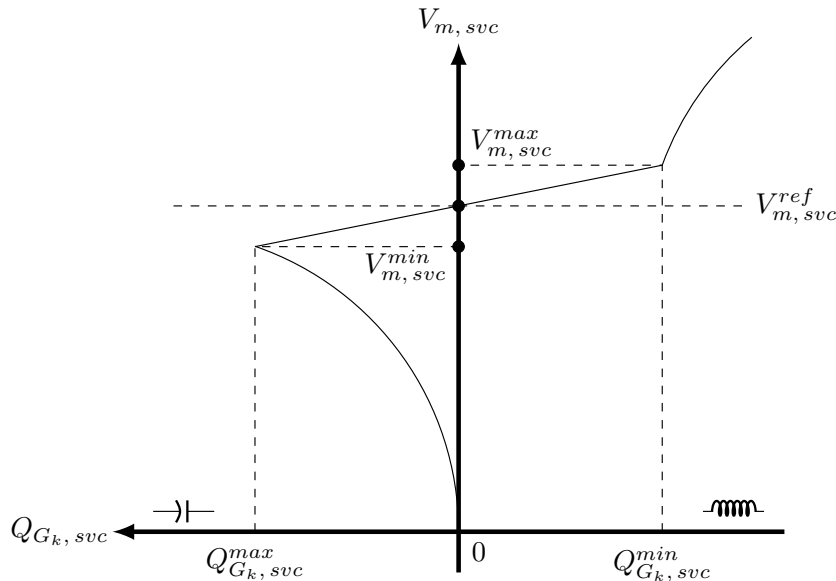
Source: Adapted from Passos Filho (2000).

$$\begin{cases} Q_{G_k,svc} = B_{svc}^{cap} \cdot V_{k,svc}^2 & \text{if } V_{m,svc} \leq V_{m,svc}^{min}, \\ Q_{G_k,svc} = \frac{V_{m,svc} - V_{m,svc}^{ref}}{r} & \text{if } V_{m,svc}^{min} < V_{m,svc} < V_{m,svc}^{max}, \\ Q_{G_k,svc} = B_{svc}^{ind} \cdot V_{k,svc}^2 & \text{if } V_{m,svc} \geq V_{m,svc}^{max}, \end{cases} \tag{2.19}$$

Note that the reactive power equation that models the linear operational region is characterized by a *droop*, defined by the 'r' variable. The *droop* is responsible for adjusting the SVC's controlled bus voltage magnitude around a reference value ($V_{m,svc}^{ref}$) according to the network behavior.

In his proposed methodology, Passos Filho (2000) considers a *full* Newton implementation. Hence, new control equations are incorporated into the Jacobian matrix based on the set of inequations (2.19) and the SVC reactive power generation variable is considered a new state variable (or control variable) in the PF. In addition, since the reactive power generation is given by (2.19) and not by (2.7), the PQ bus type is considered for SVCs.

2.1.2.2 *SVC current injection methodology*

Similarly to the previous methodology, the SVC current injection methodology proposed by Passos Filho (2000) is based on the control device steady-state VI characteristic curve, as illustrated by Figure 7. This curve details the relationship between SVC's controlled bus voltage magnitude ($V_{m,svc}$) and its current generation ($I_{k,svc}$). It is considered a SVC connected at bus k, controlling the voltage magnitude of bus m. From

Figure 7, three regions define the SVC operative behavior, nominated as: capacitive, linear and inductive.

Figure 7 – Static VAr Compensator voltage magnitude per current generation characteristic.
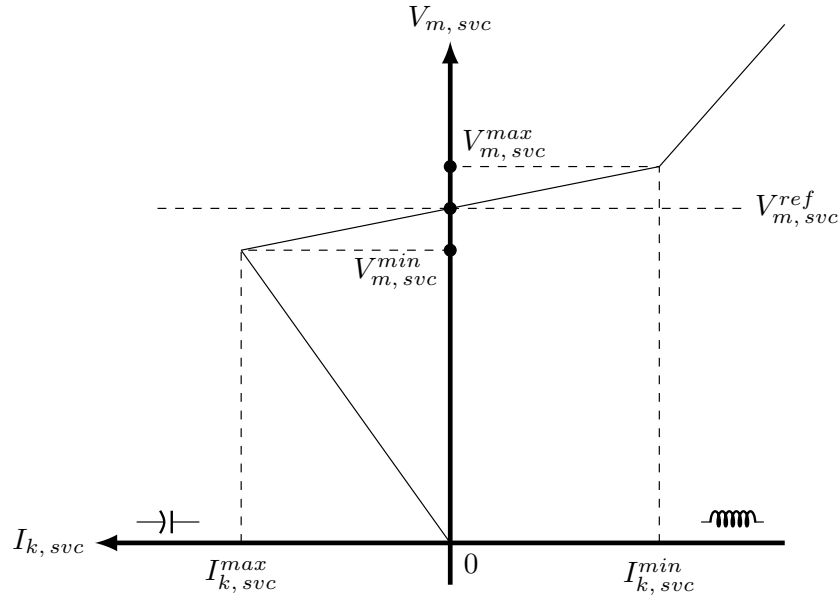
Each SVC's operational region is identically delimited as the reactive power injection methodology, detailed in the previous section. A difference, however, is noted on the inequations that model these operational regions, given the relationship between reactive power generation and current generation:

$$I_{svc} = \frac{Q_{G,svc}}{V_{svc}} \tag{2.20}$$

$$\begin{cases} I_{k,svc} = B_{svc}^{cap} \cdot V_{k,svc} & \text{if } V_{m,svc} \leq V_{m,svc}^{min}, \\ I_{k,svc} = \frac{V_{m,svc} - V_{m,svc}^{ref}}{r} & \text{if } V_{m,svc}^{min} < V_{m,svc} < V_{m,svc}^{max}, \\ I_{k,svc} = B_{svc}^{ind} \cdot V_{k,svc} & \text{if } V_{m,svc} \geq V_{m,svc}^{max}, \end{cases} \tag{2.21}$$

Note that the current equation that models the linear operational region is characterized by a *droop*, defined by the 'r' variable. The *droop*, once more, is responsible for adjusting the SVC's controlled bus voltage magnitude around a reference value ($V_{m,svc}^{ref}$) according to the network behavior.

In his proposed methodology, Passos Filho (2000) considers a *full* Newton implementation. Hence, new control equations are incorporated into the Jacobian matrix based on the set of inequations (2.21) and the SVC current generation variable is considered a new state variable (or control variable) in the PF. In addition, the PQ bus type is considered for SVCs, considering the (2.20) relationship between I_{svc} and $Q_{G,svc}$ variables.

2.1.2.3 *SVC thyristor firing-angle methodology*

The steady-state SVC thyristor firing-angle methodology proposed by Ambriz-Perez, Acha and Fuerte-Esquivel (2000) is based on the control device equivalent reactance and susceptance equations, as respectively defined by (2.22) and (2.23), considering the SVC FC-TCR topology configuration (MILLER *et al.*, 1982; ERINMEZ, 1986; KUNDUR, 1994).

$$x_{eq}\left(\alpha_{k,\,svc}\right) = \frac{X_C \cdot X_L}{\left(\frac{X_C}{\pi}\right) \cdot \left[2 \cdot \left(\pi - \alpha_{k,\,svc}\right) + \sin\left(2\alpha_{k,\,svc}\right)\right] - X_L} \tag{2.22}$$

$$b_{eq}\left(\alpha_{k,\,svc}\right) = -\frac{\left(\frac{X_C}{\pi}\right) \cdot \left[2 \cdot \left(\pi - \alpha_{k,\,svc}\right) + \sin\left(2\alpha_{k,\,svc}\right)\right] - X_L}{X_C \cdot X_L} \tag{2.23}$$

The thyristor firing-angle inferior and superior limits are 90° and 180°, respectively. The firing-angle variable is not allowed to vary between other range of angle values (KUNDUR, 1994). Considering k as the SVC's bus and m as the SVC's controlled bus, variable $\alpha_{k,\,svc}$ varies between its limits in order to adjust the equivalent susceptance value and, consequently, the SVC reactive power generation value:

$$Q_{G_k,\,svc} = V_{k,\,svc}^2 \cdot b_{eq}\left(\alpha_{k,\,svc}\right) \tag{2.24}$$

In this methodology the reactive power generated by the SVC is calculated in terms of the equivalent susceptance equation due to its continuity, which configures a better numerical behavior when linearized into the Jacobian matrix in comparison to the equivalent reactance outputs (AMBRIZ-PEREZ; ACHA; FUERTE-ESQUIVEL, 2000). In Figure 8, the relationship between the SVC equivalent reactance, and susceptance, equations and the thyristor firing-angle variable is depicted. For the proposed example, the capacitive and inductive reactances are equal to 50Ω and 25Ω, respectively.

According to the illustration, this SVC methodology only defines two operational regions for the control device, which are separated by the $\alpha_{k,\,svc}^0$ value (thyristor firing-angle for null reactive power generation). For values of $\alpha_{k,\,svc}$ smaller than $\alpha_{k,\,svc}^0$, the equipment characteristic is inductive. On the other hand, for values of $\alpha_{k,\,svc}$ bigger than $\alpha_{k,\,svc}^0$ the characteristic is capacitive.

In view of the relationship between reactive power generation and thyristor firing-angle in (2.24), the set of inequations that model this proposed SVC methodology is given by:

Figure 8 – Static VAr Compensator (a) equivalent reactance and (b) equivalent susceptance outputs as functions of the thyristor firing-angle.
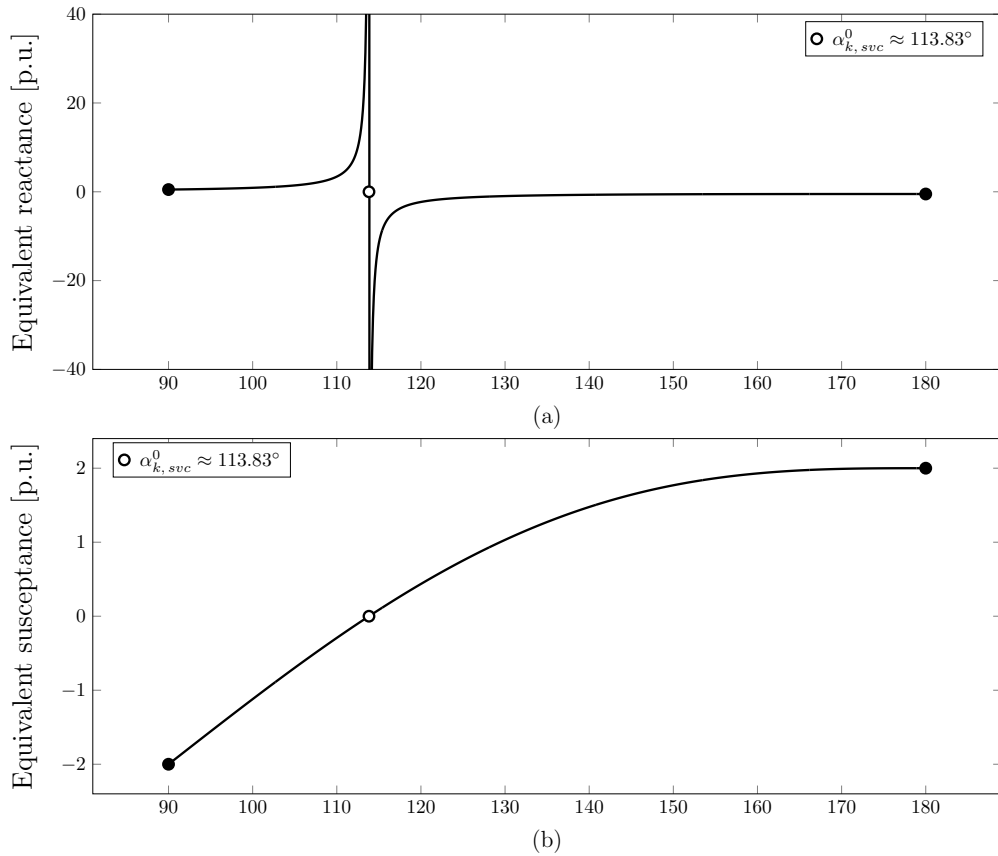
Static VAr Compensator FC-TCR thyristor firing-angle α [°C]

Source: Adapted from Ambriz-Perez, Acha and Fuerte-Esquivel (2000).

$$\text{For } 90° \leq \alpha_{k,svc} \leq 180° : \begin{cases} Q_{G_k,svc} = V_{k,svc}^2 \cdot b_{eq}\left(180°\right) & \text{if } V_{m,svc} < V_{m,svc}^{ref} \\ Q_{G_k,svc} = V_{k,svc}^2 \cdot b_{eq}\left(\alpha_{k,svc}\right) & \text{if } V_{m,svc} = V_{m,svc}^{ref} \\ Q_{G_k,svc} = V_{k,svc}^2 \cdot b_{eq}\left(90°\right) & \text{if } V_{m,svc} > V_{m,svc}^{ref} \end{cases} \quad (2.25)$$

In their proposed methodology, Ambriz-Perez, Acha and Fuerte-Esquivel (2000) alter the current reactive power generation equation (2.7) by reason of the SVC reactive power equation (2.24). This equation is then linearized into the Jacobian matrix based on the set of inequations (2.25) and the SVC thyristor firing-angle variable is considered a new state variable (or control variable) in the PF. In addition, the PQ bus type is considered for SVCs.

Although the Ambriz-Perez, Acha and Fuerte-Esquivel (2000) methodology correctly models SVCs steady-state behavior in the PF problem, a simplification on the control device *droop* is still carried out. Ideally, the SVC would be able to control the voltage magnitude of bus *m* at a reference value. However, a *droop* value between 1% and 5%

must be adopted in the SVC model in order to correctly represent its behavior in an EPS during PF analysis (TAYLOR; SCOTT; HAMMAD, 1994).

With the proposed *droop* implementation, the SVC thyristor firing-angle methodology becomes equivalent to the SVC reactive power injection methodology.

2.2 PARTIAL CONCLUSIONS

This chapter presented a brief review of the current and traditional literature on the steady-state PF formulation and modeling is made. The power system nonlinear equations are synthesized by (2.10), whereas the set of inequation constraints responsible for modeling electric device controls and operational limits are synthesized by (2.16).

Moreover, the main traditional steady-state modelings of generators and SVCs found in the PF literature were presented in this chapter. According to each proposed methodology, a set of inequations can be incorporated into the PF system of equations.

The methodologies presented in this chapter served as the basis for the implementations proposed in chapters 4 and 5. The proposed implementations consider the PF formulation detailed in Chapter 3, defined as Smooth Power Flow (SPF).

In conclusion, on account of the SVC thyristor firing-angle methodology, an improvement is proposed from the use of a *droop* variable. An analysis of the results obtained with the proposed improvement, in the SPF approach, is detailed in Chapter 5.

3 SMOOTH POWER FLOW FORMULATION

In this chapter, a brief review of the current works developed in the SPF research area is made. In particular, the work elaborated by Neves (2022) will be used as a reference, with due proportions.

An introduction to the Smooth Power Flow (SPF) formulation implemented in this work is made. It is proposed the employment of switches based on sigmoid function in the models of electric devices controls and operational limits in order to introduce the desired smoothness to the traditional PF formulation problem.

In the following sections, a study on the sigmoid function followed by its employment justification on the proposed SPF formulation process is presented. Additionally, an explanation on how to implement sigmoid switches to model different control equipments in the SPF problem is also given.

3.1 INITIAL CONSIDERATIONS

The SPF is a recent research methodology in the PF literature. It is based on the traditional PF formulation problem, adopting the same nonlinear system of equations to model an EPS as detailed in (2.10). The proposed methodology consists in modeling electric devices control and operational limits with the intention of enhancing voltage stability analysis for power systems. Therefore, a new formulation process is adopted for the system of inequations (2.16) that is incorporated to the traditional PF formulation.

A breakthrough work was developed by Neves (2022), introducing solid mathematical foundation for the SPF formulation as well as innovative contributions to current voltage stability literature. In this work, not only the modeling of different electrical devices control and operational limits is presented, but also new methods for contingency ranking and Voltage Stability Margin (VSM) are proposed and justified via the SPF methodology.

Besides the aforementioned work, other papers can be found in the PF literature regarding the advantages of the SPF formulation. An introductory work was published by Kataoka (2005), considering the modeling of reactive power generation limits via the use of a hyperbolic function or sigmoid function, transforming an *undifferentiable* condition into a *differentiable* condition.

A similar reactive power generation limits methodology was developed by Pontes, Passos Filho and La Gatta (2018, 2018). In its work, it is proposed the use of sigmoid function based switches in order to model generators operational behaviors. As a conclusion, it was observed that the traditional bus type re-specification is not needed (PV $\leftrightarrow$ PQ) and the overall number of iterations remain small with no alteration on the solution accuracy.

In Ju *et al.* (2020) is proposed a three-phase smooth power flow methodology. The proposed work considers a power flow analysis of microgrid systems, adopting a projected Levenberg-Marquardt (PLM) model after non-smooth constraints are converted into smooth functions. The non-smooth constraints of distributed generation models are analyzed in this work.

A new reactive power generation limit methodology is proposed in Neves, Alberto and Chiang (2020). In its approach, the proposed smooth model is applied for fast detecting LIBs caused by violations of reactive power generation limits. Based on the aforementioned work, Neves and Alberto (2020) explores the proposed methodology and determines new voltage stability indexes considering loading parameter uncertainties.

In sequence, new SPF models are proposed for different electric devices by Neves, Alberto and Chiang (2022b), considering their "*control limits and saturation effects approximations*". Additionally, the work details that every static bifurcation obtained via traditional PF simulation is then transformed into SNBs in the SPF formulation. This breakthrough information is then applied in estimating load margin for contingency screening and ranking in voltage stability analysis (NEVES; ALBERTO; CHIANG, 2022a).

More recently, the SPF reactive power generation limits model is employed for the review of power flow accuracy and load margin calculation based on bus-type switching (ZENG *et al.*, 2023). Two smooth functions are proposed and multiple power flow solutions are analyzed based on different PV to PQ switching schemes.

Regarding the use of sigmoid functions, it has been the focus of many works published in many research areas. In Uykan and Koivo (2004) the function is applied on the of development of cellular radio systems control algorithms. The sigmoid function is applied in a transmission expansion planning problem in Oliveira *et al.* (2005) to evaluate the best investment strategy. A work analyzing solar panel characteristics by applying sigmoid functions under various values of temperature and solar irradiance was published by Sapteka *et al.* (2018).

In this work, the sigmoid function is employed in the modeling of control limits of generators and SVCs. The methodology proposed by Pontes, Passos Filho and La Gatta (2018), Pontes (2018) is adopted for the aforementioned electric devices modelings and a special focus is given in voltage stability analysis. As mathematically proven by Neves, Alberto and Chiang (2022b), Neves (2022), the employment of smooth functions into the traditional PF formulation possibilitates the transformation of LIBs into corresponding SNBs. This condition is set to introduce great improvements in VSA, as it will be further explored in this work.

As mentioned before, the work developed in Neves (2022) introduces solid mathematical foundation for the SPF formulation and, therefore, it will be used as a main reference to the proposed PF smoothness introduced in this work.

3.2   THE SIGMOID FUNCTION

The sigmoid function equation is defined as follows:

$$sig\left(x\right) = \frac{1}{1 + e^{-slp \cdot \left(x - lim\right)}} \tag{3.1}$$

where x is the input variable, slp is the slope variable and lim is the inflection point variable.

According to Weisstein (2023) and based on (3.1), the sigmoid function derivative is given by:

$$\frac{\partial\, sig\left(x\right)}{\partial x} = slp \cdot \left(1 - sig\left(x\right)\right) \cdot sig\left(x\right) \tag{3.2}$$

This derivative property will be applied in Appendix A, where new Jacobian matrix terms are calculated.

Sigmoid functions most common output consists of the range of 0 to 1, although another commonly output range is from -1 to 1. In this work, the former output option is set default for the proposed sigmoid function applications. A representation on the sigmoid function output range of 0 to 1 is shown in Figure 9.

Figure 9 – Sigmoid function.
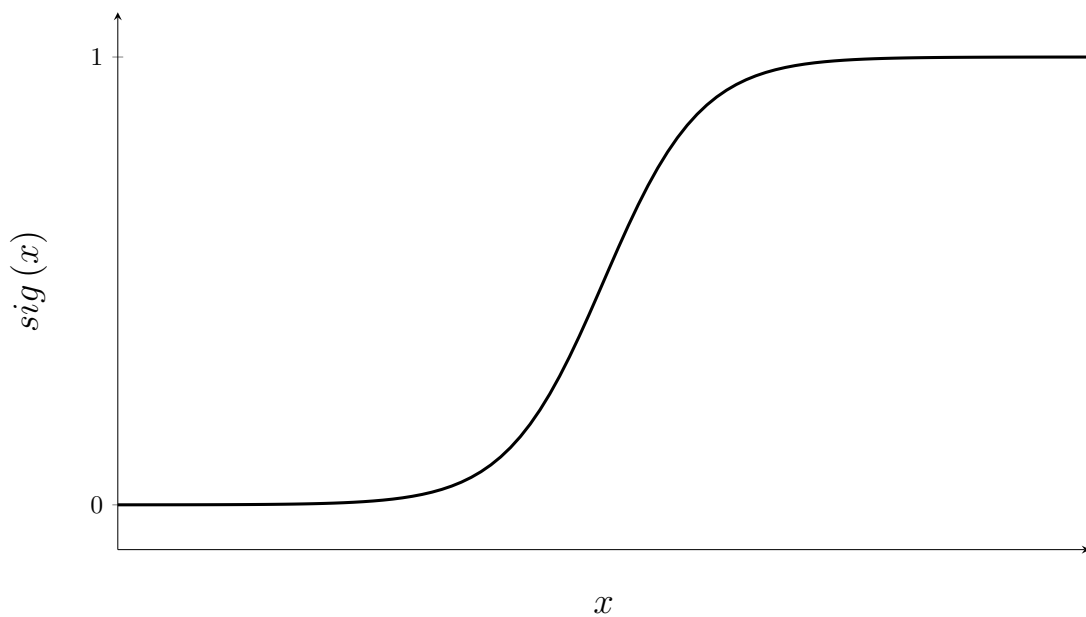
Source: Adapted from Pontes (2018).

If the exponential term (slp value) in the sigmoid function Euler's variable e becomes positive, then an inverse output behavior is noted. This condition is illustrated by Figure 10.

Figure 10 – Sigmoid function inverse behavior.
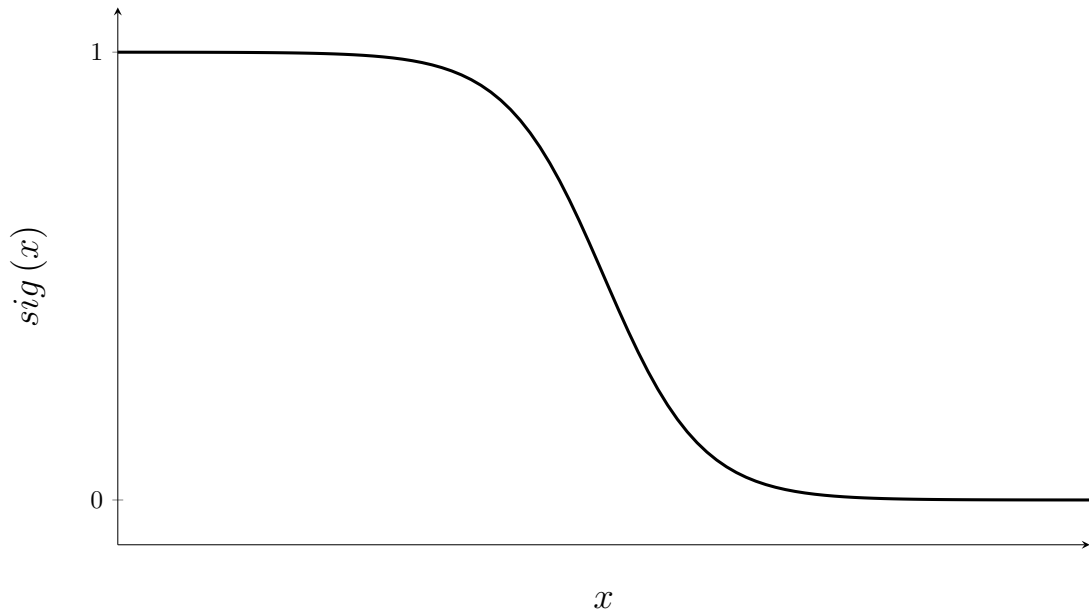
Source: Adapted from Pontes (2018).

The sigmoid function slope variable slp determines the curve inclination. As illustrated by Figure 11, a small slope value configures a slower transition between 0 and 1, whereas a big slope value configures a faster transition between 0 to 1.

Figure 11 – Sigmoid function slope variation.
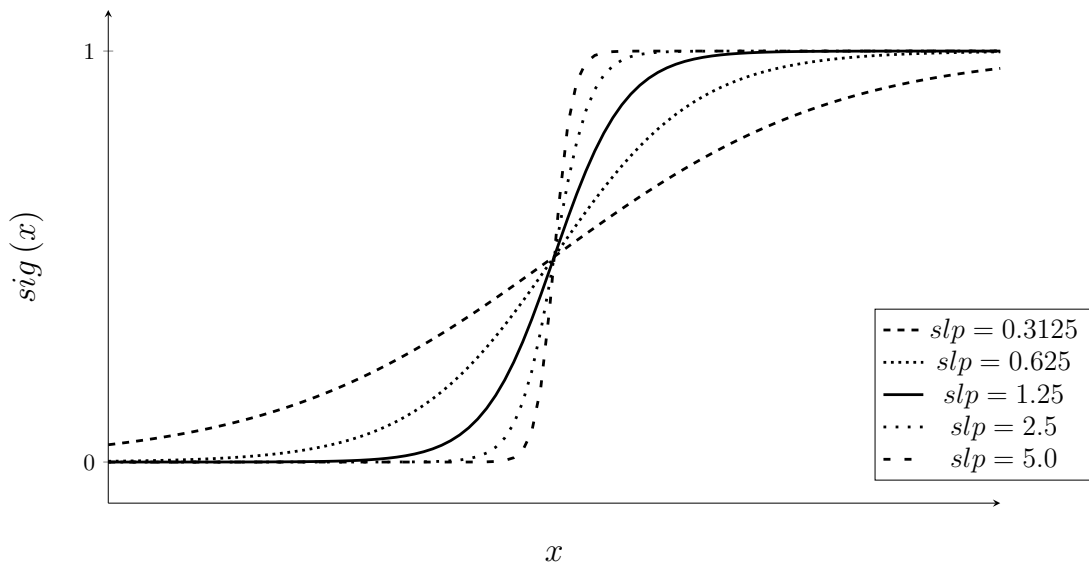
Source: Adapted from Pontes (2018).

Additionally, the sigmoid function inflection point variable lim configures the point where the transition happens. In Figure 12 is detailed how lim influences on the transition between the aforementioned default output range.

Figure 12 – Sigmoid function inflection point variation.
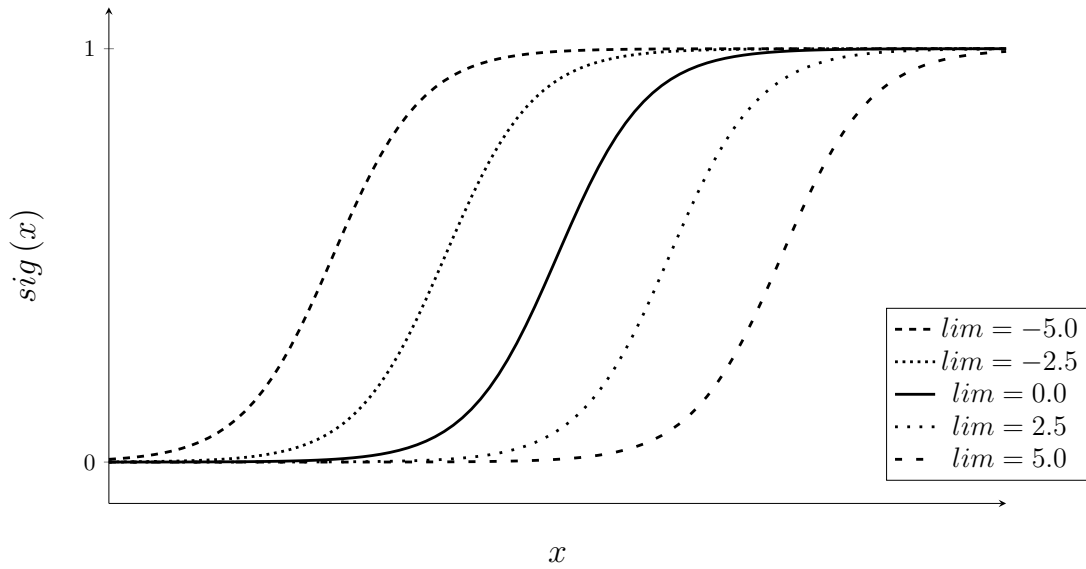
Source: Adapted from Pontes (2018).

3.2.1 Smoothness validity

Consider that control limits in PF, such as (2.18), can be represented in the xy-plane as shown in Figure 13, with x being the input variable and y the output variable (assume $y_1 < y_2$). The Transition Point (TP) indicates that a system structure changes between saturated and unsaturated modes and, therefore, a point (x, y) in Figure 13 should belong in any PF solution (NEVES, 2022).

Figure 13 – Control limits enabling transition between electric device operational behaviors based on the traditional modeling.
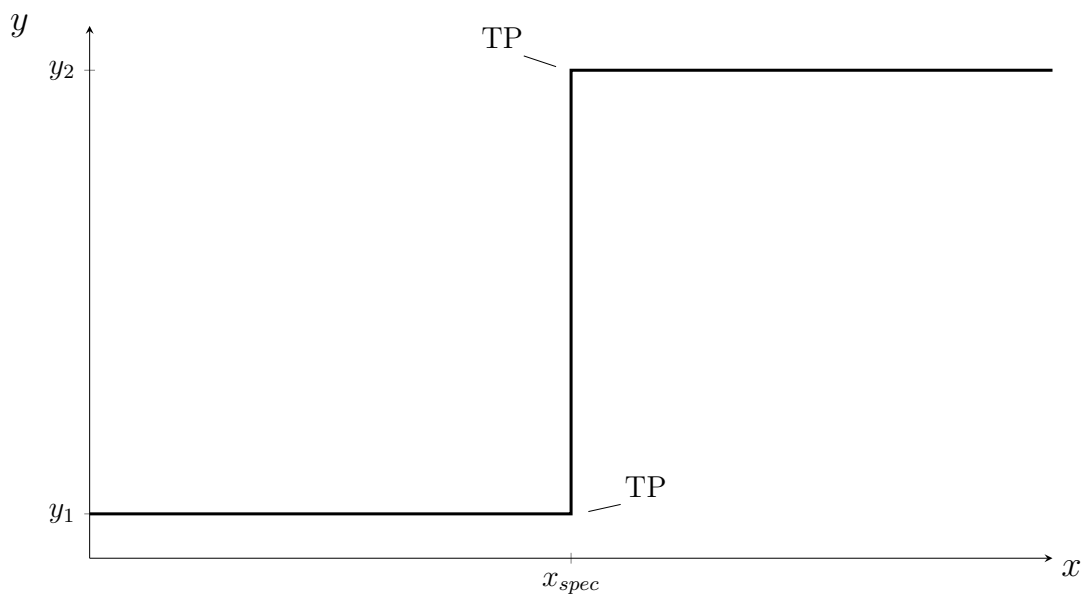
Source: Adapted from Neves (2022).

A main problem, however, consists of the discontinuities instanced in all inequations.

In the SPF formulation, therefore, it is proposed the adoption of *smooth step function* to model the inequations related to electric devices control and operational limits, also defined as saturated and unsaturated modes. The *smooth step function* is adopted in order to discard the discontinuity problems observed in the traditional PF formulation. In Neves (2022), a definition and equation for *smooth step function* are given, which are hereinafter detailed:

Definition 1 (Smooth step function). *A smooth step function is a family of C^1 functions $g_\gamma : \mathbb{R}^4 \to \mathbb{R}$, parameterized by a scalar variable $\gamma > 0$ and satisfying the following properties:*

[I] $\lim_{\gamma \to 0^+} g_\gamma(y, y_{spec}, u_1, u_2) = u_1 \ \forall \ y < y_{spec}$;

[II] $\lim_{\gamma \to 0^+} g_\gamma(y, y_{spec}, u_1, u_2) = u_2 \ \forall \ y > y_{spec}$;

[III] *there is $\alpha \in (0, |u_1 - u_2|)$ such that $\min\{u_1, u_2\} + \alpha \le g_\gamma(y, y_{spec}, u_1, u_2) \le \max\{u_1, u_2\} - \alpha$ for all γ;*

[IV] *there is $\zeta > 0$ such that $\min\{u_1, u_2\} \le g_\gamma(y, y_{spec}, u_1, u_2) \le \max\{u_1, u_2\} \ \forall \ y \in [y_{spec} - \zeta, y_{spec} + \zeta]$ for all γ;*

[V] *for all γ, g_γ changes concavity in relation to y only at $y = y_{spec}$.*

An example of smooth step function is defined by Neves (2022) as follows:

$$g_\gamma(y) = \begin{cases} u_1, & \text{if } y \le y_{spec} - \frac{\gamma}{2}, \\ u_2, & \text{if } y \ge y_{spec} + \frac{\gamma}{2}, \\ p(y), & \text{otherwise}, \end{cases} \tag{3.3}$$

for p being a cubic polynomial in variable y:

$$p(y) = \frac{u_1 + u_2}{2} + \left(\frac{u_2 - u_1}{2}\right) \cdot \left[3 \cdot \left(\frac{y - y_{spec}}{\gamma}\right) - 4 \cdot \left(\frac{y - y_{spec}}{\gamma}\right)^3\right] \tag{3.4}$$

which satisfies the following equations:

$$p\left(y_{spec} - \frac{\gamma}{2}\right) = u_1 \qquad (3.5\text{a}) \qquad\qquad p\left(y_{spec} + \frac{\gamma}{2}\right) = u_2 \qquad (3.5\text{c})$$

$$p'\left(y_{spec} - \frac{\gamma}{2}\right) = 0, \qquad (3.5\text{b}) \qquad\qquad p'\left(y_{spec} + \frac{\gamma}{2}\right) = 0, \qquad (3.5\text{d})$$

Despite the differences between the sigmoid function (3.1) and the smooth function (3.3), (3.4) adopted by Neves (2022), it can be easily verified that the properties in Definition 1 are satisfied by the sigmoid function. The sigmoid function validity will be based on an adapted version of the aforementioned definition, considering the differences between functions.

Properties [I] and [II] are satisfied considering the adoption of a high slope value $(slp \rightarrow +\infty \equiv \gamma \rightarrow 0^+)$. The sigmoid function slope variable is associated with the cubic polynomial function γ variable.

Property [III] is satisfied if the input variable x is equal to the inflection point variable lim, returning $sig\,(x = lim) = \frac{1}{2}$. Since the sigmoid function adopted output consists of the range of 0 to 1, $sig\,(x = lim) = g_\gamma\,(y_{spec}) = p\,(y_{spec}) = \frac{u_1+u_2}{2}$ whenever $u_1 \neq u_2$.

Property [IV] is satisfied considering $0 \leq sig\,(x) \leq 1 \,\forall\, x \,\in\, [x_{spec} - slp, x_{spec} + slp]$. The slope variable has great influence on the sigmoid function output, as it is detailed in Figure 14.

Property [V] is satisfied for the reason that sigmoid function also changes concavity in the mean of its critical points, at $\frac{(x_{spec}-slp)+(x_{spec}+slp)}{2} = x_{spec}$, similar to the cubic polynomial function (3.4).

As a result, the sigmoid function fits within the *smooth step function* definition and, therefore, can be implemented in a SPF formulation proposal. The control limit transition between saturated and unsaturated modes illustrated in Figure 13 can be reformulated considering now the sigmoid function, as shown in Figure 14. The main difference between figures consists on the slope value adopted, since that, as slp tends to ∞, both illustrations will be equal (NEVES, 2022).

In the following section, a representation of how the sigmoid function is applied in the modeling of electric devices control and operational limits is detailed. The inequations that model an electric device saturated and unsaturated modes will be reformulated considering the implementation of sigmoid function based switches.

3.2.2 Implementation process

As previously mentioned, the SPF principle considers a reformulation on the set of inequations (2.16) that model eletric devices controls and operational limits. In Neves (2022), Neves, Alberto and Chiang (2022a), a set of control models are reformulated considering the cubic polynomial function (3.3), (3.4). Correspondingly, sigmoid function based switches are employed in the modeling of reactive power generation limits in Pontes, Passos Filho and La Gatta (2018).

The SPF approach taken by (PONTES; PASSOS FILHO; LA GATTA, 2018) was

Figure 14 – Control limits enabling transition between electric device operational behaviors based on sigmoid function approach.
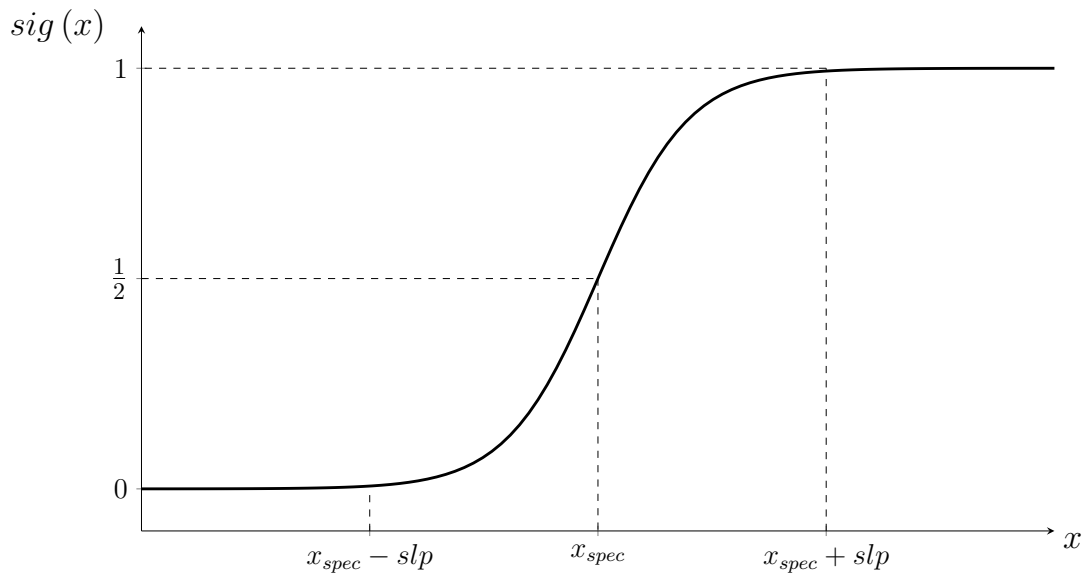
Source: Adapted from Neves (2022).

implemented in this work and is hereinafter detailed.

The main objective is to associate a pair of sigmoid function based switches to each PF state variable, or control variable, responsible for the control modeling. In general, if the modeling of an electric device considers N operative modes, the number of sigmoid switches adopted must be N-1.

Independently on the number of sigmoid function based switches adopted, the switches are arranged to control equations that model the electric devices saturated or unsaturated modes. Afterwards, the control equations corresponding to each mode are combined together into one equivalent control equation.

In order to arrange the sigmoid function based switches to control equations, it is applied the mathematical logic of truth tables. Since the sigmoid functions default outputs are in the range of 0 to 1, the switches can be considered as logical variables. In order to do so, a very high value must be assigned to the slope variable, approximating Figure 14 to Figure 13 as mentioned previously.

The invention of truth tables is accredited to Ludwig Wittgenstein, in his work *Tractatus Logico-Philosophicus* published in 1922. Since then, it has been focus of many works that involves combination of logical variables (ENDERTON, 2001). In the field of electrical engineering, truth tables and mathematical logic is commonly applied in the development of digital systems and circuits.

The following example details how truth tables and sigmoid function based switches are applied together for the modeling of electric devices controls and operational limits.

To clearify, the expressions "switches" or "sigmoid switches" will be used in place

of "sigmoid function based switches".

3.2.2.1 *Example*

Let a generic control of an electric device be represented by the following inequations:

$$\begin{cases} A = A^{min} & \text{if } B > B^{ref} \\ A^{min} < A < A^{max} & \text{if } B = B^{ref} \\ A = A^{max} & \text{if } B < B^{ref} \end{cases} \tag{3.6}$$

where A and B are variables in the PF problem.

Considering that the electric device possesses three different operational states and only variable A is needed to determine them, then a total of two sigmoid switches are employed in the given SPF modeling. Each switch is associated with a control equation, and a combination of switches is associated with the control equation remaining.

In order to correctly model the electric device control in the proposed formulation, the adopted sigmoid switches must have alternating behaviors. In other words, while $swa1$ alters from 0 to 1, $swa2$ must alter from 1 to 0, as illustrated by Figure 15. Therefore, the combination of these sigmoid switches possibilitates a correct control equation output.

Figure 15 – Sigmoid switches *swa1* and *swa2* values in accordance to electric device control limits. Adopted slope $slp = 10^8$.
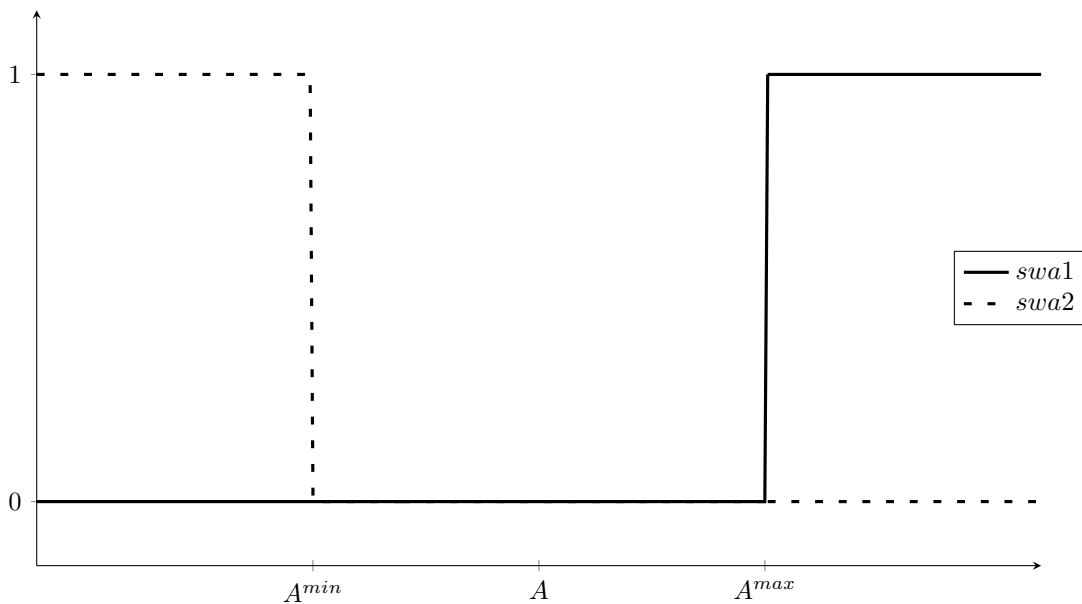
Source: Elaborated by the author (2023).

If the control equation $yc1$ depends on $A = A^{max}$, which in turn is associated with $swa1$ high output, then the truth table is given by Table 1. Similarly, if the control

equation $yc2$ depends on $A = A^{min}$, which in turn is associated with $swa2$ high output, then the truth table is given by Table 2.

Table 1 – Truth table for control equation $yc1$.

$swa1$	$swa2$	$yc1$		
0	0	0		
0	1	0		
1	0	1	$\Rightarrow$	$swa1$
1	1	×		

Source: Elaborated by the author (2023).

Table 2 – Truth table for control equation $yc2$.

$swa1$	$swa2$	$yc2$		
0	0	0		
0	1	1	$\Rightarrow$	$swa2$
1	0	0		
1	1	×		

Source: Elaborated by the author (2023).

Note that the condition where both switches present high value is never achieved, as illustrated in Figure 15 and defined in Tables 1 and 2 by the × output value. Therefore, for the remainder control equation $yc3$, switches are combined as $(\neg swa1) \land (\neg swa2)$.

Combining the results presented, the corresponding control equation yc for the model analyzed by inequations in Equation 3.6 is defined by (3.7). This control equation can, therefore, be incorporated in the PF system of nonlinear equations to complete the SPF formulation process.

$$yc = swa1 \cdot yc1 + swa2 \cdot yc2 + (1 - swa1) \cdot (1 - swa2) \cdot yc3 \qquad (3.7)$$

Another scenario could be analyzed if the state variable B also influences in the electric device operational states. In this case, two more operational modes as well as two more sigmoid switches must be considered in the proposed SPF modeling. This increases the complexity on the truth table analysis as well as the corresponding control equation outcome but not impossibilitates the SPF control model formulation.

3.3 PARTIAL CONCLUSIONS

This chapter presented a review of the current works developed in the SPF. Among the published works, a special emphasis should be given to Kataoka (2005) for first

developing work in this research area, to Pontes, Passos Filho and La Gatta (2018), Pontes (2018) for first introducing sigmoid switches in the modeling of reactive power generation control limits, and to Neves (2022) for laying out a solid mathematical foundation for the SPF formulation analysis, along with all the works published by the author.

The implementation of sigmoid function based switches to model electric devices controls and operational limits is justified according to the definition in Neves (2022). It was certified that sigmoid function fits the *smooth step function* requirements in order to introduce the desired smoothness to the traditional PF formulation problem, and how the nonsmooth control limits can be approximated by the sigmoid function approach.

In conclusion, not only was the sigmoid function characteristics detailed but also the implementation process was made in this chapter. This implementation process will be applied in the modeling of generators reactive power limits and SVCs, as it will be presented in Chapters 4 and 5, respectively. Later, in Chapter 6, a deeper analysis on the smoothness introduced by the sigmoid function will be presented.

4 REACTIVE POWER GENERATION LIMITS

In this chapter, the main methodology to model generators' reactive power limits presented in Chapter 2 will be reformulated based on Chapter 3 SPF proposition.

For the smooth methodology here developed, the Jacobian matrix dimension must be redefined considering the number of active generators in the power system ($2\text{N}_{\text{BUS}} + \text{N}_{\text{GEN}}$). Due to the *full* Newton characteristic, the new control equations are incorporated internally in the Jacobian matrix. Therefore, a dimension redefinition must be made during the PF or the CPF simulations.

The proposed methodology was first introduced by Pontes (2018), Pontes, Passos Filho and La Gatta (2018). It considers the implementation of sigmoid switches in order to model generators different *modus operandi*, nominated as: "normal", reactive power generation "superior limit violation" and reactive power generation "inferior limit violation". A total of four sigmoid switches are employed to model generators' reactive power limits, allowing a *backoff* routine to take place and correctly assign the best operational state for the device during the PF iterative process.

The following sections will detail the respective SPF formulation proposed to model generators' reactive power limits. To clarify, the expressions "switches" or "sigmoid switches" will be used in place of "sigmoid function based switches".

4.1 SPF-GENERATORS' REACTIVE POWER LIMITS

Four sigmoid switches were employed in the SPF-Generators' reactive power generation limits methodology (PONTES, 2018; PONTES; PASSOS FILHO; LA GATTA, 2018). The switches expressions are detailed in Equations (4.1) to (4.4). For this methodology, the new state variable is the reactive power generated by the control device $Q_{G_k, gen}$.

$$sw1 = \frac{1}{1 + e^{-slp \cdot (Q_{G_k, gen} - lim_q^{sup})}}, \tag{4.1}$$

$$sw2 = \frac{1}{1 + e^{+slp \cdot (Q_{G_k, gen} - lim_q^{inf})}}, \tag{4.2}$$

$$sw3 = \frac{1}{1 + e^{+slp \cdot (V_{k, gen} - lim_v^{sup})}}, \tag{4.3}$$

$$sw4 = \frac{1}{1 + e^{-slp \cdot (V_{k, gen} - lim_v^{inf})}}, \tag{4.4}$$

where:

- lim_q^{sup} is equal to $Q_{G_k, gen}^{max} - tol_q$,

- lim_q^{inf} is equal to $Q_{G_k, gen}^{min} - tol_q$,

- lim_v^{sup} is equal to $V_{k, gen}^{ref} - tol_v$,

- lim_v^{inf} is equal to $V_{k, gen}^{ref} - tol_v$.

The main operative objective of generators, when connected to a k-bus, is to supply active and reactive power generation in order to meet the power systems load demand. Switches *sw1* and *sw2* correspond to the reactive power generated by the equipment, with transition points occuring at lim_q^{sup} and lim_q^{inf}, respectively. On the other hand, switches *sw3* and *sw4* correspond to the generator bus voltage magnitude, with transition points occuring at lim_v^{sup} and lim_v^{inf}, respectively. The operative behavior of each pair of switches are illustrated in Figures 16 and 17, respectively.

Figure 16 – Sigmoid switches *sw1* and *sw2* values in accordance to generators' reactive power limits. Adopted slope $slp = 10^8$.
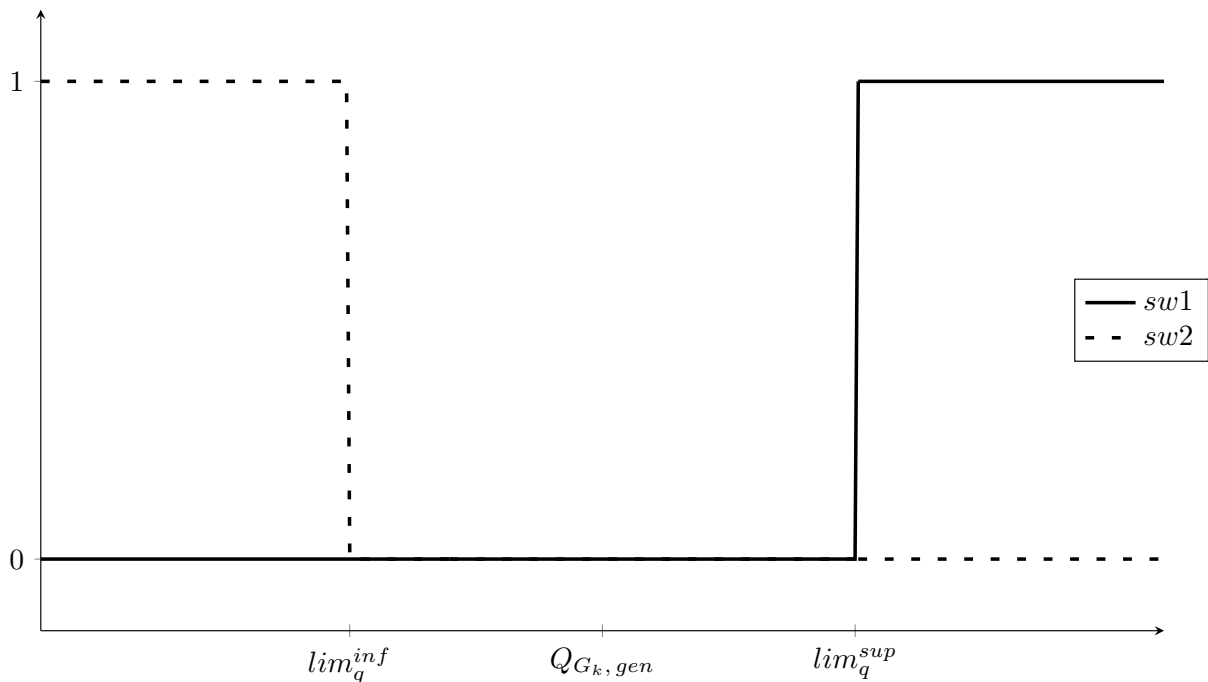
As it can be observed, switches *sw1* and *sw2* have an inverse operation behavior in comparison with switches *sw3* and *sw4*. This condition is not problematic for the SPF-Generator modeling. On the contrary, the conjunction of the two pair of switches allows a better transition between generator's operational states, as it will be further detailed.

Figure 17 – Sigmoid switches *sw3* and *sw4* values in accordance to generators' reactive power limits. Adopted slope $slp = 10^8$.
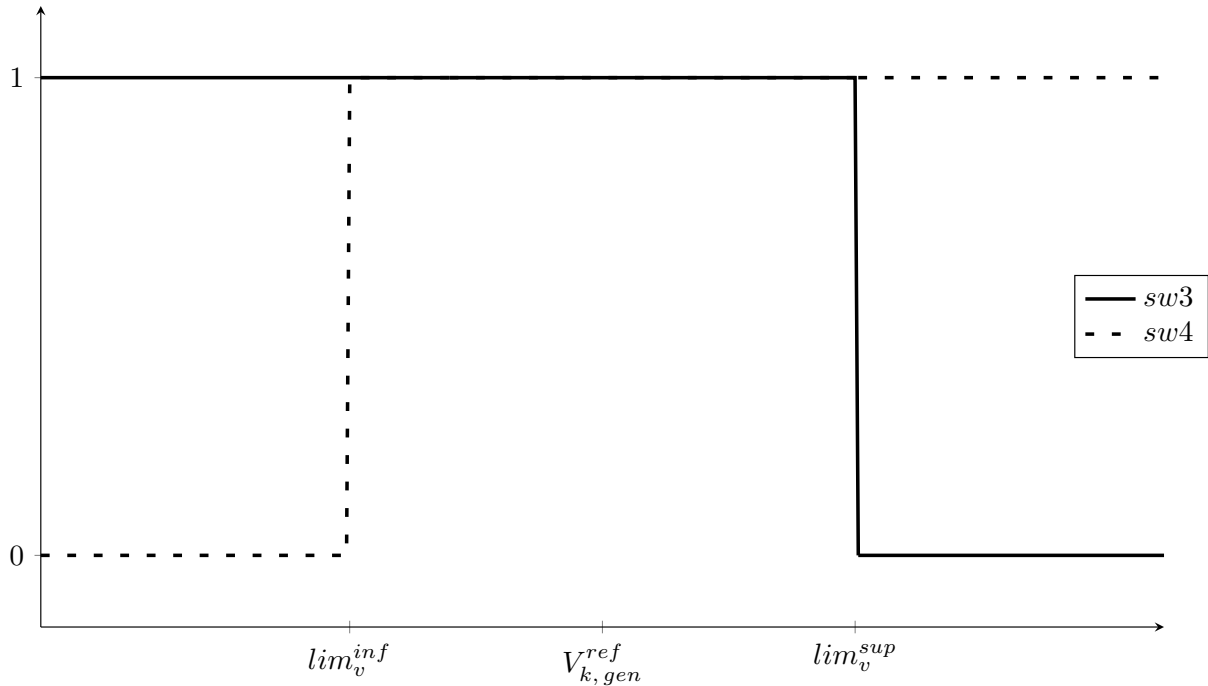
Source: Adapted from Pontes (2018).

Once again, the switches are associated with the generator's control equations that best describes each operative state. As a result, Equation (4.5) combines the aforementioned switches and operative regions equations in one only control equation which will then be linearized and incorporated into the Jacobian matrix traditional PF formulation.

$$
\begin{aligned}
y \ = \ & (sw1 \cdot sw3) \cdot (1 - sw2 \cdot sw4) \cdot \left(Q_{G_k, gen} - Q_{G_k, gen}^{max}\right) \cdots \\
& + (1 - sw1 \cdot sw3) \cdot (1 - sw2 \cdot sw4) \cdot \left(V_{k, gen} - V_{k, gen}^{ref}\right) \cdots \\
& + (1 - sw1 \cdot sw3) \cdot (sw2 \cdot sw4) \cdot \left(Q_{G_k, gen} - Q_{G_k, gen}^{min}\right).
\end{aligned}
\tag{4.5}
$$

In the above equation, the reactive power generation variable $Q_{G_k, gen}$ is the new state variable. Regarding the multiple control equations within (4.5), due to the use of four sigmoid switches, a better modeling of the switches should be made in order to avoid undesirable transition conflicts. In Table 3 it is described control equation (4.5) residue for each operational state of the SVC.

Each generator's operational states is better explained below. Due to the presence of four sigmoid switches, a better and detailed transition between operational states is made. As it is informed in Table 3, the four sigmoid switches allow a *backoff* routine to take place. The multiple $\times$ visible in Table 3 can be interpreted as non-interfering value of the sigmoid switch on the overall output result.

Table 3 – Generators' sigmoid switches operation and control equation output.

	Operational State	sw1	sw2	sw3	sw4	Δy
1	Superior Limit Violation	1	0	1	$\times$	$Q_{G_k,gen}^{max} - Q_{G_k,gen}$
2	Superior Limit *Backoff*	1	0	0	$\times$	
3	Normal	0	0	$\times$	$\times$	$V_{k,gen}^{ref} - V_{k,gen}$
4	Inferior Limit *Backoff*	0	1	$\times$	0	
5	Inferior Limit Violation	0	1	$\times$	1	$Q_{G_k,gen}^{min} - Q_{G_k,gen}$

Source: Elaborated by the author (2023).

- Operation 1 is active when the reactive power generated is greater than or equal to the maximum supported ($Q_{G_k,gen} \geq Q_{G_k,gen}^{max}$);

- Operation 2 is active when the reactive power generation is greater than or equal to the maximum supported and the voltage magnitude is greater than the referenced value ($Q_{G_k,gen} \geq Q_{G_k,gen}^{max}$ & $V_{k,gen} > V_k^{ref}$);

- Operation 3 is active when the reactive power generated is within the limits ($Q_{G_k,gen}^{min} < Q_{G_k,gen} < Q_{G_k,gen}^{max}$);

- Operation 4 is active when the reactive power generation is less than or equal to the minimum supported and the voltage magnitude is less than the referenced value ($Q_{G_k,gen} \leq Q_{G_k,gen}^{min}$ & $V_{k,gen} < V_k^{ref}$);

- Operation 5 is active when the reactive power generated is less than or equal to the minimum supported ($Q_{G_k,gen} \leq Q_{G_k,gen}^{min}$).

On account of the control equation (4.5) and the new state variable, the Jacobian matrix shape is redefined. New line and column will be appended to the original matrix formation for each generator active on the electrical system. Therefore, new differential terms will be present in the augmented Jacobian matrix, which are shown in Equation (4.6).

The new differential terms corresponds to differentiating the state equations $\boldsymbol{P}$ and $\boldsymbol{Q}$ in terms of the new state variable, and to differentiating the new control equation in terms of the state variables $\boldsymbol{\theta}$, $\boldsymbol{V}$ and $\boldsymbol{Q_{G_k,gen}}$. The mathematical calculation of each new differential term can be found in Appendix A.

$$
\begin{bmatrix}
\vdots \\
\Delta P_k \\
\Delta P_m \\
\vdots \\
\Delta Q_k \\
\Delta Q_m \\
\vdots \\
\Delta y \\
\vdots
\end{bmatrix}
=
\begin{bmatrix}
\ddots & \vdots & \vdots & \cdots & \vdots & \vdots & \cdots & \vdots & \iddots \\
\cdots & \frac{\partial P_k}{\partial \theta_k} & \frac{\partial P_k}{\partial \theta_m} & \cdots & \frac{\partial P_k}{\partial V_k} & \frac{\partial P_k}{\partial V_m} & \cdots & \frac{\partial P_k}{\partial Q_{G_k,gen}} & \cdots \\
\cdots & \frac{\partial P_m}{\partial \theta_k} & \frac{\partial P_m}{\partial \theta_m} & \cdots & \frac{\partial P_m}{\partial V_k} & \frac{\partial P_m}{\partial V_m} & \cdots & \frac{\partial P_m}{\partial Q_{G_k,gen}} & \cdots \\
\cdots & \vdots & \vdots & \cdots & \vdots & \vdots & \cdots & \vdots & \cdots \\
\cdots & \frac{\partial Q_k}{\partial \theta_k} & \frac{\partial Q_k}{\partial \theta_m} & \cdots & \frac{\partial Q_k}{\partial V_k} & \frac{\partial Q_k}{\partial V_m} & \cdots & \frac{\partial Q_k}{\partial Q_{G_k,gen}} & \cdots \\
\cdots & \frac{\partial Q_m}{\partial \theta_k} & \frac{\partial Q_m}{\partial \theta_m} & \cdots & \frac{\partial Q_m}{\partial V_k} & \frac{\partial Q_m}{\partial V_m} & \cdots & \frac{\partial Q_m}{\partial Q_{G_k,gen}} & \cdots \\
\cdots & \vdots & \vdots & \cdots & \vdots & \vdots & \cdots & \vdots & \cdots \\
\cdots & \frac{\partial y}{\partial \theta_k} & \frac{\partial y}{\partial \theta_m} & \cdots & \frac{\partial y}{\partial V_k} & \frac{\partial y}{\partial V_m} & \cdots & \frac{\partial y}{\partial Q_{G_k,gen}} & \cdots \\
\iddots & \vdots & \vdots & \cdots & \vdots & \vdots & \cdots & \vdots & \ddots
\end{bmatrix}
\cdot
\begin{bmatrix}
\vdots \\
\Delta \theta_k \\
\Delta \theta_m \\
\vdots \\
\Delta V_k \\
\Delta V_m \\
\vdots \\
\Delta Q_{G_k,gen} \\
\vdots
\end{bmatrix}
\tag{4.6}
$$

4.2 SPF-GENERATOR FLOWCHART

On account of the proposed SPF-Generator methodology, Figure 18 flowchart describes a standard algorithm to implement the model in the PF traditional formulation.

In this flowchart, a definition for the sigmoid switches value is made for the respective proposed methodology implemented. Along with that, the new control variable ($Q_{G_k,gen}$) is incorporated in the nonlinear system of equations.

The proposed implementation methodology considers the *full* Newton approach. The control equations related to each actively operating generator present in the electric power system are linearized and solved together with the state equations that model the electric power system in study.

4.3 PARTIAL CONCLUSIONS

This chapter presents a relevant contribution to the current literature on generator's reactive power limits model. This contribution is described in the following item:

- A SPF-Generator methodology to model reactive power generation limits in the PF problem. The proposed methodology is implemented via *full* Newton approach by the incorporation of new control equations into the nonlinear system of equations.

As it will be described in Chapter 6, the proposed SPF-Generator modeling also presents new contributions to power systems' voltage stability.

Figure 18 – SPF-Generator standard flowchart.
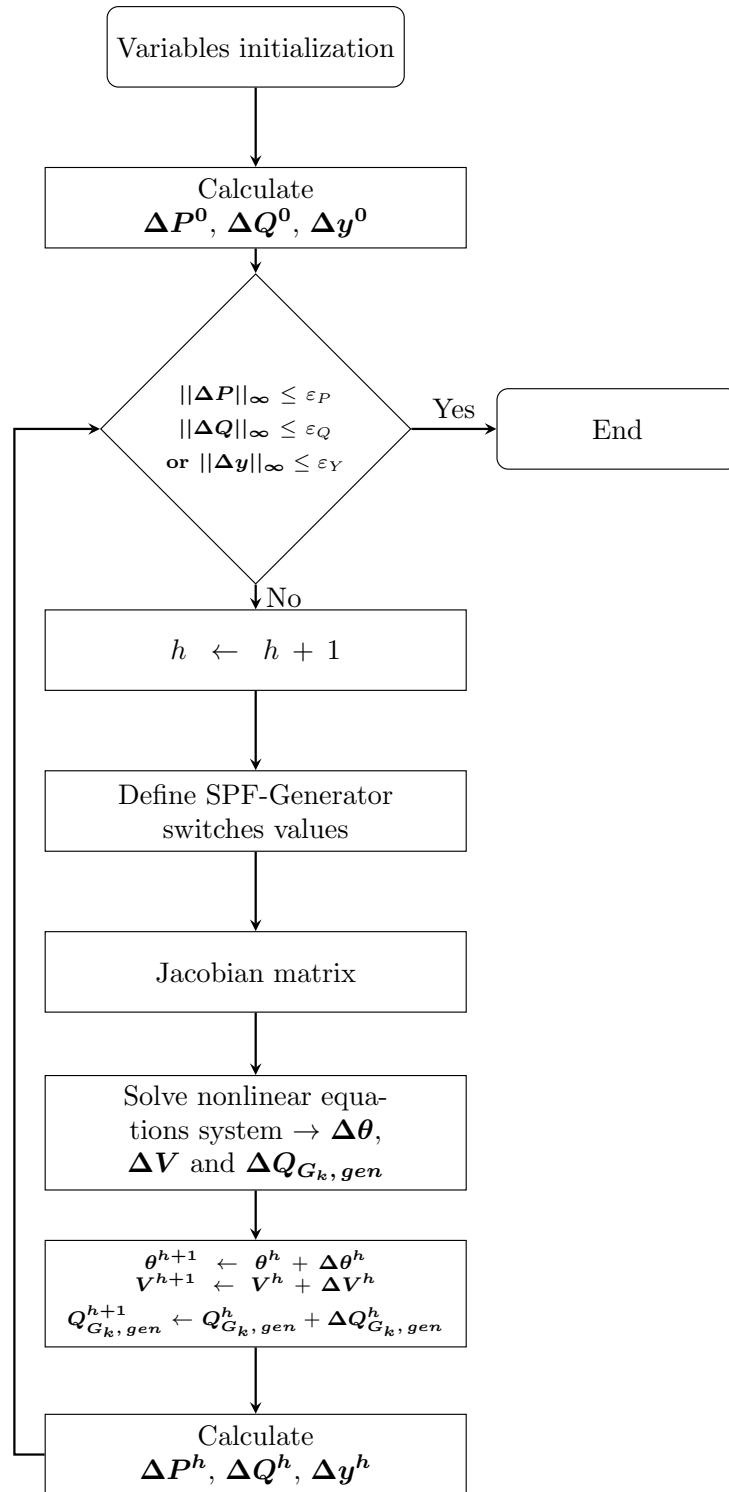
Source: Elaborated by the author (2023).

5 STATIC VAr COMPENSATOR

In this chapter, the main SVCs methodologies presented in Chapter 2 will be reformulated based on Chapter 3 SPF proposition.

For every smooth methodology here developed, the Jacobian matrix dimension must be redefined considering the number of active SVCs in the power system ($2N_{BUS} + N_{SVC}$). Due to the *full* Newton characteristic, the new control equations are incorporated internally in the Jacobian matrix. Therefore, a dimension redefinition must be made during the PF or the CPF simulations.

First, the proposed SPF will be employed to model two methodologies, based on the work developed by Passos Filho (2000). Despite the similarities between both methodologies, each possesses different analytical purposes. Later, the SPF will be employed to model the thyristor firing-angle methodology (AMBRIZ-PEREZ; ACHA; FUERTE-ESQUIVEL, 2000).

In conclusion, Section 5.4 details observations upon each proposed SPF-SVC methodology. The proposed improvement into the thyristor firing-angle model, mentioned in Chapter 2, will also be discussed in Section 5.3.

To clarify, the expressions "switches" or "sigmoid switches" will be used throughout the next sections in place of "sigmoid function based switches".

5.1 SPF-SVC REACTIVE POWER INJECTION METHODOLOGY

Two sigmoid switches are employed to model SVCs based on the reactive power injection methodology (PASSOS FILHO, 2000). It was opted to employ two sigmoid switches in this SPF-SVC model due to the direct relationship between reactive power generation and controlled bus voltage magnitude, illustrated by Figure 6.

The switches expressions are detailed in Equations (5.1) and (5.2). For this methodology, the new state variable is the reactive power generated by the control device $Q_{G_k, svc}$.

$$sw5 = \frac{1}{1 + e^{-slp \cdot (V_{m, svc} - lim_v^{sup})}}, \tag{5.1}$$

$$sw6 = \frac{1}{1 + e^{+slp \cdot (V_{m, svc} - lim_v^{inf})}}, \tag{5.2}$$

where:

- lim_v^{sup} is equal to $\left(V_{m,svc}^{ref} + r \cdot B_{svc}^{ind} \cdot V_{k,svc}^2\right) + tol_v$,

- lim_v^{inf} is equal to $\left(V_{m,svc}^{ref} + r \cdot B_{svc}^{cap} \cdot V_{k,svc}^2\right) - tol_v$,

$$B_{svc}^{cap} = B_{svc}^{max} = b_{eq}(\alpha_{k,svc} = 180°) = \frac{Q_{G_k,svc}^{max}}{\left(V_{k,svc}^{min}\right)^2}, \tag{5.3}$$

$$B_{svc}^{ind} = B_{svc}^{min} = b_{eq}(\alpha_{k,svc} = 90°) = \frac{Q_{G_k,svc}^{min}}{\left(V_{k,svc}^{max}\right)^2}. \tag{5.4}$$

The main operative objective of the SVC, when connected to k-bus, is to control a specified bus voltage magnitude at a reference value $V_{m,svc}^{ref}$. Hence, switches *sw5* and *sw6* transition points occur at lim_v^{sup} and lim_v^{inf}, respectively. The transition points are evaluated in respect to the new state variable as well as to SVC's constructive characteristics.

In order to elucidate how *sw5* and *sw6* work, Figure 19 illustrates the switches values for each operative region of the control device. Equation (5.1) is associated with the transition between SVC's "Linear" and "Inductive" operative regions, whereas (5.2) is associated with SVC's "Linear" and "Capacitive" operative regions transition.

Figure 19 – Sigmoid switches *sw5* and *sw6* values in accordance to SVC's operative region. Adopted slope $slp = 10^8$.
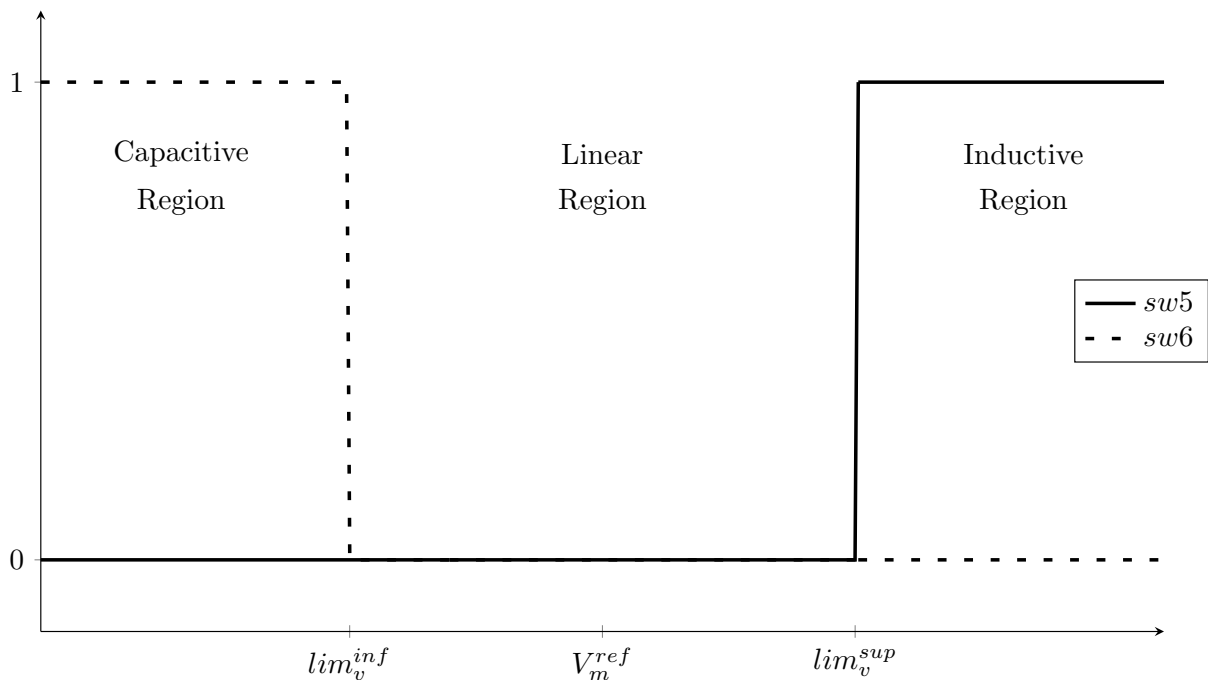
As mentioned in Chapter 3, the switches are modeled in order to return high or low binary values (1 or 0) and avoid undesired transitions. Therefore, the switches are associated with the SVC's control equations that best describes each operative region, as also detailed in Chapter 3.

As a result, Equation (5.5) combines the aforementioned switches and operative regions equations in only one control equation which will then be linearized and incorporated into the Jacobian matrix traditional PF formulation.

$$y = sw5 \cdot \left(Q_{G_k, svc} - V_{k, svc}^2 \cdot B_{svc}^{ind}\right) + sw6 \cdot \left(Q_{G_k, svc} - V_{k, svc}^2 \cdot B_{svc}^{cap}\right) \cdots \qquad (5.5)$$
$$+ \left(1 - sw5\right) \cdot \left(1 - sw6\right) \cdot \left(V_{m, svc} - V_{m, svc}^{ref} - r \cdot Q_{G_k, svc}\right).$$

As mentioned, the above equation will be linearized and fully incorporated into the Jacobian matrix. Regarding the multiple control equations within (5.5), there will be no conflict of linearization during the PF iterative process if the sigmoid switches slope and transition points are modeled correctly. Therefore, only one control equation in (5.5) will be active and linearized into the Jacobian matrix, in accordance to the SVC current operational situation.

In Table 4, control equation (5.5) residue is described for each operational state of the SVC. It is worth noting that the condition upon which *sw5* and *sw6* present high binary value is never achieved, as also illustrated in Figure 19.

Table 4 – SPF-SVC reactive power injection methodology sigmoid switches operation and control equation residue output.

Operational Region		**sw5**	**sw6**	**Δy**
1	Inductive	1	0	$V_{k, svc}^2 \cdot B_{svc}^{ind} - Q_{G_k, svc}$
2	Linear	0	0	$V_{m, svc}^{ref} + r \cdot Q_{G_k, svc} - V_{m, svc}$
3	Capacitive	0	1	$V_{k, svc}^2 \cdot B_{svc}^{cap} - Q_{G_k, svc}$

Source: Elaborated by the author (2023).

Each SVC operational state is better explained below. The modeling takes into account the equipment constructive characteristics and reactive power generation, as illustrated in Figure 6.

- Operation 1 is active when the reactive power generated by the SVC is greater than or equal to the maximum supported by the equipment ($Q_{G_k, svc} \geq Q_{G_k, svc}^{max}$);

- Operation 2 is active when the reactive power generated is within the limits ($Q_{G_k, svc}^{min} < Q_{G_k, svc} < Q_{G_k, svc}^{max}$);

- Operation 3 is active when the reactive power generated is less than or equal to the minimum supported ($Q_{G_k, svc} \leq Q_{G_k, svc}^{min}$).

On account of the control equation (5.5) and the new state variable, the Jacobian matrix shape is redefined. New line and column will be appended to the original matrix formation for each SVC connected on the electrical system. Therefore, new differential terms will be present on the augmented Jacobian matrix, which are shown in (5.6).

The new differential terms correspond to differentiating the state equations $\boldsymbol{P}$ and $\boldsymbol{Q}$ in terms of the new state variable, and to differentiating the new control equation in terms of the state variables $\boldsymbol{\theta}$, $\boldsymbol{V}$ and $\boldsymbol{Q_{G_k, svc}}$. The mathematical calculation of each new differential term can be found in Appendix A.

$$
\begin{bmatrix}
\vdots \\
\Delta P_k \\
\Delta P_m \\
\vdots \\
\Delta Q_k \\
\Delta Q_m \\
\vdots \\
\Delta y \\
\vdots
\end{bmatrix}
=
\begin{bmatrix}
\ddots & \vdots & \vdots & \cdots & \vdots & \vdots & \cdots & \vdots & \iddots \\
\cdots & \frac{\partial P_k}{\partial \theta_k} & \frac{\partial P_k}{\partial \theta_m} & \cdots & \frac{\partial P_k}{\partial V_k} & \frac{\partial P_k}{\partial V_m} & \cdots & \frac{\partial P_k}{\partial Q_{G_k, svc}} & \cdots \\
\cdots & \frac{\partial P_m}{\partial \theta_k} & \frac{\partial P_m}{\partial \theta_m} & \cdots & \frac{\partial P_m}{\partial V_k} & \frac{\partial P_m}{\partial V_m} & \cdots & \frac{\partial P_m}{\partial Q_{G_k, svc}} & \cdots \\
\cdots & \vdots & \vdots & \cdots & \vdots & \vdots & \cdots & \vdots & \cdots \\
\cdots & \frac{\partial Q_k}{\partial \theta_k} & \frac{\partial Q_k}{\partial \theta_m} & \cdots & \frac{\partial Q_k}{\partial V_k} & \frac{\partial Q_k}{\partial V_m} & \cdots & \frac{\partial Q_k}{\partial Q_{G_k, svc}} & \cdots \\
\cdots & \frac{\partial Q_m}{\partial \theta_k} & \frac{\partial Q_m}{\partial \theta_m} & \cdots & \frac{\partial Q_m}{\partial V_k} & \frac{\partial Q_m}{\partial V_m} & \cdots & \frac{\partial Q_m}{\partial Q_{G_k, svc}} & \cdots \\
\cdots & \vdots & \vdots & \cdots & \vdots & \vdots & \cdots & \vdots & \cdots \\
\cdots & \frac{\partial y}{\partial \theta_k} & \frac{\partial y}{\partial \theta_m} & \cdots & \frac{\partial y}{\partial V_k} & \frac{\partial y}{\partial V_m} & \cdots & \frac{\partial y}{\partial Q_{G_k, svc}} & \cdots \\
\iddots & \vdots & \vdots & \cdots & \vdots & \vdots & \cdots & \vdots & \ddots
\end{bmatrix}
\cdot
\begin{bmatrix}
\vdots \\
\Delta \theta_k \\
\Delta \theta_m \\
\vdots \\
\Delta V_k \\
\Delta V_m \\
\vdots \\
\Delta Q_{G_k, svc} \\
\vdots
\end{bmatrix}
$$

$$\tag{5.6}$$

5.2 SPF-SVC CURRENT INJECTION METHODOLOGY

Since the reactive power and current injections methodologies are similar considering the traditional power flow, the same will prevail in the SPF-SVC methodology.

Two sigmoid switches are employed to model SVCs based on the current injection methodology (PASSOS FILHO, 2000). It was opted to employ two sigmoid switches in this SPF-SVC model due to the direct relationship between current injection and controlled bus voltage magnitude, illustrated by Figure 7.

The switches expressions are detailed in Equations (5.7) and (5.8). For this methodology, the new state variable is the current supplied by the control device $I_{k, svc}$.

$$
sw7 = \frac{1}{1 + e^{-slp \cdot (V_{m, svc} - lim_v^{sup})}}, \tag{5.7}
$$

$$sw8 = \frac{1}{1 + e^{+slp \cdot (V_{m,\,svc} \,-\, lim_v^{inf})}}, \qquad (5.8)$$

where:

- lim_v^{sup} is equal to $\left(V_{m,\,svc}^{ref} + r \cdot B_{svc}^{ind} \cdot V_{k,\,svc}\right) + tol_v$,

- lim_v^{inf} is equal to $\left(V_{m,\,svc}^{ref} + r \cdot B_{svc}^{cap} \cdot V_{k,\,svc}\right) - tol_v$,

$$I_{k,\,svc} = \frac{Q_{G_k,\,svc}}{V_{k,\,svc}}, \qquad (5.9)$$

$$B_{svc}^{cap} = B_{svc}^{max} = b_{eq}(\alpha_{k,\,svc} = 180°) = \frac{I_{k,\,svc}^{max}}{\left(V_{k,\,svc}^{min}\right)}, \qquad (5.10)$$

$$B_{svc}^{ind} = B_{svc}^{min} = b_{eq}(\alpha_{k,\,svc} = 90°) = \frac{I_{k,\,svc}^{min}}{\left(V_{k,\,svc}^{max}\right)}. \qquad (5.11)$$

The main operative objective of the SVC, when connected to k-bus, is to control a specified bus voltage magnitude at a reference value $V_{m,\,svc}^{ref}$. Hence, switches $sw7$ and $sw8$ transition points occur at lim_v^{sup} and lim_v^{inf}, respectively. The transition points are evaluated in respect to the new state variable as well as to SVC's constructive characteristics.

Switches $sw7$ and $sw8$ operative behavior is similar to switches $sw5$ and $sw6$ behaviors, respectively. Hence, Figure 19 also illustrates the switches values for each operative region of the control device.

Equation (5.7) is associated with the transition between SVC's "Linear" and "Inductive" operative regions, whereas (5.8) is associated with SVC's "Linear" and "Capacitive" operative regions transition.

As mentioned in Chapter 3, the switches are modeled in order to return high or low binary values (1 or 0) and avoid undesired transitions. Therefore, the switches are associated with the SVC's control equations that best describes each operative region, as also detailed in Chapter 3.

As a result, Equation (5.12) combines the aforementioned switches and operative regions equations in only one control equation which will then be linearized and incorporated into the Jacobian matrix traditional PF formulation.

$$y = sw7 \cdot \left(I_{k,\,svc} - V_{k,\,svc} \cdot B_{svc}^{ind}\right) + sw8 \cdot \left(I_{k,\,svc} - V_{k,\,svc} \cdot B_{svc}^{cap}\right) \cdots \quad (5.12)$$
$$+ \left(1 - sw7\right) \cdot \left(1 - sw8\right) \cdot \left(V_{m,\,svc} - V_{m,\,svc}^{ref} - r \cdot I_{k,\,svc}\right).$$

As mentioned, the above equation will be linearized and fully incorporated into the Jacobian matrix. Regarding the multiple control equations within (5.12), there will be no conflict of linearization during the PF iterative process if the sigmoid switches slope and transition points are modeled correctly. Therefore, only one control equation in (5.12) will be active and linearized into the Jacobian matrix, in accordance to the SVC current operational situation.

In Table 5, control equation (5.12) residue is described for each operational state of the SVC. It is worth noting that the condition on which $sw7$ and $sw8$ present high binary value is never achieved.

Table 5 – SPF-SVC current injection methodology sigmoid switches operation and control equation residue output.

	Operational Region	$sw7$	$sw8$	Δy
1	Inductive	1	0	$V_{k,\,svc} \cdot B_{svc}^{ind} - I_{k,\,svc}$
2	Linear	0	0	$V_{m,\,svc}^{ref} + r \cdot I_{k,\,svc} - V_{m,\,svc}$
3	Capacitive	0	1	$V_{k,\,svc} \cdot B_{svc}^{cap} - I_{k,\,svc}$

Source: Elaborated by the author (2023).

Each SVC operational states are better explained below. The modeling takes into account the equipment's constructive characteristics and current supply, as illustrated in Figure 7.

- Operation 1 is active when the reactive power generated by the SVC is greater than or equal to the maximum supported by the equipment ($I_{k,\,svc} \geq I_{k,\,svc}^{max}$);

- Operation 2 is active when the reactive power generated is within the limits ($I_{k,\,svc}^{min} < I_{k,\,svc} < I_{k,\,svc}^{max}$);

- Operation 3 is active when the reactive power generated is less than or equal to the minimum supported ($I_{k,\,svc} \leq I_{k,\,svc}^{min}$).

On account of the control equation (5.12) and the new state variable, the Jacobian matrix shape is redefined. New line and column will be appended to the original matrix formation for each SVC connected on the electrical system. Therefore, new differential terms will be present on the augmented Jacobian matrix, which are shown in (5.13).

The new differential terms corresponds to differentiating the state equations $\boldsymbol{P}$ and $\boldsymbol{Q}$ in terms of the new state variable, and to differentiating the new control equation in terms of the state variables $\boldsymbol{\theta}$, $\boldsymbol{V}$ and $\boldsymbol{I_{k,\,svc}}$. The mathematical calculation of each new differential term can be found in Appendix A.

$$
\begin{bmatrix}
\vdots \\
\Delta P_k \\
\Delta P_m \\
\vdots \\
\Delta Q_k \\
\Delta Q_m \\
\vdots \\
\Delta y \\
\vdots
\end{bmatrix}
=
\begin{bmatrix}
\ddots & \vdots & \vdots & \cdots & \vdots & \vdots & \cdots & \vdots & \cdot^{\cdot^{\cdot}} \\
\cdots & \frac{\partial P_k}{\partial \theta_k} & \frac{\partial P_k}{\partial \theta_m} & \cdots & \frac{\partial P_k}{\partial V_k} & \frac{\partial P_k}{\partial V_m} & \cdots & \frac{\partial P_k}{\partial I_{k,\,svc}} & \cdots \\
\cdots & \frac{\partial P_m}{\partial \theta_k} & \frac{\partial P_m}{\partial \theta_m} & \cdots & \frac{\partial P_m}{\partial V_k} & \frac{\partial P_m}{\partial V_m} & \cdots & \frac{\partial P_m}{\partial I_{k,\,svc}} & \cdots \\
\cdots & \vdots & \vdots & \cdots & \vdots & \vdots & \cdots & \vdots & \cdots \\
\cdots & \frac{\partial Q_k}{\partial \theta_k} & \frac{\partial Q_k}{\partial \theta_m} & \cdots & \frac{\partial Q_k}{\partial V_k} & \frac{\partial Q_k}{\partial V_m} & \cdots & \frac{\partial Q_k}{\partial I_{k,\,svc}} & \cdots \\
\cdots & \frac{\partial Q_m}{\partial \theta_k} & \frac{\partial Q_m}{\partial \theta_m} & \cdots & \frac{\partial Q_m}{\partial V_k} & \frac{\partial Q_m}{\partial V_m} & \cdots & \frac{\partial Q_m}{\partial I_{k,\,svc}} & \cdots \\
\cdots & \vdots & \vdots & \cdots & \vdots & \vdots & \cdots & \vdots & \cdots \\
\cdots & \frac{\partial y}{\partial \theta_k} & \frac{\partial y}{\partial \theta_m} & \cdots & \frac{\partial y}{\partial V_k} & \frac{\partial y}{\partial V_m} & \cdots & \frac{\partial y}{\partial I_{k,\,svc}} & \cdots \\
\cdot^{\cdot^{\cdot}} & \vdots & \vdots & \cdots & \vdots & \vdots & \cdots & \vdots & \ddots
\end{bmatrix}
\cdot
\begin{bmatrix}
\vdots \\
\Delta \theta_k \\
\Delta \theta_m \\
\vdots \\
\Delta V_k \\
\Delta V_m \\
\vdots \\
\Delta I_{k,\,svc} \\
\vdots
\end{bmatrix}
\tag{5.13}
$$

5.3 SPF-SVC THYRISTOR FIRING-ANGLE METHODOLOGY

Differently to the aforementioned methodologies, four sigmoid switches are employed in the SPF-SVC methodology based on the model developed by Ambriz-Perez, Acha and Fuerte-Esquivel (2000). It was opted to employ four sigmoid switches in this SPF-SVC model due to an inverse relationship between the thyristor firing-angle and the controlled bus voltage magnitude, illustrated by Figure 8 and Equation (2.23).

The switches expressions are detailed in Equations (5.14) through (5.17). For this methodology, the new state variable is the SVC's thyristor firing-angle $\alpha_{k,\,svc}$.

$$
sw9 = \frac{1}{1 + e^{-slp \cdot (\alpha_{k,\,svc} \,-\, lim_{\alpha}^{sup})}}, \tag{5.14}
$$

$$
sw10 = \frac{1}{1 + e^{+slp \cdot (\alpha_{k,\,svc} \,-\, lim_{\alpha}^{inf})}}, \tag{5.15}
$$

$$
sw11 = \frac{1}{1 + e^{-slp \cdot (V_m \,-\, lim_{v}^{sup})}}, \tag{5.16}
$$

$$
sw12 = \frac{1}{1 + e^{+slp \cdot (V_m \,-\, lim_{v}^{inf})}}, \tag{5.17}
$$

where:

- lim_α^{sup} is equal to $180° - tol_\alpha$,

- lim_α^{inf} is equal to $90° + tol_\alpha$,

- lim_v^{sup} is equal to $\left(V_{m,svc}^{ref} + r \cdot b_{eq}(90°) \cdot V_{k,svc}^2\right) + tol_v$,

- lim_v^{inf} is equal to $\left(V_{m,svc}^{ref} + r \cdot b_{eq}(180°) \cdot V_{k,svc}^2\right) - tol_v$,

$$Q_{G_k,svc} = V_{k,svc}^2 \cdot b_{eq}(\alpha_{k,svc}), \tag{5.18}$$

$$b_{eq}(\alpha = 180°) = B_{svc}^{cap} = B_{svc}^{max} = \frac{Q_{G_k,svc}^{max}}{\left(V_{k,svc}^{min}\right)^2}, \tag{5.19}$$

$$b_{eq}(\alpha = 90°) = B_{svc}^{ind} = B_{svc}^{min} = \frac{Q_{G_k,svc}^{min}}{\left(V_{k,svc}^{max}\right)^2}. \tag{5.20}$$

Regarding the SVC thyristor firing-angle, it controls the equipment equivalent susceptance value and, consequently, its reactive power generation by (5.18). Therefore, switches *sw9* and *sw10* are developed to model the device control reactive power generation, with transition points set at lim_α^{sup} and lim_α^{inf}, respectively. Additionally, switches *sw11* and *sw12* transition points occur at lim_v^{sup} and lim_v^{inf}, in order to control the specified bus voltage magnitude at a reference value $V_{m,svc}^{ref}$.

The operative behavior of switches *sw9* and *sw10* and switches *sw11* and *sw12* are illustrated in Figures 20 and 21.

As it can be observed, both pair of switches have the same behavior. These switches can have low binary values at the same time, but the same does not apply for high binary values. The main difference between Figures 20 and 21, however, consists of the SVC operational regions order. This condition is not problematic for the SPF-SVC modeling. On the contrary, the conjunction of the two pair of switches allows a better transition between SVC's operational regions, as it will further be detailed.

Once again, the switches are associated with the SVC's control equations that best describes each operative region, as detailed in Chapter 3. As a result, Equation (5.21) combines the aforementioned switches and operative regions equations in one only control equation which will then be linearized and incorporated into the Jacobian matrix traditional PF formulation.

Figure 20 – Sigmoid switches *sw9* and *sw10* values in accordance to SVC's operative region. Adopted slope $slp = 10^8$.
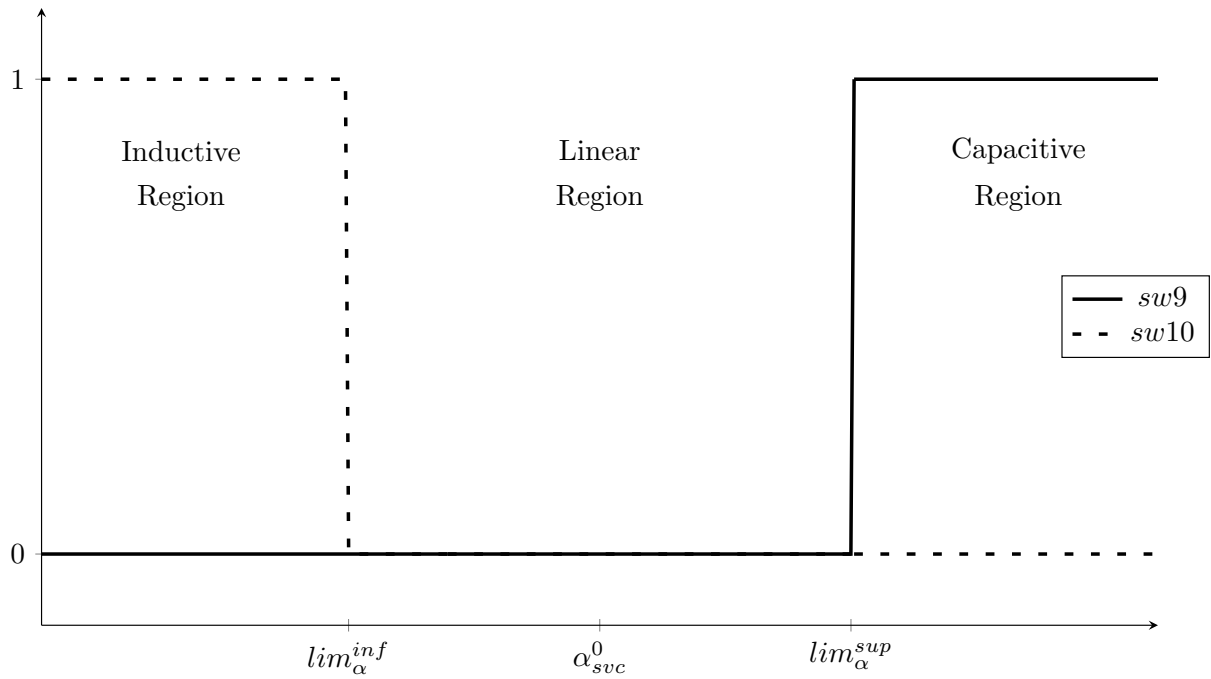
Source: Elaborated by the author (2023).

Figure 21 – Sigmoid switches *sw11* and *sw12* values in accordance to SVC's operative region. Adopted slope $slp = 10^8$.
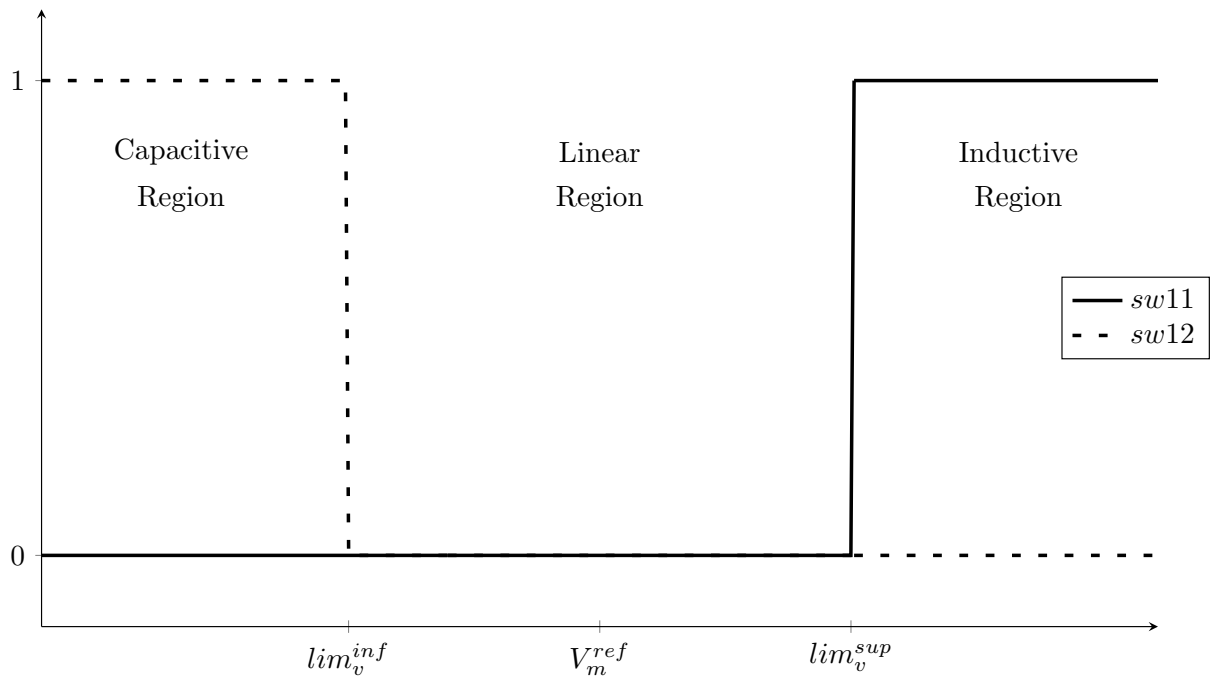
Source: Elaborated by the author (2023).

$$
\begin{aligned}
y \;=\; & sw10 \cdot \left(1 - sw12\right) \cdot \left(\alpha_{k,svc} - 90°\right) + sw9 \cdot \left(1 - sw11\right) \cdot \left(\alpha_{k,svc} - 180°\right) \cdots \\
& + \Big[sw11 \cdot (1 - sw10) \cdot (1 - sw12) + sw12 \cdot (1 - sw9) \cdot (1 - sw11) \cdots \\
& + (1 - sw9) \cdot (1 - sw10) \cdot (1 - sw11) \cdot (1 - sw12) \Big] \cdot \left(V_{m,svc} - V_{m,svc}^{ref} - r \cdot Q_{G_k,svc}\right).
\end{aligned}
$$

$$(5.21)$$

In the above equation, the reactive power generation variable $Q_{G_k,svc}$ is given by (5.18). Regarding the multiple control equations within (5.21), due to the use of four sigmoid switches, a better modeling of the switches should be made in order to avoid undesired transition conflicts. In Table 6 it is described control equation (5.21) residue, for each operational state of the SVC.

Table 6 – SPF-SVC thyristor firing-angle methodology sigmoid switches operation and control equation output.

	Operational Region	sw9	sw10	sw11	sw12	Δy
1	Inductive	0	1	0	0	$90° - \alpha_{k,svc}$
2	Inductive *Backoff*	0	1	0	1	
3	Linear	0	0	0	0	$V_{m,svc}^{ref} + r \cdot V_{k,svc}^2 \cdot b_{eq}\left(\alpha\right) - V_{m,svc}$
4	Capacitive *Backoff*	1	0	1	0	
5	Capacitive	1	0	0	0	$180° - \alpha_{k,svc}$

Source: Elaborated by the author (2023).

Each SVC operational states are better explained below. Due to presence of four sigmoid switches, a better and detailed transition between SVC operational regions is made. As it is detailed in Table 6, the four sigmoid switches allows a *backoff* routine to take place in order to correctly assign the best SVC operational state during the the PF iterative process.

The modeling takes into account the equipment constructive characteristics, specifically the equivalent susceptance, as illustrated in Figure 8(b), as well as the objective of controlling the voltage magnitude of a specific bus.

- Operation 1 is active when the thyristor firing-angle is less than or equal to the minimum supported $(\alpha_{k,svc} \leq 90°)$;

- Operation 2 is active when the thyristor firing-angle is less than or equal to the minimum supported $(\alpha_{k,svc} \leq 90°)$ and the controlled bus voltage magnitude is less than or equal to the minimum supported $(V_{m,svc} \leq V_{m,svc}^{min})$;

- Operation 3 is active when the thyristor firing-angle and the controlled bus magnitude are within their limits $(90° < \alpha_{k,svc} < 180°$ and $V_{m,svc}^{min} < V_m < V_{m,svc}^{max})$;

- Operation 4 is active when the thyristor firing-angle is greater than or equal to the maximum supported ($\alpha_{k,\,svc} \geq 180°$) and the controlled bus voltage magnitude is greater than or equal to the maximum supported ($V_{m,\,svc} \geq V_{m,\,svc}^{max}$);

- Operation 5 is active when the thyristor firing-angle is greater than or equal to the maximum supported ($\alpha_{k,\,svc} \geq 180°$).

On account of the control equation (5.21) and the new state variable, the Jacobian matrix shape is redefined. New line and column will be appended to the original matrix formation for each SVC connected on the electrical system. Therefore, new differential terms will be present on the augmented Jacobian matrix, which are shown in (5.22).

The new differential terms corresponds to differentiating the state equations $\boldsymbol{P}$ and $\boldsymbol{Q}$ in terms of the new state variable, and to differentiating the new control equation in terms of the state variables $\boldsymbol{\theta}$, $\boldsymbol{V}$ and $\boldsymbol{\alpha_{k,\,svc}}$. The mathematical calculation of each new differential term can be found in Appendix A.

$$
\begin{bmatrix}
\vdots \\
\Delta P_k \\
\Delta P_m \\
\vdots \\
\Delta Q_k \\
\Delta Q_m \\
\vdots \\
\Delta y \\
\vdots
\end{bmatrix}
=
\begin{bmatrix}
\ddots & \vdots & \vdots & \cdots & \vdots & \vdots & \cdots & \vdots & \iddots \\
\cdots & \frac{\partial P_k}{\partial \theta_k} & \frac{\partial P_k}{\partial \theta_m} & \cdots & \frac{\partial P_k}{\partial V_k} & \frac{\partial P_k}{\partial V_m} & \cdots & \frac{\partial P_k}{\partial \alpha_{k,\,svc}} & \cdots \\
\cdots & \frac{\partial P_m}{\partial \theta_k} & \frac{\partial P_m}{\partial \theta_m} & \cdots & \frac{\partial P_m}{\partial V_k} & \frac{\partial P_m}{\partial V_m} & \cdots & \frac{\partial P_m}{\partial \alpha_{k,\,svc}} & \cdots \\
\cdots & \vdots & \vdots & \cdots & \vdots & \vdots & \cdots & \vdots & \cdots \\
\cdots & \frac{\partial Q_k}{\partial \theta_k} & \frac{\partial Q_k}{\partial \theta_m} & \cdots & \frac{\partial Q_k}{\partial V_k} & \frac{\partial Q_k}{\partial V_m} & \cdots & \frac{\partial Q_k}{\partial \alpha_{k,\,svc}} & \cdots \\
\cdots & \frac{\partial Q_m}{\partial \theta_k} & \frac{\partial Q_m}{\partial \theta_m} & \cdots & \frac{\partial Q_m}{\partial V_k} & \frac{\partial Q_m}{\partial V_m} & \cdots & \frac{\partial Q_m}{\partial \alpha_{k,\,svc}} & \cdots \\
\cdots & \vdots & \vdots & \cdots & \vdots & \vdots & \cdots & \vdots & \cdots \\
\cdots & \frac{\partial y}{\partial \theta_k} & \frac{\partial y}{\partial \theta_m} & \cdots & \frac{\partial y}{\partial V_k} & \frac{\partial y}{\partial V_m} & \cdots & \frac{\partial y}{\partial \alpha_{k,\,svc}} & \cdots \\
\iddots & \vdots & \vdots & \cdots & \vdots & \vdots & \cdots & \vdots & \ddots
\end{bmatrix}
\cdot
\begin{bmatrix}
\vdots \\
\Delta \theta_k \\
\Delta \theta_m \\
\vdots \\
\Delta V_k \\
\Delta V_m \\
\vdots \\
\Delta \alpha_{k,\,svc} \\
\vdots
\end{bmatrix}
\tag{5.22}
$$

5.4 OBSERVATIONS

The *droop* implementation in the thyristor firing-angle methodology is set clear in (5.21), the SVC linear operational region equation, where the reactive power variable $Q_{G_k,\,svc}$ is multiplied by the *droop* variable "r". Considering this, the improved thyristor firing-angle methodology returns the same results as the reactive power injection methodology. In order to illustrate the *droop* implementation, Figures 22 and 23 present the SVC controlled bus voltage variation per reactive power generated and per thyristor firing-angle methodologies, respectively.

In both Figures, the SVC thyristor firing-angle with 0% *droop* implementation refers to the methodology proposed by Ambriz-Perez, Acha and Fuerte-Esquivel (2000). Although the SVC 0% *droop* model is able to control the bus voltage magnitude at the

Figure 22 – SVC Controlled Bus Voltage Magnitude per Reactive Power Generated.
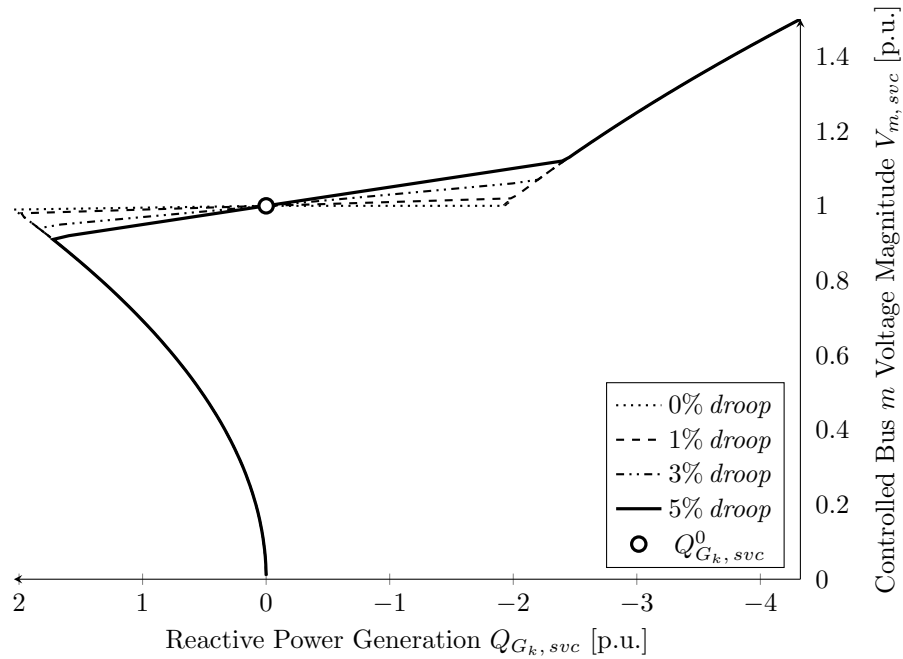
Source: Elaborated by the author (2023).

Figure 23 – SVC Controlled Bus Voltage Magnitude per Thyristor Firing-Angle.
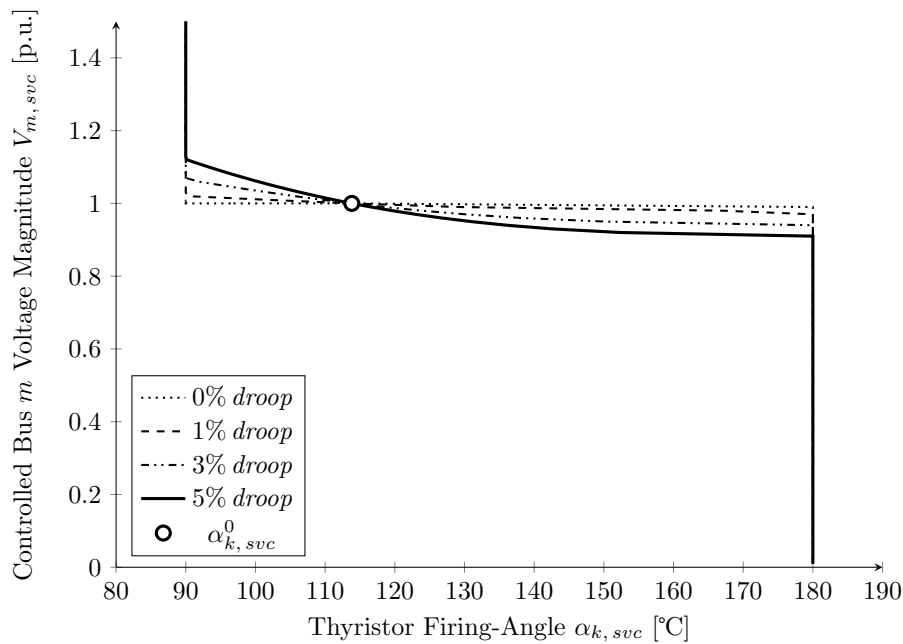
Source: Elaborated by the author (2023).

scheduled value during the linear region, this operation is in fact idealized and does not occur due to physical operational limitations of the equipment.

By implementing *droop* in the steady-state SVC thyristor firing-angle model, a more realistic operation by the control device is obtained (BARBOSA; PASSOS FILHO, 2022). Hence, as it can be seen in Figures 22 and 23, the *droop* implementation affects

directly the reactive power generated and the thyristor firing-angle when the control device is operating in the linear region.

In terms of PF simulations, all SPF-SVC proposed methodologies implementations results in equal amount of iterations. Therefore, it can be concluded that the difference in the number of switches employed in each methodology does not result in an increase of iterations, once the switches are configured correctly.

Additionally, to avoid direct transition between inductive and capacitive regions, a step through the linear region is performed, equaling the controlled bus voltage magnitude to its reference value and the specified state variable to result in null reactive power by the SVC.

As mentioned in the beginning of this chapter, each SPF-SVC proposed methodology is best suited for a specific research goal. According to Ambriz-Perez, Acha and Fuerte-Esquivel (2000), the thyristor firing-angle methodology is best suited for harmonics and electromagnetic transients studies (MILLER *et al.*, 1982). The reactive power and current injections methodologies, in turn, have a more general approach, being appropriated to studies related to the impacts of reactive power and current injections in the electric power system, respectively. Nevertheless, all SPF-SVC methodologies approaches are recommended for power flow studies.

5.5   SPF-SVC FLOWCHART

On account of the proposed SPF-SVC methodologies, Figure 24 flowchart describes a standard algorithm to implement the SPF-SVCs models in the PF traditional formulation.

In this flowchart, a definition for the sigmoid switches value is made for the respective proposed methodology implemented. Along with that, the new control variable is incorporated in the nonlinear system of equations. As detailed in Subsections 5.1, 5.2 and 5.3, the new control variable can be $Q_{G_k, svc}$, $I_{k, svc}$ or $\alpha_{k, svc}$, respectively.

The proposed implementation methodology considers the *full* Newton approach. The control equations related to each actively operating SVC present in the electric power system are linearized and solved together with the state equations that model the electric power system in study.

5.6   PARTIAL CONCLUSIONS

This chapter presents relevant contributions to the current literature on SVC steady-state models. These contributions are described in the following items:

- A SPF-SVC reactive power injection methodology to represent SVCs in the steady-state PF problem. This methodology relates the reactive power generated by the

control device with the controlled bus voltage magnitude values. This results in a better analysis of the impacts of reactive power generation by SVCs in order to control a bus voltage magnitude.

- A SPF-SVC current injection methodology to represent SVCs in the steady-state PF problem. This methodology relates the current injected by the control device with the controlled bus voltage magnitude values. This results in a better analysis of the impacts of current injection by SVCs in order to control a bus voltage magnitude.

Figure 24 – SPF-SVC standard flowchart.
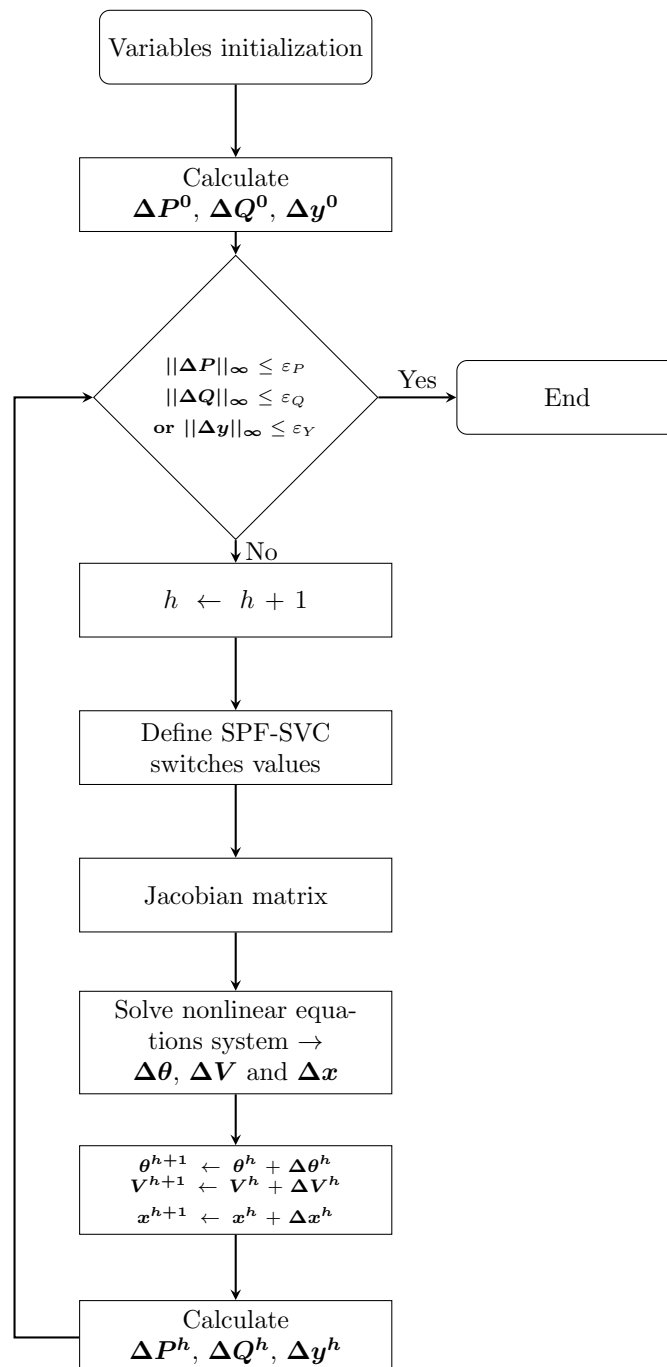
Source: Elaborated by the author (2023).

- A SPF-SVC thyristor firing-angle methodology to represent SVCs in the steady-state PF problem. This methodology relates the reactive power generated, by means of the control device thyristor firing-angle, with the controlled bus voltage magnitude values. This results in a better analysis of the impacts of reactive power generation by SVCs in order to control a bus voltage magnitude.

- An enhancement to traditional SVC thyristor firing-angle methodology, by incorporating a *droop* variable in the proposed SPF-SVC thyristor firing-angle methodology. The *droop* consideration approximates the SVC steady-state model simulations to real operational conditions.

As it will be described in Chapter 6, the proposed SPF-SVCs modelings also presents new contributions to power systems' voltage stability.

6 VOLTAGE STABILITY IMPACTS

The previous chapters presented a thorough review of the traditional power flow formulation and the proposed smooth power flow formulation via sigmoid functions, as well as the proposed SPF methodologies for modeling reactive power generation limits and SVCs in the power flow problem. The use of sigmoid functions in the proposed SPF methodology correctly models electric devices for steady-state analysis, once the switches are responsible for enabling the control equation that best represents the operational behavior at each iteration of the PF simulation. However, a further mathematical analysis can be made with the intent of better understanding the impacts of the proposed methodology in VSA.

For that reason, in this chapter a special focus will be on the improvements regarding voltage collapse and bifurcations due to the SPF formulation. As mentioned in Section 3.1, it is mathematically proven in Neves (2022), Neves, Alberto and Chiang (2022a) that the introduction of smoothness in the PF formulation transforms every bifurcation into SNBs. In the following sections it is proposed a numerical demonstration of this condition, evaluating the voltage stability of EPS, when the same tend to collapse, via modal analysis.

The CPF formulation and the eigenproperties detailed in Apendices B and C, respectively, were applied in the proposed SPF formulation to evaluate voltage stability in EPSs.

6.1 INITIAL CONSIDERATIONS

Voltage stability analysis is a widely research subject in electrical engineering, once that the growing increase in load demand directly affects the concern to prevent EPSs from collapsing. Many published works assess the problem of voltage stability by means of an steady-state analysis of power systems, as Neves (2022, p.52) properly mentions (VENIKOV *et al.*, 1975; ABE *et al.*, 1978; TAMURA; MORI; IWAMOTO, 1983; KWATNY; PASRIJA; BAHAR, 1986; SAUER; PAI, 1990; FLATABO; OGNEDAL; CARLSEN, 1990; SCHLUETER *et al.*, 1991; CUTSEM, 1991; MORISON; GAO; KUNDUR, 1993; CANIZARES, 1995).

The Continuation Power Flow (CPF) method stands out among the different simulation tools capable of evaluating voltage stability of EPSs in terms of load demand increments. It was first introduced in the literature of power flow research and applications by Ajjarapu and Christy (1992) and, according to the authors, consists of "a class of techniques used to find a path of equilibrium solutions of a set of nonlinear equations (SEYDEL, 1988; RHEINBOLDT, 1986; RHEINBOLDT; BURKARDT, 1983; RIKS, 1987)".

By correctly implementing the CPF method, it is possible to analyze how close an EPS is to the MLP. Despite the natural differences between EPSs, it is important to

properly model all electric devices actively operating, considering their control limits and saturation behaviors, in order to obtain simulation results as close as possible to reality (PASSOS FILHO, 2000).

In a general point of view, the voltage collapse is considered as a power system's point of maximum loadability, on the threshold of voltage stability. In a mathematical point of view, however, the voltage collapse is characterized as a point where a bifurcation occurs (CHIANG *et al.*, 1990). Since power flow solves a system of nonlinear equations, and the CPF determines a sequence of nonlinear equations solutions, Bifurcation Points (BPs) can be present throughout power flow analysis and simulations.

According to Neves (2022), the loss of a solution of (2.10) in a BP can be caused when the system reaches the limit of function f itself (loss of equilibrium point due loadability limit) or when some of the admittable solutions violate one of the inequality constraints determined in g (2.16). Bifurcations can, therefore, be classified into different categories. However, in this work, an emphasis will be made in analyzing SNB and LIB bifurcations, which are described below:

1. Saddle-Node Bifurcation (SNB): when f is $C^{1,2}$ but f_X is singular at the BP;

2. Limit-Induced Bifurcation (LIB): when f is not C^1 at the BP. In this case, the bifurcation occurs due to control variables changing electric devices operational behavior from unsaturated to saturated or vice-versa..

The aforementioned classifications consider the assumptions of the Implicit Function Theorem, as detailed by Neves (2022, p.56). It also considers the analysis on account of the traditional PF formulation.

Once a desired smoothness is introduced in the traditional PF formulation, transforming it into a SPF formulation, "the Implicit Function Theorem ensures that all static bifurcations points, without exception," are points where the smoothed f_X exists and is singular (NEVES, 2022).

By way of explanation, every static bifurcation is now classified as SNB in the SPF formulation. This condition is made possible due to the continuity characteristic of *smooth step functions*, such as the sigmoid function, as detailed in Subsection 3.2.1, and the mathematical theorems regarding SPF formulation, thoroughly detailed by (NEVES, 2022).

As mentioned by Neves, Alberto and Chiang (2020), Neves, Alberto and Chiang (2022b), there are a few published works in voltage stability literature that developed techniques to detect LIB. The voltage collapse of EPSs classified as LIB commonly occurs

---

[2]   For C^1-class functions, the zeroth and first derivatives are continuous.

due to electric devices operational behavior variation, such as generators reactive power generation limits and SVCs limits (TAYLOR, 1994; CUTSEM; VOURNAS, 2007).

To qualitatively evaluate the impact of the SPF formulation in bifurcation analysis, the eigenproperties associated with modal analysis are employed. Despite the computational burden, modal analysis is a widely applied tool in power systems research for voltage stability evaluation via the $\mathbf{J_R}$ matrix sensitivity (GAO; MORISON; KUNDUR, 1992; MORISON; GAO; KUNDUR, 1993; KUNDUR, 1994; PASSOS FILHO, 2005).

According to Taylor (1994, p.238):

> The relationship between voltage stability and eigenvalues of the $\mathbf{J_R}$ matrix is best understood by relating the eigenvalues with the V-Q sensitivities of each bus (which must be positive for stability). $\mathbf{J_R}$ can be taken as a symmetric matrix and therefore the eigenvalues of $\mathbf{J_R}$ are close to being purely real. If all the eigenvalues are positive, $\mathbf{J_R}$ is positive definite and the V-Q sensitivities are also positive, indicating that the system is voltage stable.

By implementing CPF and modal analysis in the proposed SPF formulation, the condition of EPSs tending to voltage collapse is analyzed and the electric devices responsible for the instability are easily identified.

In this work, therefore, a special analysis is made in the transformation from LIBs to SNBs. The proposed SPF generator methodology detailed in Chapter 4 is considered with the intent of numerically verify the proposed analysis.

6.2   BIFURCATIONS AND MODAL ANALYSIS

The precise mathematical definitions of SNB and LIB classifications are detailed in the first two subsections, adapted from Neves (2022). In sequence, the condition by which generic bifurcations are transformed into SNB in the SPF is succintly discussed. These definitions will be applied in the proposed modal analysis based on a specific mathematical theorem detailed in Neves (2022), as described in the last subsection.

6.2.1   **Saddle-Node Bifurcation**

This subsection title is identical to Neves (2022, p.72) on purposed. The Saddle-Node Bifurcation (SNB) definition shown in his work is adapted and detailed hereinafter.

Definition 2 (Saddle-Node Bifurcation). *The system of N equations and N + 1 variables given by:*

$$\boldsymbol{f}\left(\boldsymbol{X}, \lambda\right) = \boldsymbol{0} \tag{6.1}$$

where:

- $\boldsymbol{X} \in \mathbb{R}^n$;

- $\lambda \in \mathbb{R}$;

- $\boldsymbol{f} : \mathbb{R}^n \times \mathbb{R} \to \mathbb{R}^n$;

undergoes a saddle-node bifurcation at point $\left(\boldsymbol{X^{crit}}, \lambda^{crit} \right)$ if the following conditions hold:

[I] $\boldsymbol{f} \left(\boldsymbol{X^{crit}}, \lambda^{crit} \right) = \boldsymbol{0}$;

[II] $\boldsymbol{f}$ *is continuously differentiable at* $\left(\boldsymbol{X^{crit}}, \lambda^{crit} \right)$;

[III] $\boldsymbol{f_X} \left(\boldsymbol{X^{crit}}, \lambda^{crit} \right)$ *is singular;*

[IV] *There is an unique solution branch passing through* $\left(\boldsymbol{X^{crit}}, \lambda^{crit} \right)$, *which can be parameterized by* $s \in \mathbb{R}$ *and denoted by* $(\boldsymbol{X}(s), \lambda(s))$ *such that* $(\boldsymbol{X}(s), \lambda(s)) = \left(\boldsymbol{X^{crit}}, \lambda^{crit} \right)$ *when* $s = \hat{s}$. *In addition,* $s = \hat{s}$ *is a critical point of function* $\lambda(s)$.

According to Neves (2022), the point $\left(\boldsymbol{X^{crit}}, \lambda^{crit} \right)$ is classified as *critical point* of $\boldsymbol{f}(\boldsymbol{X}, \lambda)$ if there is a neighborhood $\mathbb{U}$ of $\left(\boldsymbol{X^{crit}}, \lambda^{crit} \right)$ such that:

- $\boldsymbol{f}(\boldsymbol{X}, \lambda) \geq \boldsymbol{f} \left(\boldsymbol{X^{crit}}, \lambda^{crit} \right) \ \forall \ (\boldsymbol{X}, \lambda) \in \overline{\mathbb{U}}$ and
  $\boldsymbol{f}(\boldsymbol{X}, \lambda) > \boldsymbol{f} \left(\boldsymbol{X^{crit}}, \lambda^{crit} \right) \ \forall \ (\boldsymbol{X}, \lambda) \in \partial\mathbb{U}$;

  or

- $\boldsymbol{f}(\boldsymbol{X}, \lambda) \leq \boldsymbol{f} \left(\boldsymbol{X^{crit}}, \lambda^{crit} \right) \ \forall \ (\boldsymbol{X}, \lambda) \in \overline{\mathbb{U}}$ and
  $\boldsymbol{f}(\boldsymbol{X}, \lambda) < \boldsymbol{f} \left(\boldsymbol{X^{crit}}, \lambda^{crit} \right) \ \forall \ (\boldsymbol{X}, \lambda) \in \partial\mathbb{U}$;

The Definition 2 is illustrated by Figure 25, where the SNB is given by $\left(\boldsymbol{X^{crit}}, \lambda^{crit} \right)$ and there is no solution point $(\boldsymbol{X}, \lambda)$ that satisfies (6.1) for $\lambda > \lambda^{crit}$.

6.2.2 Limit-Induced Bifurcation

This subsection title is identical to Neves (2022, p.72) on purposed. The Limit-Induced Bifurcation (LIB) definition shown in his work is adapted and detailed hereinafter.

Definition 3 (Limit-Induced Bifurcation)**.** *The system of N equations and $N+1$ variables given by:*

$$\boldsymbol{f}(\boldsymbol{X}, \lambda) = \boldsymbol{0} \tag{6.2a}$$

$$\begin{cases} a(\boldsymbol{X}, \lambda) = \boldsymbol{0}, \ if \ b(\boldsymbol{X}, \lambda) > \boldsymbol{0}, \\ a(\boldsymbol{X}, \lambda) \geq \boldsymbol{0}, \ if \ b(\boldsymbol{X}, \lambda) = \boldsymbol{0} \end{cases} \tag{6.2b}$$

Figure 25 – Saddle-Node Bifurcation.
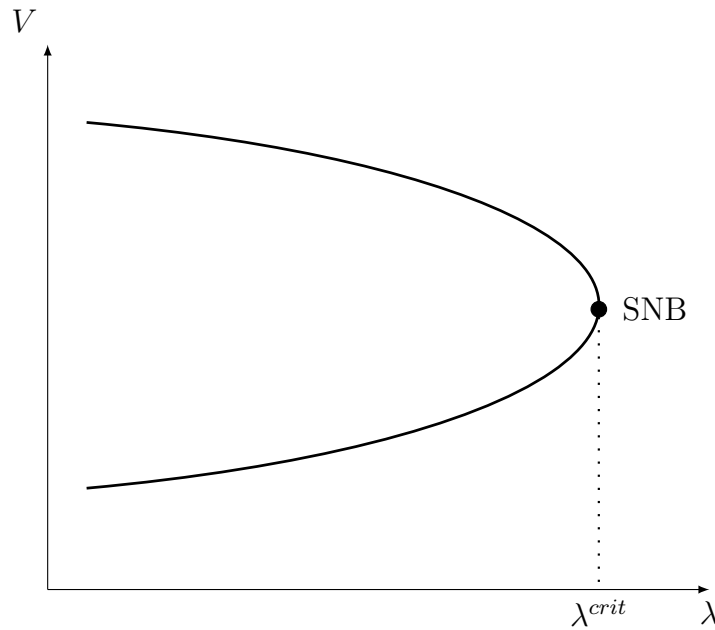
Source: Adapted from Neves (2022).

where:

- $\boldsymbol{X} \in \mathbb{R}^n$;

- $\lambda \in \mathbb{R}$;

- $\boldsymbol{f} : \mathbb{R}^n \times \mathbb{R} \to \mathbb{R}^{n-1}$;

- $a : \mathbb{R}^n \times \mathbb{R} \to \mathbb{R}$;

- $b : \mathbb{R}^n \times \mathbb{R} \to \mathbb{R}$;

undergoes a limit-induced bifurcation at point $\left(\boldsymbol{X^{crit}}, \lambda^{crit} \right)$ *if the following conditions hold:*

[I] $\boldsymbol{f} \left(\boldsymbol{X^{crit}}, \lambda^{crit} \right) = \boldsymbol{0}$, $a \left(\boldsymbol{X^{crit}}, \lambda^{crit} \right) = \boldsymbol{0}$ *and* $b \left(\boldsymbol{X^{crit}}, \lambda^{crit} \right) = \boldsymbol{0}$;

[II] $\boldsymbol{f}$, a, b *are continuously differentiable at* $\left(\boldsymbol{X^{crit}}, \lambda^{crit} \right)$;

[III] *both* $\begin{bmatrix} \boldsymbol{f_X} \\ a_{\boldsymbol{X}} \end{bmatrix}$ *and* $\begin{bmatrix} \boldsymbol{f_X} \\ b_{\boldsymbol{X}} \end{bmatrix}$ *are nonsingular at* $\left(\boldsymbol{X^{crit}}, \lambda^{crit} \right)$;

[IV] $(b_{\boldsymbol{X}} \cdot \boldsymbol{\alpha} + b_\lambda) \cdot (a_{\boldsymbol{X}} \cdot \boldsymbol{\beta} + a_\lambda) > 0$ *at* $\left(\boldsymbol{X^{crit}}, \lambda^{crit} \right)$, *where* $\boldsymbol{\alpha}$ *is the unique solution of* $\begin{bmatrix} \boldsymbol{f_X} \\ a_{\boldsymbol{X}} \end{bmatrix} \cdot \boldsymbol{\alpha} + \begin{bmatrix} \boldsymbol{f_\lambda} \\ a_\lambda \end{bmatrix} = \boldsymbol{0}$ *and* $\boldsymbol{\beta}$ *is the unique solution of* $\begin{bmatrix} \boldsymbol{f_X} \\ b_{\boldsymbol{X}} \end{bmatrix} \cdot \boldsymbol{\beta} + \begin{bmatrix} \boldsymbol{f_\lambda} \\ b_\lambda \end{bmatrix} = \boldsymbol{0}$.

According to Neves (2022), Definition 3 restricts LIB points to points where there is an unsaturated

$$\boldsymbol{f}\left(\boldsymbol{X}, \lambda\right) = \boldsymbol{0} \qquad (6.3a)$$

$$a\left(\boldsymbol{X}, \lambda\right) = \boldsymbol{0} \qquad (6.3b)$$

to saturated change

$$\boldsymbol{f}\left(\boldsymbol{X}, \lambda\right) = \boldsymbol{0} \qquad (6.4a)$$

$$b\left(\boldsymbol{X}, \lambda\right) = \boldsymbol{0} \qquad (6.4b)$$

in the system behavior, or vice versa.

The Definition 3 is best explained by means of the illustrations in Figures 26 and 27. Consider that Curves 1 and 2 represent solutions of a state variable V under different conditions: Curve 1 is a solution curve for the system (6.2a) when a generator is modelled as constant V; Curve 2 is a solution curve for the system (6.2a) when a generator is modelled as constant Q. The Actual Curve, in turn, is the true variation of the state variable V based on the generator operational behavior.

Figure 26 – Transition Point followed by a Saddle-Node Bifurcation.
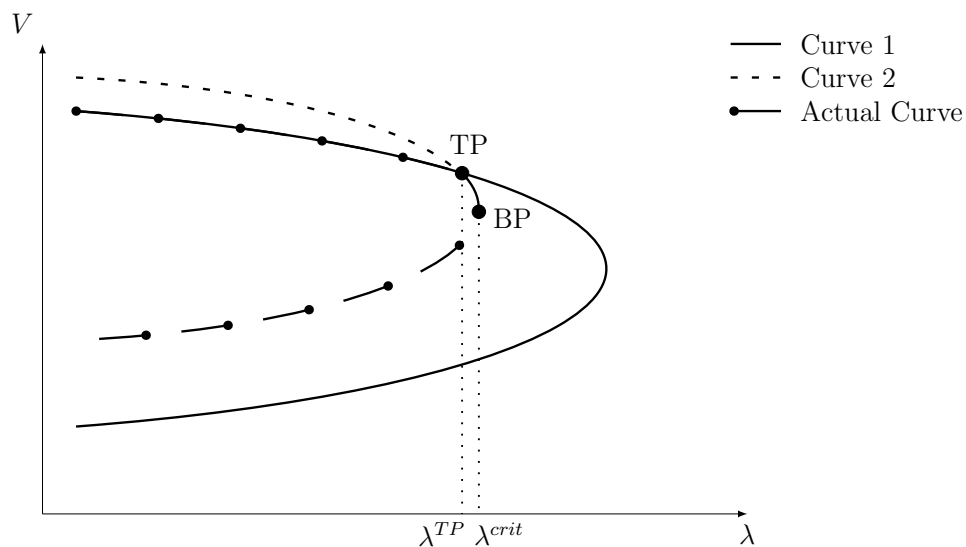
Source: Adapted from Neves, Alberto and Chiang (2022b).

From Figure 26, the state variable V varies in accordance to Curve 1 until a first limit is encountered ($\lambda = \lambda^{TP}$). This limit is justified by a variation in the generator operational behavior, once it reaches its reactive power maximum or minimum generation capacity. Although the generator's limit is reached, the EPS can withstand this condition

and, therefore, λ keep increasing (NEVES; ALBERTO; CHIANG, 2022b). The state variable V continues to vary, but now in accordance with Curve 2 and until the EPS collapses ($\lambda = \lambda^{crit}$).

The first limit encountered is classified as a TP, a generic point where there is a saturated to unsaturated (or vice versa) change in the system behavior. This limit cannot be classified as a LIB by reason that it does not satisfy condition [IV] stated in Definition 3 (NEVES, 2022). The second limit encountered is classified as a Bifurcation Point (BP) due to the fact that the solution points of (6.2a) coalesce and vanish for $\lambda > \lambda^{crit}$ (NEVES; ALBERTO; CHIANG, 2022b). Therefore, the BP is characterized as a *critical point* and can also be classified as SNB.

Figure 27 – Limit-Induced Bifurcation.
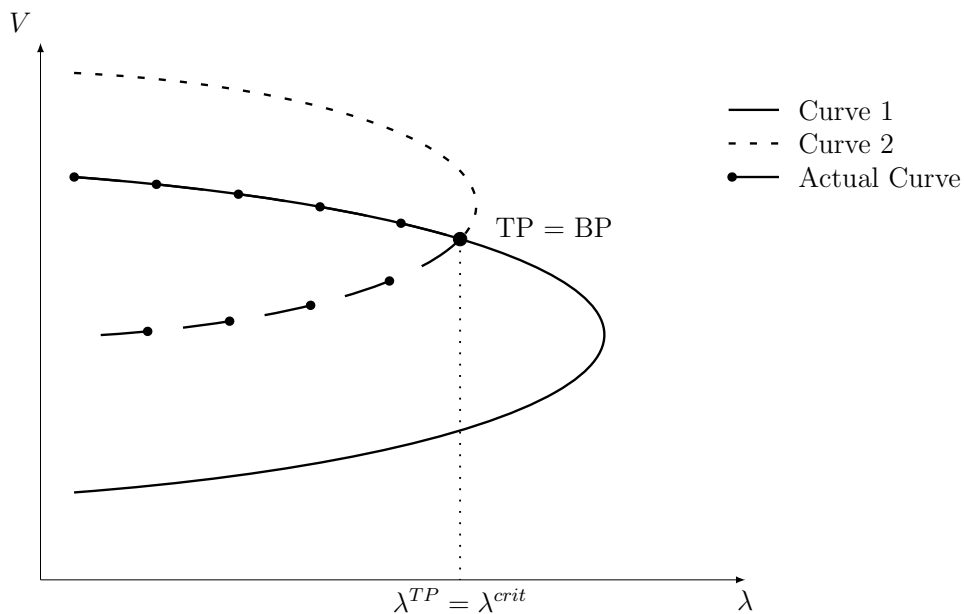
Source: Adapted from Neves, Alberto and Chiang (2022b).

A different condition is analyzed in Figure 27. Similarly, the state variable V initially vary in accordance with Curve 1 until a limit is encountered ($\lambda = \lambda^{TP}$). This limit is also justified by a variation in the generator operational behavior, once it reaches its reactive power maximum or minimum generation capacity. In contrast, in this situation the EPS cannot withstand the generator's limit condition being reached and, therefore, a voltage collapse occurs.

The limit encountered can no longer be classified solely as a TP, but also a BP, with the solution points of (6.2a) coalescing and vanishing for $\lambda > \lambda^{TP}$ (NEVES, 2022). No alteration on the generator's operational behavior, either from saturated to unsaturated or vice versa, solves the solution of (6.2a). Hence, the limit point featured in Figure 27 is classified as LIB.

6.2.3 **Bifurcations in the Smooth Power Flow** (NEVES, 2022, p.86)

As detailed in the previous subsections, a power system defined by (6.1) can have its instability classified as SNB and LIB according to Definitions 2 and 3, respectively. Based on the discussion presented in Subsection 6.2.2 and the TP condition illustrated in Figure 13, these bifurcations can also be represented in the xy-plane by Figures 28 and 29, as properly mentioned by (NEVES, 2022). In these figures, the dots indicate solution points and the arrows indicate a set of solution points found due to increase in λ (NEVES, 2022).

Figure 28 – Saddle-Node Bifurcation occurence in the xy-plane, assuming $y_1 < y_2$ and two solutions disappear with the increase of λ.

(a) BP for $y = y_1$ (b) BP for $x = x_{spec}$
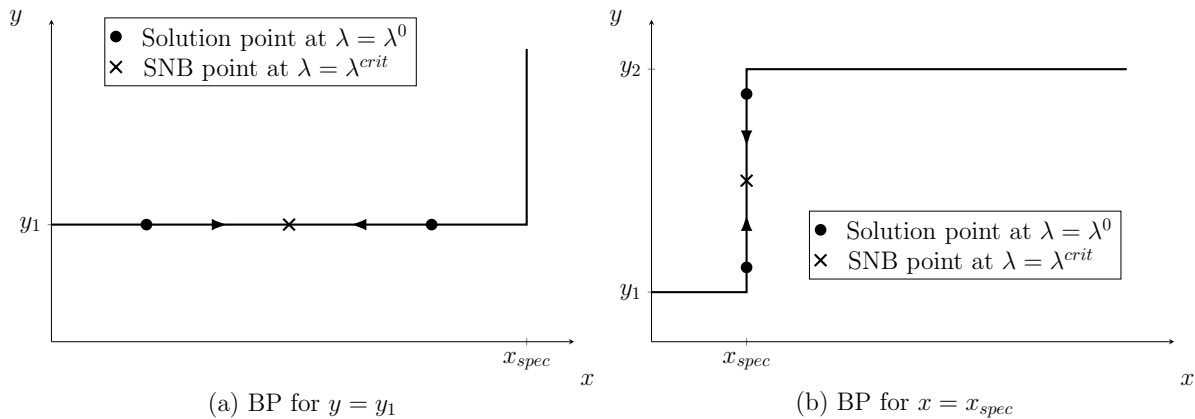
Source: Adapted from Neves (2022).

In Figure 28, the condition illustrated by Figure 26 is reproduced in the xy-plane. The bifurcation occurs when the generator is not switching between operating modes, and is either represented by control equation y_1 or y_2 in the power flow problem, as illustrated by Figure 28(a). The bifurcation also occurs when the generator is in the midst of switching its operating modes, as illustrated by Figure 28(b). For both cases, the bifurcation is not caused by the generator reaching its reactive power generation limit, but for an unknown condition in the EPS. The MLP emphasized by "×" corresponds to a BP ($\lambda = \lambda^{crit}$), with a TP being considered before the BP ($\lambda^{TP} < \lambda^{crit}$) or not as detailed in Figure 28(b) and (a), respectively.

In comparison, the condition illustrated by Figure 27 is represented in the xy-plane by Figure 29. In this case, the bifurcation truly occurs when the generator reaches its reactive power generation limit and is switching between operating modes, from saturated to unsaturated mode or vice versa, or also from control equation y_1 to y_2 (or vice versa) in the power flow problem. In this situation, the MLP emphasized by "×" corresponds to a TP being also characterized as a BP ($\lambda = \lambda^{TP} = \lambda^{crit}$).

Based on the condition detailed by Figures 27 and 29, Neves (2022) presents a series of mathematical theorems in order to demonstrate that bifurcations in the SPF are

Figure 29 – Limit-Induced Bifurcation occurence in the xy-plane, assuming $y_1 < y_2$ and two solutions disappear with the increase of λ.

(a) BP at (x_{spec}, y_1) (b) BP at (x_{spec}, y_2)
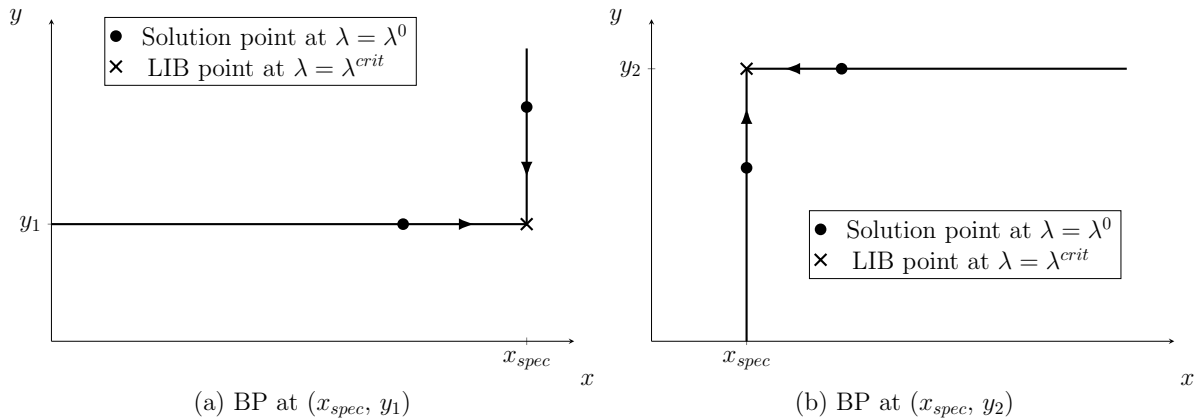
Source: Adapted from Neves (2022).

classified as SNB. These theorems are based on the *smooth step function* characteristics (Definition 1), which are responsible for discarding discontinuity problems observed in the traditional PF formulation.

Among the introduced theorems, Theorem 9 (NEVES, 2022, p.90) "proves the existence of a SNB of the smoothed system corresponding to the LIB of the original system.". Hence, the condition highlighted in Figures 27 and 29 is further explored with the introduction of smooth functions, mathematically proving that there is a SNB arbitrarily close to a LIB.

Figure 30 – Smooth Power Flow identification of Saddle-Node Bifurcation arbitrarily close to Limit-Induced Bifurcation.
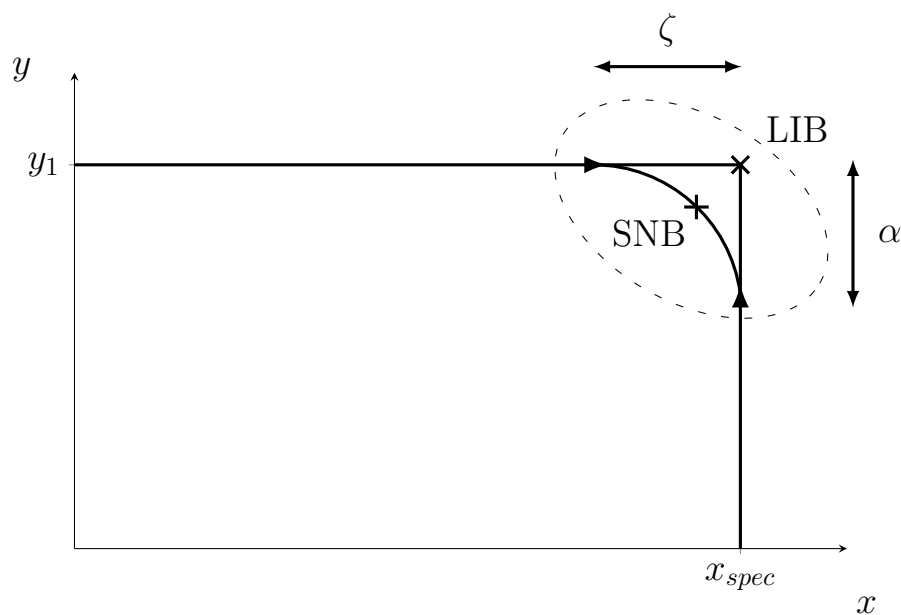
Source: Adapted from Neves (2022).

The Theorem 9 proof is illustrated in Figure 30, according to Neves (2022). The

dashed lines delimit an arbitrarily close region where both BPs are close to each other, the arrows indicate a set of solution points found due to increase in λ, and the variables ζ and α indicates the validation of properties [III] and [IV] from Definition 1 (NEVES, 2022). These two variables guarantee a solution point for (6.2a) which is not classified as a LIB, but as a SNB ($\tilde{\lambda}^{crit} < \lambda^{crit}$).

6.2.4 **Proposed modal analysis**

All things considered, it is proposed the implementation of modal analysis for numerical verification of Theorem 9. As mentioned before, it is applied the generator reactive power limit methodology detailed in Chapter 4 along with the CPF formulation, stressing EPSs until it collapses.

The eigenvalues and eigenvectors will be extracted from the proposed SPF-Generator Jacobian matrix, defined by (4.6) and (A.37), in its reduced form. The eigenvalues will identify the interaction modes between generators control equations, whereas the eigenvectors fill in sensitive information regarding the eigenvalues controllability and observability (PASSOS FILHO, 2005).

In respect of the reduced Jacobian matrix, some initial considerations must be made. The Jacobian matrix, as presented in (2.13), is detailed as follows:

$$\mathbf{J} = \begin{bmatrix} \mathbf{J}_{P\theta} & \mathbf{J}_{PV} \\ \mathbf{J}_{Q\theta} & \mathbf{J}_{QV} \end{bmatrix} \tag{6.5}$$

where $\mathbf{J}_{P\theta}, \mathbf{J}_{PV}, \mathbf{J}_{Q\theta}$ and $\mathbf{J}_{QV}$ are the submatrices of the Jacobian matrix that corresponds to the active and reactive power state equations ($\boldsymbol{P}$ and $\boldsymbol{Q}$) linearization in respect to the state variables ($\boldsymbol{\theta}$ and $\boldsymbol{V}$).

Considering now the incorporation of generator control equations, the augmented Jacobian matrix presented in (4.6) can be rewritten as:

$$\mathbf{J} = \begin{bmatrix} \mathbf{J}_{P\theta} & \mathbf{J}_{PV} & \mathbf{J}_{PX_G} \\ \mathbf{J}_{Q\theta} & \mathbf{J}_{QV} & \mathbf{J}_{QX_G} \\ \mathbf{J}_{Y_G\theta} & \mathbf{J}_{Y_GV} & \mathbf{J}_{Y_GX_G} \end{bmatrix} \tag{6.6}$$

where the new submatrices corresponds to the active and reactive power state equations linearization in respect to the generators control variables ($\boldsymbol{X_G}$) and also the linearization of the generators control equations ($\boldsymbol{Y_G}$) in respect to all the power flow state variables ($\boldsymbol{\theta}$, $\boldsymbol{V}$ and $\boldsymbol{X_G}$).

The Jacobian matrix from (6.6) can be further expanded, once it is considered the CPF formulation. In this case, the new submatrices will correspond to relationship of

state equations and control equations in regard to the control variable λ, as detailed in Appendix B. However, for the purpose of modal analysis, the Jacobian matrix expansion in (6.6) is adequate.

By reducing the Jacobian matrix, a new matrix is defined as $\mathbf{J_R}$ (GAO; MORISON; KUNDUR, 1992; MORISON; GAO; KUNDUR, 1993; KUNDUR, 1994). In this work, three attempts were made to reduce the Jacobian matrix, which are presented in the following subsubsections.

6.2.4.1 *Attempt #1*

In the first attempt, the Jacobian matrix detailed in (6.6) is manipulated, altering the state variables order:

$$
\mathbf{J} = \left[\begin{array}{ccc} \mathbf{J}_{P\theta} & \mathbf{J}_{PX_G} & \mathbf{J}_{PV} \\ \mathbf{J}_{Y_G\theta} & \mathbf{J}_{Y_GX_G} & \mathbf{J}_{Y_GV} \\ \mathbf{J}_{Q\theta} & \mathbf{J}_{QX_G} & \mathbf{J}_{QV} \end{array} \right] \tag{6.7}
$$

Considering the problem of voltage collapse due to generators reactive power generation limit, the manipulation is justified because an attempt is made in order to facilitate a simple correlation $\boldsymbol{QV}$ via modal analysis, as follows:

$$
\boldsymbol{\Delta Q} = \mathbf{J}_R \cdot \boldsymbol{\Delta V} \tag{6.8}
$$

where:

$$
\mathbf{J}_R = \left[\mathbf{J}_{QV} - \mathbf{J}_{Q\theta X_G} \cdot \mathbf{J}_{PY_G\theta X_G}^{-1} \cdot \mathbf{J}_{PY_GV} \right]_{(\mathrm{N_{BUS}})\times(\mathrm{N_{BUS}})} \tag{6.9}
$$

$$
\mathbf{J}_{Q\theta X_G} = \left[\begin{array}{cc} \mathbf{J}_{Q\theta} & \mathbf{J}_{QX_G} \end{array} \right]_{(\mathrm{N_{BUS}})\times(\mathrm{N_{BUS}}+\mathrm{N_{GEN}})} \tag{6.10}
$$

$$
\mathbf{J}_{PY_G\theta X_G} = \left[\begin{array}{cc} \mathbf{J}_{P\theta} & \mathbf{J}_{PX_G} \\ \mathbf{J}_{Y_G\theta} & \mathbf{J}_{Y_GX_G} \end{array} \right]_{(\mathrm{N_{BUS}}+\mathrm{N_{GEN}})\times(\mathrm{N_{BUS}}+\mathrm{N_{GEN}})} \tag{6.11}
$$

$$
\mathbf{J}_{PY_GV} = \left[\begin{array}{c} \mathbf{J}_{PV} \\ \mathbf{J}_{Y_GV} \end{array} \right]_{(\mathrm{N_{BUS}}+\mathrm{N_{GEN}})\times(\mathrm{N_{BUS}})} \tag{6.12}
$$

This Jacobian matrix reduction correlates the reactive power generation and voltage magnitude for all buses in the analyzed EPS, given that the $\mathbf{J_R}$ dimension is $N_{\text{BUS}} \times N_{\text{BUS}}$. However, it was observed in simulations that all bifurcations encountered were classified as LIB. Therefore, a new Jacobian matrix reduction attempt is made and is presented in the following subsubsection.

6.2.4.2 *Attempt #2*

In the second attempt, the Jacobian matrix detailed in (6.6) is considered as it is, with no manipulations being made. Once again, the $\boldsymbol{QV}$ correlation is analyzed via modal analysis, as follows:

$$\boldsymbol{\Delta Q} = \mathbf{J}_R \cdot \boldsymbol{\Delta V} \tag{6.13}$$

where:

$$\mathbf{J}_R = \left[\mathbf{J}_{QY_G V X_G} - \mathbf{J}_{QY_G \theta} \cdot \mathbf{J}_{P\theta}^{-1} \cdot \mathbf{J}_{PV X_G} \right]_{(N_{\text{BUS}}+N_{\text{GEN}}) \times (N_{\text{BUS}}+N_{\text{GEN}})} \tag{6.14}$$

$$\mathbf{J}_{QY_G V X_G \theta} = \begin{bmatrix} \mathbf{J}_{QV} & \mathbf{J}_{QX_G} \\ \mathbf{J}_{Y_G V} & \mathbf{J}_{Y_G X_G} \end{bmatrix}_{(N_{\text{BUS}}+N_{\text{GEN}}) \times (N_{\text{BUS}}+N_{\text{GEN}})} \tag{6.15}$$

$$\mathbf{J}_{QY_G \theta} = \begin{bmatrix} \mathbf{J}_{Q\theta} \\ \mathbf{J}_{Y_G \theta} \end{bmatrix}_{(N_{\text{BUS}}+N_{\text{GEN}}) \times (N_{\text{BUS}})} \tag{6.16}$$

$$\mathbf{J}_{PV X_G} = \begin{bmatrix} \mathbf{J}_{PV} & \mathbf{J}_{PX_G} \end{bmatrix}_{(N_{\text{BUS}}) \times (N_{\text{BUS}}+N_{\text{GEN}})} \tag{6.17}$$

In comparison with the previous attempt, the reduced Jacobian matrix increases dimension in terms of the number of generators (N_{GEN}) in the EPS , as detailed in (6.14). This dimension increment of $\mathbf{J_R}$ means that the reactive power generation limit control equations are included in the correlation between reactive power generation and voltage magnitude for all buses in the analyzed EPS.

Since the control equations were included in the $\boldsymbol{QV}$ modal analysis, SNB bifurcations were encountered during simulations. Not all bifurcations were classified as SNB though, once that it depends on how close the BPs are from each other, as explained by (NEVES, 2022) and illustrated by Figure 30.

The SNB bifurcations were identified due to the presence of eigenvalues values tending to zero in the reduced Jacobian matrix ($\mathbf{J_R}$). In all cases analyzed, the mode-shape and participation factors for the given small eigenvalues always pointed to the control equations incorporated into the Jacobian matrix. Therefore, a new Jacobian matrix reduction attempt is made and is presented in the following subsubsection.

6.2.4.3 *Attempt # 3*

In the third and final attempt, the Jacobian matrix detailed in (6.6) is considered as it is, with no manipulations being made. In this turn, it is opted to obtain the correlation between control equations and the voltage magnitude state variable ($\boldsymbol{YV}$), as follows:

$$\boldsymbol{\Delta Y} = \mathbf{J_R} \cdot \boldsymbol{\Delta V} \tag{6.18}$$

where:

$$\mathbf{J_R} = \left[\mathbf{J}_{Y_G X_G} - \mathbf{J}_{Y_G \theta V} \cdot \mathbf{J}_{PQ\theta V}^{-1} \cdot \mathbf{J}_{PQX_G} \right]_{(\text{N}_{\text{GEN}}) \times (\text{N}_{\text{GEN}})} \tag{6.19}$$

$$\mathbf{J}_{Y_G \theta V} = \left[\begin{array}{cc} \mathbf{J}_{Y_G \theta} & \mathbf{J}_{Y_G V} \end{array} \right]_{(\text{N}_{\text{GEN}}) \times (2\text{N}_{\text{BUS}})} \tag{6.20}$$

$$\mathbf{J}_{PQ\theta V} = \left[\begin{array}{cc} \mathbf{J}_{P\theta} & \mathbf{J}_{PV} \\ \mathbf{J}_{Q\theta} & \mathbf{J}_{QV} \end{array} \right]_{(2\text{N}_{\text{BUS}}) \times (2\text{N}_{\text{BUS}})} \tag{6.21}$$

$$\mathbf{J}_{PQX_G} = \left[\begin{array}{c} \mathbf{J}_{PX_G} \\ \mathbf{J}_{QX_G} \end{array} \right]_{(2\text{N}_{\text{BUS}}) \times (\text{N}_{\text{GEN}})} \tag{6.22}$$

Differently from the previous attempts, the reduced Jacobian matrix dimension in (6.19) depends only on the amount of generator's reactive power limits control equations that are incorporated into the system of nonlinear equations. That means that is particularly analyzed the correlation between generator's control equations and voltage magnitude for EPSs (N_{GEN}).

Since only the control equations are being analyzed in the modal analysis, it could be observed that all SNB bifurcations encountered during simulations ($\mathbf{J_R}$ small eingenvalues) resulted from them. This analysis is valid once that the SPF formulation smoothness is introduced precisely by the control equations incorporated into the Jacobian matrix.

Hence, the Jacobian matrix reduction (6.19) proposed in this subsubsection will be considered in the simulations presented in Chapter 7. The modal analysis properties presented in Appendix C will be implemented onto the reduced Jacobian matrix given in (6.19). The sensitivity between a generator, at bus k, reactive power generation and voltage magnitude will be evaluated as follows:

$$\frac{\partial Q_{G_k, gen}}{\partial V_{k, gen}} = \sum_{i=1}^{\mathrm{N}_{BUS}+\mathrm{N}_{GEN}} \phi_{ki} \cdot \lambda_i^{eig} \cdot \psi_{ik} \qquad (6.23)$$

Within the modal analysis, the goal is to identify which generator is associated with critical eigenvalue via modal-shape and participation factor analyzes. The critical eigenvalue are responsible for the Jacobian matrix singularity, as detailed in property [II] of Definition 2, which, therefore, characterizes a voltage collapse classified as SNB.

6.3 PARTIAL CONCLUSIONS

This chapter presents relevant mathematical concepts regarding EPSs voltage collapse classifications considering the traditional PF formulation and the SPF formulation. These concepts have solid mathematical foundation provided by theorems, which are thoroughly detailed by Neves (2022).

Although this chapter only considered the SPF-Generator methodology for the analysis of voltage collapse classified as SNBs, the same analysis can be extended for SPF-SVCs methodologies. Regarding the proposed modal analysis, the following chapter presents simulation results which validates the identification of SNBs via SPF formulation.

7 SIMULATION RESULTS

In this chapter, the steady-state SPF simulations results obtained from the implementation of the proposed SPF-Generator and SPF-SVCs modelings are presented. The proposed methodologies were simulated in both tutorial systems and well-known *Institute of Electric and Electronic Engineers* (IEEE) systems, under different conditions. To obtain the desired results, a Python-based program was developed employing the CPF formulation detailed in Appendix B together with the SPF methodologies.

To validate the simulation results, a production-grade academic version software provided by Electric Energy Research Center (CEPEL) was used. In all systems simulations, the following parameters were applied:

- Base apparent power: (S_B) = 100 MVA;

- Base electrical frequency: (f_B) = 60 Hz;

- Active power convergence tolerance: $\varepsilon_P = 10^{-6}$ p.u.;

- Rective power convergence tolerance: $\varepsilon_Q = 10^{-6}$ p.u.;

- Control equations convergence tolerance: $\varepsilon_Y = 10^{-6}$ p.u.;

Other simulation parameters such as sigmoid switches slope and tolerance, and also CPF convergence parameters, will be defined on case-by-case basis. For all case studies detailed hereinafter, the load model considered was constant power.

First, in Section 7.1, the results simulations and discussions regarding the SPF-Generators methodology are presented. On account of the SPF-Generator methodology, the respective results presented hereinafter consider only the voltage stability analysis proposed in Subsection 6.2.3, once that this model steady-state results have already been validated by Pontes (2018), Pontes, Passos Filho and La Gatta (2018).

Later, Section 7.2 presents the results simulations and discussions regarding the steady-state SPF-SVC methodologies. A comparison is made between each proposed SPF-SVC methodology, as the *droop* enhancement for the thyristor firing-angle methodology returns same results as the reactive power injection methodology (BARBOSA; PASSOS FILHO, 2022). An evaluation of SNB classifications being caused by SVC reaching reactive power limits is also analyzed in two case studies.

7.1 GENERATORS

Three different case studies were created and simulated, as described below:

- **Case I: Tutorial system.** Consists of a 2 bus system, similar to the one presented by (MILANO, 2010, p.103). For this system, the CPF formulation will be applied in order to observe voltage collapse classified as SNB via SPF formulation.

- **Case II: Tutorial system (mirrored).** It is based on the previous case tutorial system, mirror-expanded, and contains 4 buses. For this system, the CPF formulation will be applied in order to observe voltage collapse classified as SNB via SPF formulation.

- **Case III: IEEE 118 bus system (modified).** It is a medium size power system that contains 118 buses, over 170 lines and over 50 generators terminals, representing a real EPS (CHRISTIE, 1999). A modification is proposed similarly as presented in Greene, Dobson and Alvarado (1997). For this system, the CPF formulation will be applied in order to observe voltage collapse classified as SNB via SPF formulation.

The Jacobian matrix reduction detailed in Subsubsection 6.2.4.3 was implemented in all the case studies, which are detailed in the following subsections.

7.1.1 Case I: Tutorial system I

This 2 bus system is based on the EPS developed by Milano (2010) for discussions regarding the continuation power flow analysis and voltage stability analysis. From this tutorial power system, both SNB and LIB voltage collapse conditions can be simulated, depending mainly on the generators maximum reactive power limit setted value. This power system topology and data are shown in Figure 31.

Figure 31 – Tutorial system I topology.

$V\theta$ PQ

$y_{se}^{-1} = j0.15788$

$\overline{V}_\infty = 1 \angle 0°$

$Q_{G,\infty}^{max} = 0.65$

$(0.1 + j0)$
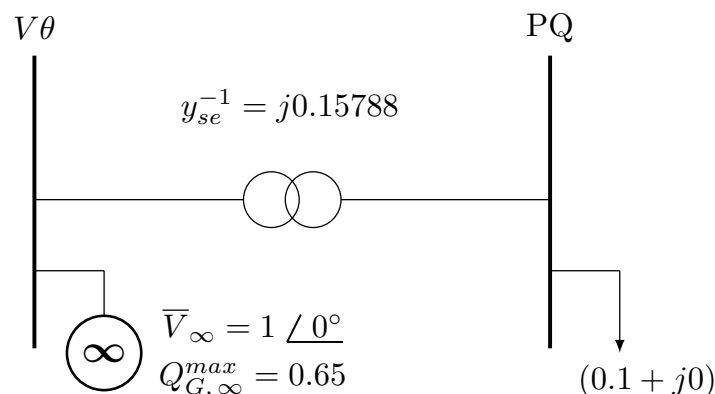
Source: Adapted from Milano (2010).

For the proposed SPF-Generator methodology and voltage stability analysis (identification of SNBs), the following parameters values were adopted:

- Active power convergence tolerance: $\varepsilon_P = 10^{-10}$ p.u.;

- Rective power convergence tolerance: $\varepsilon_Q = 10^{-10}$ p.u.;

- Control equations convergence tolerance: $\varepsilon_Y = 10^{-10}$ p.u.;

- Sigmoid switches $sw1$ through $sw4$ slope: $slp = 10^{15}$;

- Sigmoid switches $sw1$ and $sw2$ tolerances: $tol_q^{sup} = tol_q^{inf} = 10^{-20}$;

- Sigmoid switches $sw3$ and $sw4$ tolerances: $tol_v^{sup} = tol_v^{inf} = 10^{-20}$;

- Slack bus maximum reactive power generation: $Q_{G_k, \infty}^{max} = 0.65$ p.u.;

- CPF loading parameter step: $\lambda^{step} = 10\%$.

As a result of applying the CPF formulation along with the SPF-Generator methodology, a SNB bifurcation was successfully identified instead of a LIB. The information regarding the SNB bifurcation appointed in Table 7.

Table 7 – Simulation results identifying SNB in tutorial system I through SPF-Generator methodology.

Critical loading parameter $\left(\tilde{\boldsymbol{\lambda}}^{crit}\right)$	1822.1214646199573%
Reactive power generated by $\boldsymbol{Q_{G,\infty}}$	0.6499999999975472 p.u.
$\mathbf{J_R}$ determinant	0.001467898289992188
$\mathbf{J_R}$ eigenvalue	[0.0014679]

Source: Elaborated by the author (2023).

This result verifies the mathematical property of the SPF formulation ability of transforming LIBs into SNBs, as stated by Neves (2022), and demonstrates the proposed application of modal analysis for the indentification of SNBs. Furthermore, Figure 32 highlight the participation factor based on the SNB eigenvalue as detailed in Table 7.

As it can be observed from Figure 32, the $\mathbf{J_R}$ eigenvalue indicates the highest possible participation factor for the slack bus generator. The column refers to the slack bus reactive power generation limits control equation linearized in the Jacobian matrix. It can be observed that the collapse is caused 100% because the slack bus generator reaches its limit.

The mode-shape analysis was not reproduced for this simulation once it only presents one eigenvalue and, therefore, it is not possible to analyze the impact of the control variable perturbation in other control variables. In fact, the result would be similar to the participation factor shown in Figure 32.

In addition, the condition illustrated in Figure 30 is reproduced by the sigmoid switches output. As mentioned in Chapter 3, sigmoid function with high slope value enables a fast transition between output 1 and 0, and vice versa. However, at the SNB

Figure 32 – Tutorial system I participation factor for $\lambda^{eig} = 0.0014679$.
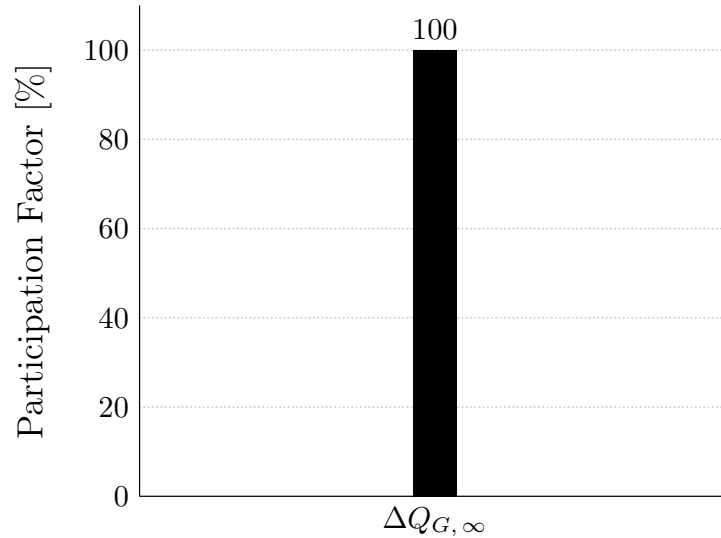
Source: Elaborated by the author (2023).

point of collapse, the slack bus sigmoid switches $sw1$, $sw2$, $sw3$ and $sw4$ possess the values displayed in Table 8.

Table 8 – SPF-Generator sigmoid switches outputs in SNB indentification for tutorial system I.

$sw1$	$sw2$	$sw3$	$sw4$
1.00	0.00	0.02	0.98

Source: Elaborated by the author (2023).

The switches values correctly indicates that the slack bus reactive power generation is reaching maximum limit and is on the verge of transitioning from normal mode control equation to superior limit violation mode control equation, detailed in Chapter 4. Interestingly, the electric device steady-state control equations were traditionally developed to represent each generator operational mode individually. With the result presented in Table 8, it is observed a mix of two control equations, which is justified by the adoption of *smooth step function* continuity characteristic (Definition 1).

7.1.2 Case II: Tutorial system I (mirrored)

This 4 bus system is a mirrored version of the aforementioned EPS. The ideia behind the modification of tutorial system I is to analyze, through modal analysis, a similar result as shown in Subsection 7.1.1 for eigenvalues, mode-shape and participation factor once that an SNB is identified via SPF-Generator methodology.

To mirror the tutorial system I, a branch with high impedance value was adopted connecting both PQ buses, creating two electrical areas. Both areas are capable of attending their load demands. The main goal is to simulate SNB voltage collapse condition

caused by the slack bus generator reactive power reaching maximum limit. The power system topology and data are shown in Figure 33.

Figure 33 – Tutorial system I (mirrored) topology.
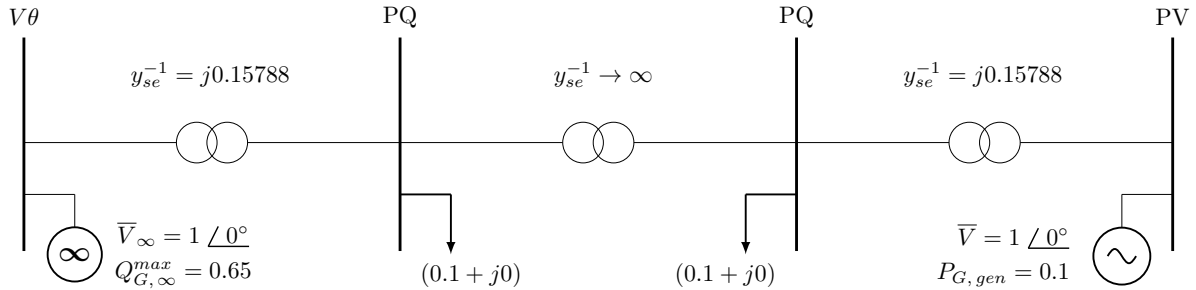
Source: Elaborated by the author (2023).

For the proposed SPF-Generator methodology and voltage stability analysis, the following parameters values were adopted:

- Active power convergence tolerance: $\varepsilon_P = 10^{-10}$ p.u.;

- Rective power convergence tolerance: $\varepsilon_Q = 10^{-10}$ p.u.;

- Control equations convergence tolerance: $\varepsilon_Y = 10^{-10}$ p.u.;

- Sigmoid switches $sw1$ through $sw4$ slope: $slp = 0.9235 \cdot 10^{14}$;

- Sigmoid switches $sw1$ and $sw2$ tolerances: $tol_q^{sup} = tol_q^{inf} = 10^{-20}$;

- Sigmoid switches $sw3$ and $sw4$ tolerances: $tol_v^{sup} = tol_v^{inf} = 10^{-20}$;

- Slack bus maximum reactive power generation: $Q_{G_k,\infty}^{max} = 0.65$ p.u.;

- PV bus maximum reactive power generation: $Q_{G_k,gen}^{max} = \infty$;

- CPF loading parameter step: $\lambda^{step} = 10\%$.

It is important to inform that the CPF loading parameter was applied only for the PQ bus connected to the slack bus, while the other PQ load remained constant throughout the whole simulation. As a result of applying the CPF formulation along with the SPF-Generator methodology, a SNB bifurcation was identified instead of a LIB. The information regarding the SNB bifurcation is detailed in Table 9.

This result once again verifies the mathematical property of the SPF formulation ability of transforming LIBs into SNBs, as stated by Neves (2022). Moreover, Figures 34 and 35 highlights the mode-shape and participation factor based on the SNB smallest eigenvalue obtained in simulations.

Table 9 – Simulation results identifying SNB in tutorial system I (mirrored) through SPF-Generator methodology.

Critical loading parameter $\left(\tilde{\boldsymbol{\lambda}}^{crit}\right)$	1822.121465441%
Reactive power generated by $\boldsymbol{Q_{G,\infty}}$	0.6499999999999866 p.u.
$\mathbf{J_R}$ determinant	2.6442422689774046
$\mathbf{J_R}$ eigenvalues	$[0.00835568031\ 316.460440]$

Source: Elaborated by the author (2023).

Figure 34 – Tutorial system I (mirrored) mode-shape for $\lambda^{eig} = 0.00835568031$.
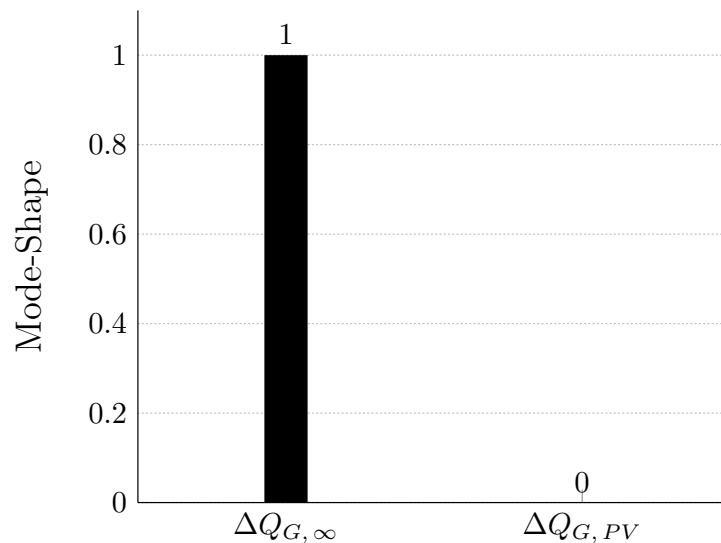
Source: Elaborated by the author (2023).

From the mode-shape analysis, illustrated in Figure 34, it can be observed how a perturbation in a control variable impacts other control variables. In this case, it is analyzed the slack bus reactive power generation perturbation impacts on the reactive power generated by the PV bus. As illustrated by Figure 34, the variation on the reactive power generation by the slack bus has no impact on the reactive power generated by the PV bus. This condition was expected once that these two buses are located in different electrical areas with a high impedance branch connecting (and isolating) both areas.

As it can be observed from Figure 35, the smallest $\mathbf{J_R}$ eigenvalue indicates highest possible participation factor for the slack bus generator and a null participation factor for the PV bus generator. Therefore, it can be concluded by analyzing Figure 35 that the PV bus generator has no interference in the EPS voltage collapse, which is caused 100% because of the slack bus generator reaching its limit.

Analyzing the sigmoid switches values for the slack bus generator, in Table 10, and PV bus generator, in Table 11, it can also be inferred that the PV bus has no intereference in the EPS voltage collapse. The slack bus generator switches values correctly indicate that the reactive power generation is reaching maximum limit, transitioning from normal mode control equation to superior limit violation mode control equation.

Figure 35 – Tutorial system I (mirrored) participation factor for $\lambda^{eig} = 0.00835568031$.
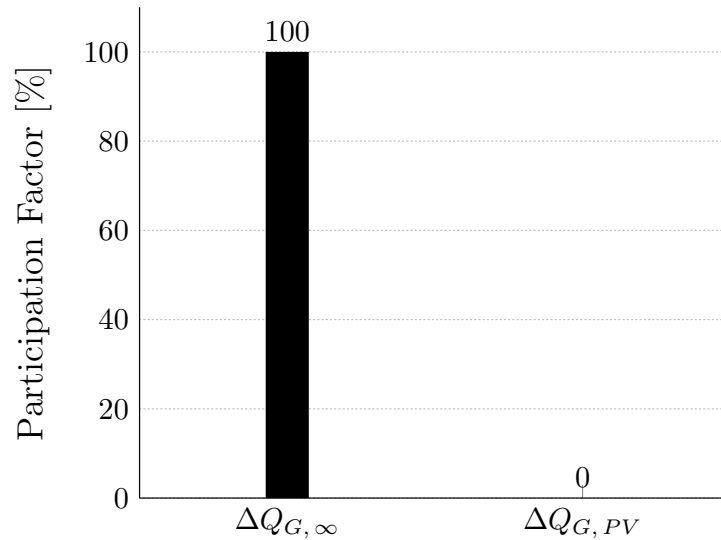
Source: Elaborated by the author (2023).

Table 10 – Slack bus SPF-Generator sigmoid switches outputs in SNB indentification for tutorial system I (mirrored).

$sw1$	$sw2$	$sw3$	$sw4$
0.25	0.00	0.33	0.67

Source: Elaborated by the author (2023).

On the other hand, the PV bus generator switches values correctly indicate that it is in normal operating mode at the MLP. Sigmoid switches $sw3$ and $sw4$ values at 0.50 in Table 11 are a result of a small value adopted for the voltage magnitude tolerance tol_v^{sup} and tol_v^{inf}.

Table 11 – PV bus SPF-Generator sigmoid switches outputs in SNB indentification for tutorial system I (mirrored).

$sw1$	$sw2$	$sw3$	$sw4$
0.00	0.00	0.50	0.50

Source: Elaborated by the author (2023).

Regarding the results shown in this subsection, it is noticed that they are very close to those presented in the Subsection 7.1.1, mainly on account of the critical loading parameter ($\tilde{\lambda}^{crit}$) shown in Tables 7 and 9. This result was expected to happen once the EPS is divided in two separate electrical areas, given by the high impedance branch. Although the power system presents multiple areas, the voltage collapse still happens due to the slack bus generator reaching its maximum generation limit.

7.1.3 **Case III: IEEE 118 bus system (modified)**

A similar LIB voltage collapse as presented in Greene, Dobson and Alvarado (1997), Neves, Alberto and Chiang (2020) was simulated in this case study for the IEEE 118 bus. It is considered a proportional increase to the base case in generation and load demand. The EPS system topology is illustrated in Figure 38, whereas its data is available in Christie (1999).

In this case study, the following CPF as well as SPF-Generator parameters were adopted:

- Active power convergence tolerance: $\varepsilon_P = 10^{-10}$ p.u.;

- Rective power convergence tolerance: $\varepsilon_Q = 10^{-10}$ p.u.;

- Control equations convergence tolerance: $\varepsilon_Y = 10^{-10}$ p.u.;

- Sigmoid switches $sw1$ through $sw4$ slope: $slp = 10^{10}$;

- Sigmoid switches $sw1$ and $sw2$ tolerances: $tol_q^{sup} = tol_q^{inf} = 10^{-17}$;

- Sigmoid switches $sw3$ and $sw4$ tolerances: $tol_v^{sup} = tol_v^{inf} = 10^{-8}$;

- CPF loading parameter step: $\lambda^{step} = 10\%$.

By using CEPEL production-grade academic version software, which applies the traditional modeling for generators, a LIB voltage collapse was identified in the system due to generator located at bus 4 reaching its maximum reactive power limit. In turn, by using the developed Python program and the proposed SPF-Generator methodology, a SNB voltage collapse was identified for the same generator bus. The information regarding the SNB bifurcation is detailed in Table 12.

Table 12 – Simulation results identifying SNB in IEEE 118 bus system through SPF-Generator methodology.

Critical loading parameter $\left(\tilde{\boldsymbol{\lambda}}^{crit}\right)$	100.7694%
Reactive power generated by $\boldsymbol{Q_{G,4}}$	2.9999992291 p.u.
$\mathbf{J}_R$ eigenvalues	[(. . .) 0.01390944 0.01267277 0.02319254 0.02779360 0.03126189 (. . .)]

Source: Elaborated by the author (2023).

Differently from Tables 7 and 9, in Table 12 the five smallest eigenvalues among the 54 available are shown. Based on these eigenvalues, an interesting analysis is made by observing its respective participation factors, which are shown in Figures 36 to 41.

Figures 36, 37, 39 and 40 correspond to eigenvalues that indicate control conflicts between two or more buses. These conflicts are related to generator buses reactive power

generation output in order to control their own bus voltage magnitude. However, a conflict arises by reason of these generator buses being electrically close to each other, or even connected to each other, and for having different control goals.

Figure 36 – IEEE 118 bus system participation factor for $\lambda^{eig} = 0.01390944$.
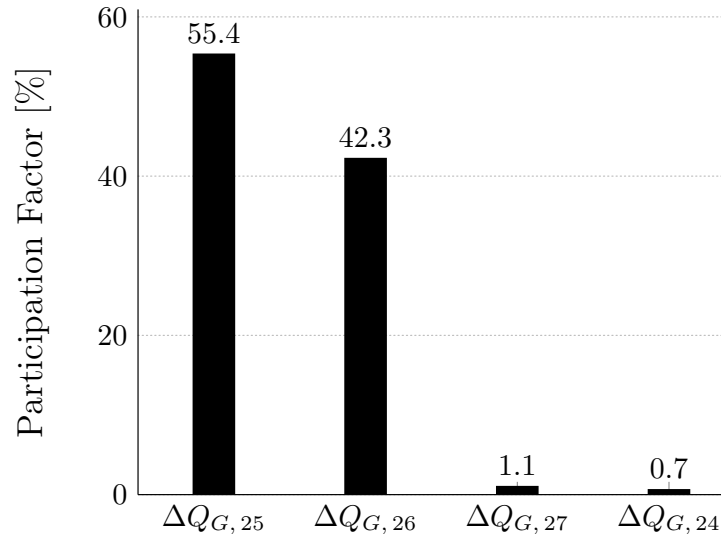
Source: Elaborated by the author (2023).

In Figure 36, the main conflict consists on the control goals related to the reactive power generation of buses 25 and 26. By analyzing the IEEE 118 bus system topology, it can be seen that both buses are connected to each other. Since each generator controls their own bus voltage magnitude at a specific value, the conflict arises.

Figure 37 – IEEE 118 bus system participation factor for $\lambda^{eig} = 0.01267277$.
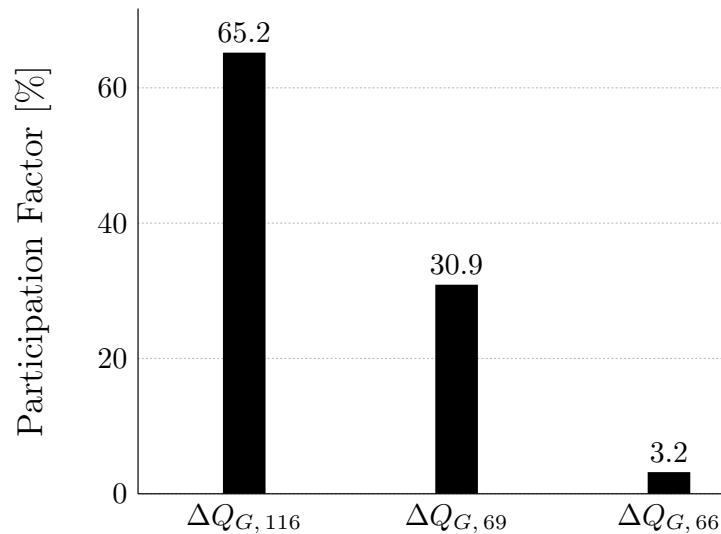
Source: Elaborated by the author (2023).

In Figure 37, the conflict arises from buses 116, 69 and 66 reactive power generation, due to the same reason aforementioned. In this case, the buses are not directly connected at each other but are electrically close.

Figure 38 – IEEE 118 bus system topology.

Figure 39 – IEEE 118 bus system participation factor for $\lambda^{eig} = 0.02319254$.
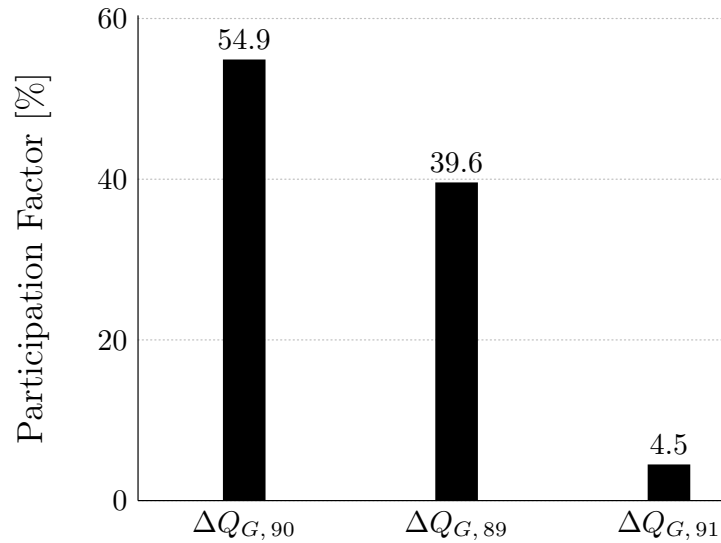
Source: Elaborated by the author (2023).

Figure 40 – IEEE 118 bus system participation factor for $\lambda^{eig} = 0.03126189$.
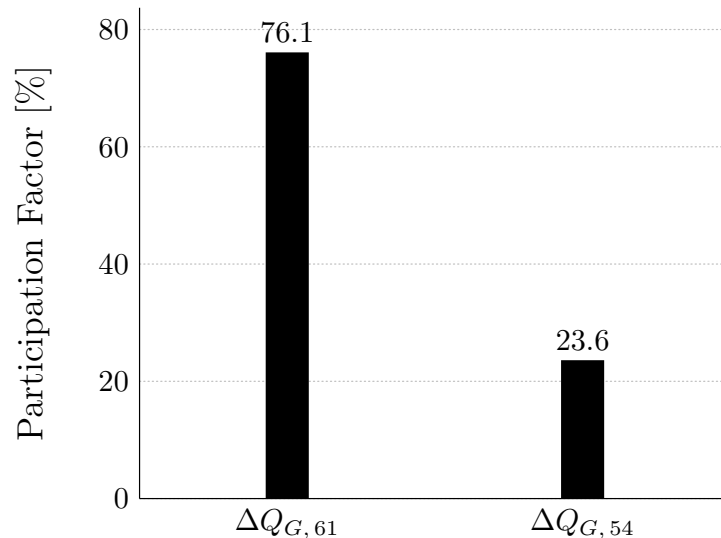
Source: Elaborated by the author (2023).

In Figures 39 and 40, the same conflict condition is observed. Therefore, the eigenvalues associated with this condition does not represent voltage collapse scenarios for the analyzed system, even though how small the eigenvalues are.

On the other hand, Figure 41 shows participation factors for buses which are not electrically close or connected to each other (buses 4, 40 and 113). Therefore, it can be concluded from this figure analysis that it corresponds to a voltage collapse condition in the EPS. Not only that, it is a voltage collapse classified as SNB which is caused 90.2% because of the generator bus 4 reaching its maximum reactive power limit.

Although the eigenvalue associated with Figure 41 is not the smallest one, it

Figure 41 – IEEE 118 bus system participation factor for $\lambda^{eig} = 0.02779360$.
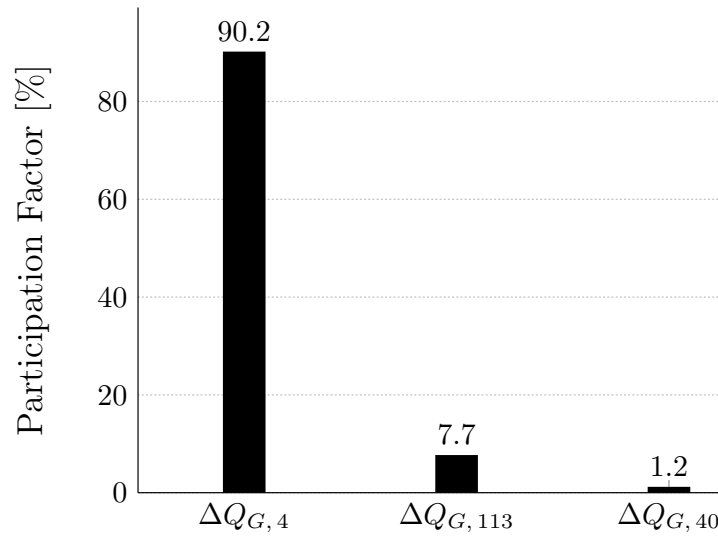
Source: Elaborated by the author (2023).

correctly corresponds to a voltage collapse scenario classified as SNB. As mentioned before, in Greene, Dobson and Alvarado (1997), Neves, Alberto and Chiang (2020) the same voltage collapse simulated via traditional PF formulation is classified as LIB. This condition was verified via simulations conducted in CEPEL's production-grade academic version software.

7.2 STATIC VAr COMPENSATORS

A total of five different case studies were created and simulated, as described below:

- **Case I: Tutorial system II.** Consists of a 4 bus system developed by (PASSOS FILHO, 2000) to validate the methodology. The SPF-SVCs methodologies result will be compared to the results presented in the aforementioned work.

- **Case II: Tutorial system III.** Consists of a 3 bus system used in EPSs voltage stability studies (KUNDUR, 1994, p.968). For this system, the CPF formulation will be applied in order to observe SVCs operational behavior variation.

- **Case III: Nordic system.** It is a fictitious system based on a real EPS that contains 74 buses, over 100 branches and 20 generator terminals (CUTSEM *et al.*, 2015; CUTSEM *et al.*, 2020). For this system, the CPF formulation will be applied in order to observe SVCs operational behavior variation.

- **Case IV: Tutorial system IV.** Consists of a SVC connected to an infinite bus used by Chen and Min (2007) to evaluate voltage collapse being caused by the control device reaching reactive power generation limit. For this system, the CPF

formulation will be applied in order to observe voltage collapse classified as SNB via SPF-SVC reactive power injection methodology.

- **Case V: IEEE 30 bus system.** It is a system based on a real EPS that contains 30 buses, 41 branches and 6 generator terminals (CHRISTIE, 1999). SVCs are introduced into this power system, as detailed in Chen and Min (2007), with the intention of evaluating voltage collapse being caused by the control device reaching reactive power generation limit. For this system, the CPF formulation will be applied in order to observe voltage collapse classified as SNB via SPF-SVC reactive power injection methodology.

These case studies are detailed in the following subsections.

7.2.1 Case I: Tutorial system II

For this case study, the EPS system topology along with bus and line data are illustrated in Figure 42. The SVC is connected at a low-side bus with the intent of controlling the high-side bus voltage magnitude. The *flat start* condition is applied to initiate the simulation.

Figure 42 – Tutorial system II topology.
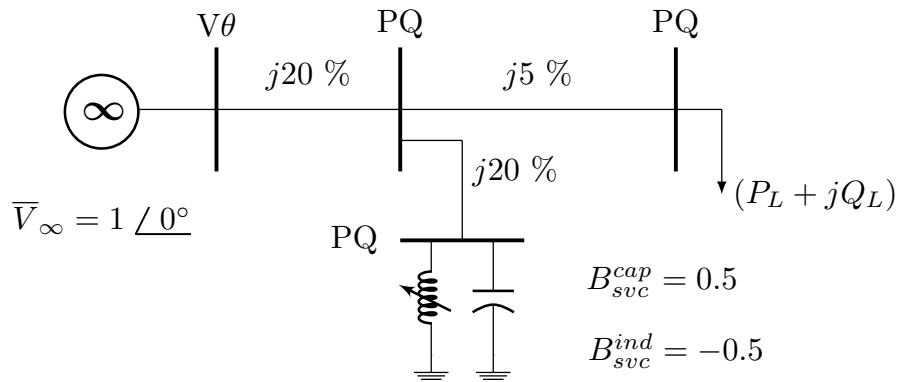
Source: Adapted from Passos Filho (2000).

The SPF-SVC parameters employed in this simulation are given below:

- SVC linear operating region *droop*: $r = 3\%$;

- SVC controlled bus voltage magnitude reference: $V_{m,svc}^{ref} = 1$ p.u.;

- Sigmoid switches $sw5$ through $sw12$ slope: $slp = 10^8$;

- Sigmoid switches $sw5$ through $sw8$, $sw11$ and $sw12$ tolerances: $tol_v^{sup} = tol_v^{inf} = 10^{-6}$;

- Sigmoid switches $sw9$ and $sw10$ tolerances: $tol_\alpha^{sup} = tol_\alpha^{inf} = 10^{-6}$;

The same simulation protocol adopted by Passos Filho (2000) was employed in this case study and is shown in Tables 13, 14 and 15. Initially, a transition between SVC linear and capacitive operational regions is demonstrated. Later, the transition is made between SVC linear and inductive operational regions. This transition is made possible by a variation on the system's load demand.

Table 13 – SPF-SVC reactive power injection methodology simulation results.

Simulation	Voltage Magnitude [p.u.]		SVC		Load Demand		Iterations
	Low-side	High-side	Mode	Generation [p.u.]	Active [MW]	Reactive [MVAr]	
1	0.988	1.008	Linear	0.411	120.0	0.0	5*
2	0.985	1.010	Linear	0.509	132.0	0.0	5*
3	0.985	1.010	Linear	0.509	132.1	0.0	5*
4	0.985	1.010	Capacitive	0.510	132.2	0.0	5
5	0.982	1.007	Capacitive	0.507	133.0	0.0	6
6	0.951	0.976	Capacitive	0.476	140.0	0.0	6
7	1.012	0.992	Linear	-0.407	50.0	-60.0	5*
8	1.014	0.990	Linear	-0.476	50.0	-70.0	4
9	1.015	0.990	Linear	-0.489	50.0	-72.0	5
10	1.015	0.990	Inductive	-0.490	50.0	-72.1	4
11	1.015	0.990	Inductive	-0.490	50.0	-72.4	4
12	1.025	1.000	Inductive	-0.500	50.0	-80.0	4

Source: Elaborated by the author (2023).

Table 14 – SPF-SVC current injection methodology simulation results.

Simulation	Voltage Magnitude [p.u.]		SVC		Load Demand		Iterations
	Low-side	High-side	Mode	Generation [p.u.]	Active [MW]	Reactive [MVAr]	
1	0.988	1.008	Linear	0.411	120.0	0.0	5*
2	0.985	1.010	Linear	0.509	132.0	0.0	5*
3	0.985	1.010	Linear	0.509	132.1	0.0	5*
4	0.985	1.010	Capacitive	0.509	132.2	0.0	5
5	0.982	1.007	Capacitive	0.507	133.0	0.0	6*
6	0.951	0.976	Capacitive	0.476	140.0	0.0	6
7	1.012	0.992	Linear	-0.407	50.0	-60.0	5*
8	1.014	0.990	Linear	-0.476	50.0	-70.0	4
9	1.015	0.990	Linear	-0.489	50.0	-72.0	5
10	1.015	0.990	Inductive	-0.490	50.0	-72.1	5*
11	1.015	0.990	Inductive	-0.490	50.0	-72.4	4
12	1.025	1.000	Inductive	-0.500	50.0	-80.0	4

Source: Elaborated by the author (2023).

The results shown in Tables 13 and 14 are in accordance with the ones presented in Passos Filho (2000). A novelty is presented in Table 15, which details the same results as the aforementioned tables, but for the SPF-SVC thyristor firing-angle methodology.

Table 15 – SPF-SVC thyristor firing-angle methodology simulation results.

Simulation	Voltage Magnitude [p.u.]		SVC		Load Demand		Iterations
	Low-side	High-side	Mode	Generation [p.u.]	Active [MW]	Reactive [MVAr]	
1	0.988	1.008	Linear ($\alpha = 144.24°$)	0.411	120.0	0.0	6**
2	0.985	1.010	Linear ($\alpha = 171.7°$)	0.509	132.0	0.0	10**
3	0.985	1.010	Linear ($\alpha = 174.2°$)	0.509	132.1	0.0	10**
4	0.985	1.010	Capacitive ($\alpha = 180°$)	0.51	132.2	0.0	10**
5	0.982	1.007	Capacitive ($\alpha = 180°$)	0.507	133.0	0.0	9**
6	0.951	0.976	Capacitive ($\alpha = 180°$)	0.476	140.0	0.0	8**
7	1.012	0.992	Linear ($\alpha = 93.88°$)	-0.407	50.0	-60.0	6**
8	1.014	0.990	Linear ($\alpha = 90.65°$)	-0.476	50.0	-70.0	5**
9	1.015	0.990	Linear ($\alpha = 90.01°$)	-0.489	50.0	-72.0	6**
10	1.015	0.990	Inductive ($\alpha = 90°$)	-0.490	50.0	-72.1	10**
11	1.015	0.990	Inductive ($\alpha = 90°$)	-0.490	50.0	-72.4	10**
12	1.025	1.000	Inductive ($\alpha = 90°$)	-0.500	50.0	-80.0	10**

Source: Elaborated by the author (2023).

The results obtained are satisfactory and validate the correct functioning of the sigmoid switch in all SPF-SVC methodologies proposed.

The single asterisk mark (*) in the "Iterations" column represents Python simulations which resulted in one iteration count higher than CEPEL's production-grade academic version software. The double asterisk mark (**), in turn, represent Python simulations which resulted in two or more iteration count higher than CEPEL's.

The higher number of iterations for the SPF-SVC thyristor firing-angle methodology is justified by reason that the control variable α tends to be more sensitive than the control variable $Q_{G_k, svc}$ or $I_{k, svc}$. This sensitivity is reassured in Figure 8, where it is illustrated that small variations of α provoke large variations in the control device equivalent susceptance, and, consequently, in the reactive power generated by the equipment.

7.2.2 Case II: Tutorial system III

Based on the validity of all the proposed SPF-SVC methodologies in power flow steady-state analysis, in this case study the CPF formulation will be employed only with the SPF-SVC thyristor firing-angle methodology. The intent is to analyze the proposed *droop* enhancement detailed in Section 5.4 and to compare the validated methodology with other forms of SVC representation in the steady-state analysis, as mentioned in Subsection 2.1.2.

An adapted version of the EPS system topology along with bus and line data are illustrated in Figure 43. It consists of a 3 bus system used in EPSs voltage stability studies as properly mentioned by Kundur (1994, p.968). For all steady-state SVC representations, the equipment is considered to be connected at bus PQ and controlling the PQ load bus voltage magnitude at the reference value of 1 p.u.. The *flat start* condition is applied

Figure 43 – Tutorial system III topology.
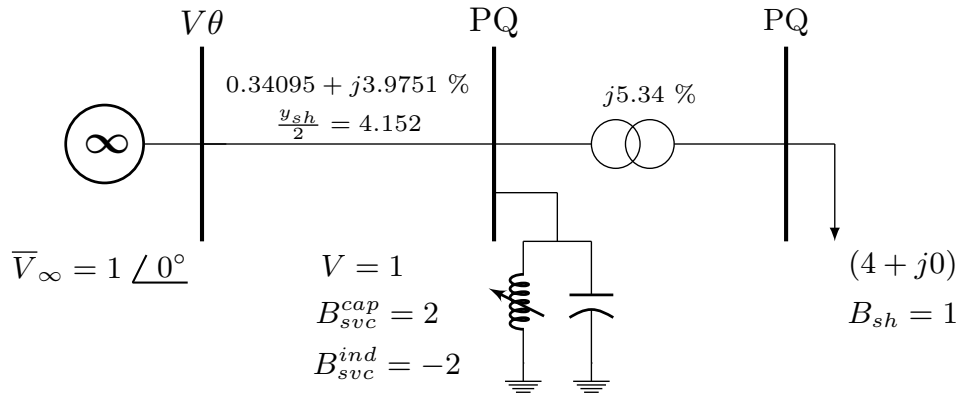
Source: Adapted from Kundur (1994, p.968).

before initiating the CPF simulation.

In this case study, the SPF-SVC parameters employed are detailed hereinafter and the simulation results are presented in Figure 44, which illustrates the PQ bus voltage behavior due to load increments.

- SVC linear operating region *droop r* is subject to variations;

- SVC controlled bus voltage magnitude reference: $V_{m,svc}^{ref} = 1$ p.u.;

- Sigmoid switches $sw9$ through $sw12$ slope: $slp = 10^8$;

- Sigmoid switches $sw11$ and $sw12$ tolerances: $tol_v^{sup} = tol_v^{inf} = 10^{-6}$;

- Sigmoid switches $sw9$ and $sw10$ tolerances: $tol_\alpha^{sup} = tol_\alpha^{inf} = 10^{-6}$;

By modeling the SVC as a synchronous condenser or via the traditional thyristor firing-angle methodology, the PQ load bus voltage magnitude is controlled at the reference value throughout most of the load increment. This condition is ideal once that a *droop* between 1% and 5% must be considered for the equipment (TAYLOR, 1994; MILLER *et al.*, 1982).

Additionally, the synchronous condenser is not a valid representation of SVCs in steady-state power flow analysis by reason of, once that reactive power generation limits are reached, the behavior of both electric devices are not equal. This condition is illustrated in Figure 44 and also explained by (7.1).

$$Q_{G_k,gen}^{lim} \neq b_{eq}\left(\alpha = 90° \text{ or } 180°\right) \cdot V_{k,svc}^2 \qquad (7.1)$$

Therefore, the synchronous condenser model is replaced by the SPF-SVC thyristor firing-angle model, which considers the *droop* implementation. The different *droop* values

Figure 44 – Tutorial system III load bus PV curve.
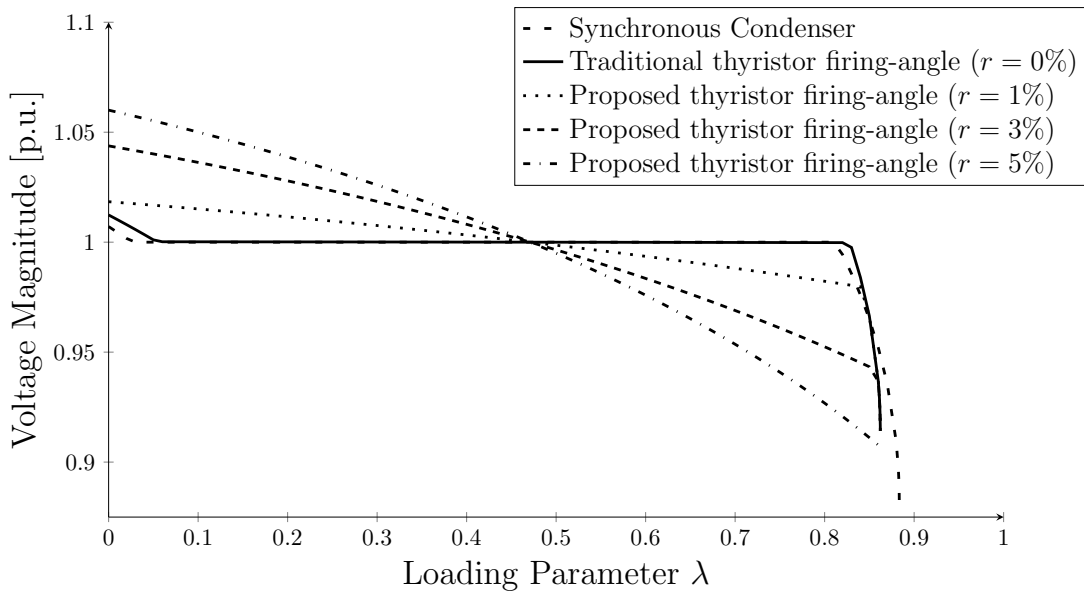
Source: Adapted from Barbosa and Passos Filho (2022).

configure a better bus voltage magnitude profile, closer to the control device realistic operational behavior, and simulate different impacts on voltage stability and loading margin in an EPS. Based on Figure 44, adopting *droop* of 1% results in a voltage profile that varies little in comparison to the other *droop* values simulated for the same load increment margin.

The result presented was validated with CEPEL's production-grade academic version software, where the traditional reactive power injection methodology is employ to model SVC in the steady-state power flow problem (PASSOS FILHO, 2000).

7.2.3 **Case III: Nordic system**

The already validated SPF-SVC thyristor firing-angle methodology is employed in this case study, considering now simulations analyzes on the well-known Nordic system (CUTSEM *et al.*, 2015; CUTSEM *et al.*, 2020). Once again, the intent is to analyze the proposed *droop* enhancement detailed in Section 5.4 and compare the validated methodology with other forms of SVC representation in the steady-state analysis, as mentioned in Subsection 2.1.2.

The Nordic system topology A was considered in this case study, and it consists of 74 buses, over 100 branches and 20 generator terminals (CUTSEM *et al.*, 2015; CUTSEM *et al.*, 2020). By applying the CPF in this EPS base case condition, it was observed that bus 1041 has the most critical profile. Therefore, it is proposed the analysis of a SVC connected at and controlling the voltage magnitude profile of this same bus.

In this case study, the SPF-SVC parameters employed are detailed hereinafter and

Figure 45 – Nordic system A topology.
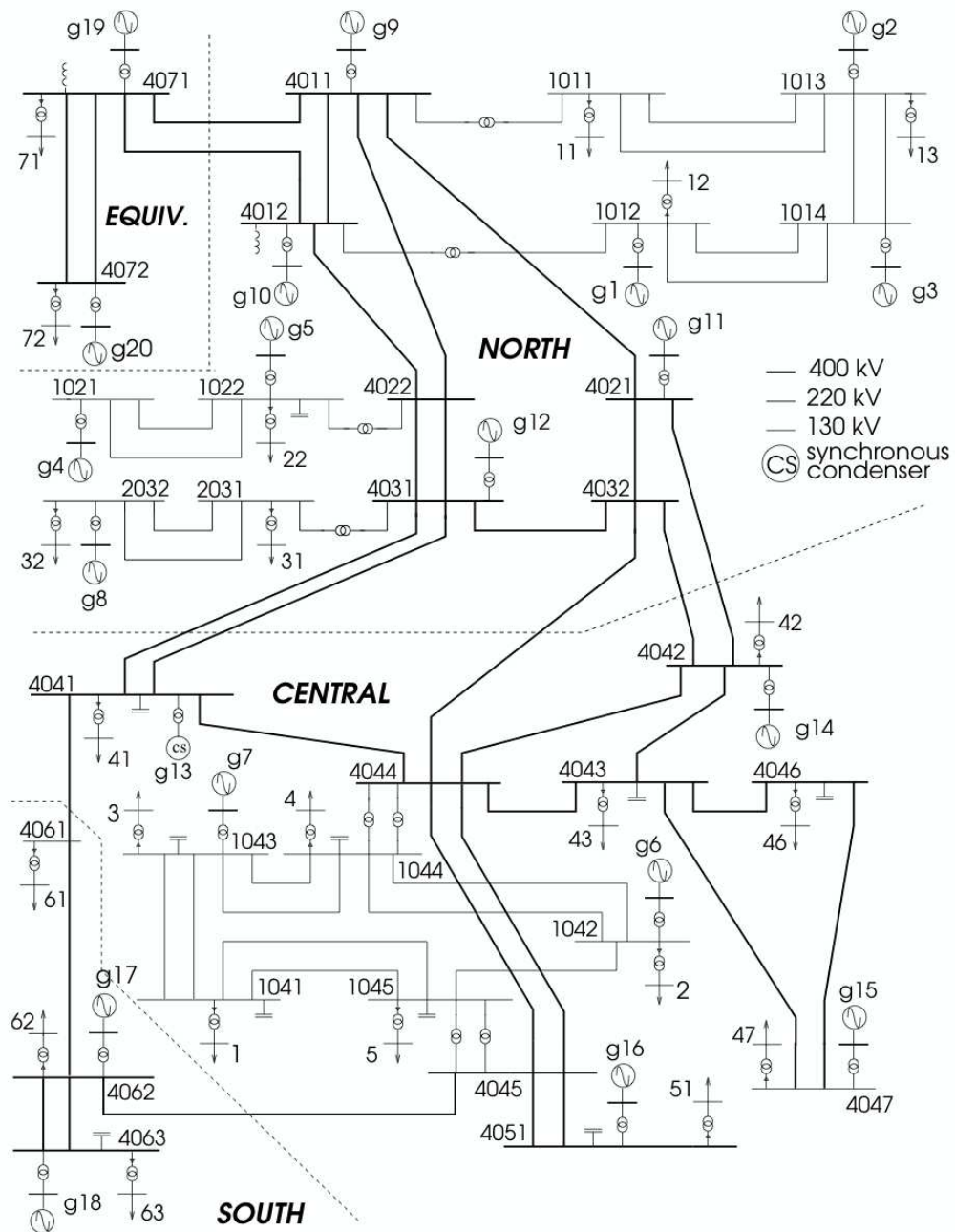
Source: Cutsem *et al.* (2015), Cutsem *et al.* (2020).

the simulation results are presented in Figures 46 and 47, which illustrate the bus 1041 voltage behavior and reactive power generation due to load increments, respectively.

- SVC linear operating region *droop r* is subject to variations;

- SVC controlled bus voltage magnitude reference: $V_{m,svc}^{ref} = 1$ p.u.;

- Sigmoid switches $sw9$ through $sw12$ slope: $slp = 10^8$;

- Sigmoid switches $sw11$ and $sw12$ tolerances: $tol_v^{sup} = tol_v^{inf} = 10^{-6}$;

- Sigmoid switches $sw9$ and $sw10$ tolerances: $tol_\alpha^{sup} = tol_\alpha^{inf} = 10^{-6}$;

- SVC capacitive susceptance: $b_{eq}(\alpha = 180°) = B_{svc}^{cap} = 2$ p.u.;

- SVC inductive susceptance: $b_{eq}(\alpha = 90°) = B_{svc}^{ind} = -2$ p.u.;

Figure 46 – Nordic system A bus 1041 PV curve.
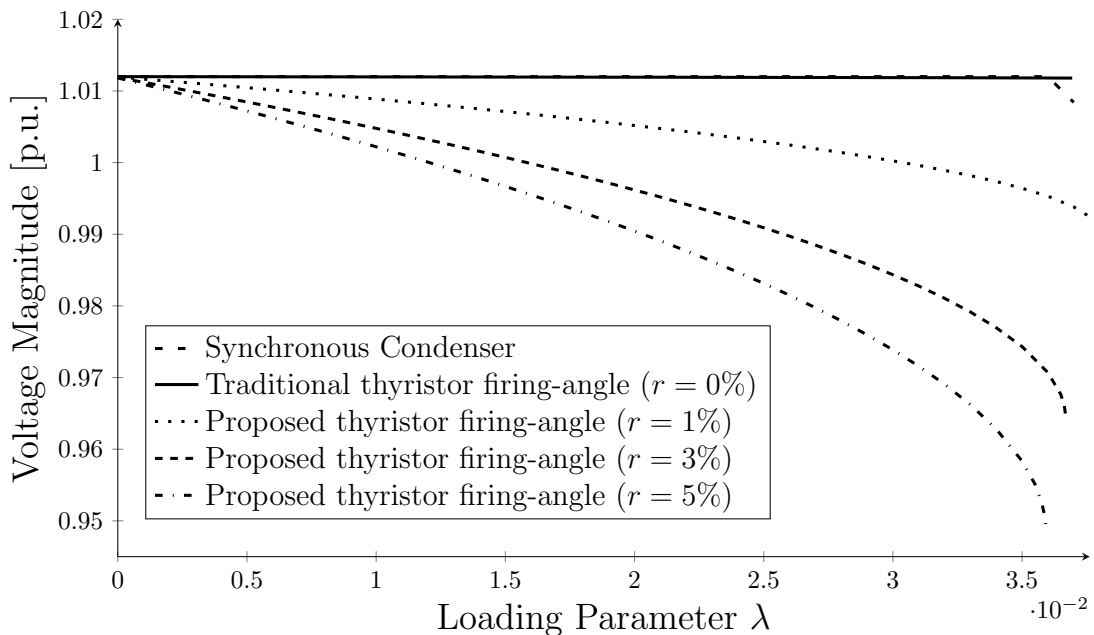
Source: Elaborated by the author (2023).

Once more, as illustrated in Figure 46, the synchronous condenser and traditional thyristor firing-angle SVC modelings are able to maintain the voltage profile for bus 1041 at the referenced value throughout most of the power flow continuation simulation. This operational condition, however, is acceptable only for generators once that a *droop* must be taken into consideration for SVC modelings (TAYLOR; SCOTT; HAMMAD, 1994; MILLER *et al.*, 1982).

Although each *droop* implementation value results in different controlled bus voltage profiles, the employment of SVC in an EPS is responsible for enhancing the voltage profile and load margin of the power system as a whole. In order to elucidate this characteristic, Table 16 highlights the benefits that SVCs provides to EPSs in terms of VSM and critical voltage magnitude.

Based on the information given in Table 16, it can be inferred that the best *droop* value to adopt in this case study is 1%, once that it presents the best results. As an

Table 16 – Impacts of adopted SVC *droop* values on voltage stability.

Parameters	Base Case	SVC *Droop*		
		1%	**3%**	**5%**
Loading Margin [MW]	265.44	416.07	405.65	397.36
Critical Voltage Magnitude [p.u.]	0.9485	0.9923	0.9646	0.9485

Source: Elaborated by the author (2023).

example, if a minimum voltage magnitude limit is set at 0.95 p.u. for the EPS, it can be observed that not only does the control device enhances the voltage magnitude at bus 1041, but also improves the system VSM overall. In sense of transmission system expansion problem, such benefits guaranteed by SVCs are translated into a 2 or 3 year load increase for an EPS.

Figure 47 – Nordic system A SVC bus 1041 reactive power generation variation per network load increment.
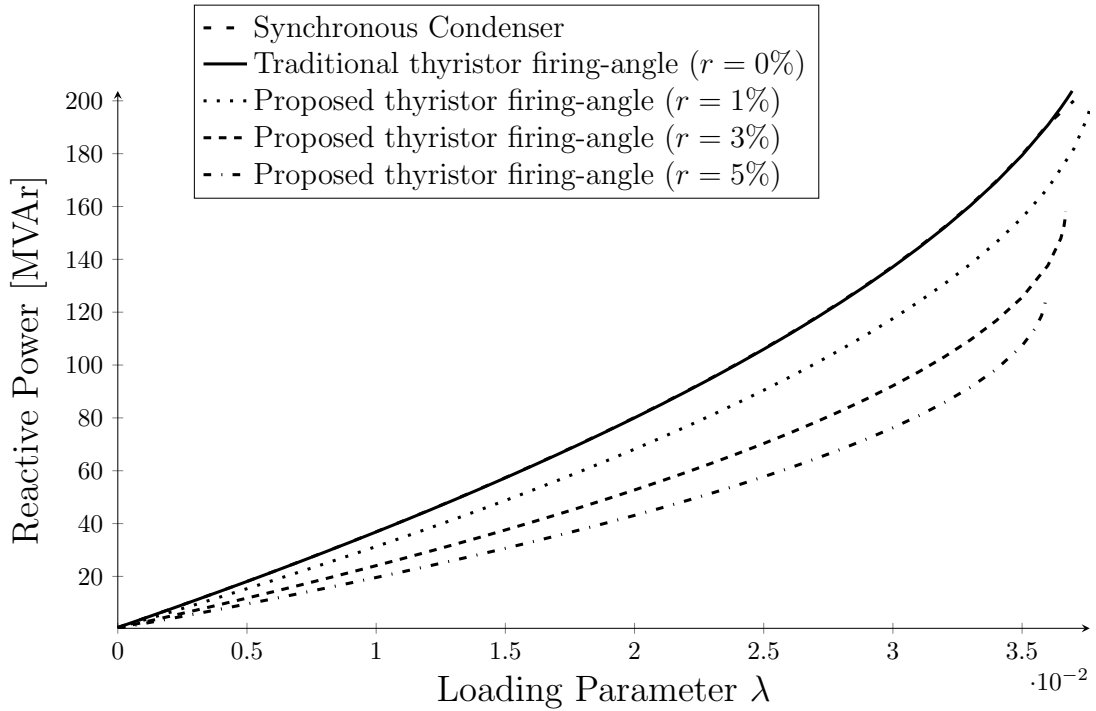
Source: Elaborated by the author (2023).

The different adopted *droop* values also imply in different reactive power generation variation during CPF simulation, as it can be seen in Figure 47. From this figure, it can be observed that modeling the SVC with higher *droop* results in a broader range of reactive power generation within the SVC linear region of operation. Considering that the maximum and minimum reactive power generation of the SVC is known, as informed in the beginning of this subsection, the smaller the *droop* value is, the greater the reactive power generation variation will be within the specified limits.

7.2.4 **Case IV: Tutorial system IV**

This 2 bus system is based on the EPS developed by Chen and Min (2007) for discussions regarding voltage collapse being caused by SVC reaching maximum reactive power limit. In his work, Chen and Min (2007) is able to identify a voltage collapse classified as LIB being caused by the SVC traditional modeling. By implementing the SPF-SVC reactive power injection methodology, presented in Chapter 5, it is intended to observe the LIB voltage collapse classified as SNB.

This power system topology and data are shown in Figure 48. It is assumed that the SVC is connected to a PQ bus, controlling its own bus voltage magnitude.

Figure 48 – Tutorial system IV topology.
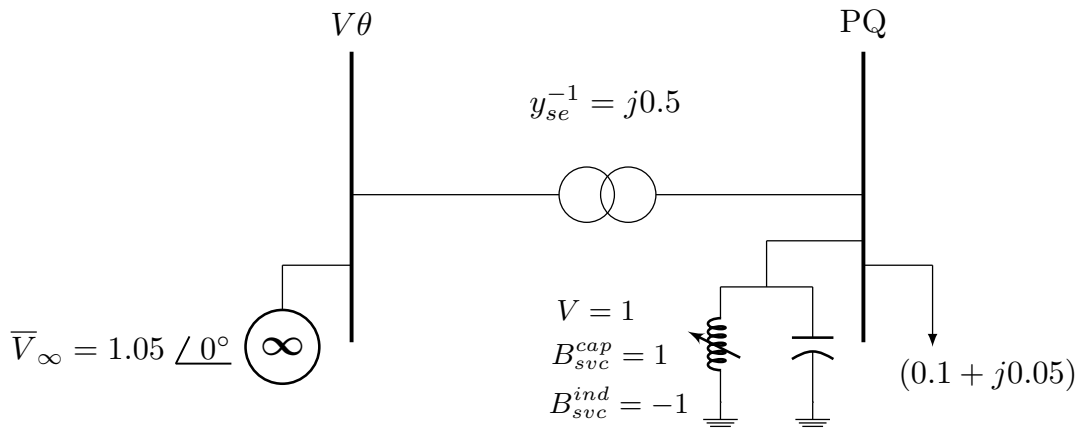
Source: Adapted from Chen and Min (2007).

For the proposed SPF-SVC reactive power injection methodology and voltage stability analysis, the following parameters values were adopted:

- Active power convergence tolerance: $\varepsilon_P = 10^{-10}$ p.u.;

- Reactive power convergence tolerance: $\varepsilon_Q = 10^{-10}$ p.u.;

- Control equations convergence tolerance: $\varepsilon_Y = 10^{-10}$ p.u.;

- Sigmoid switches $sw5$ and $sw6$ slope: $slp = 0.965 \cdot 10^8$;

- Sigmoid switches $sw5$ and $sw6$ tolerances: $tol_v^{sup} = tol_v^{inf} = 10^{-14}$;

- SVC linear operational region *droop*: $r = 5\%$;

- CPF loading parameter step: $\lambda^{step} = 10\%$.

As a result of applying the CPF formulation along with the SPF-SVC reactive power injection methodology, a SNB bifurcation was successfully identified instead of a LIB. The information regarding the SNB bifurcation is detailed in Table 17.

Table 17 – Simulation results identifying SNB in tutorial system IV through SPF-SVC reactive power injection methodology.

Critical loading parameter $\left(\tilde{\boldsymbol{\lambda}}^{crit}\right)$	1173.5360136855%
Reactive power generated by $\boldsymbol{Q_{G,svc}}$	0.910976198541199 p.u.
$\mathbf{J_R}$ determinant	0.0035957063551577137
$\mathbf{J_R}$ eigenvalue	[0.00359571]

Source: Elaborated by the author (2023).

This result verifies the mathematical property of the SPF formulation ability of transforming LIBs into SNBs, as stated by Neves (2022). It also demonstrates the proposed application of modal analysis for the indentification of SNBs for SVCs reaching reactive power generation limits. A complementary analysis is made in terms of the participation factor based on the SNB smallest eigenvalue appointed in Table 17, as illustrated by Figure 49.

Figure 49 – Tutorial system IV participation factor for $\lambda^{eig} = 0.00359571$.
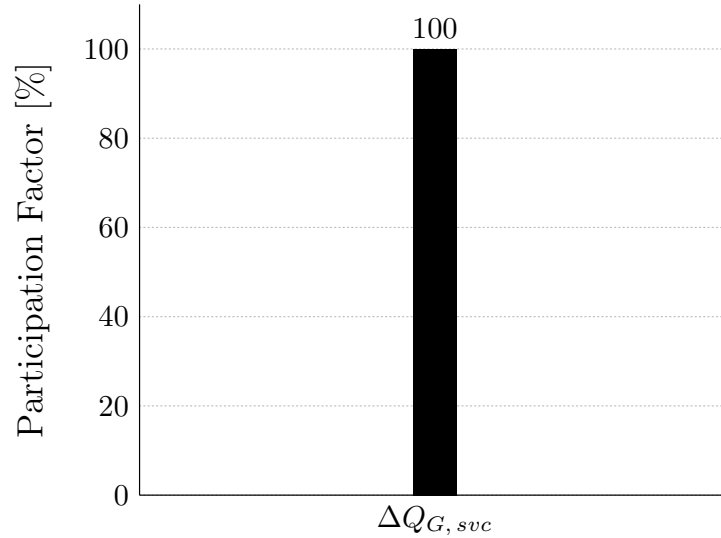
Source: Elaborated by the author (2023).

As it can be observed from Figure 49, the $\mathbf{J_R}$ eigenvalue indicates the highest possible participation factor for the SVC reactive power generation. It can be observed that the collapse is caused 100% because of the SVC reaching its limit. Regarding the reactive power generated by the SVC detailed in Table 17, it is not equal to the equipment's maximum susceptance value because it also depends on the connected bus voltage magnitude, as detailed in (5.3).

The mode-shape analysis was not reproduced for this simulation once it only presents one eigenvalue and, therefore, it is not possible to analyze the impact of the control variable perturbation in other control variables. In fact, the result would be similar to the participation factor shown in Figure 49.

The SPF-SVC reactive power injection methodology sigmoid switches values at the MLP are detailed in Table 18. The switches correctly indicate that the SVC is transitioning from normal operational mode to superior limit violation mode, detailed in Section 5.1. As also commented in previous subsections, an output value between 0 and 1 for the sigmoid switches represents a mix of control equations. This condition is justified by the adoption of *smooth step function* continuity characteristic detailed in Definition 1.

Table 18 – SPF-SVC reactive power injection methodology sigmoid switches outputs in SNB indentification for tutorial system IV.

$sw5$	$sw6$
0.0	0.49

Source: Elaborated by the author (2023).

7.2.5 Case V: IEEE 30 bus system

In Chen and Min (2007) the authors identify a voltage collapse classified as LIB in the IEEE 30 bus system, which is caused by SVC connected at bus 30 reaching maximum reactive power limit, as illustrated by Figures 50 and 51. This power system topology is shown in Figure 53, whereas its data are available at Christie (1999).

Figure 50 – IEEE 30 bus system SVCs reactive power generation per network load increment.
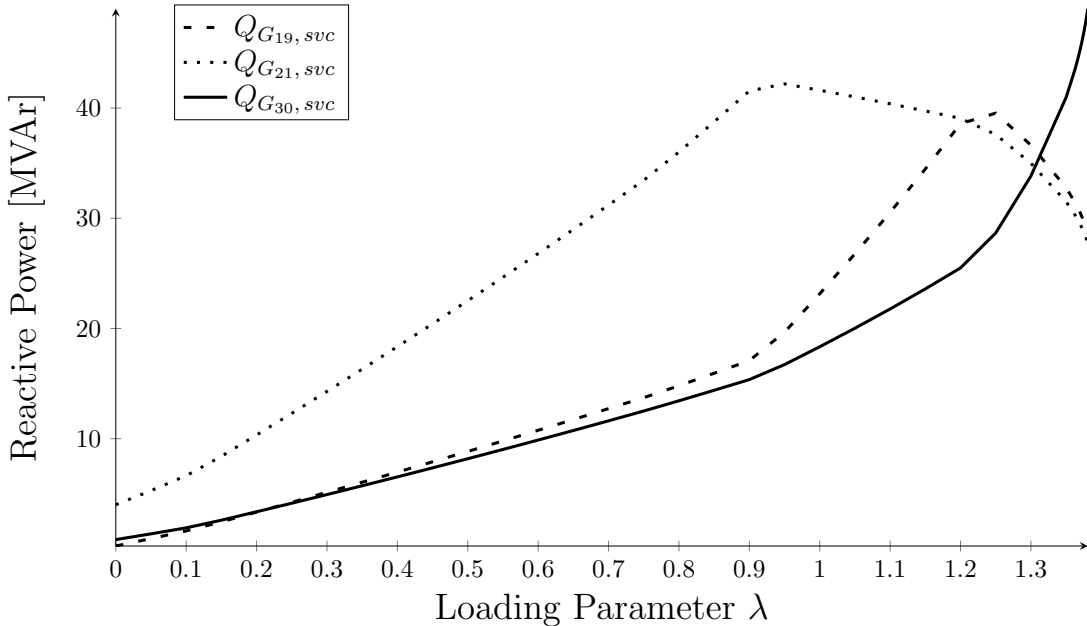
Source: Elaborated by the author (2023).

The parameters values for each SVC actively operating in the IEEE 30 bus system are detailed in Table 19, as defined by Chen and Min (2007). It is assumed that the SVC

Figure 51 – IEEE 30 bus system voltage collapse scenario.
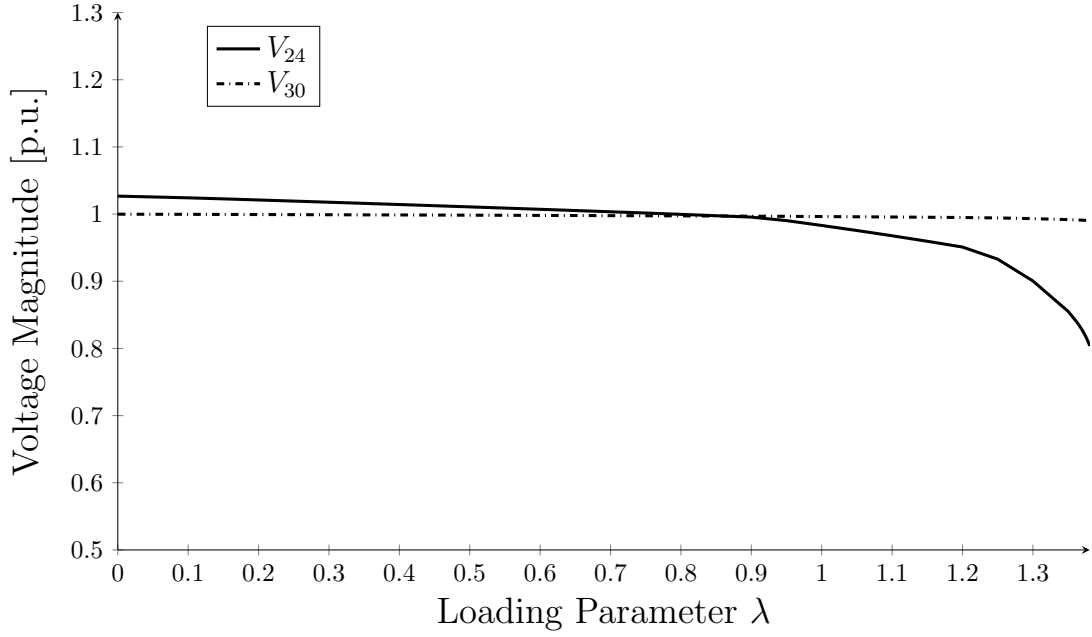
Source: Adapted from Chen and Min (2007).

is connected to a PQ bus, controlling its own bus voltage magnitude and that generators' reactive power generation limits are also considered in simulations.

Table 19 – SVC parameters for LIB indentification in IEEE 30 bus system.

Bus	V_m^{ref} [p.u.]	*Droop* [%]	Capacitive Limit [MVAr]
19	1.030	5	40.0
21	1.040	2	40.0
30	1.000	2	50.0

Source: Adapted from Chen and Min (2007).

By implementing the SPF-SVC reactive power injection methodology, presented in Chapter 5, along with the CPF formulation, it is intended to observe the LIB voltage collapse to be classified now as SNB. For the proposed SPF-SVC reactive power injection methodology and voltage stability analysis, the following parameters values were adopted:

- Active power convergence tolerance: $\varepsilon_P = 10^{-10}$ p.u.;

- Reactive power convergence tolerance: $\varepsilon_Q = 10^{-10}$ p.u.;

- Control equations convergence tolerance: $\varepsilon_Y = 10^{-10}$ p.u.;

- Sigmoid switches $sw5$ and $sw6$ slope: $slp = 1.5 \cdot 10^7$;

- Sigmoid switches $sw5$ and $sw6$ tolerances: $tol_v^{sup} = tol_v^{inf} = 10^{-10}$;

- CPF loading parameter step: $\lambda^{step} = 10\%$.

As a result of applying the CPF formulation along with the SPF-SVC reactive power injection methodology, a SNB bifurcation was successfully identified instead of a LIB. The information regarding the SNB bifurcation is detailed in Table 20.

Table 20 – Simulation results identifying SNB in IEEE 30 bus system through SPF-SVC reactive power injection methodology.

Critical loading parameter $\left(\tilde{\boldsymbol{\lambda}}^{crit}\right)$	138.0792974308%
Reactive power generated by $\boldsymbol{Q_{G_{30},svc}}$	0.49024314002829115 p.u.
$\mathbf{J}_R$ determinant	0.0002244651201469047
$\mathbf{J}_R$ eigenvalues	$[(\dots)\, 0.000452123879\ 1.03539813$ $0.897219043\ 0.534423518\ (\dots)]$

Source: Elaborated by the author (2023).

Table 20 only displays the top 4 smallest eigenvalues for the SNB MLP. The mode-shape and participation factors will be analyzed for each of them, following Table 20 presented order, as illustrated by Figures 52 through 60.

Figure 52 – IEEE 30 bus system mode-shape for $\lambda^{eig} = 0.000452123879$.
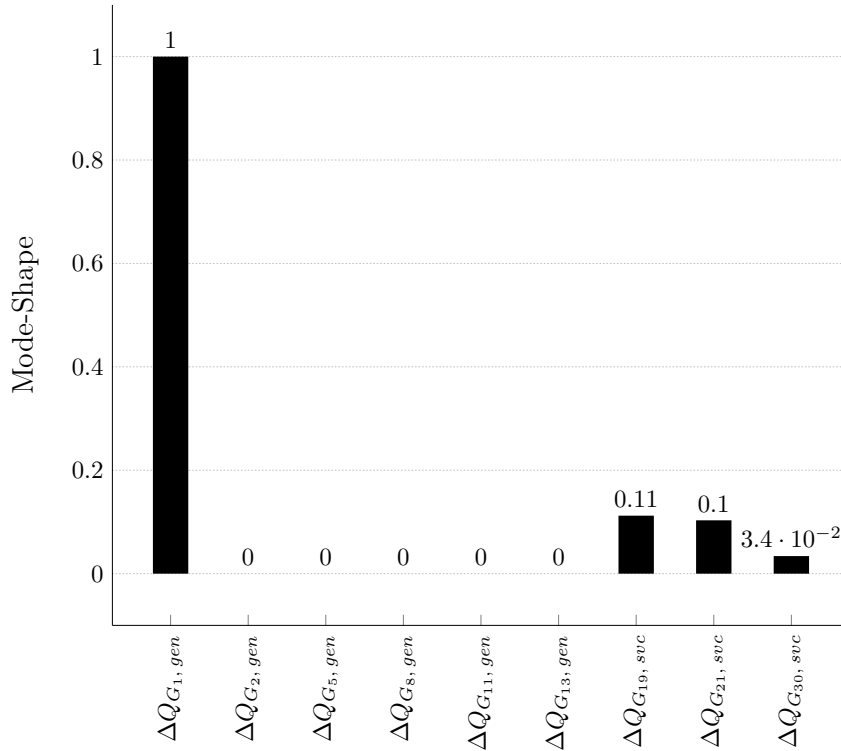
Source: Elaborated by the author (2023).

Figure 53 – IEEE 30 bus system topology.
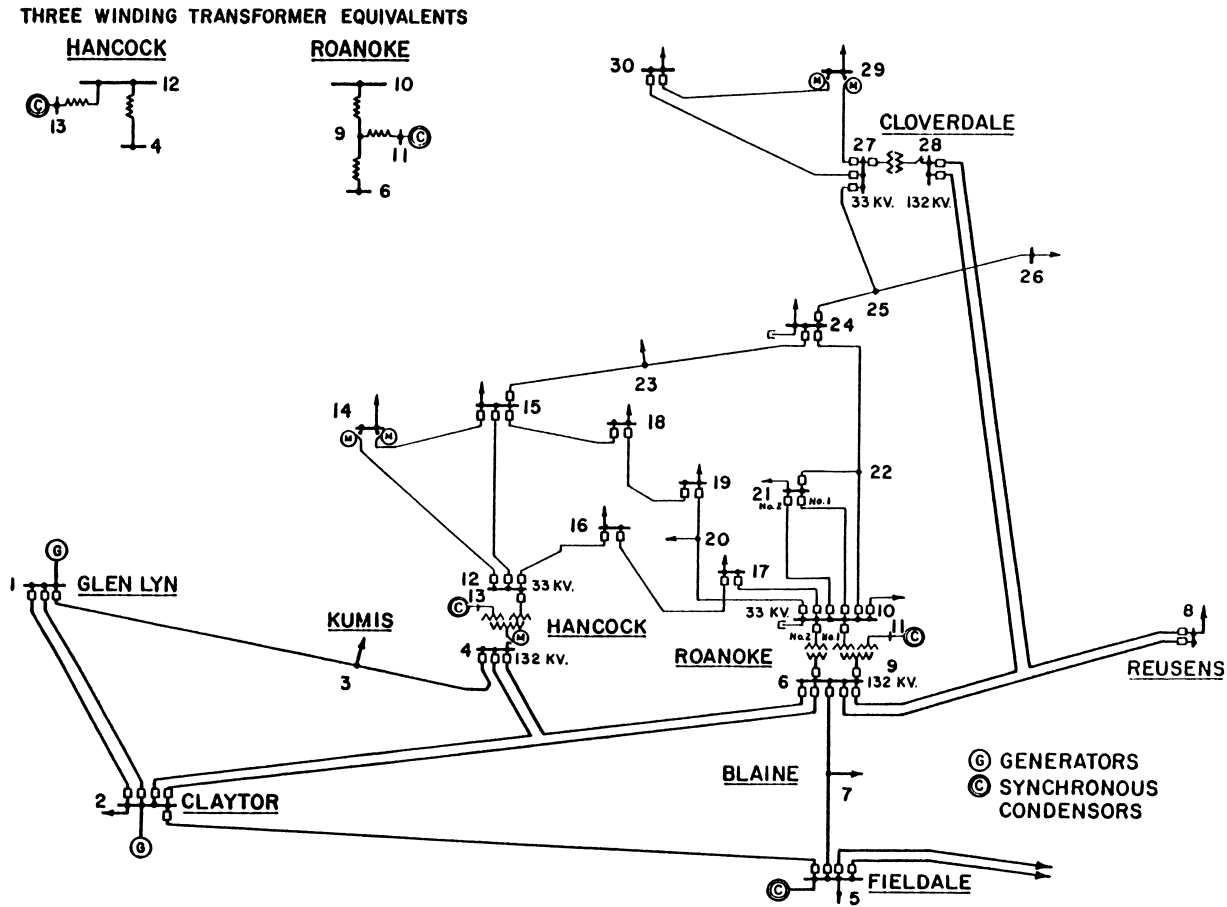
Figure 52 illustrates the mode-shape analysis for the eigenvalue $\lambda^{eig} = 0.000452123879$ and, as it can be observed, this eigenvalue is associated with the slack bus reactive power generation ($Q_{G_1,gen}$). A perturbation on the slack bus reactive power generation results in a little to none variation on the other control variables. The null results observed in Figure 52 corresponds to electric devices that reached reactive power generation limits and, therefore, do not suffer any variation once $Q_{G_1,gen}$ is perturbed. The small mode-shape values correspond to the reactive power generated by the SVCs, which suffer little impact once $Q_{G_1,gen}$ is perturbed by reason of the buses are electrically distant from each other.

Figure 54 – IEEE 30 bus system participation factor for $\lambda^{eig} = 0.000452123879$.
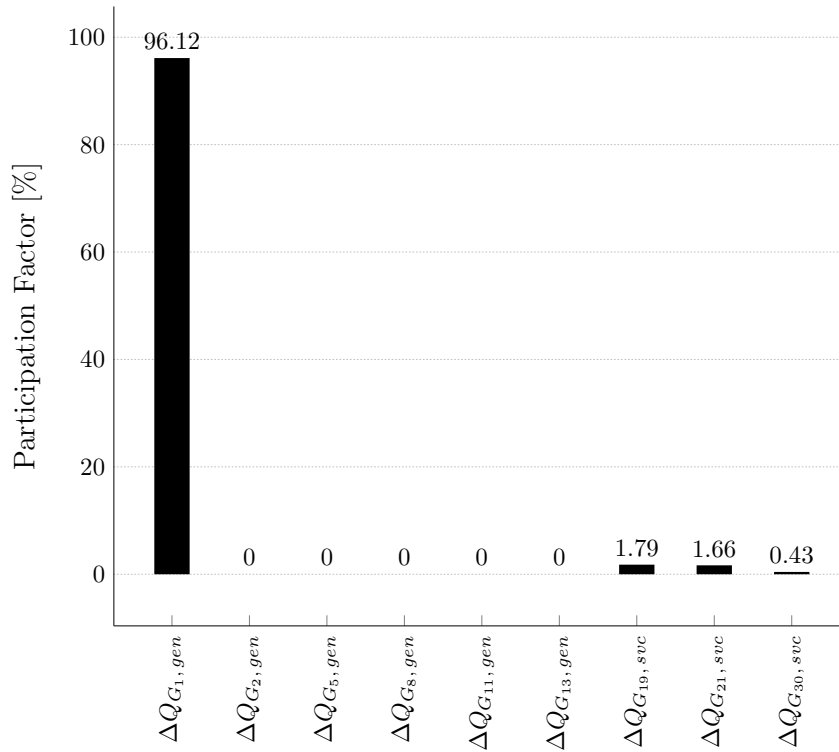
Source: Elaborated by the author (2023).

The corresponding participation factor for eigenvalue $\lambda^{eig} = 0.000452123879$ is illustrated in Figure 54. At the MLP, the slack bus reactive power generation participates 96.12% in the reactive power generation balance for the EPS. Associated with this eigenvalue, the SVCs reactive power generation in buses 19, 21 and 30 have small participation factor. Therefore, it can be observed a predominance characteristic of reactive power generation by the generator at bus 1 in the MLP associated with voltage collapse scenario analysis for the EPS.

In Figure 55 it is illustrated the mode-shape related to eigenvalue $\lambda^{eig} = 1.03539813$. As it can be observed, this eigenvalue is correlated to the reactive power generated by the SVC connected at bus 21 ($Q_{G_{21},svc}$). From the mode-shape analysis, it can be concluded that a perturbation in $Q_{G_{21},svc}$ results in small variations for the slack bus and SVC at bus 19 reactive power generations.

Figure 55 – IEEE 30 bus system mode-shape for $\lambda^{eig} = 1.03539813$.
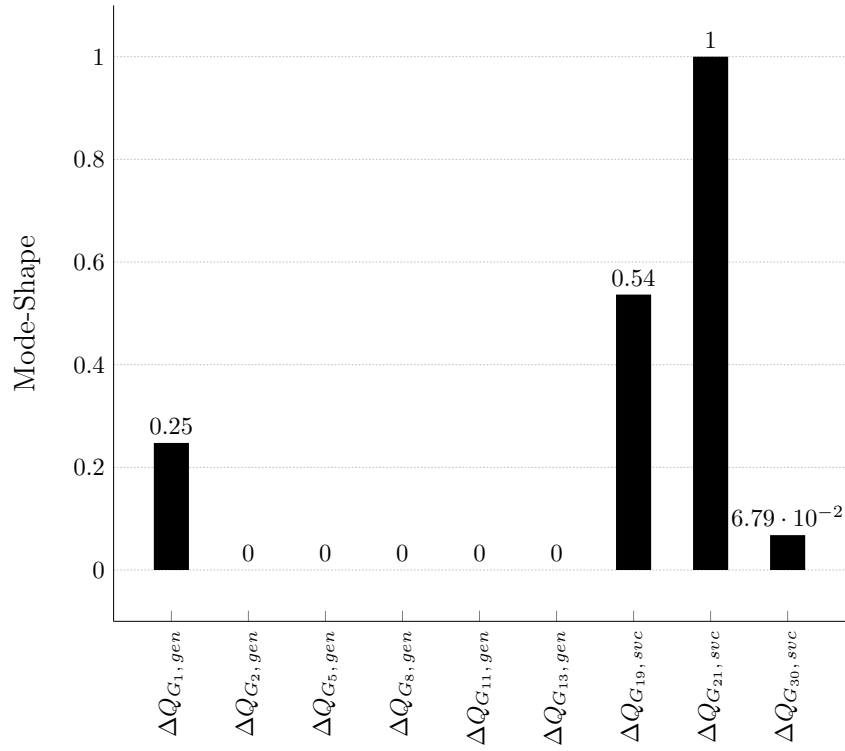
Figure 56 – IEEE 30 bus system participation factor for $\lambda^{eig} = 1.03539813$.
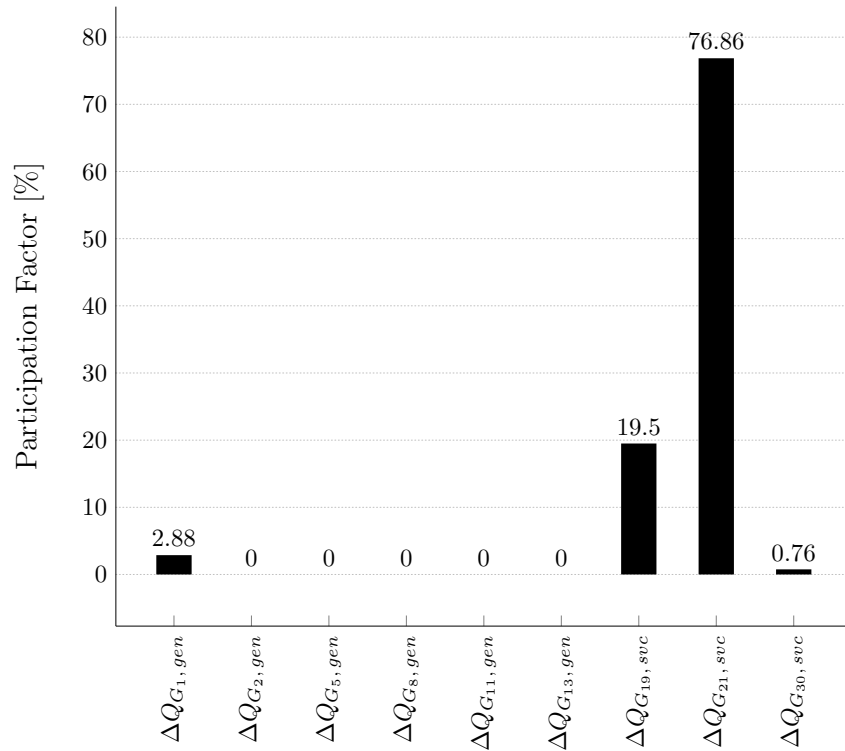
In addition, the participation factor analysis illustrated in Figure 56 indicates a

small conflict control with the SVC connected at bus 19. This conflict happens due to the electrical proximity between buses 19 and 21, and the different control goals by their own SVCs when the EPS is closer to the MLP.

Furthermore, it is said that there is a conflict because the mode-shape and participation factor from Figures 55 and 56 are similarly replicated in Figures 57 and 58, respectively. In these last two figures the eigenvalue $\lambda^{eig} = 0.897219043$ is associated with the reactive power generation by the SVC connected at bus 19.

Figure 57 – IEEE 30 bus system mode-shape for $\lambda^{eig} = 0.897219043$.
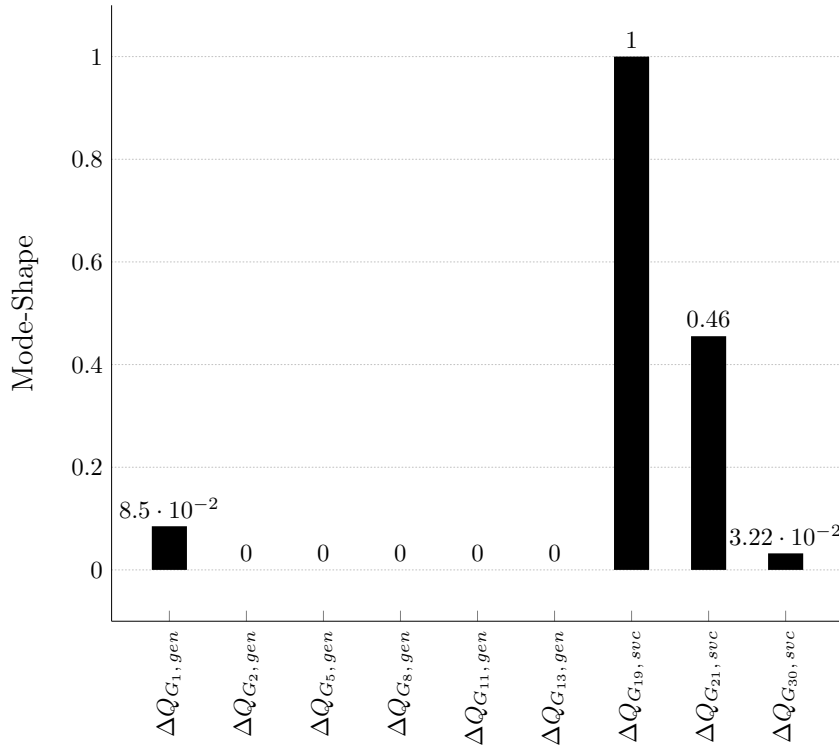
Source: Elaborated by the author (2023).

In conclusion, Figures 59 and 60 indicate the mode-shape and participation factor for the eigenvalue $\lambda^{eig} = 0.534423518$. From the mode-shape analysis it can be observed that a variation on the reactive power generation by the SVC located at bus 30 causes little to none variation impact on the other control variables. The null results observed in Figure 59 corresponds to electric devices that reached reactive power generation limits and, therefore, do not suffer any variation once $Q_{G_{30}, svc}$ is perturbed. The small mode-shape values correspond to the reactive power generated by the SVCs, which suffer little impact once $Q_{G_{30}, svc}$ is perturbed by reason of the buses are electrically distant from each other.

In addition, the participation factor shown in Figure 60 corresponds to a voltage collapse condition in the EPS, classified as SNB and which is caused 98.95% because of the SVC at bus 30 reaching its maximum reactive power limit. This conclusion can be made once that the reactive power generated by that SVC is close to the maximum limit,

Figure 58 – IEEE 30 bus system participation factor for $\lambda^{eig} = 0.897219043$.
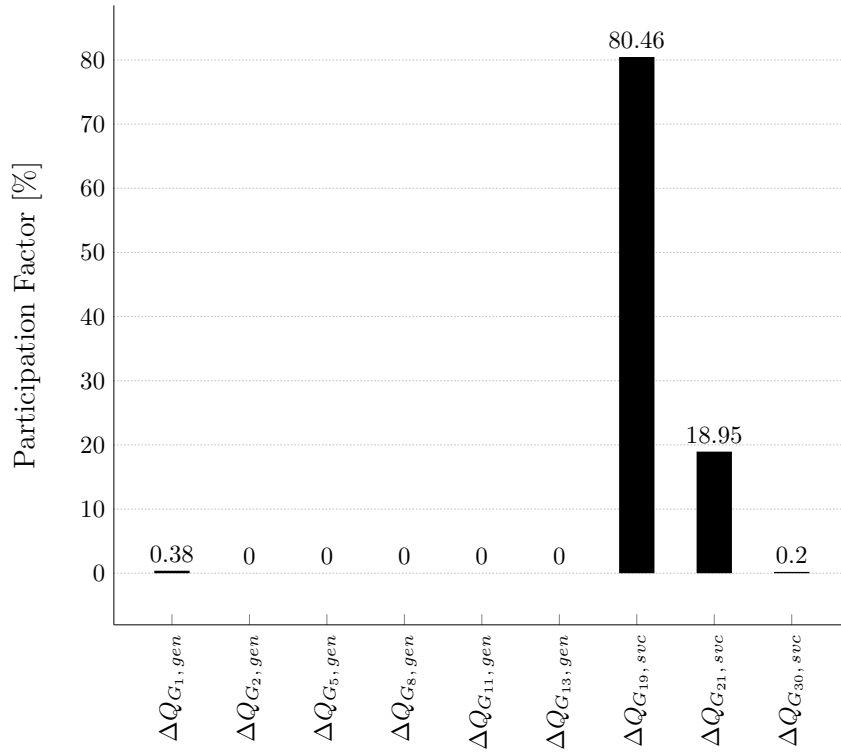
Figure 59 – IEEE 30 bus system mode-shape for $\lambda^{eig} = 0.534423518$.
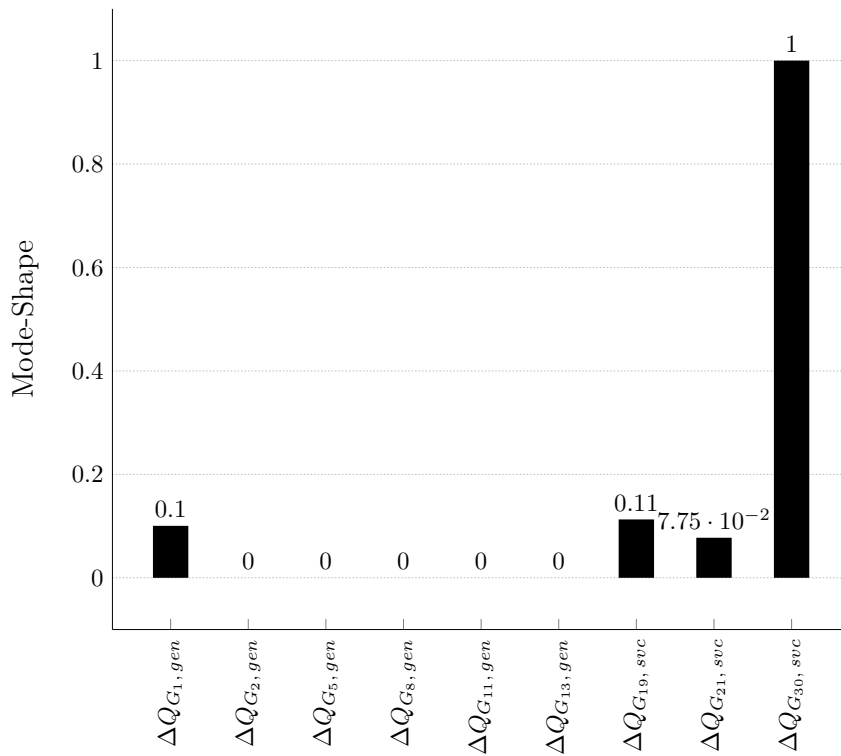
as detailed in Table 20 and illustrated in Figure 50, and cannot participate more in the voltage magnitude control of its own bus.

Figure 60 – IEEE 30 bus system participation factor for $\lambda^{eig} = 0.534423518$.
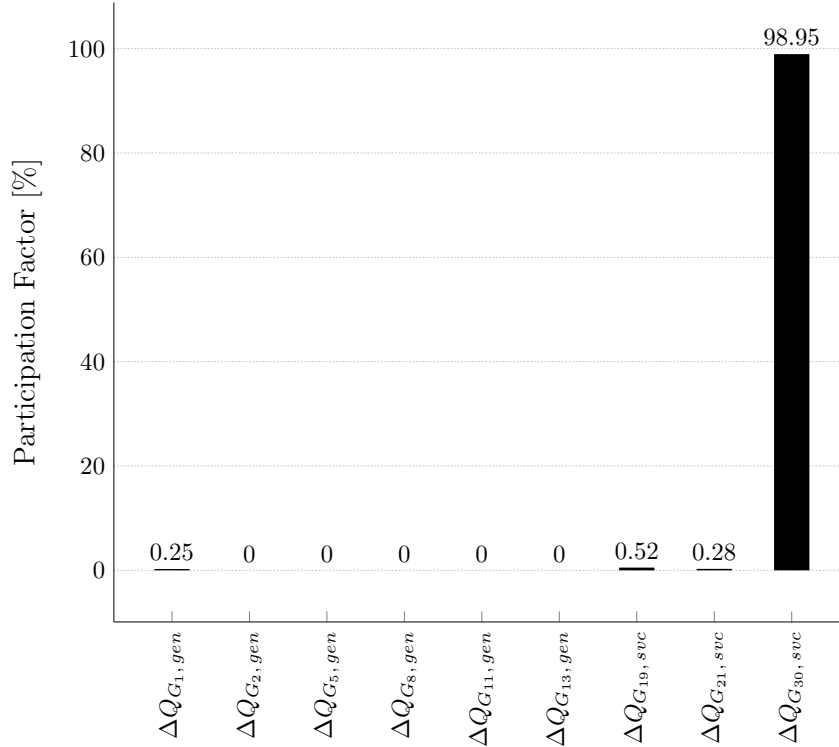
Source: Elaborated by the author (2023).

Although the eigenvalue associated with the slack bus reactive power generation ($\lambda^{eig} = 0.000452123879$) is smaller than the eigenvalue associated with the reactive power generation by the SVC located at bus 30 ($\lambda^{eig} = 534423518$), the eigenanalysis shown in Figure 60 indicates greater participation of the SVC in the voltage collapse scenario of the EPS. Nevertheless, it demonstrates the proposed application of modal analysis for the indentification of SNBs for SVCs reaching reactive power generation limits.

The SPF-SVC reactive power injection methodology sigmoid switches values at the MLP are detailed in Table 21. The switches correctly indicate that the SVC at bus 30 is transitioning from normal operational mode to superior limit violation mode, detailed in Section 5.1.

Table 21 – SPF-SVC reactive power injection methodology sigmoid switches outputs for SVC at bus 30 in SNB indentification for IEEE 30 bus system.

$sw5$	$sw6$
0.0	0.35

Source: Elaborated by the author (2023).

7.3 PARTIAL CONCLUSIONS

This chapter presents the simulation results of the proposed generator and SVC methodologies as well as the proposed modal analysis for voltage stability evaluation, which were detailed in previous chapters of this work.

In Section 7.1 the SPF-Generator methodology successfully identified SNBs bifurcations, as described in Chapter 6, in different EPS simulations. Both tutorial systems as well as the IEEE 118 bus system simulations were stressed via the CPF formulation and returned results which demonstrates the mathematical theory described by Neves (2022).

Additionally, in Section 7.2 the proposed SPF-SVC methodologies were able to successfully return steady-state results as described in Passos Filho (2000). Not only that, it was also proved the proposed enhancement on the SVC traditional firing-angle methodology by the implementation of *droop* variable in the proposed control.

In conclusion, the SNB bifurcation analysis described in Chapter 6 was also extended to the proposed SPF-SVC methodology, returning successful simulation results. Regarding the results shown in Subsection 7.2.5, the developed Python program was unable to simulate the same voltage collapse condition as presented in Chen and Min (2007), being detailed, therefore, a similar condition in the subsection. All Python simulation results were validated via CEPEL's production-grade software with due proportions, comparting the SPF results with the traditional PF approach.

8 CONCLUSIONS

This work presents a thorough analysis on the advantages of the SPF formulation regarding voltage collapse. The work developed by Neves (2022) was used as a main reference, as the mathematical theorems described in it served as foundation for studies related to the SPF formulation.

This work also presents steady-state methodologies for two electric devices, generators and SVCs, which are presented in Chapters 4 and 5, respectively. The proposed methodologies consider the *full* Newton implementation, responsible for updating in the power flow system of nonlinear equations the control equations that best describe the control device operational behavior during simulation. The *full* Newton implementation was considered in the proposed methodology because it improves the Jacobian matrix sparsity characteristic by the addition of new linearized equations, increasing the matrix dimension according with the number of generators (N_{GEN}) or SVCs (N_{SVC}) active in the EPS.

The SPF-Generator methodology proposed in Chapter 4 is based on the work developed by Pontes (2018), Pontes, Passos Filho and La Gatta (2018). Hence, no alteration on the proposed methodology is made in this work, and was mainly implemented for studies related to indentification and evaluation of voltage collapse in the SPF formulation problem.

On the other hand, new steady-state methodologies of representing SVC in the power flow problem were proposed. On account of the SVCs methodologies described in Chapter 5, the reactive power injection methodology tends to be the most common applied in power flow research considering the equations and state variables involved in the methodology. The current injection and thyristor firing-angle methodologies can also be implemented in the power flow analysis, the former being more adaptable for a rectangular formulation approach whereas the latter is more recommended for harmonics and electromagnetic transients studies. All models, nevertheless, are appropriate for representing SVCs in the power flow problem.

Regarding the SPF-SVC thyristor firing-angle methodology, detailed in Section 5.3, the proposed *droop* enhancement improves the traditional methodology developed by Ambriz-Perez, Acha and Fuerte-Esquivel (2000). The results obtained in simulation by using this methodology show the effectiveness of the proposed alteration, and returns identical solution to the SPF-SVC reactive power injection model. This methodology, however, presents a higher number of iterations by reason of its control variable $\alpha_{k,svc}$ is more sensitive to variations than the control variable $Q_{G_k,svc}$, from the reactive power injection methodology.

For the proposed SPF-Generator and SPF-SVCs methodologies, a set of sigmoid

switches is incorporated in the devices control equations. The adoption of switches based on sigmoid function introduces smoothness to the traditional PF formulation and is justified by the *smooth step function* in Definition 1. Additionally, the results shown in Chapter 7 prove that the implementation of sigmoid switches does not intefere negatively in the solution of power flow problems.

In respect of the simulation results presented in Chapter 7, it successfully demonstrate the effectiveness of the proposed methodologies. In Section 7.1, EPSs were stressed via the CPF formulation and the SPF-Generator methodology was able to correctly identify SNB bifurcations at the MLP. The numerical results obtained via modal analysis demonstrates the mathematical theorems described in Neves (2022).

Additionally, in Section 7.2 different results are shown regarding the proposed SPF-SVC methodologies. Despite the multiple study cases, all simulations returned correct solutions for the steady-state analysis (Subsection 7.2.1), for CPF formulation analysis (Subsections 7.2.2 and 7.2.3) and also for the indentification of SNBs at the MLP via modal analysis (Subsections 7.2.4 and 7.2.5).

In conclusion, the developed Python program was able to correctly simulate all EPS. The CEPEL production-grade academic version software was used in this work in order to validate the simulation results. As the methodologies employed in the software are based on the traditional control models via PF formulation, the software was used in order to validate the steady-state analysis results, CPF simulation results, such as PV curves, and also for the identification of voltage collapse classified as LIB in the analyzed EPS. No computational burden was analyzed in this work.

8.1 FUTURE WORKS

As future works, the author suggests the following subjects:

- Extend the SPF methodology via sigmoid switches for other electric devices control modelings;

- Improve the SPF bifurcation analysis with a fast and accurate computational simulation, with respect to voltage stability;

- Optimal analysis for the adoption of sigmoid function slope variable (slp) in the SPF formulation;

- Development of a voltage stability assessment computational tool to facilitate the indentification of SNBs arbitrarily close to LIBs;

- Advanced research on stability attraction regions and surfaces for power systems analysis and voltage stability assessment.

REFERENCES

ABE, S.; HAMADA, N.; ISONO, A.; OKUDA, K. Load flow convergence in the vicinity of a voltage stability limit. **IEEE transactions on power apparatus and systems**, IEEE, n. 6, p. 1983–1993, 1978.

AJJARAPU, V.; CHRISTY, C. The continuation power flow: a tool for steady state voltage stability analysis. **IEEE transactions on Power Systems**, IEEE, v. 7, n. 1, p. 416–423, 1992.

ALVARADO, F.; DEMARCO, C. Computational tools for planning and operation involving facts devices. In: **Proceedings of Workshop on FACTS**. [S.l.: s.n.], 1995.

AMBRIZ-PEREZ, H.; ACHA, E.; FUERTE-ESQUIVEL, C. Advanced svc models for newton-raphson load flow and newton optimal power flow studies. **IEEE transactions on power systems**, IEEE, v. 15, n. 1, p. 129–136, 2000.

BARBOSA, J. P. P.; PASSOS FILHO, J. A. Avaliação e aprimoramento de metodologias para representação de CER no problema de fluxo de potência. **Simpósio Brasileiro de Sistemas Elétricos-SBSE**, v. 2, n. 1, 2022.

CANIZARES, C. A. On bifurcations, voltage collapse and load modeling. **IEEE transactions on power systems**, IEEE, v. 10, n. 1, p. 512–522, 1995.

CHEN, L.; MIN, Y. Limit induced bifurcation caused by svc capacity limit. In: IEEE. **2007 IEEE Lausanne Power Tech**. [S.l.], 2007. p. 250–254.

CHIANG, H.-D.; DOBSON, I.; THOMAS, R. J.; THORP, J. S.; FEKIH-AHMED, L. On voltage collapse in electric power systems. **IEEE Transactions on Power systems**, IEEE, v. 5, n. 2, p. 601–611, 1990.

CHIANG, H.-D.; FLUECK, A. J.; SHAH, K. S.; BALU, N. Cpflow: A practical tool for tracing power system steady-state stationary behavior due to load and generation variations. **IEEE Transactions on Power Systems**, IEEE, v. 10, n. 2, p. 623–634, 1995.

CHRISTIE, R. **Power Systems Test Case Archive**. 1999. https://labs.ece.uw.edu/pstca/.

CORSI, S.; TARANTO, G. N. Voltage instability-the different shapes of the "nose". In: IEEE. **2007 iREP Symposium-Bulk Power System Dynamics and Control-VII. Revitalizing Operational Reliability**. [S.l.], 2007. p. 1–16.

CUTSEM, T. V. A method to compute reactive power margins with respect to voltage collapse. **IEEE Transactions on Power Systems**, IEEE, v. 6, n. 1, p. 145–156, 1991.

CUTSEM, T. V.; GLAVIC, M.; ROSEHART, W.; SANTOS, J. Andrade dos; CAÑIZARES, C.; KANATAS, M.; LIMA, L.; MILANO, F.; PAPANGELIS, L.; RAMOS, R. A. *et al.* Test systems for voltage stability analysis and security assessment. IEEE, 2015.

CUTSEM, T. V.; GLAVIC, M.; ROSEHART, W.; CANIZARES, C.; KANATAS, M.; LIMA, L.; MILANO, F.; PAPANGELIS, L.; RAMOS, R. A.; SANTOS, J. A. dos *et al.* Test systems for voltage stability studies. **IEEE Transactions on Power Systems**, IEEE, v. 35, n. 5, p. 4078–4087, 2020.

CUTSEM, T. V.; VOURNAS, C. **Voltage stability of electric power systems**. [S.l.]: Springer Science & Business Media, 2007. ISBN 978-0-387-75535-9.

ENDERTON, H. B. **A mathematical introduction to logic**. [S.l.]: Elsevier, 2001.

ERINMEZ, I. Static var compensators. In: INTERNATIONAL CONFERENCE ON LARGE HIGH VOLTAGE ELECTRIC SYSTEMS. [S.l.], 1986.

FERRAZ, J. C. R. Fluxo de potência continuado e análise modal na avaliação da estabilidade de tensão de grande porte. **Rio de Janeiro, Rio de Janeiro, Brasil: Dissertação de Mestrado. Programa de Pós-Graduação em Engenharia Elétrica. COPPE/UFRJ**, 1998.

FLATABO, N.; OGNEDAL, R.; CARLSEN, T. Voltage stability condition in a power transmission system calculated by sensitivity methods. **IEEE Transactions on Power Systems**, IEEE, v. 5, n. 4, p. 1286–1293, 1990.

GAO, B.; MORISON, G.; KUNDUR, P. Voltage stability evaluation using modal analysis. **IEEE transactions on power systems**, IEEE, v. 7, n. 4, p. 1529–1542, 1992.

GREENE, S.; DOBSON, I.; ALVARADO, F. L. Sensitivity of the loading margin to voltage collapse with respect to arbitrary parameters. **IEEE Transactions on Power Systems**, IEEE, v. 12, n. 1, p. 262–272, 1997.

HATZIARGYRIOU, N.; MILANOVIC, J.; RAHMANN, C.; AJJARAPU, V.; CANIZARES, C.; ERLICH, I.; HILL, D.; HISKENS, I.; KAMWA, I.; PAL, B. *et al.* Definition and classification of power system stability–revisited & extended. **IEEE Transactions on Power Systems**, IEEE, v. 36, n. 4, p. 3271–3281, 2020.

JU, Y.; WANG, J.; ZHANG, Z.; HUANG, Y.; LIN, Y. A calculation method for three-phase power flow in micro-grid based on smooth function. **IEEE Transactions on Power Systems**, IEEE, v. 35, n. 6, p. 4896–4903, 2020.

KATAOKA, Y. A smooth power flow model of electric power system with generator reactive power limits taken into consideration. In: IEEE. **2005 IEEE International Symposium on Circuits and Systems**. [S.l.], 2005. p. 5286–5289.

KUNDUR, P.; PASERBA, J.; AJJARAPU, V.; ANDERSSON, G.; BOSE, A.; CANIZARES, C.; HATZIARGYRIOU, N.; HILL, D.; STANKOVIC, A.; TAYLOR, C. *et al.* Definition and classification of power system stability ieee/cigre joint task force on stability terms and definitions. **IEEE transactions on Power Systems**, IEEE, v. 19, n. 3, p. 1387–1401, 2004.

KUNDUR, P. S. **Power system stability and control**. [S.l.]: McGraw-Hill Education, 1994. ISBN 0-07-035958-X.

KWATNY, H.; PASRIJA, A.; BAHAR, L. Static bifurcations in electric power networks: Loss of steady-state stability and voltage collapse. **IEEE transactions on circuits and systems**, IEEE, v. 33, n. 10, p. 981–991, 1986.

MATHUR, R. M.; VARMA, R. K. **Thyristor-based FACTS controllers for electrical transmission systems**. [S.l.]: John Wiley & Sons, 2002.

MILANO, F. **Power system modelling and scripting**. [S.l.]: Springer Science & Business Media, 2010. ISBN 978-3-642-13668-9.

MILLER, T. J. E. *et al.* **Reactive power control in electric systems**. [S.l.]: Wiley New York, 1982. v. 2.

MONTICELLI, A. J. **Fluxo de carga em redes de energia elétrica**. [S.l.]: E. Blucher, 1983.

MONTICELLI, A. J.; GARCIA, A. **Introdução a sistemas de energia elétrica**. [S.l.]: Ed Unicamp, 1999.

MORISON, G.; GAO, B.; KUNDUR, P. Voltage stability analysis using static and dynamic approaches. **IEEE transactions on Power Systems**, IEEE, v. 8, n. 3, p. 1159–1171, 1993.

NEVES, L. S. **Fast methods for voltage stability analysis and control selection considering parameter uncertainties**. Tese (Doutorado) — Universidade de São Paulo, 2022.

NEVES, L. S.; ALBERTO, L. F. C. On the computation of the locally closest bifurcation point considering loading uncertainties and reactive power limits. **IEEE Transactions on Power Systems**, IEEE, v. 35, n. 5, p. 3885–3894, 2020.

NEVES, L. S.; ALBERTO, L. F. C.; CHIANG, H.-D. A fast method for detecting limit-induced bifurcation in electric power systems. **Electric Power Systems Research**, Elsevier, v. 180, p. 106101, 2020.

NEVES, L. S.; ALBERTO, L. F. C.; CHIANG, H.-D. Fast contingency screening for voltage stability analysis considering both snbs and sibs. **Electric Power Systems Research**, Elsevier, v. 213, p. 108303, 2022.

NEVES, L. S.; ALBERTO, L. F. C.; CHIANG, H.-D. Smooth power flow model for unified voltage stability assessment: theory and computation. **IEEE Transactions on Power Systems**, IEEE, v. 37, n. 6, p. 4579–4589, 2022.

OLIVEIRA, E. J. de; SILVA, I. D.; PEREIRA, J. L. R.; CARNEIRO, S. Transmission system expansion planning using a sigmoid function to handle integer investment variables. **IEEE Transactions on Power Systems**, IEEE, v. 20, n. 3, p. 1616–1621, 2005.

PASSOS FILHO, J. A. Modelagem e incorporação de dispositivos de controle no problema de fluxo de potência. **Juiz de Fora, Minas Gerais, Brasil: Dissertação de Mestrado. Programa de Pós-Graduação em Engenharia Elétrica. UFJF**, 2000.

PASSOS FILHO, J. A. **Representação e avaliação do desempenho de dispositivos de controle no problema de fluxo de potência**. Tese (Doutorado) — Universidade Federal do Rio de Janeiro, 2005.

PÉREZ-ARRIAGA, I. J.; VERGHESE, G. C.; SCHWEPPE, F. C. Selective modal analysis with applications to electric power systems, part i: Heuristic introduction. **ieee transactions on power apparatus and systems**, IEEE, n. 9, p. 3117–3125, 1982.

PEREZ, M.; MESSINA, A.; FUERTE-ESQUIVEL, C. Application of facts devices to improve steady state voltage stability. In: IEEE. **2000 Power Engineering Society Summer Meeting (Cat. No. 00CH37134)**. [S.l.], 2000. v. 2, p. 1115–1120.

PONTES, R. d. P. Nova metodologia full newton para consideração dos limites de geração de potência reativa no problema de fluxo de potência. **Juiz de Fora, Minas Gerais, Brasil: Dissertação de Mestrado. Programa de Pós-Graduação em Engenharia Elétrica. UFJF**, 2018. Disponível em: https://repositorio.ufjf.br/jspui/handle/ufjf/6933.

PONTES, R. d. P.; PASSOS FILHO, J. A.; LA GATTA, P. O. A full newton approach to consider reactive power generation limits in power flow problem using sigmoid switches. In: IEEE. **2018 Simposio Brasileiro de Sistemas Eletricos (SBSE)**. [S.l.], 2018. p. 1–6.

RHEINBOLDT, W. C. **Numerical analysis of parametrized nonlinear equations**. [S.l.]: Wiley-Interscience, 1986.

RHEINBOLDT, W. C.; BURKARDT, J. V. A locally parameterized continuation process. **ACM Transactions on Mathematical Software (TOMS)**, ACM New York, NY, USA, v. 9, n. 2, p. 215–235, 1983.

RIKS, E. Progress in collapse analyses. 1987.

SAPTEKA, A.; NAROTTAMA, A.; WINARTA, A.; YASA, K. A.; PRIAMBODO, P.; PUTRA, N. Modelling of electric characteristics of 150-watt peak solar panel using boltzmann sigmoid function under various temperature and irradiance. In: IOP PUBLISHING. **Journal of Physics: Conference Series**. [S.l.], 2018. v. 953, n. 1, p. 012048.

SAUER, P.; PAI, M. Power system steady-state stability and the load-flow jacobian. **IEEE Transactions on power systems**, IEEE, v. 5, n. 4, p. 1374–1383, 1990.

SCHLUETER, R.; HU, I.-P.; CHANG, M.-W.; LO, J.; COSTI, A. Methods for determining proximity to voltage collapse. **IEEE Transactions on power systems**, IEEE, v. 6, n. 1, p. 285–292, 1991.

SEYDEL, R. **From equilibrium to chaos: practical bifurcation and stability analysis**. [S.l.]: Elsevier Science Limited, 1988.

SPIEGEL, M. R.; LIPSCHUTZ, S.; LIU, J. **Schaum's Outlines: Mathematical Handbook of Formulas and Tables**. [S.l.]: McGraw-Hill, 2009. v. 2. ISBN 978-0070602243.

STOTT, B. Review of load-flow calculation methods. **Proceedings of the IEEE**, IEEE, v. 62, n. 7, p. 916–929, 1974.

TAMURA, Y.; MORI, H.; IWAMOTO, S. Relationship between voltage instability and multiple load flow solutions in electric power systems. **IEEE Transactions on power apparatus and systems**, IEEE, n. 5, p. 1115–1125, 1983.

TAYLOR, C. W. **Power system voltage stability**. [S.l.]: McGraw-Hill New York, NY, USA, 1994. ISBN 0-07-113708-4.

TAYLOR, C. W.; SCOTT, G.; HAMMAD, A. Static var compensator models for power flow and dynamic performance simulation. **IEEE Transactions on Power Systems (Institute of Electrical and Electronics Engineers);(United States)**, v. 9, n. 1, 1994.

TINNEY, W. F.; HART, C. E. Power flow solution by newton's method. **IEEE Transactions on Power Apparatus and systems**, Ieee, n. 11, p. 1449–1460, 1967.

UYKAN, Z.; KOIVO, H. N. Sigmoid-basis nonlinear power-control algorithm for mobile radio systems. **IEEE Transactions on Vehicular Technology**, IEEE, v. 53, n. 1, p. 265–270, 2004.

VENIKOV, V.; STROEV, V.; IDELCHICK, V.; TARASOV, V. Estimation of electrical power system steady-state stability in load flow calculations. **IEEE Transactions on Power Apparatus and Systems**, IEEE, v. 94, n. 3, p. 1034–1041, 1975.

WEISSTEIN, E. W. **Sigmoid Function. From MathWorld—A Wolfram Web Resource**. 2023. http://mathworld.wolfram.com/SigmoidFunction.html. Accessed on 23-03-2023.

ZENG, L.; CHIANG, H.-D.; NEVES, L. S.; ALBERTO, L. F. C. On the accuracy of power flow and load margin calculation caused by incorrect logical pv/pq switching: Analytics and improved methods. **International Journal of Electrical Power & Energy Systems**, Elsevier, v. 147, p. 108905, 2023.

APPENDIX A – JACOBIAN NEW DIFFERENTIAL TERMS

The proposed SPF-Generator and SPF-SVCs methodologies take into consideration new control equations to be incorporated into the traditional PF system of nonlinear equations formulation. To do so, these equations are set to be linearized and included in a augmented Jacobian matrix. Additionally, the state equations must also be linearized in terms of the new state variables.

The linearization of every new control equations take into consideration the pre-existing state variables and the new state variables present in the system of nonlinear equations. Therefore, this Appendix chapter goal is to introduce the mathematical calculations necessary to comprehend the proposed SPF methodologies control equations linearization.

Primarily, three mathematical properties will be used in order to define the new Jacobian differential terms (SPIEGEL; LIPSCHUTZ; LIU, 2009). These are differentiating a sum of variables, differentiating a product of variables and differentiating a fraction in terms of a general variable "z". Equations (A.1) to (A.3) details the aforementioned mathematical properties, respectively.

$$\frac{\partial}{\partial z}\left(u \pm v \pm w \pm \cdots\right) = \frac{\partial u}{\partial z} \pm \frac{\partial v}{\partial z} \pm \frac{\partial w}{\partial z} \pm \cdots \tag{A.1}$$

$$\frac{\partial}{\partial z}\left(u \cdot v \cdot w\right) = \frac{\partial u}{\partial z} \cdot \left(v \cdot w\right) + \frac{\partial v}{\partial z} \cdot \left(u \cdot w\right) + \frac{\partial w}{\partial z} \cdot \left(u \cdot v\right) \tag{A.2}$$

$$\frac{\partial}{\partial z}\left(\frac{u}{v}\right) = \frac{\frac{\partial u}{\partial z} \cdot v - u \cdot \frac{\partial v}{\partial z}}{v^2} \tag{A.3}$$

Additionally, the sigmoid function derivative (3.2) will also be used in order to determine the sigmoid switches derivatives.

These properties will be applied in the linearization of the new control equations in terms of the state variables $\boldsymbol{\theta}$, $\boldsymbol{V}$ and $\boldsymbol{x}$, where $\boldsymbol{x}$ is the vector of new state variables associated to each proposed SPF methodology. In order to do so, and to simplify the linearization calculation, the new control equations will be divided into three terms.

In the following sections, the mathematical calculations to linearize the SPF-Generator control equations and the SPF-SVCs proposed methodologies control equations will be presented.

A.1   SPF-GENERATORS REACTIVE POWER LIMITS METHODOLOGY

The SPF-Generator control equation (4.5) will be subdivided into three terms, following:

$$y = A + B + C, \tag{A.4}$$

where:

$$
\begin{aligned}
A &= (sw1 \cdot sw3) \cdot (1 - sw2 \cdot sw4) \cdot \left(Q_{G_k, gen} - Q_{G_k, gen}^{max}\right) \\
B &= (1 - sw1 \cdot sw3) \cdot (1 - sw2 \cdot sw4) \cdot \left(V_{k, gen} - V_{k, gen}^{ref}\right) \\
C &= (1 - sw1 \cdot sw3) \cdot (sw2 \cdot sw4) \cdot \left(Q_{G_k, gen} - Q_{G_k, gen}^{min}\right)
\end{aligned}
\tag{A.5}
$$

As detailed in Equation (4.5), the only active state variables in the proposed methodologies are $V_{k, gen}$ and $Q_{G_k, gen}$, which corresponds to V_k and Q_{G_k}, respectively. Therefore, differentiating the control equation y in terms of θ_k, θ_m or V_m are equal to zero.

$$\frac{\partial y}{\partial \theta_k} = \frac{\partial A}{\partial \theta_k} + \frac{\partial B}{\partial \theta_k} + \frac{\partial C}{\partial \theta_k} = 0 \tag{A.6}$$

$$\frac{\partial y}{\partial \theta_m} = \frac{\partial A}{\partial \theta_m} + \frac{\partial B}{\partial \theta_m} + \frac{\partial C}{\partial \theta_m} = 0 \tag{A.7}$$

$$\frac{\partial y}{\partial V_m} = \frac{\partial A}{\partial V_m} + \frac{\partial B}{\partial V_m} + \frac{\partial C}{\partial V_m} = 0 \tag{A.8}$$

It remains only to differentiate the control equation in terms of $V_{k, gen}$ and $Q_{G_k, gen}$, and differentiating the state equations in terms of the new state variable. These new differentiating terms will be detailed in the following Subsections.

A.1.1   **Differentiating the control equation in terms of $V_{k, gen}$**

The control equation (A.5) differentiation in terms of V_k is given below:

$$\frac{\partial y}{\partial V_k} = \frac{\partial A}{\partial V_k} + \frac{\partial B}{\partial V_k} + \frac{\partial C}{\partial V_k} \neq 0. \tag{A.9}$$

Applying the mathematical property (A.2) in (A.9) results in:

$$\frac{\partial A}{\partial V_k} = \frac{\partial \left(sw1 \cdot sw3 \right)}{\partial V_k} \cdot \left(1 - sw2 \cdot sw4 \right) \cdot \left(Q_{G_k, gen} - Q_{G_k, gen}^{max} \right) +$$
$$+ \left(sw1 \cdot sw3 \right) \cdot \frac{\partial \left(1 - sw2 \cdot sw4 \right)}{\partial V_k} \cdot \left(Q_{G_k, gen} - Q_{G_k, gen}^{max} \right) + \quad \text{(A.10)}$$
$$+ \left(sw1 \cdot sw3 \right) \cdot \left(1 - sw2 \cdot sw4 \right) \cdot \frac{\partial \left(Q_{G_k, gen} - Q_{G_k, gen}^{max} \right)}{\partial V_k}$$

$$\frac{\partial B}{\partial V_k} = \frac{\partial \left(1 - sw1 \cdot sw3 \right)}{\partial V_k} \cdot \left(1 - sw2 \cdot sw4 \right) \cdot \left(V_{k, gen} - V_{k, gen}^{ref} \right) +$$
$$+ \left(1 - sw1 \cdot sw3 \right) \cdot \frac{\partial \left(1 - sw2 \cdot sw4 \right)}{\partial V_k} \cdot \left(V_{k, gen} - V_{k, gen}^{ref} \right) + \quad \text{(A.11)}$$
$$+ \left(1 - sw1 \cdot sw3 \right) \cdot \left(1 - sw2 \cdot sw4 \right) \cdot \frac{\partial \left(V_{k, gen} - V_{k, gen}^{ref} \right)}{\partial V_k}$$

$$\frac{\partial C}{\partial V_k} = \frac{\partial \left(1 - sw1 \cdot sw3 \right)}{\partial V_k} \cdot \left(sw2 \cdot sw4 \right) \cdot \left(Q_{G_k, gen} - Q_{G_k, gen}^{min} \right) +$$
$$+ \left(1 - sw1 \cdot sw3 \right) \cdot \frac{\partial \left(sw2 \cdot sw4 \right)}{\partial V_k} \cdot \left(Q_{G_k, gen} - Q_{G_k, gen}^{min} \right) + \quad \text{(A.12)}$$
$$+ \left(1 - sw1 \cdot sw3 \right) \cdot \left(sw2 \cdot sw4 \right) \cdot \frac{\partial \left(Q_{G_k, gen} - Q_{G_k, gen}^{min} \right)}{\partial V_k}$$

Since switches *sw1* and *sw2* corresponds to the reactive power generation variable, their differentation in terms of V_k equals to zero. Therefore, must be only analyzed the differentiating terms of switches *sw3* and *sw4*, which corresponds to the *k*-bus voltage magnitude where the Generator is connected.

$$\frac{\partial sw1}{\partial V_k} = 0 \quad \text{(A.13)}$$

$$\frac{\partial sw2}{\partial V_k} = 0 \quad \text{(A.14)}$$

$$\frac{\partial sw3}{\partial V_k} = -slp \cdot \left(1 - sw3 \right) \cdot sw3 \quad \text{(A.15)}$$

$$\frac{\partial sw4}{\partial V_k} = slp \cdot \left(1 - sw4 \right) \cdot sw4 \quad \text{(A.16)}$$

Therefore, Equations (A.10), (A.11) and (A.12) respectively results in:

$$\frac{\partial A}{\partial V_k} = sw1 \cdot [-slp \cdot (1 - sw3) \cdot sw3] \cdot (1 - sw2 \cdot sw4) \cdot \left(Q_{G_k,gen} - Q_{G_k,gen}^{max}\right) + \quad (A.17)$$
$$+ \; (sw1 \cdot sw3) \cdot [1 - sw2 \cdot slp \cdot (1 - sw4) \cdot sw4] \cdot \left(Q_{G_k,gen} - Q_{G_k,gen}^{max}\right)$$

$$\frac{\partial B}{\partial V_k} = [1 + sw1 \cdot slp \cdot (1 - sw3) \cdot sw3] \cdot (1 - sw2 \cdot sw4) \cdot \left(V_{k,gen} - V_{k,gen}^{ref}\right) + \quad (A.18)$$
$$+ \; (1 - sw1 \cdot sw3) \cdot [1 - sw2 \cdot slp \cdot (1 - sw4) \cdot sw4] \cdot \left(V_{k,gen} - V_{k,gen}^{ref}\right) +$$
$$+ \; (1 - sw1 \cdot sw3) \cdot (1 - sw2 \cdot sw4) \cdot 1$$

$$\frac{\partial C}{\partial V_k} = [1 + sw1 \cdot slp \cdot (1 - sw3) \cdot sw3] \cdot (sw2 \cdot sw4) \cdot \left(Q_{G_k,gen} - Q_{G_k,gen}^{min}\right) + \quad (A.19)$$
$$+ \; (1 - sw1 \cdot sw3) \cdot [sw2 \cdot slp \cdot (1 - sw4) \cdot sw4] \cdot \left(Q_{G_k,gen} - Q_{G_k,gen}^{min}\right)$$

Therefore, by analyzing Equations (A.17) through (A.19), the control equation differentiation in terms of $V_{k,gen}$ is defined:

$$\frac{\partial y}{\partial V_k} = \frac{\partial A}{\partial V_k} + \frac{\partial B}{\partial V_k} + \frac{\partial C}{\partial V_k} \quad (A.20)$$

A.1.2 Differentiating the control equation in terms of $Q_{G_k,gen}$

The control equation (A.5) differentiation in terms of Q_{G_k} is given below:

$$\frac{\partial y}{\partial Q_{G_k}} = \frac{\partial A}{\partial Q_{G_k}} + \frac{\partial B}{\partial Q_{G_k}} + \frac{\partial C}{\partial Q_{G_k}} \neq 0. \quad (A.21)$$

Applying the mathematical property (A.2) in (A.21) results in:

$$\frac{\partial A}{\partial Q_{G_k}} = \frac{\partial (sw1 \cdot sw3)}{\partial Q_{G_k}} \cdot (1 - sw2 \cdot sw4) \cdot \left(Q_{G_k,gen} - Q_{G_k,gen}^{max}\right) +$$
$$+ \; (sw1 \cdot sw3) \cdot \frac{\partial (1 - sw2 \cdot sw4)}{\partial Q_{G_k}} \cdot \left(Q_{G_k,gen} - Q_{G_k,gen}^{max}\right) + \quad (A.22)$$
$$+ \; (sw1 \cdot sw3) \cdot (1 - sw2 \cdot sw4) \cdot \frac{\partial \left(Q_{G_k,gen} - Q_{G_k,gen}^{max}\right)}{\partial Q_{G_k}}$$

$$\frac{\partial B}{\partial Q_{G_k}} = \frac{\partial \left(1 - sw1 \cdot sw3\right)}{\partial Q_{G_k}} \cdot \left(1 - sw2 \cdot sw4\right) \cdot \left(V_{k,\,gen} - V_{k,\,gen}^{ref}\right) +$$
$$+ \left(1 - sw1 \cdot sw3\right) \cdot \frac{\partial \left(1 - sw2 \cdot sw4\right)}{\partial Q_{G_k}} \cdot \left(V_{k,\,gen} - V_{k,\,gen}^{ref}\right) + \qquad \text{(A.23)}$$
$$+ \left(1 - sw1 \cdot sw3\right) \cdot \left(1 - sw2 \cdot sw4\right) \cdot \frac{\partial \left(V_{k,\,gen} - V_{k,\,gen}^{ref}\right)}{\partial Q_{G_k}}$$

$$\frac{\partial C}{\partial Q_{G_k}} = \frac{\partial \left(1 - sw1 \cdot sw3\right)}{\partial Q_{G_k}} \cdot \left(sw2 \cdot sw4\right) \cdot \left(Q_{G_k,\,gen} - Q_{G_k,\,gen}^{min}\right) +$$
$$+ \left(1 - sw1 \cdot sw3\right) \cdot \frac{\partial \left(sw2 \cdot sw4\right)}{\partial Q_{G_k}} \cdot \left(Q_{G_k,\,gen} - Q_{G_k,\,gen}^{min}\right) + \qquad \text{(A.24)}$$
$$+ \left(1 - sw1 \cdot sw3\right) \cdot \left(sw2 \cdot sw4\right) \cdot \frac{\partial \left(Q_{G_k,\,gen} - Q_{G_k,\,gen}^{min}\right)}{\partial Q_{G_k}}$$

Since switches *sw3* and *sw4* corresponds to the voltage magnitude variable, their differentiation in terms of Q_{G_k} equals to zero. Therefore, must be only analyzed the differentiating terms of switches *sw1* and *sw2*, which corresponds to the *k*-bus reactive power generation where the Generator is connected.

$$\frac{\partial sw1}{\partial Q_{G_k}} = slp \cdot \left(1 - sw1\right) \cdot sw1 \qquad \text{(A.25)}$$

$$\frac{\partial sw2}{\partial Q_{G_k}} = -slp \cdot \left(1 - sw2\right) \cdot sw2 \qquad \text{(A.26)}$$

$$\frac{\partial sw3}{\partial Q_{G_k}} = 0 \qquad \text{(A.27)}$$

$$\frac{\partial sw4}{\partial Q_{G_k}} = 0 \qquad \text{(A.28)}$$

Therefore, Equations (A.22), (A.23) and (A.24) respectively results in:

$$\frac{\partial A}{\partial Q_{G_k}} = \left[slp \cdot \left(1 - sw1\right) \cdot sw1\right] \cdot sw3 \cdot \left(1 - sw2 \cdot sw4\right) \cdot \left(Q_{G_k,\,gen} - Q_{G_k,\,gen}^{max}\right) + \quad \text{(A.29)}$$
$$+ \left(sw1 \cdot sw3\right) \cdot \left[1 + slp \cdot \left(1 - sw2\right) \cdot sw2\right] \cdot sw4 \cdot \left(Q_{G_k,\,gen} - Q_{G_k,\,gen}^{max}\right) +$$
$$+ \left(sw1 \cdot sw3\right) \cdot \left(1 - sw2 \cdot sw4\right) \cdot 1$$

$$\frac{\partial B}{\partial Q_{G_k}} = [1 - slp \cdot (1 - sw1) \cdot sw1] \cdot sw3 \cdot (1 - sw2 \cdot sw4) \cdot \left(V_{k,gen} - V_{k,gen}^{ref}\right) + \quad \text{(A.30)}$$

$$+ (1 - sw1 \cdot sw3) \cdot [1 + slp \cdot (1 - sw2) \cdot sw2] \cdot sw4 \cdot \left(V_{k,gen} - V_{k,gen}^{ref}\right) +$$

$$\frac{\partial C}{\partial Q_{G_k}} = [1 - slp \cdot (1 - sw1) \cdot sw1] \cdot sw3 \cdot (sw2 \cdot sw4) \cdot \left(Q_{G_k,gen} - Q_{G_k,gen}^{min}\right) + \quad \text{(A.31)}$$

$$+ (1 - sw1 \cdot sw3) \cdot [-slp \cdot (1 - sw2) \cdot sw2] \cdot sw4 \cdot \left(Q_{G_k,gen} - Q_{G_k,gen}^{min}\right) +$$

$$+ (1 - sw1 \cdot sw3) \cdot (sw2 \cdot sw4) \cdot 1$$

Therefore, by analyzing Equations (A.29) through (A.31), the control equation differentiation in terms of $Q_{G_k,gen}$ is defined:

$$\frac{\partial y}{\partial Q_{G_k}} = \frac{\partial A}{\partial Q_{G_k}} + \frac{\partial B}{\partial Q_{G_k}} + \frac{\partial C}{\partial Q_{G_k}} \quad \text{(A.32)}$$

A.1.3 Differentiating the state equations in terms of $Q_{G_k,gen}$

Differentiating the PF state equations, which define each bus active and reactive power injections value ($\boldsymbol{P}$ and $\boldsymbol{Q}$), in terms of the new state variable $Q_{G_k,gen}$ - which is equivalent to Q_{G_k} - results in:

$$\frac{\partial P_k}{\partial Q_{G_k,gen}} = \frac{\partial P_k}{\partial Q_{G_k}} = \frac{\partial \left[P_k^{cal} - (P_{G_k} - P_{L_k})\right]}{\partial Q_{G_k}} = 0 \quad \text{(A.33)}$$

$$\frac{\partial P_m}{\partial Q_{G_k,gen}} = \frac{\partial P_m}{\partial Q_{G_k}} = \frac{\partial \left[P_m^{cal} - (P_{G_m} - P_{L_m})\right]}{\partial Q_{G_k}} = 0 \quad \text{(A.34)}$$

$$\frac{\partial Q_k}{\partial Q_{G_k,gen}} = \frac{\partial Q_k}{\partial Q_{G_k}} = \frac{\partial \left[Q_k^{cal} - (Q_{G_k} - Q_{L_k})\right]}{\partial Q_{G_k}} = -1 \quad \text{(A.35)}$$

$$\frac{\partial Q_m}{\partial Q_{G_k,gen}} = \frac{\partial Q_m}{\partial Q_{G_k}} = \frac{\partial \left[Q_m^{cal} - (Q_{G_m} - Q_{L_m})\right]}{\partial Q_{G_k}} = 0 \quad \text{(A.36)}$$

Therefore, the only non-zero differentiating term is (A.35).

A.1.4 **Augmented Jacobian matrix**

The augmented Jacobian matrix values detailed in Equation (4.6) are simplified in (A.37). For the steady-state SPF-Generator reactive power limits methodology, the new differential terms are given in Equations (A.20), (A.32) and (A.35).

The augmented Jacobian matrix values are detailed in Equation (A.37) for the SPF-Generator modeling:

$$
\begin{bmatrix}
\vdots \\
\Delta P_k \\
\Delta P_m \\
\vdots \\
\Delta Q_k \\
\Delta Q_m \\
\vdots \\
\Delta y \\
\vdots
\end{bmatrix}
=
\begin{bmatrix}
\ddots & \vdots & \vdots & \cdots & \vdots & \vdots & \cdots & \vdots & \reflectbox{$\ddots$} \\
\cdots & \frac{\partial P_k}{\partial \theta_k} & \frac{\partial P_k}{\partial \theta_m} & \cdots & \frac{\partial P_k}{\partial V_k} & \frac{\partial P_k}{\partial V_m} & \cdots & 0 & \cdots \\
\cdots & \frac{\partial P_m}{\partial \theta_k} & \frac{\partial P_m}{\partial \theta_m} & \cdots & \frac{\partial P_m}{\partial V_k} & \frac{\partial P_m}{\partial V_m} & \cdots & 0 & \cdots \\
\cdots & \vdots & \vdots & \cdots & \vdots & \vdots & \cdots & \vdots & \cdots \\
\cdots & \frac{\partial Q_k}{\partial \theta_k} & \frac{\partial Q_k}{\partial \theta_m} & \cdots & \frac{\partial Q_k}{\partial V_k} & \frac{\partial Q_k}{\partial V_m} & \cdots & \frac{\partial Q_k}{\partial Q_{G_k,gen}} & \cdots \\
\cdots & \frac{\partial Q_m}{\partial \theta_k} & \frac{\partial Q_m}{\partial \theta_m} & \cdots & \frac{\partial Q_m}{\partial V_k} & \frac{\partial Q_m}{\partial V_m} & \cdots & 0 & \cdots \\
\cdots & \vdots & \vdots & \cdots & \vdots & \vdots & \cdots & \vdots & \cdots \\
\cdots & 0 & 0 & \cdots & \frac{\partial y}{\partial V_k} & 0 & \cdots & \frac{\partial y}{\partial Q_{G_k,gen}} & \cdots \\
\reflectbox{$\ddots$} & \vdots & \vdots & \cdots & \vdots & \vdots & \cdots & \vdots & \ddots
\end{bmatrix}
\cdot
\begin{bmatrix}
\vdots \\
\Delta \theta_k \\
\Delta \theta_m \\
\vdots \\
\Delta V_k \\
\Delta V_m \\
\vdots \\
\Delta Q_{G_k,gen} \\
\vdots
\end{bmatrix}
\tag{A.37}
$$

A.2 SPF-SVC REACTIVE POWER INJECTION METHODOLOGY

The SPF-SVC reactive power injection control equation (5.5) will be subdivided into three terms, following:

$$y = A + B + C, \tag{A.38}$$

where:

$$
\begin{aligned}
A &= sw5 \cdot \left(Q_{G_k,svc} - V_{k,svc}^2 \cdot B_{svc}^{ind} \right) \\
B &= (1 - sw5) \cdot (1 - sw6) \cdot \left(V_{m,svc} - V_{m,svc}^{ref} - r \cdot Q_{G_k,svc} \right) \\
C &= sw6 \cdot \left(Q_{G_k,svc} - V_{k,svc}^2 \cdot B_{svc}^{cap} \right)
\end{aligned}
\tag{A.39}
$$

As detailed in Equation (5.5), the only active state variables in the proposed methodologies are $V_{k,svc}$, $V_{m,svc}$ and $Q_{G_k,svc}$, which corresponds to V_k, V_m and Q_{G_k}, respectively. Therefore, differentiating the control equation y in terms of θ_k or θ_m are equal to zero.

$$\frac{\partial y}{\partial \theta_k} = \frac{\partial A}{\partial \theta_k} + \frac{\partial B}{\partial \theta_k} + \frac{\partial C}{\partial \theta_k} = 0 \tag{A.40}$$

$$\frac{\partial y}{\partial \theta_m} = \frac{\partial A}{\partial \theta_m} + \frac{\partial B}{\partial \theta_m} + \frac{\partial C}{\partial \theta_m} = 0 \tag{A.41}$$

It remains only to differentiate the control equation in terms of $V_{k,svc}$, $V_{m,svc}$ and $Q_{G_k,svc}$, and differentiating the state equations in terms of the new state variable. These new differentiating terms will be detailed in the following subsections.

A.2.1 Differentiating the control equation in terms of $V_{k,svc}$

The control equation (A.39) differentiation in terms of V_k is given below:

$$\frac{\partial y}{\partial V_k} = \frac{\partial A}{\partial V_k} + \frac{\partial B}{\partial V_k} + \frac{\partial C}{\partial V_k} \neq 0. \tag{A.42}$$

Applying the mathematical property (A.2) in (A.42) results in:

$$\frac{\partial A}{\partial V_k} = \frac{\partial sw5}{\partial V_k} \cdot \left(Q_{G_k,svc} - V_{k,svc}^2 \cdot B_{svc}^{ind} \right) + \tag{A.43}$$
$$+ \; sw5 \cdot \frac{\partial \left(Q_{G_k,svc} - V_{k,svc}^2 \cdot B_{svc}^{ind} \right)}{\partial V_k}$$

$$\frac{\partial B}{\partial V_k} = \frac{\partial \left(1 - sw5\right)}{\partial V_k} \cdot \left(1 - sw6\right) \cdot \left(V_{m,svc} - V_{m,svc}^{ref} - r \cdot Q_{G_k,svc} \right) +$$
$$+ \; \left(1 - sw5\right) \cdot \frac{\partial \left(1 - sw6\right)}{\partial V_k} \cdot \left(V_{m,svc} - V_{m,svc}^{ref} - r \cdot Q_{G_k,svc} \right) + \tag{A.44}$$
$$+ \; \left(1 - sw5\right) \cdot \left(1 - sw6\right) \cdot \frac{\partial \left(V_{m,svc} - V_{m,svc}^{ref} - r \cdot Q_{G_k,svc} \right)}{\partial V_k}$$

$$\frac{\partial C}{\partial V_k} = \frac{\partial sw6}{\partial V_k} \cdot \left(Q_{G_k,svc} - V_{k,svc}^2 \cdot B_{svc}^{cap} \right) + \tag{A.45}$$
$$+ \; sw6 \cdot \frac{\partial \left(Q_{G_k,svc} - V_{k,svc}^2 \cdot B_{svc}^{cap} \right)}{\partial V_k}$$

Since switches *sw5* and *sw6* corresponds to the controlled m-bus voltage magnitude variable, their differentation in terms of V_k equals to zero. Also, the B-term in (A.39) does not differentiate in terms of V_k. Therefore:

$$\frac{\partial A}{\partial V_k} = sw5 \cdot \left(-2 \cdot V_{k,\,svc} \cdot B_{svc}^{ind}\right) \tag{A.46}$$

$$\frac{\partial B}{\partial V_k} = 0 \tag{A.47}$$

$$\frac{\partial C}{\partial V_k} = sw6 \cdot \left(-2 \cdot V_{k,\,svc} \cdot B_{svc}^{cap}\right) \tag{A.48}$$

Analyzing Equations (A.46) to (A.48), it is assured that the only non-zero differential terms are:

$$\begin{aligned} \frac{\partial y}{\partial V_k} &= \frac{\partial A}{\partial V_k} + \frac{\partial C}{\partial V_k} \\ &= sw5 \cdot \left(-2 \cdot V_{k,\,svc} \cdot B_{svc}^{ind}\right) + sw6 \cdot \left(-2 \cdot V_{k,\,svc} \cdot B_{svc}^{cap}\right) \end{aligned} \tag{A.49}$$

A.2.2 Differentiating the control equation in terms of $V_{m,\,svc}$

The control equation (A.39) differentiation in terms of V_m is given below:

$$\frac{\partial y}{\partial V_m} = \frac{\partial A}{\partial V_m} + \frac{\partial B}{\partial V_m} + \frac{\partial C}{\partial V_m} \neq 0. \tag{A.50}$$

Applying the mathematical property (A.2) in (A.50) results in:

$$\begin{aligned} \frac{\partial A}{\partial V_m} &= \frac{\partial sw5}{\partial V_m} \cdot \left(Q_{G_k,\,svc} - V_{k,\,svc}^2 \cdot B_{svc}^{ind}\right) + \\ &\quad + sw5 \cdot \frac{\partial \left(Q_{G_k,\,svc} - V_{k,\,svc}^2 \cdot B_{svc}^{ind}\right)}{\partial V_m} \end{aligned} \tag{A.51}$$

$$\begin{aligned} \frac{\partial B}{\partial V_m} &= \frac{\partial \left(1 - sw5\right)}{\partial V_m} \cdot (1 - sw6) \cdot \left(V_{m,\,svc} - V_{m,\,svc}^{ref} - r \cdot Q_{G_k,\,svc}\right) + \\ &\quad + (1 - sw5) \cdot \frac{\partial \left(1 - sw6\right)}{\partial V_m} \cdot \left(V_{m,\,svc} - V_{m,\,svc}^{ref} - r \cdot Q_{G_k,\,svc}\right) + \\ &\quad + (1 - sw5) \cdot (1 - sw6) \cdot \frac{\partial \left(V_{m,\,svc} - V_{m,\,svc}^{ref} - r \cdot Q_{G_k,\,svc}\right)}{\partial V_m} \end{aligned} \tag{A.52}$$

$$\frac{\partial C}{\partial V_m} = \frac{\partial sw6}{\partial V_m} \cdot \left(Q_{G_k, svc} - V_{k, svc}^2 \cdot B_{svc}^{cap} \right) + \tag{A.53}$$
$$+ \; sw6 \cdot \frac{\partial \left(Q_{G_k, svc} - V_{k, svc}^2 \cdot B_{svc}^{cap} \right)}{\partial V_m}$$

Since switches *sw5* and *sw6* corresponds to the controlled *m*-bus voltage magnitude variable, their differentation in terms of V_m do not equal to zero, at first:

$$\frac{\partial sw5}{\partial V_m} = -slp \cdot (1 - sw5) \cdot sw5, \tag{A.54}$$

$$\frac{\partial sw6}{\partial V_m} = slp \cdot (1 - sw6) \cdot sw6. \tag{A.55}$$

Therefore, Equations (A.51), (A.52) and (A.53) respectively results in:

$$\frac{\partial A}{\partial V_m} = -\, slp \cdot (1 - sw5) \cdot sw5 \cdot \left(Q_{G_k, svc} - V_{k, svc}^2 \cdot B_{svc}^{ind} \right) \tag{A.56}$$

$$\frac{\partial B}{\partial V_m} = [1 + slp \cdot (1 - sw5) \cdot sw5] \cdot (1 - sw6) \cdot \left(V_{m, svc} - V_{m, svc}^{ref} - r \cdot Q_{G_k, svc} \right) + \tag{A.57}$$
$$+ \; (1 - sw5) \cdot [1 - slp \cdot (1 - sw6) \cdot sw6] \cdot \left(V_{m, svc} - V_{m, svc}^{ref} - r \cdot Q_{G_k, svc} \right) +$$
$$+ \; (1 - sw5) \cdot (1 - sw6) \cdot 1$$

$$\frac{\partial C}{\partial V_m} = slp \cdot (1 - sw6) \cdot sw6 \cdot \left(Q_{G_k, svc} - V_{k, svc}^2 \cdot B_{svc}^{cap} \right) \tag{A.58}$$

Therefore, by analyzing Equation (A.56) through (A.58), the control equation differentiation in terms of $V_{m, svc}$ is defined:

$$\frac{\partial y}{\partial V_m} = \frac{\partial A}{\partial V_m} + \frac{\partial B}{\partial V_m} + \frac{\partial C}{\partial V_m} \tag{A.59}$$

A.2.3 Differentiating the control equation in terms of $Q_{G_k, svc}$

The control equation (A.39) differentiation in terms of Q_{G_k} is given below:

$$\frac{\partial y}{\partial Q_{G_k}} = \frac{\partial A}{\partial Q_{G_k}} + \frac{\partial B}{\partial Q_{G_k}} + \frac{\partial C}{\partial Q_{G_k}} \neq 0. \tag{A.60}$$

Applying the mathematical property (A.2) in (A.60) results in:

$$\frac{\partial A}{\partial Q_{G_k}} = \frac{\partial sw5}{\partial Q_{G_k}} \cdot \left(Q_{G_k, svc} - V_{k, svc}^2 \cdot B_{svc}^{ind}\right) + \tag{A.61}$$
$$+ \; sw5 \cdot \frac{\partial \left(Q_{G_k, svc} - V_{k, svc}^2 \cdot B_{svc}^{ind}\right)}{\partial Q_{G_k}}$$

$$\frac{\partial B}{\partial Q_{G_k}} = \frac{\partial (1 - sw5)}{\partial Q_{G_k}} \cdot (1 - sw6) \cdot \left(V_{m, svc} - V_{m, svc}^{ref} - r \cdot Q_{G_k, svc}\right) +$$
$$+ \; (1 - sw5) \cdot \frac{\partial (1 - sw6)}{\partial Q_{G_k}} \cdot \left(V_{m, svc} - V_{m, svc}^{ref} - r \cdot Q_{G_k, svc}\right) + \tag{A.62}$$
$$+ \; (1 - sw5) \cdot (1 - sw6) \cdot \frac{\partial \left(V_{m, svc} - V_{m, svc}^{ref} - r \cdot Q_{G_k, svc}\right)}{\partial Q_{G_k}}$$

$$\frac{\partial C}{\partial Q_{G_k}} = \frac{\partial sw6}{\partial Q_{G_k}} \cdot \left(Q_{G_k, svc} - V_{k, svc}^2 \cdot B_{svc}^{cap}\right) + \tag{A.63}$$
$$+ \; sw6 \cdot \frac{\partial \left(Q_{G_k, svc} - V_{k, svc}^2 \cdot B_{svc}^{cap}\right)}{\partial Q_{G_k}}$$

Since switches *sw5* and *sw6* corresponds to the controlled m-bus voltage magnitude variable, their differentiation in terms of Q_{G_k} equals to zero. Therefore, analyzing Equations (A.61) to (A.63), it is assured that the only non-zero differential terms are:

$$\frac{\partial y}{\partial Q_{G_k}} = \frac{\partial A}{\partial Q_{G_k}} + \frac{\partial B}{\partial Q_{G_k}} + \frac{\partial C}{\partial Q_{G_k}} \tag{A.64}$$
$$= sw5 - r \cdot (1 - sw5) \cdot (1 - sw6) + sw6$$

A.2.4 Differentiating the state equations in terms of $Q_{G_k, svc}$

Differentiating the PF state equations, which define each bus active and reactive power injections value ($\boldsymbol{P}$ and $\boldsymbol{Q}$), in terms of the new state variable $Q_{G_k, svc}$ - which is equivalent to Q_{G_k} - results in:

$$\frac{\partial P_k}{\partial Q_{G_k, svc}} = \frac{\partial P_k}{\partial Q_{G_k}} = \frac{\partial \left[P_k^{cal} - (P_{G_k} - P_{L_k})\right]}{\partial Q_{G_k}} = 0 \tag{A.65}$$

$$\frac{\partial P_m}{\partial Q_{G_k, svc}} = \frac{\partial P_m}{\partial Q_{G_k}} = \frac{\partial \left[P_m^{cal} - (P_{G_m} - P_{L_m})\right]}{\partial Q_{G_k}} = 0 \tag{A.66}$$

$$\frac{\partial Q_k}{\partial Q_{G_k, svc}} = \frac{\partial Q_k}{\partial Q_{G_k}} = \frac{\partial \left[Q_k^{cal} - (Q_{G_k} - Q_{L_k}) \right]}{\partial Q_{G_k}} = -1 \qquad (A.67)$$

$$\frac{\partial Q_m}{\partial Q_{G_k, svc}} = \frac{\partial Q_m}{\partial Q_{G_k}} = \frac{\partial \left[Q_m^{cal} - (Q_{G_m} - Q_{L_m}) \right]}{\partial Q_{G_k}} = 0 \qquad (A.68)$$

Therefore, the only non-zero differentiating term is (A.67).

A.2.5 Augmented Jacobian matrix

The augmented Jacobian matrix values detailed in Equation (5.6) are simplified in (A.69). For the steady-state SPF-SVC reactive power injection methodology, the new differential terms are given in Equations (A.49), (A.59), (A.64) and (A.67).

$$
\begin{bmatrix}
\vdots \\
\Delta P_k \\
\Delta P_m \\
\vdots \\
\Delta Q_k \\
\Delta Q_m \\
\vdots \\
\Delta y \\
\vdots
\end{bmatrix}
=
\begin{bmatrix}
\ddots & \vdots & \vdots & \cdots & \vdots & \vdots & \cdots & \vdots & \reflectbox{$\ddots$} \\
\cdots & \frac{\partial P_k}{\partial \theta_k} & \frac{\partial P_k}{\partial \theta_m} & \cdots & \frac{\partial P_k}{\partial V_k} & \frac{\partial P_k}{\partial V_m} & \cdots & 0 & \cdots \\
\cdots & \frac{\partial P_m}{\partial \theta_k} & \frac{\partial P_m}{\partial \theta_m} & \cdots & \frac{\partial P_m}{\partial V_k} & \frac{\partial P_m}{\partial V_m} & \cdots & 0 & \cdots \\
\cdots & \vdots & \vdots & \cdots & \vdots & \vdots & \cdots & \vdots & \cdots \\
\cdots & \frac{\partial Q_k}{\partial \theta_k} & \frac{\partial Q_k}{\partial \theta_m} & \cdots & \frac{\partial Q_k}{\partial V_k} & \frac{\partial Q_k}{\partial V_m} & \cdots & \frac{\partial Q_k}{\partial Q_{G_k, svc}} & \cdots \\
\cdots & \frac{\partial Q_m}{\partial \theta_k} & \frac{\partial Q_m}{\partial \theta_m} & \cdots & \frac{\partial Q_m}{\partial V_k} & \frac{\partial Q_m}{\partial V_m} & \cdots & 0 & \cdots \\
\cdots & \vdots & \vdots & \cdots & \vdots & \vdots & \cdots & \vdots & \cdots \\
\cdots & 0 & 0 & \cdots & \frac{\partial y}{\partial V_k} & \frac{\partial y}{\partial V_m} & \cdots & \frac{\partial y}{\partial Q_{G_k, svc}} & \cdots \\
\reflectbox{$\ddots$} & \vdots & \vdots & \cdots & \vdots & \vdots & \cdots & \vdots & \ddots
\end{bmatrix}
\cdot
\begin{bmatrix}
\vdots \\
\Delta \theta_k \\
\Delta \theta_m \\
\vdots \\
\Delta V_k \\
\Delta V_m \\
\vdots \\
\Delta Q_{G_k, svc} \\
\vdots
\end{bmatrix}
$$

$$(A.69)$$

A.3 SPF-SVC CURRENT INJECTION METHODOLOGY

The SPF-SVC current injection control equation (5.12) will be subdivided into three terms, following:

$$y = A + B + C, \qquad (A.70)$$

where:

$$
\begin{aligned}
A &= sw7 \cdot \left(I_{k,\,svc} - V_{k,\,svc} \cdot B_{svc}^{ind} \right) \\
B &= (1 - sw7) \cdot (1 - sw8) \cdot \left(V_{m,\,svc} - V_{m,\,svc}^{ref} - r \cdot I_{k,\,svc} \right) \\
C &= sw8 \cdot \left(I_{k,\,svc} - V_{k,\,svc} \cdot B_{svc}^{cap} \right)
\end{aligned}
\tag{A.71}
$$

As detailed in Equation (5.12), the only active state variables in the proposed methodologies are $V_{k,\,svc}$, $V_{m,\,svc}$ and $I_{k,\,svc}$, which corresponds to V_k, V_m and I_k, respectively. Therefore, differentiating the control equation y in terms of θ_k or θ_m are equal to zero.

$$
\frac{\partial y}{\partial \theta_k} = \frac{\partial A}{\partial \theta_k} + \frac{\partial B}{\partial \theta_k} + \frac{\partial C}{\partial \theta_k} = 0
\tag{A.72}
$$

$$
\frac{\partial y}{\partial \theta_m} = \frac{\partial A}{\partial \theta_m} + \frac{\partial B}{\partial \theta_m} + \frac{\partial C}{\partial \theta_m} = 0
\tag{A.73}
$$

It remains only to differentiate the control equation in terms of $V_{k,\,svc}$, $V_{m,\,svc}$ and $I_{k,\,svc}$, and differentiating the state equations in terms of the new state variable. These new differentiating terms will be detailed in the following subsections.

A.3.1 Differentiating the control equation in terms of $V_{k,\,svc}$

The control equation (A.71) differentiation in terms of V_k is given below:

$$
\frac{\partial y}{\partial V_k} = \frac{\partial A}{\partial V_k} + \frac{\partial B}{\partial V_k} + \frac{\partial C}{\partial V_k} \neq 0.
\tag{A.74}
$$

Applying the mathematical property (A.2) in (A.74) results in:

$$
\frac{\partial A}{\partial V_k} = \frac{\partial sw7}{\partial V_k} \cdot \left(I_{k,\,svc} - V_{k,\,svc} \cdot B_{svc}^{ind} \right) +
\tag{A.75}
$$
$$
+ \, sw7 \cdot \frac{\partial \left(I_{k,\,svc} - V_{k,\,svc} \cdot B_{svc}^{ind} \right)}{\partial V_k}
$$

$$
\begin{aligned}
\frac{\partial B}{\partial V_k} &= \frac{\partial (1 - sw7)}{\partial V_k} \cdot (1 - sw8) \cdot \left(V_{m,\,svc} - V_{m,\,svc}^{ref} - r \cdot I_{k,\,svc} \right) + \\
&+ \, (1 - sw7) \cdot \frac{\partial (1 - sw8)}{\partial V_k} \cdot \left(V_{m,\,svc} - V_{m,\,svc}^{ref} - r \cdot I_{k,\,svc} \right) + \\
&+ \, (1 - sw7) \cdot (1 - sw8) \cdot \frac{\partial \left(V_{m,\,svc} - V_{m,\,svc}^{ref} - r \cdot I_{k,\,svc} \right)}{\partial V_k}
\end{aligned}
\tag{A.76}
$$

$$\frac{\partial C}{\partial V_k} = \frac{\partial sw8}{\partial V_k} \cdot (I_{k,\,svc} - V_{k,\,svc} \cdot B_{svc}^{cap}) + \tag{A.77}$$

$$+ \; sw8 \cdot \frac{\partial \left(I_{k,\,svc} - V_{k,\,svc} \cdot B_{svc}^{cap} \right)}{\partial V_k}$$

Since switches $sw7$ and $sw8$ corresponds to the controlled m-bus voltage magnitude variable, their differentation in terms of V_k equals to zero. Considering that I_k is given by Equation (5.9), applying the mathematical property (A.3) results in:

$$\frac{\partial I_k}{\partial V_k} = \frac{\partial}{\partial V_k} \cdot \left(\frac{Q_k}{V_k} \right) = -\frac{Q_k}{V_k^2} \tag{A.78}$$

Therefore, Equations (A.75) to (A.77) results in:

$$\frac{\partial A}{\partial V_k} = sw7 \cdot \left(-\frac{Q_k}{V_k^2} - B_{svc}^{ind} \right) \tag{A.79}$$

$$\frac{\partial B}{\partial V_k} = (1 - sw7) \cdot (1 - sw8) \cdot \left(r \cdot \frac{Q_k}{V_k^2} \right) \tag{A.80}$$

$$\frac{\partial C}{\partial V_k} = sw8 \cdot \left(-\frac{Q_k}{V_k^2} - B_{svc}^{cap} \right) \tag{A.81}$$

Analyzing Equations (A.79) to (A.81), it is assured that the only non-zero differential terms are:

$$\begin{aligned} \frac{\partial y}{\partial V_k} &= \frac{\partial A}{\partial V_k} + \frac{\partial B}{\partial V_k} + \frac{\partial C}{\partial V_k} \\ &= \left[sw7 \cdot \left(-\frac{Q_k}{V_k^2} - B_{svc}^{ind} \right) \right] + \left[sw8 \cdot \left(-\frac{Q_k}{V_k^2} - B_{svc}^{cap} \right) \right] + \\ &+ \left[(1 - sw7) \cdot (1 - sw8) \cdot \left(r \cdot \frac{Q_k}{V_k^2} \right) \right] \end{aligned} \tag{A.82}$$

A.3.2 Differentiating the control equation in terms of $V_{m,\,svc}$

The control equation (A.71) differentiation in terms of V_m is given below:

$$\frac{\partial y}{\partial V_m} = \frac{\partial A}{\partial V_m} + \frac{\partial B}{\partial V_m} + \frac{\partial C}{\partial V_m} \neq 0. \tag{A.83}$$

Applying the mathematical property (A.2) in (A.83) results in:

$$\frac{\partial A}{\partial V_m} = \frac{\partial sw7}{\partial V_m} \cdot \left(I_{k,svc} - V_{k,svc} \cdot B_{svc}^{ind} \right) + \tag{A.84}$$
$$+ \; sw7 \cdot \frac{\partial \left(I_{k,svc} - V_{k,svc} \cdot B_{svc}^{ind} \right)}{\partial V_m}$$

$$\frac{\partial B}{\partial V_m} = \frac{\partial \left(1 - sw7 \right)}{\partial V_m} \cdot \left(1 - sw8 \right) \cdot \left(V_{m,svc} - V_{m,svc}^{ref} - r \cdot I_{k,svc} \right) +$$
$$+ \; \left(1 - sw7 \right) \cdot \frac{\partial \left(1 - sw8 \right)}{\partial V_m} \cdot \left(V_{m,svc} - V_{m,svc}^{ref} - r \cdot I_{k,svc} \right) + \tag{A.85}$$
$$+ \; \left(1 - sw7 \right) \cdot \left(1 - sw8 \right) \cdot \frac{\partial \left(V_{m,svc} - V_{m,svc}^{ref} - r \cdot I_{k,svc} \right)}{\partial V_m}$$

$$\frac{\partial C}{\partial V_m} = \frac{\partial sw8}{\partial V_m} \cdot \left(I_{k,svc} - V_{k,svc} \cdot B_{svc}^{cap} \right) + \tag{A.86}$$
$$+ \; sw8 \cdot \frac{\partial \left(I_{k,svc} - V_{k,svc} \cdot B_{svc}^{cap} \right)}{\partial V_m}$$

Since switches $sw7$ and $sw8$ corresponds to the controlled m-bus voltage magnitude variable, their differentation in terms of V_m do not equal to zero:

$$\frac{\partial sw7}{\partial V_m} = -slp \cdot \left(1 - sw7 \right) \cdot sw7, \tag{A.87}$$

$$\frac{\partial sw8}{\partial V_m} = slp \cdot \left(1 - sw8 \right) \cdot sw8. \tag{A.88}$$

Therefore, Equations (A.84), (A.85) and (A.86) respectively results in:

$$\frac{\partial A}{\partial V_m} = -slp \cdot \left(1 - sw7 \right) \cdot sw7 \cdot \left(I_{k,svc} - V_{k,svc} \cdot B_{svc}^{ind} \right) \tag{A.89}$$

$$\frac{\partial B}{\partial V_m} = \left[1 + slp \cdot \left(1 - sw7 \right) \cdot sw7 \right] \cdot \left(1 - sw8 \right) \cdot \left(V_{m,svc} - V_{m,svc}^{ref} - r \cdot I_{k,svc} \right) + \tag{A.90}$$
$$+ \; \left(1 - sw7 \right) \cdot \left[1 - slp \cdot \left(1 - sw8 \right) \cdot sw8 \right] \cdot \left(V_{m,svc} - V_{m,svc}^{ref} - r \cdot I_{k,svc} \right) +$$
$$+ \; \left(1 - sw7 \right) \cdot \left(1 - sw8 \right) \cdot 1$$

$$\frac{\partial C}{\partial V_m} = slp \cdot (1 - sw8) \cdot sw8 \cdot (I_{k,\,svc} - V_{k,\,svc} \cdot B_{svc}^{cap}) \tag{A.91}$$

Therefore, by analyzing Equations (A.89) through (A.91), the control equation differentiation in terms of $V_{m,\,svc}$ is defined:

$$\frac{\partial y}{\partial V_m} = \frac{\partial A}{\partial V_m} + \frac{\partial B}{\partial V_m} + \frac{\partial C}{\partial V_m} \tag{A.92}$$

A.3.3 Differentiating the control equation in terms of $I_{k,\,svc}$

The control equation (A.71) differentiation in terms of I_k is given below:

$$\frac{\partial y}{\partial I_k} = \frac{\partial A}{\partial I_k} + \frac{\partial B}{\partial I_k} + \frac{\partial C}{\partial I_k} \neq 0. \tag{A.93}$$

Applying the mathematical property (A.2) in (A.93) results in:

$$\begin{aligned}
\frac{\partial A}{\partial I_k} &= \frac{\partial sw7}{\partial I_k} \cdot \left(I_{k,\,svc} - V_{k,\,svc} \cdot B_{svc}^{ind}\right) + \\
&+ sw7 \cdot \frac{\partial \left(I_{k,\,svc} - V_{k,\,svc}^2 \cdot B_{svc}^{ind}\right)}{\partial I_k}
\end{aligned} \tag{A.94}$$

$$\begin{aligned}
\frac{\partial B}{\partial I_k} &= \frac{\partial (1 - sw7)}{\partial I_k} \cdot (1 - sw8) \cdot \left(V_{m,\,svc} - V_{m,\,svc}^{ref} - r \cdot I_{k,\,svc}\right) + \\
&+ (1 - sw7) \cdot \frac{\partial (1 - sw8)}{\partial I_k} \cdot \left(V_{m,\,svc} - V_{m,\,svc}^{ref} - r \cdot I_{k,\,svc}\right) + \\
&+ (1 - sw7) \cdot (1 - sw8) \cdot \frac{\partial \left(V_{m,\,svc} - V_{m,\,svc}^{ref} - r \cdot I_{k,\,svc}\right)}{\partial I_k}
\end{aligned} \tag{A.95}$$

$$\begin{aligned}
\frac{\partial C}{\partial I_k} &= \frac{\partial sw8}{\partial I_k} \cdot (I_{k,\,svc} - V_{k,\,svc} \cdot B_{svc}^{cap}) + \\
&+ sw8 \cdot \frac{\partial (I_{k,\,svc} - V_{k,\,svc} \cdot B_{svc}^{cap})}{\partial I_k}
\end{aligned} \tag{A.96}$$

Since switches $sw7$ and $sw8$ corresponds to the controlled m-bus voltage magnitude variable, their differentiation in terms of I_k equals to zero. Therefore, analyzing Equations (A.94) to (A.96), it is assured that the only non-zero differential terms are:

$$\begin{aligned}
\frac{\partial y}{\partial I_k} &= \frac{\partial A}{\partial I_k} + \frac{\partial B}{\partial I_k} + \frac{\partial C}{\partial I_k} \\
&= sw7 - r \cdot (1 - sw7) \cdot (1 - sw8) + sw8
\end{aligned} \tag{A.97}$$

A.3.4 Differentiating the state equations in terms of $I_{k,\,svc}$

Differentiating the PF state equations, which define each bus active and reactive power injections values ($\boldsymbol{P}$ and $\boldsymbol{Q}$), in terms of the new state variable $I_{k,\,svc}$ - which is equivalent to I_k - results in:

$$\frac{\partial P_k}{\partial I_{k,\,svc}} = \frac{\partial P_k}{\partial I_k} = \frac{\partial \left[P_k^{cal} - (P_{G_k} - P_{L_k}) \right]}{\partial I_k} = 0 \tag{A.98}$$

$$\frac{\partial P_m}{\partial I_{k,\,svc}} = \frac{\partial P_m}{\partial I_k} = \frac{\partial \left[P_m^{cal} - (P_{G_m} - P_{L_m}) \right]}{\partial I_k} = 0 \tag{A.99}$$

$$\frac{\partial Q_k}{\partial I_{k,\,svc}} = \frac{\partial Q_k}{\partial I_k} = \frac{\partial \left[Q_k^{cal} - (Q_{G_k} - Q_{L_k}) \right]}{\partial I_k} = -V_k \tag{A.100}$$

$$\frac{\partial Q_m}{\partial I_{k,\,svc}} = \frac{\partial Q_m}{\partial I_k} = \frac{\partial \left[Q_m^{cal} - (Q_{G_m} - Q_{L_m}) \right]}{\partial I_k} = 0 \tag{A.101}$$

An additional differential term must also be considered in the Jacobian matrix. This new differential term is the SVC reactive power generated (5.9) by it bus voltage magnitude, and must be added to the pre-existing term:

$$\frac{\partial Q_k}{\partial V_k} = \frac{\partial Q_k}{\partial V_k} + \frac{\partial \left[Q_k^{cal} - (Q_{G_k,\,svc} - Q_{L_k}) \right]}{\partial V_{k,\,svc}} = \frac{\partial Q_k}{\partial V_k} - (I_{k,\,svc}) \tag{A.102}$$

A.3.5 Augmented Jacobian matrix

The augmented Jacobian matrix values detailed in Equation (5.13) are simplified in (A.103). For the steady-state SPF-SVC current injection methodology, the new differential terms are given in Equations (A.82), (A.92), (A.97), (A.100) and (A.102).

$$
\begin{bmatrix}
\vdots \\
\Delta P_k \\
\Delta P_m \\
\vdots \\
\Delta Q_k \\
\Delta Q_m \\
\vdots \\
\Delta y \\
\vdots
\end{bmatrix}
=
\begin{bmatrix}
\ddots & \vdots & \vdots & \cdots & \vdots & \vdots & \cdots & \vdots & \iddots \\
\cdots & \frac{\partial P_k}{\partial \theta_k} & \frac{\partial P_k}{\partial \theta_m} & \cdots & \frac{\partial P_k}{\partial V_k} & \frac{\partial P_k}{\partial V_m} & \cdots & 0 & \cdots \\
\cdots & \frac{\partial P_m}{\partial \theta_k} & \frac{\partial P_m}{\partial \theta_m} & \cdots & \frac{\partial P_m}{\partial V_k} & \frac{\partial P_m}{\partial V_m} & \cdots & 0 & \cdots \\
\cdots & \vdots & \vdots & \cdots & \vdots & \vdots & \cdots & \vdots & \cdots \\
\cdots & \frac{\partial Q_k}{\partial \theta_k} & \frac{\partial Q_k}{\partial \theta_m} & \cdots & \frac{\partial Q_k}{\partial V_k} & \frac{\partial Q_k}{\partial V_m} & \cdots & \frac{\partial Q_k}{\partial I_{k,svc}} & \cdots \\
\cdots & \frac{\partial Q_m}{\partial \theta_k} & \frac{\partial Q_m}{\partial \theta_m} & \cdots & \frac{\partial Q_m}{\partial V_k} & \frac{\partial Q_m}{\partial V_m} & \cdots & 0 & \cdots \\
\cdots & \vdots & \vdots & \cdots & \vdots & \vdots & \cdots & \vdots & \cdots \\
\cdots & 0 & 0 & \cdots & \frac{\partial y}{\partial V_k} & \frac{\partial y}{\partial V_m} & \cdots & \frac{\partial y}{\partial I_{k,svc}} & \cdots \\
\iddots & \vdots & \vdots & \cdots & \vdots & \vdots & \cdots & \vdots & \ddots
\end{bmatrix}
\cdot
\begin{bmatrix}
\vdots \\
\Delta \theta_k \\
\Delta \theta_m \\
\vdots \\
\Delta V_k \\
\Delta V_m \\
\vdots \\
\Delta I_{k,svc} \\
\vdots
\end{bmatrix}
\tag{A.103}
$$

A.4   SPF-SVC THYRISTOR FIRING-ANGLE METHODOLOGY

The SPF-SVC thyristor firing-angle control equation (5.21) will be subdivided into three terms, following:

$$
y = A + B + C, \tag{A.104}
$$

where:

$$
\begin{aligned}
A &= sw10 \cdot (1 - sw12) \cdot (\alpha_{k,svc} - 90°) \\
B &= \Big[sw11 \cdot (1 - sw10) \cdot (1 - sw12) + sw12 \cdot (1 - sw9) \cdot (1 - sw11) \cdots \\
&\quad + (1 - sw9) \cdot (1 - sw10) \cdot (1 - sw11) \cdot (1 - sw12) \Big] \cdot \left(V_{m,svc} - V_{m,svc}^{ref} - r \cdot Q_{G_k,svc} \right) \\
C &= sw9 \cdot (1 - sw11) \cdot (\alpha_{k,svc} - 180°)
\end{aligned}
\tag{A.105}
$$

As detailed in Equations (5.18) and (5.21), the only active state variables in the proposed methodologies are $V_{k,svc}$, $V_{m,svc}$ and $\alpha_{k,svc}$, which corresponds to V_k, V_m and α_k, respectively. Therefore, differentiating the control equation y in terms of θ_k or θ_m are equal to zero.

$$
\frac{\partial y}{\partial \theta_k} = \frac{\partial A}{\partial \theta_k} + \frac{\partial B}{\partial \theta_k} + \frac{\partial C}{\partial \theta_k} = 0 \tag{A.106}
$$

$$
\frac{\partial y}{\partial \theta_m} = \frac{\partial A}{\partial \theta_m} + \frac{\partial B}{\partial \theta_m} + \frac{\partial C}{\partial \theta_m} = 0 \tag{A.107}
$$

It remains only to differentiate the control equation in terms of $V_{k,\,svc}$, $V_{m,\,svc}$ and $\alpha_{k,\,svc}$, as well as differentiating the state equations in terms of the new state variable. These new differential terms will be detailed in the following subsections.

A.4.1   **Differentiating the control equation in terms of $V_{k,\,svc}$**

The control equation (A.105) differentiation in terms of V_k is given below:

$$\frac{\partial y}{\partial V_k} = \frac{\partial A}{\partial V_k} + \frac{\partial B}{\partial V_k} + \frac{\partial C}{\partial V_k} \neq 0. \tag{A.108}$$

Applying the mathematical property (A.2) in (A.108) results in:

$$\begin{aligned}
\frac{\partial A}{\partial V_k} = {}& \frac{\partial sw10}{\partial V_k} \cdot (1 - sw12) \cdot (\alpha_{k,\,svc} - 90°) + \\
& + sw10 \cdot \frac{\partial (1 - sw12)}{\partial V_k} \cdot (\alpha_{k,\,svc} - 90°) + \\
& + sw10 \cdot (1 - sw12) \cdot \frac{\partial (\alpha_{k,\,svc} - 90°)}{\partial V_k}
\end{aligned} \tag{A.109}$$

$$\begin{aligned}
\frac{\partial B}{\partial V_k} = {}& \frac{\partial}{\partial V_k} \cdot \Big[sw11 \cdot (1 - sw10) \cdot (1 - sw12) + sw12 \cdot (1 - sw9) \cdot (1 - sw11) \cdots \\
& + (1 - sw9) \cdot (1 - sw10) \cdot (1 - sw11) \cdot (1 - sw12) \Big] \cdot \Big(V_{m,\,svc} - V_{m,\,svc}^{ref} - r \cdot Q_{G_k,\,svc} \Big)
\end{aligned} \tag{A.110}$$

$$\begin{aligned}
\frac{\partial C}{\partial V_k} = {}& \frac{\partial sw9}{\partial V_k} \cdot (1 - sw11) \cdot (\alpha_{k,\,svc} - 180°) + \\
& + sw9 \cdot \frac{\partial (1 - sw11)}{\partial V_k} \cdot (\alpha_{k,\,svc} - 180°) + \\
& + sw9 \cdot (1 - sw11) \cdot \frac{\partial (\alpha_{k,\,svc} - 180°)}{\partial V_k}
\end{aligned} \tag{A.111}$$

Since switches *sw9* and *sw10* corresponds to the thyristor firing-angle variable, and switches *sw11* and *sw12* corresponds to the controlled m-bus voltage magnitude variable, their differentation in terms of V_k equals to zero. Also, the B-term in (A.39) does not differentiate in terms of V_k. Therefore, given (5.18):

$$\frac{\partial A}{\partial V_k} = 0 \tag{A.112}$$

$$\frac{\partial B}{\partial V_k} = \Big[sw11 \cdot (1 - sw10) \cdot (1 - sw12) + sw12 \cdot (1 - sw9) \cdot (1 - sw11) \cdots \quad \text{(A.113)}$$

$$+ \ (1 - sw9) \cdot (1 - sw10) \cdot (1 - sw11) \cdot (1 - sw12) \Big] \cdot \Big[-r \cdot \frac{\partial Q_{G_k, svc}}{\partial V_k} \Big]$$

$$\frac{\partial C}{\partial V_k} = 0 \qquad\qquad\qquad \text{(A.114)}$$

where:

$$\frac{\partial Q_{G_k, svc}}{\partial V_k} = \frac{\partial V_{k, svc}^2}{\partial V_k} \cdot b_{eq}\,(\alpha_{k, svc}) = 2 \cdot V_{k, svc} \cdot b_{eq}\,(\alpha_{k, svc}). \qquad \text{(A.115)}$$

Analyzing Equations (A.112) to (A.114), it is assured that the only non-zero differential terms is:

$$\frac{\partial y}{\partial V_k} = \frac{\partial B}{\partial V_k} = \Big[sw11 \cdot (1 - sw10) \cdot (1 - sw12) + sw12 \cdot (1 - sw9) \cdot (1 - sw11) \cdots$$

$$\text{(A.116)}$$

$$+ \ (1 - sw9) \cdot (1 - sw10) \cdot (1 - sw11) \cdot (1 - sw12) \Big] \cdot \left[-2 \cdot r \cdot V_{k, svc} \cdot b_{eq}\,(\alpha_{k, svc}) \right]$$

A.4.2 Differentiating the control equation in terms of $V_{m, svc}$

The control equation (A.105) differentiation in terms of V_m is given below:

$$\frac{\partial y}{\partial V_m} = \frac{\partial A}{\partial V_m} + \frac{\partial B}{\partial V_m} + \frac{\partial C}{\partial V_m} \neq 0. \qquad \text{(A.117)}$$

Applying the mathematical property (A.2) in (A.117) results in:

$$\frac{\partial A}{\partial V_m} = \frac{\partial sw10}{\partial V_m} \cdot (1 - sw12) \cdot (\alpha_{k, svc} - 90°) +$$

$$+ \ sw10 \cdot \frac{\partial \,(1 - sw12)}{\partial V_m} \cdot (\alpha_{k, svc} - 90°) + \qquad \text{(A.118)}$$

$$+ \ sw10 \cdot (1 - sw12) \cdot \frac{\partial \,(\alpha_{k, svc} - 90°)}{\partial V_m}$$

$$\frac{\partial B}{\partial V_m} = \frac{\partial}{\partial V_m} \cdot \Big[sw11 \cdot (1 - sw10) \cdot (1 - sw12) + sw12 \cdot (1 - sw9) \cdot (1 - sw11) \cdots$$

$$\text{(A.119)}$$

$$+ \ (1 - sw9) \cdot (1 - sw10) \cdot (1 - sw11) \cdot (1 - sw12) \Big] \cdot \Big(V_{m, svc} - V_{m, svc}^{ref} - r \cdot Q_{G_k, svc} \Big)$$

$$\frac{\partial C}{\partial V_m} = \frac{\partial sw9}{\partial V_m} \cdot (1 - sw11) \cdot (\alpha_{k,\,svc} - 180°) +$$
$$+ \; sw9 \cdot \frac{\partial (1 - sw11)}{\partial V_m} \cdot (\alpha_{k,\,svc} - 180°) + \qquad \text{(A.120)}$$
$$+ \; sw9 \cdot (1 - sw11) \cdot \frac{\partial (\alpha_{k,\,svc} - 180°)}{\partial V_m}$$

Since switches $sw11$ and $sw12$ corresponds to the controlled m-bus voltage magnitude variable, their differentiation in terms of V_m do not equal to zero. However, switches as $sw9$ and $sw10$ corresponds to the thyristor firing-angle variable, their differentation in terms of V_m are null:

$$\frac{\partial sw9}{\partial V_m} = 0, \qquad \text{(A.121)}$$

$$\frac{\partial sw10}{\partial V_m} = 0, \qquad \text{(A.122)}$$

$$\frac{\partial sw11}{\partial V_m} = -slp \cdot (1 - sw11) \cdot sw11, \qquad \text{(A.123)}$$

$$\frac{\partial sw12}{\partial V_m} = slp \cdot (1 - sw12) \cdot sw12. \qquad \text{(A.124)}$$

Therefore, Equations (A.118), (A.119) and (A.120) respectively results in:

$$\frac{\partial A}{\partial V_m} = sw10 \cdot [1 - slp \cdot (1 - sw12) \cdot sw12] \cdot (\alpha_{k,\,svc} - 90°) \qquad \text{(A.125)}$$

$$\frac{\partial B}{\partial V_m} = [-slp \cdot (1 - sw11) \cdot sw11] \cdot (1 - sw10) \cdot (1 - sw12) \cdot \left(V_{m,\,svc} - V_{m,\,svc}^{ref} - r \cdot Q_{G_k,\,svc} \right) +$$
$$\text{(A.126)}$$
$$+ \; sw11 \cdot (1 - sw10) \cdot [1 - slp \cdot (1 - sw12) \cdot sw12] \cdot \left(V_{m,\,svc} - V_{m,\,svc}^{ref} - r \cdot Q_{G_k,\,svc} \right) +$$
$$+ \; [slp \cdot (1 - sw12) \cdot sw12] \cdot (1 - sw9) \cdot (1 - sw11) \cdot \left(V_{m,\,svc} - V_{m,\,svc}^{ref} - r \cdot Q_{G_k,\,svc} \right) +$$
$$+ \; sw12 \cdot (1 - sw9) \cdot [1 + slp \cdot (1 - sw11) \cdot sw11] \cdot \left(V_{m,\,svc} - V_{m,\,svc}^{ref} - r \cdot Q_{G_k,\,svc} \right) +$$
$$+ \; [sw11 \cdot (1 - sw10) \cdot (1 - sw12) + sw12 \cdot (1 - sw9) \cdot (1 - sw11) \cdots$$
$$+ \; (1 - sw9) \cdot (1 - sw10) \cdot (1 - sw11) \cdot (1 - sw12)] \cdot 1$$

$$\frac{\partial C}{\partial V_m} = sw9 \cdot [1 + \text{slp} \cdot (1 - sw11) \cdot sw11] \cdot (\alpha_{k,\,svc} - 180°) \tag{A.127}$$

Therefore, by analyzing Equations (A.125) through (A.127), the control equation differentiation in terms of $V_{m,\,svc}$ is defined:

$$\frac{\partial y}{\partial V_m} = \frac{\partial A}{\partial V_m} + \frac{\partial B}{\partial V_m} + \frac{\partial C}{\partial V_m} \tag{A.128}$$

A.4.3 Differentiating the control equation in terms of $\alpha_{k,\,svc}$

The control equation (A.105) differentiation in terms of α_k is given below:

$$\frac{\partial y}{\partial \alpha_k} = \frac{\partial A}{\partial \alpha_k} + \frac{\partial B}{\partial \alpha_k} + \frac{\partial C}{\partial \alpha_k} \neq 0. \tag{A.129}$$

Applying the mathematical property (A.2) in (A.129) results in:

$$\begin{aligned}
\frac{\partial A}{\partial \alpha_k} &= \frac{\partial sw10}{\partial \alpha_k} \cdot (1 - sw12) \cdot (\alpha_{k,\,svc} - 90°) + \\
&\quad + sw10 \cdot \frac{\partial (1 - sw12)}{\partial \alpha_k} \cdot (\alpha_{k,\,svc} - 90°) + \\
&\quad + sw10 \cdot (1 - sw12) \cdot \frac{\partial (\alpha_{k,\,svc} - 90°)}{\partial \alpha_k}
\end{aligned} \tag{A.130}$$

$$\begin{aligned}
\frac{\partial B}{\partial \alpha_k} &= \frac{\partial}{\partial \alpha_k} \cdot \Big[sw11 \cdot (1 - sw10) \cdot (1 - sw12) + sw12 \cdot (1 - sw9) \cdot (1 - sw11) \cdots \\
&\quad + (1 - sw9) \cdot (1 - sw10) \cdot (1 - sw11) \cdot (1 - sw12) \Big] \cdot \left(V_{m,\,svc} - V_{m,\,svc}^{ref} - r \cdot Q_{G_k,\,svc} \right)
\end{aligned} \tag{A.131}$$

$$\begin{aligned}
\frac{\partial C}{\partial \alpha_k} &= \frac{\partial sw9}{\partial \alpha_k} \cdot (1 - sw11) \cdot (\alpha_{k,\,svc} - 180°) + \\
&\quad + sw9 \cdot \frac{\partial (1 - sw11)}{\partial \alpha_k} \cdot (\alpha_{k,\,svc} - 180°) + \\
&\quad + sw9 \cdot (1 - sw11) \cdot \frac{\partial (\alpha_{k,\,svc} - 180°)}{\partial \alpha_k}
\end{aligned} \tag{A.132}$$

Since switches *sw9* and *sw10* corresponds to the thyristor firing-angle variable, their differentiation in terms of α_k does not equals to zero. However, as switches *sw11* and

$sw12$ corresponds to the controlled m-bus voltage magnitude variable, their differentiation in terms of α_k are null:

$$\frac{\partial sw9}{\partial \alpha_k} = -slp \cdot (1 - sw9) \cdot sw9, \tag{A.133}$$

$$\frac{\partial sw10}{\partial \alpha_k} = slp \cdot (1 - sw10) \cdot sw10, \tag{A.134}$$

$$\frac{\partial sw11}{\partial \alpha_k} = 0, \tag{A.135}$$

$$\frac{\partial sw12}{\partial \alpha_k} = 0. \tag{A.136}$$

Therefore, Equations (A.130), (A.131) and (A.132) respectively results in:

$$\frac{\partial A}{\partial \alpha_k} = [slp \cdot (1 - sw10) \cdot sw10] \cdot (1 - sw12) \cdot (\alpha_{k,svc} - 90°)+ \tag{A.137}$$
$$+ \ sw10 \cdot (1 - sw12) \cdot 1$$

$$\frac{\partial B}{\partial \alpha_k} = sw11 \cdot [1 - slp \cdot (1 - sw10) \cdot sw10] \cdot (1 - sw12) \cdot \left(V_{m,svc} - V_{m,svc}^{ref} - r \cdot Q_{G_k,svc}\right)+ \tag{A.138}$$
$$+ \ sw12 \cdot [1 + slp \cdot (1 - sw9) \cdot sw9] \cdot (1 - sw11) \cdot \left(V_{m,svc} - V_{m,svc}^{ref} - r \cdot Q_{G_k,svc}\right)+$$
$$+ \ [1 + slp \cdot (1 - sw9) \cdot sw9] \cdot (1 - sw10) \cdot (1 - sw11) \cdot (1 - sw12) \cdot \left(V_{m,svc} - V_{m,svc}^{ref} - r \cdot Q_{G_k,svc}\right)+$$
$$+ \ (1 - sw9) \cdot [1 - slp \cdot (1 - sw10) \cdot sw10] \cdot (1 - sw11) \cdot (1 - sw12) \cdot \left(V_{m,svc} - V_{m,svc}^{ref} - r \cdot Q_{G_k,svc}\right)+$$
$$+ \ [sw11 \cdot (1 - sw10) \cdot (1 - sw12) + sw12 \cdot (1 - sw9) \cdot (1 - sw11) \cdots$$
$$+ \ (1 - sw9) \cdot (1 - sw10) \cdot (1 - sw11) \cdot (1 - sw12)] \cdot \left[-r \cdot \frac{\partial Q_{G_k,svc}}{\partial \alpha_k}\right]$$

$$\frac{\partial C}{\partial \alpha_k} = [-slp \cdot (1 - sw9) \cdot sw9] \cdot (1 - sw11) \cdot (\alpha_{k,svc} - 180°)+ \tag{A.139}$$
$$+ \ sw9 \cdot (1 - sw11) \cdot 1$$

where, from Equations (2.23), (2.24) and (5.18):

$$\frac{\partial Q_{G_k, svc}}{\partial \alpha_k} = V_{k, svc}^2 \cdot \frac{\partial b_{eq}\left(\alpha_{k, svc}\right)}{\partial \alpha_k} = V_{k, svc}^2 \cdot \left[\frac{2 - 2 \cdot \cos\left(2 \cdot \alpha_{k, svc}\right)}{\pi \cdot X_L}\right] \qquad \text{(A.140)}$$

Therefore, by analyzing Equations (A.137) through (A.139), the control equation differentiation in terms of $\alpha_{k, svc}$ is defined:

$$\frac{\partial y}{\partial \alpha_k} = \frac{\partial A}{\partial \alpha_k} + \frac{\partial B}{\partial \alpha_k} + \frac{\partial C}{\partial \alpha_k} \qquad \text{(A.141)}$$

A.4.4 Differentiating the state equations in terms of $\alpha_{k, svc}$

Differentiating the PF state equations, which define each bus active and reactive power injections value ($\boldsymbol{P}$ and $\boldsymbol{Q}$), in terms of the new state variable $\alpha_{k, svc}$ - which is equivalent to α_k - results in:

$$\frac{\partial P_k}{\partial \alpha_{k, svc}} = \frac{\partial P_k}{\partial \alpha_k} = \frac{\partial \left[P_k^{cal} - \left(P_{G_k} - P_{L_k}\right)\right]}{\partial \alpha_k} = 0 \qquad \text{(A.142)}$$

$$\frac{\partial P_m}{\partial \alpha_{k, svc}} = \frac{\partial P_m}{\partial \alpha_k} = \frac{\partial \left[P_m^{cal} - \left(P_{G_m} - P_{L_m}\right)\right]}{\partial \alpha_k} = 0 \qquad \text{(A.143)}$$

$$\frac{\partial Q_k}{\partial \alpha_{k, svc}} = \frac{\partial Q_k}{\partial \alpha_k} = \frac{\partial \left[Q_k^{cal} - \left(Q_{G_k} - Q_{L_k}\right)\right]}{\partial \alpha_k} = -V_{k, svc}^2 \frac{\partial b_{eq}\left(\alpha_{k, svc}\right)}{\partial \alpha_k} \qquad \text{(A.144)}$$

$$\frac{\partial Q_m}{\partial \alpha_{k, svc}} = \frac{\partial Q_m}{\partial \alpha_k} = \frac{\partial \left[Q_m^{cal} - \left(Q_{G_m} - Q_{L_m}\right)\right]}{\partial \alpha_k} = 0 \qquad \text{(A.145)}$$

An additional differential term must also be considered in the Jacobian matrix. This new differential term is the SVC reactive power generated (5.18) by it bus voltage magnitude, and must be added to the pre-existing term:

$$\frac{\partial Q_k}{\partial V_k} = \frac{\partial Q_k}{\partial V_k} + \frac{\partial \left[Q_k^{cal} - \left(Q_{G_k, svc} - Q_{L_k}\right)\right]}{\partial V_{k, svc}} = \frac{\partial Q_k}{\partial V_k} - \left[2 \cdot V_{k, svc} \cdot b_{eq}\left(\alpha_{k, svc}\right)\right] \qquad \text{(A.146)}$$

A.4.5 **Augmented Jacobian matrix**

The augmented Jacobian matrix values detailed in Equation (5.22) are simplified in (A.147). For the steady-state SPF-SVC thyristor firing-angle methodology, the new differential terms are given in Equations (A.116), (A.128), (A.141), (A.144) and (A.146).

$$
\begin{bmatrix}
\vdots \\
\Delta P_k \\
\Delta P_m \\
\vdots \\
\Delta Q_k \\
\Delta Q_m \\
\vdots \\
\Delta y \\
\vdots
\end{bmatrix}
=
\begin{bmatrix}
\ddots & \vdots & \vdots & \cdots & \vdots & \vdots & \cdots & \vdots & \iddots \\
\cdots & \frac{\partial P_k}{\partial \theta_k} & \frac{\partial P_k}{\partial \theta_m} & \cdots & \frac{\partial P_k}{\partial V_k} & \frac{\partial P_k}{\partial V_m} & \cdots & 0 & \cdots \\
\cdots & \frac{\partial P_m}{\partial \theta_k} & \frac{\partial P_m}{\partial \theta_m} & \cdots & \frac{\partial P_m}{\partial V_k} & \frac{\partial P_m}{\partial V_m} & \cdots & 0 & \cdots \\
\cdots & \vdots & \vdots & \cdots & \vdots & \vdots & \cdots & \vdots & \cdots \\
\cdots & \frac{\partial Q_k}{\partial \theta_k} & \frac{\partial Q_k}{\partial \theta_m} & \cdots & \frac{\partial Q_k}{\partial V_k} & \frac{\partial Q_k}{\partial V_m} & \cdots & \frac{\partial Q_k}{\partial \alpha_{k,svc}} & \cdots \\
\cdots & \frac{\partial Q_m}{\partial \theta_k} & \frac{\partial Q_m}{\partial \theta_m} & \cdots & \frac{\partial Q_m}{\partial V_k} & \frac{\partial Q_m}{\partial V_m} & \cdots & 0 & \cdots \\
\cdots & \vdots & \vdots & \cdots & \vdots & \vdots & \cdots & \vdots & \cdots \\
\cdots & 0 & 0 & \cdots & \frac{\partial y}{\partial V_k} & \frac{\partial y}{\partial V_m} & \cdots & \frac{\partial y}{\partial \alpha_{k,svc}} & \cdots \\
\iddots & \vdots & \vdots & \cdots & \vdots & \vdots & \cdots & \vdots & \ddots
\end{bmatrix}
\cdot
\begin{bmatrix}
\vdots \\
\Delta \theta_k \\
\Delta \theta_m \\
\vdots \\
\Delta V_k \\
\Delta V_m \\
\vdots \\
\Delta \alpha_{k,svc} \\
\vdots
\end{bmatrix}
\tag{A.147}
$$

APPENDIX B – THE CONTINUATION POWER FLOW

The CPF formulation considers the simulation of successive PF solutions. For each PF simulation, an increase on the system's overall load is implemented. This condition is mathematically represented by (B.1), where the loading parameter variation variable λ is incorporated into the traditional PF formulation equation.

$$\boldsymbol{f}\left(\boldsymbol{\theta}, \boldsymbol{V}, \lambda\right) = \boldsymbol{0} \tag{B.1}$$

On account of the loading parameter variable, the simulated MLP of a system's is labeled as λ^{crit}, as shown in (B.2). Several techniques have already been proposed in the literature with the goal of achieving a system's MLP (AJJARAPU; CHRISTY, 1992; CHIANG *et al.*, 1995; MILANO, 2010). Nevertheless, for every proposed methodology, an alteration on the system's loading capacity and generation are considered (AJJARAPU; CHRISTY, 1992). The active power demand and reactive power demand must vary in accordance to the adopted loading parameter as stated by Equations (B.3a) and (B.4a), respectively. Notice that (B.3b) and (B.4b) are simplifications of (B.3a) and (B.4a), respectively.

$$0 \leq \lambda \leq \lambda^{crit} \tag{B.2}$$

$$P_{L_k} = P_{L_k}^0 + \lambda \cdot \left(\gamma_k \cdot S_B \cdot cos\phi_k\right) \quad \text{(B.3a)} \qquad P_{L_k} = P_{L_k}^0 \cdot \left(1 + \lambda\right) \tag{B.3b}$$

$$Q_{L_k} = Q_{L_k}^0 + \lambda \cdot \left(\gamma_k \cdot S_B \cdot sin\phi_k\right) \quad \text{(B.4a)} \qquad Q_{L_k} = Q_{L_k}^0 \cdot \left(1 + \lambda\right) \tag{B.4b}$$

An additional variation on the active power generation variable can also be considered, as shown by (B.5). This is due the understanding of how PV-type buses can actively participate in the active power generation balance together with the Slack bus. Notice a non necessity of reactive generation variable variation once PV and Slack buses already participate in the reactive power generation balance.

$$P_{G_k} = P_{G_k}^0 \cdot \left(1 + \beta_k \cdot \Delta P_{L,\lambda}^{sys}\right) \tag{B.5}$$

Despite the different techniques, the CPF methodology main implementation objective is to analyze a given system's stable and unstable behavior. The stable behavior, or stability region of a CPF simulation, is defined by the variation of the loading parameter

until the critical value, or voltage collapse, is reached. On the other hand, the unstable behavior, or instability region of a CPF simulation, is defined by the simulation of a system's behavior after the MLP is reached.

Considering that the CPF implementation defines the voltage stability of a given electrical power system, it is important to understand how buses' voltage magnitude varies while load increments. A general illustration of a PV-curve, "nose" curve or a bus voltage magnitude variation in terms of loading parameter variation is shown in Figure 61.

Figure 61 – The well-known continuation power flow PV-curve.
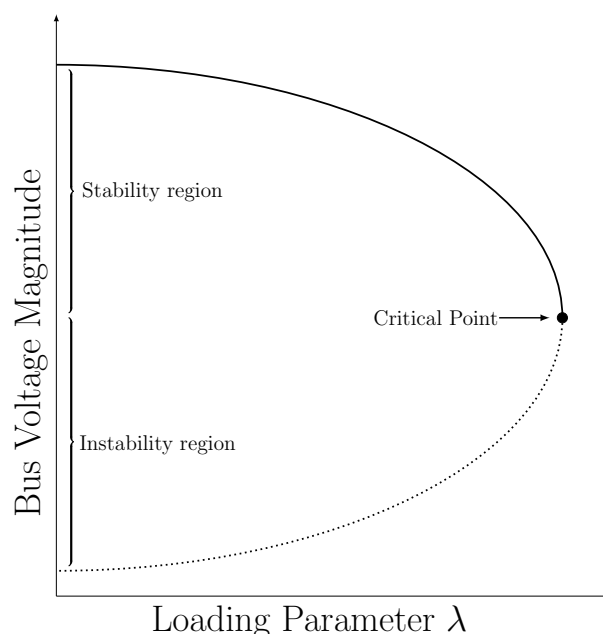
Source: Adapted from (AJJARAPU; CHRISTY, 1992; CORSI; TARANTO, 2007; CHIANG *et al.*, 1995).

In the ideal example illustrated by Figure 61 the stability region, instability region and MLP are well defined. Considering the stability region, an important characteristic related to a system's VSM can be made. The VSM is defined by the loading parameter variation until the system's collapses, being very useful on expansion planning problems and VSA.

The CPF is of great importance for power flow studies and VSA. It is known that different electrical power system's possess different behaviors (CORSI; TARANTO, 2007). Therefore, for correct simulation it is crucial to have a well implemented CPF algorithm.

In the Section B.1 will be detailed the Prediction-Correction methodology proposed by Ajjarapu and Christy (1992), which was implemented in the Python program developed in this research.

B.1   THE PREDICTION-CORRECTION METHODOLOGY

The main methodology by which the CPF is based on consists in prediction and correction steps, as illustrated in Figure 62 (AJJARAPU; CHRISTY, 1992). The CPF initiates with the PF solution for the base case, which is interpreted as the first correction step, followed by a sequence of prediction and correction steps.

Figure 62 – Predicton-Correction methodology implemented in the continuation power flow.
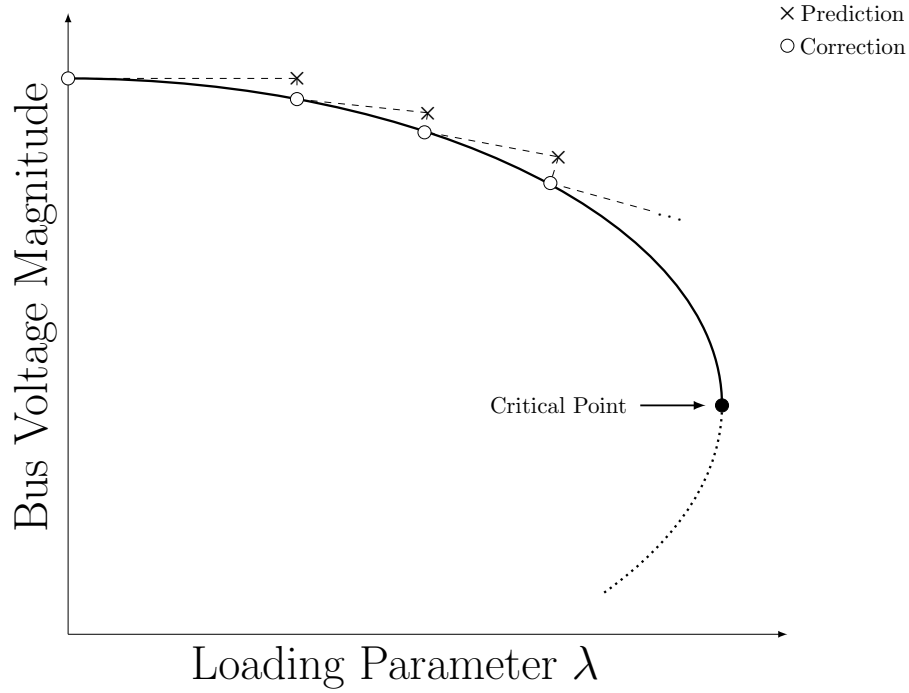
Source: Adapted from Ajjarapu and Christy (1992).

The prediction step consists on finding a solution tangent to the previously solved and converged PF system, considering an increment on the loading parameter λ. This is accomplished by differentiating the power flow system of equations (B.1):

$$\partial \left[\boldsymbol{f} \left(\boldsymbol{\theta}, \boldsymbol{V}, \lambda \right) \right] = \boldsymbol{f_\theta} \cdot \Delta \boldsymbol{\theta} + \boldsymbol{f_V} \cdot \Delta \boldsymbol{V} + \boldsymbol{f_\lambda} \cdot \Delta \lambda = 0. \tag{B.6}$$

On account of the loading parameter, which is considered as a new state variable, a new control equation must be linearized and incorporated into the system of nonlinear equations. During the prediction step, the Jacobian matrix is then reconfigured as following:

$$\begin{bmatrix} \mathbf{J}_{P\theta} & \mathbf{J}_{PV} & \mathbf{J}_{P\lambda} \\ \mathbf{J}_{Q\theta} & \mathbf{J}_{QV} & \mathbf{J}_{Q\lambda} \\ \mathbf{J}_{Y_\lambda\theta} & \mathbf{J}_{Y_\lambda V} & \mathbf{J}_{Y_\lambda\lambda} \end{bmatrix} \cdot \begin{bmatrix} \Delta\boldsymbol{\theta} \\ \Delta\boldsymbol{V} \\ \Delta\lambda \end{bmatrix}^{pred} = \begin{bmatrix} \mathbf{0} \\ \mathbf{0} \\ \lambda^{step} \end{bmatrix}^{pred} \tag{B.7}$$

The Equation (B.7) is a simplification of (B.6), considering λ^{step} as the loading parameter step variation. Notice in (B.7) the active power and reactive power residues are null in the column-matrix of state variables vectors. This condition is set during the predicition step so as to find solution for the nonlinear system of equations in terms only of the loading parameter step variable. The solution of (B.7) results in the tangent vector $\boldsymbol{t}$. The tangent vector will then be added to the previously solved and converged PF solution, in order to find the prediction solution.

$$
\boldsymbol{t} = \begin{bmatrix} \boldsymbol{\Delta\theta} \\ \boldsymbol{\Delta V} \\ \Delta\lambda \end{bmatrix}^{pred} = \begin{bmatrix} \mathbf{0} \\ \mathbf{0} \\ \lambda^{step} \end{bmatrix}^{pred} \cdot \begin{bmatrix} \mathbf{J}_{P\theta} & \mathbf{J}_{PV} & \mathbf{J}_{P\lambda} \\ \mathbf{J}_{Q\theta} & \mathbf{J}_{QV} & \mathbf{J}_{Q\lambda} \\ \mathbf{J}_{Y_\lambda\theta} & \mathbf{J}_{Y_\lambda V} & \mathbf{J}_{Y_\lambda\lambda} \end{bmatrix}^{-1}
\tag{B.8}
$$

$$
\begin{bmatrix} \boldsymbol{\theta^h} \\ \boldsymbol{V^h} \\ \lambda^h \end{bmatrix}^{pred} = \begin{bmatrix} \boldsymbol{\theta^h} \\ \boldsymbol{V^h} \\ \lambda^h \end{bmatrix} + \begin{bmatrix} \boldsymbol{\Delta\theta} \\ \boldsymbol{\Delta V} \\ \Delta\lambda \end{bmatrix}^{pred}
\tag{B.9}
$$

In succession, the correction step takes the prediction step point as an initiation value for the PF solution. The system of nonlinear equations to be solved is similar to Equation (B.7). In the correction step, however, notice in (B.10) that the loading parameter residue is null in the column-matrix of state variables vectors. This condition is set so as to "corrects" the solution point for the given loading parameter increment via Newton-Raphson PF method.

$$
\begin{bmatrix} \mathbf{J}_{P\theta} & \mathbf{J}_{PV} & \mathbf{J}_{P\lambda} \\ \mathbf{J}_{Q\theta} & \mathbf{J}_{QV} & \mathbf{J}_{Q\lambda} \\ \mathbf{J}_{Y_\lambda\theta} & \mathbf{J}_{Y_\lambda V} & \mathbf{J}_{Y_\lambda\lambda} \end{bmatrix} \cdot \begin{bmatrix} \boldsymbol{\Delta\theta} \\ \boldsymbol{\Delta V} \\ \Delta\lambda \end{bmatrix}^{corr} = \begin{bmatrix} \boldsymbol{\Delta P} \\ \boldsymbol{\Delta Q} \\ 0 \end{bmatrix}^{corr}
\tag{B.10}
$$

The sequence of prediction-correction steps are set to continue throughout the CPF simulation process. If any correction step results in a divergent solution, the loading parameter step λ^{step} must decrease in value and the prediction-correction step must continue with convergent solutions. The variable λ^{step} is set to decrease in value until a tolerance value ε_λ condition is met. Once this condition is reached, the λ^{crit} as well as the system's voltage stability are then determined. In order to trace the instability region of the PV-curve, λ^{step} sign must be negative in the prediction step.

In conclusion, the Jacobian matrix must be augmented during the prediction-correction steps. As an advantage, the additional submatrixes do not alter throughout the CPF simulation process, except the $\mathbf{J}_{Y_\lambda\lambda}$ which is an scalar equal 1 during the prediction step or an scalar equal to 0 during the correction step.

$$\mathbf{J}_{P\lambda} = \boldsymbol{P}_L^0 \qquad \text{(B.11)} \qquad\qquad \mathbf{J}_{Q\lambda} = \boldsymbol{Q}_L^0 \qquad \text{(B.12)}$$

$$\mathbf{J}_{Y_\lambda \theta} = \mathbf{0}^T \qquad \text{(B.13)} \qquad\qquad \mathbf{J}_{Y_\lambda V} = \mathbf{0}^T \qquad \text{(B.14)}$$

$$\mathbf{J}_{Y_\lambda \lambda}^{pred} = [1] \qquad \text{(B.15)} \qquad\qquad \mathbf{J}_{Y_\lambda \lambda}^{corr} = [0] \qquad \text{(B.16)}$$

B.1.1 **Observations**

In the previous section, Equations (B.7) and (B.10) consider λ as the continuation parameter. However, other parameters can also be adopted as the continuation parameter, such as bus voltage magnitude. For each continuation parameter adopted, modifications on Jacobian matrix must occur in accordance.

An modification on the continuation parameter can take place during the CPF, in order to adopt the parameter which present a higher rate of variation. At early stages of the CPF simulation the continuation parameter adopted can be λ, since the loading parameter is the variable which presents the higher rates of variation. However, as the curve simulation approximates to the critical point, the continuation parameter can alter from λ to the bus with highest rate of voltage magnitude variation (AJJARAPU; CHRISTY, 1992; FERRAZ, 1998).

Additionally, some considerations upon Equation (B.7) step parameter λ^{step} sign must be clear in order to fully simulate the CPF curve. While the prediction-correction steps are simulated in a power system's stability operational region, the λ^{step} sign must be positive. This indicates an increase in the loading parameter value. After the critical point is found, the prediction-correction steps are set to simulate a power system's instability operational region. Therefore, the λ^{step} sign must be negative, indicating a decrease in the loading parameter value.

In conclusion, in the correction step highlighted by Equation (B.10), the loading parameter value must not vary. For this reason, therefore, the loading parameter variation $\Delta\lambda$ is null. Nevertheless, in order to avoid Jacobian matrix singularity closer to the critical operational point, the augmented row and column must be maintained (FERRAZ, 1998).

B.2 IMPLEMENTATION AND VALIDATION

The Prediction-Correction CPF algorithm was implemented in the Python program developed in this research. Simulations were held on the IEEE 14 bus system and, with the intent of validation, the results obtained via Python program are compared with CEPEL's production-grade software results.

No modification was applied in the IEEE 14 bus system, by which bus data and

line data are given in Christie (1999), and topology is illustrated in Figure 63. Altogether, the following three CPF scenarios were simulated: (i) base case with increase in load; (ii) base case with increase in load and considering reactive power generation limits; and (iii) base case with increase in load and with proportional increase in active power generation. From Figure 64 to 68 only the stable portion of the "nose" curve is displayed. The reason for this is to analyze how the electrical power system behaves with load increments until the MLP is reached.

Figure 63 – Tutorial system II topology.
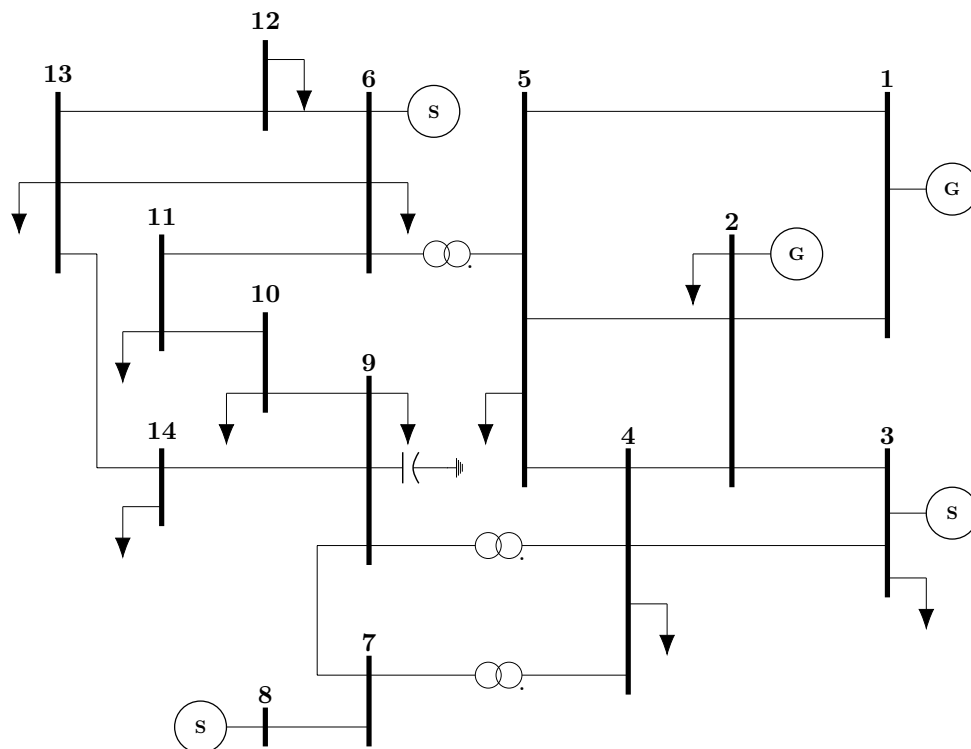
Source: Adapted from Christie (1999).

In all cases analyzed and hereafter illustrated, buses 10, 13 and 14 possessed the worst voltage magnitude profile and, therefore, their voltage profile are shown in Figures 64, 65 and 67. Additionally, Figures 66 and 68 presents the behavior of reactive power generation and active power generation due to load parameter increment, respectively. Since Generators located at bus 3, 6 and 8 behave as Synchronous Condensers, their active power generation during CPF remains null. Hence, in Figure 68, only the active power generation of Generators located at bus 1 and 2 vary during simulation.

As it can be observed, the Python program developed successfully and correctly simulated the proposed IEEE 14 bus system scenarios. All simulations were validated via CEPEL's reference software, considering the PQ constant load model.

In Figure 64, the critical loading parameter variable value was $\lambda^{crit} = 3.0067$. The IEEE 14 bus system was able to achieve high load parameter increments because no control limits were adopted on the Generators. Once the reactive power generation limits started

Figure 64 – Case (i): Voltage magnitude variation per load parameter increment.
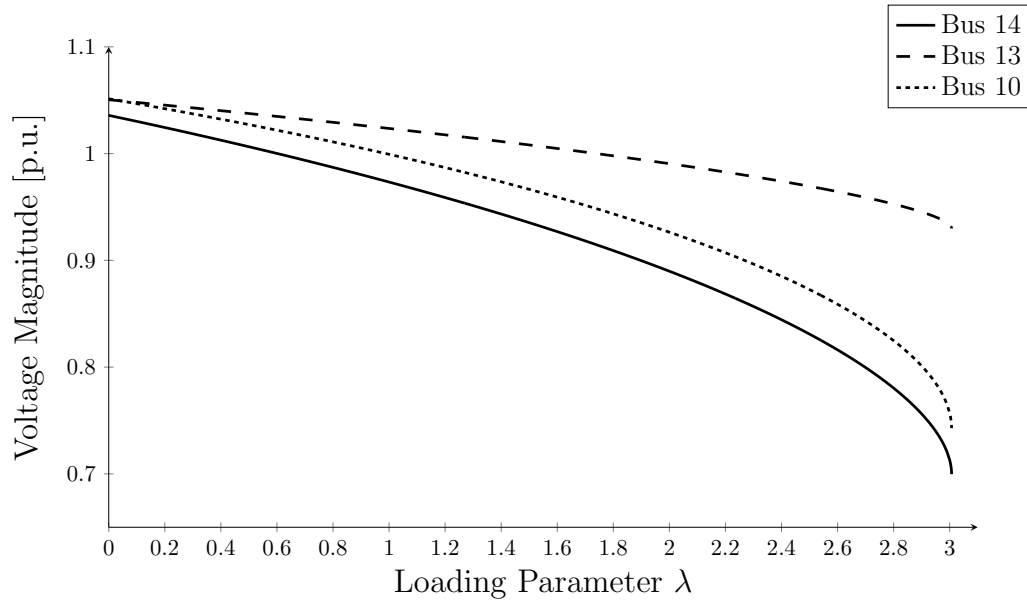
Source: Elaborated by the author.

Figure 65 – Case (ii): Voltage magnitude variation per load parameter increment, considering reactive power control limits.
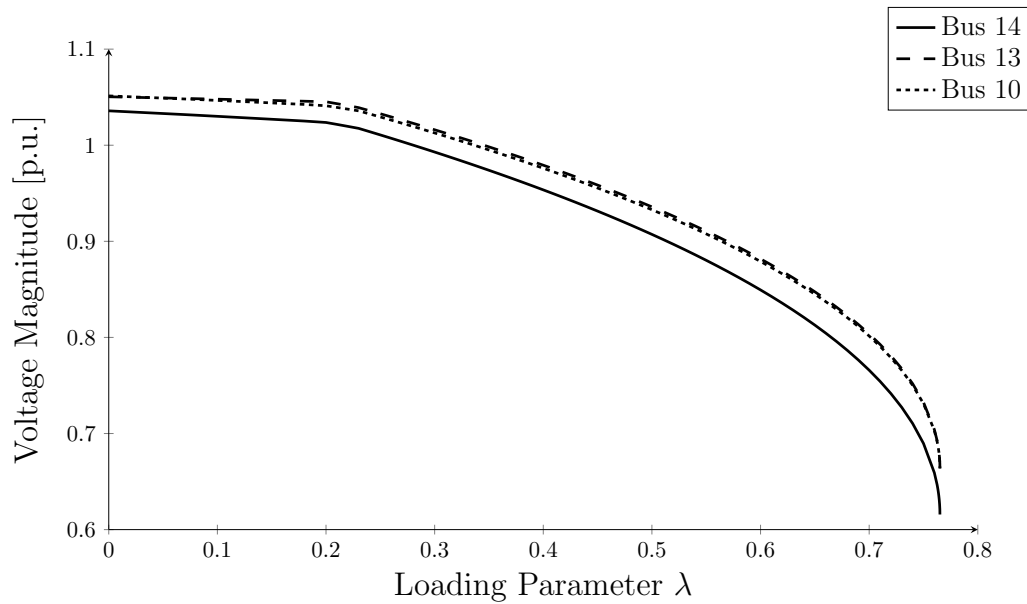
Source: Elaborated by the author.

to be controlled, in Figures 65 and 66, the loading parameter variable reached critical value at $\lambda^{crit} = 0.7651$. In conclusion, Figures 67 and 68 simulations reached a $\lambda^{crit} = 3.15$ considering no control adoptions and proportional increase in active power generation.

Figure 66 – Case (ii): Reactive power generation variation per load parameter increment, considering reactive power limits control.
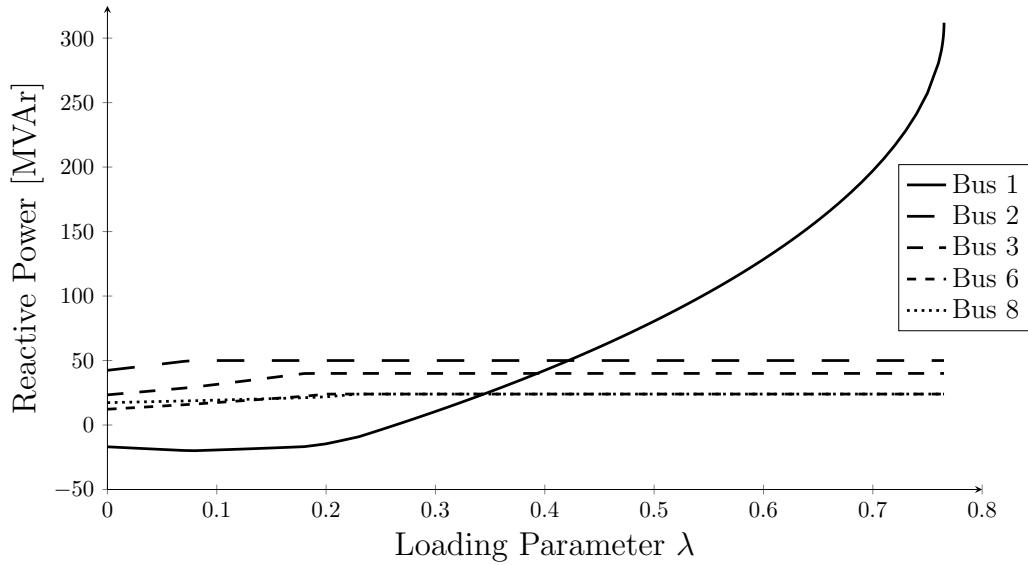
Source: Elaborated by the author.

Figure 67 – Case (iii): Voltage magnitude variation per load parameter increment, considering proportional increase in active power generation.
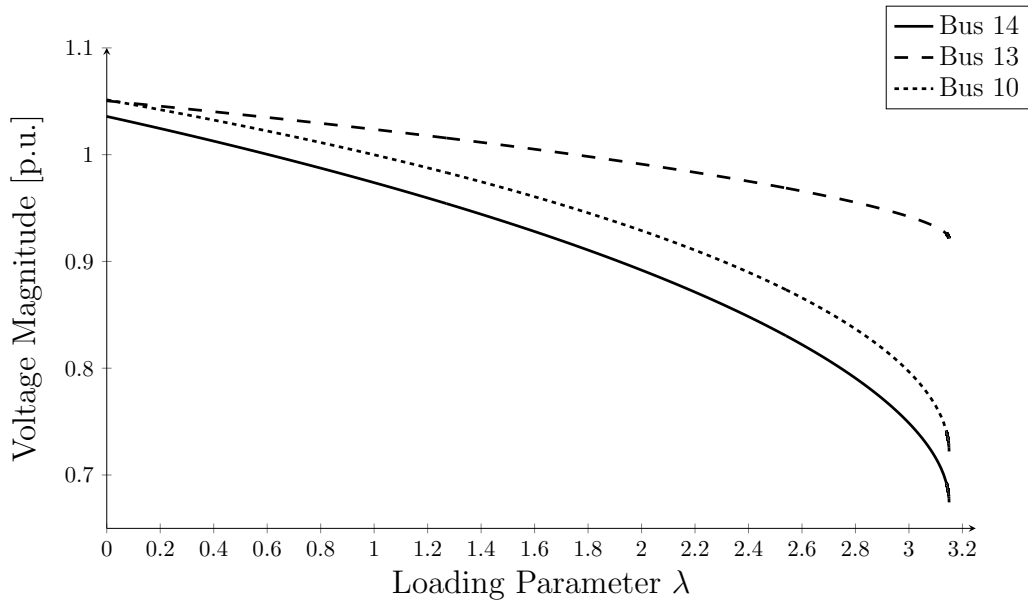
Source: Elaborated by the author.

The different λ^{crit} values obtained via Python simulation are in line with the proposed analyzed cases.

Figure 68 – Case (iii): Active power generation variation per load parameter increment, considering proportional increase in active power generation.
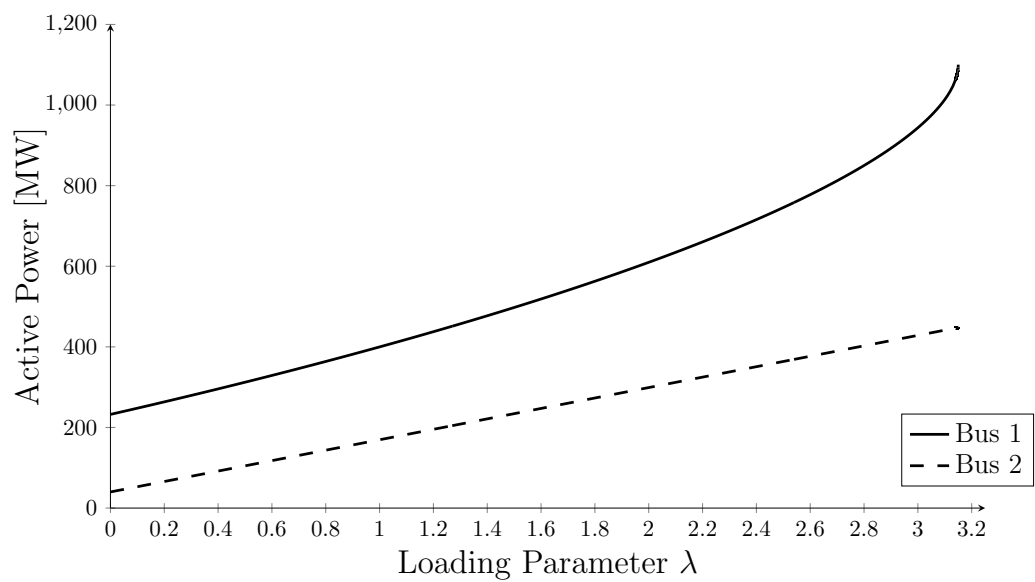
Source: Elaborated by the author.

APPENDIX C – Eigenproperties of the Jacobian matrix

The following sections presents the eigenproperties necessary for evaluating voltage stability impacts on EPSs via modal analysis. The information detailed hereinafter were mainly obtained from (GAO; MORISON; KUNDUR, 1992; KUNDUR, 1994; TAYLOR, 1994; PASSOS FILHO, 2005).

C.1 EIGENVALUES

The eigenvalues of a matrix are defined as the values of the scalar parameter λ^{eig} for which there exist non-trivial solutions other than $\phi = 0$ to the equation

$$\boldsymbol{A} \cdot \boldsymbol{\phi} = \lambda^{eig} \cdot \boldsymbol{\phi} \tag{C.1}$$

where $\boldsymbol{A}$ is a NxN matrix and $\boldsymbol{\phi}$ is a Nx1 vector.

The N eigenvalues corresponding to matrix $\boldsymbol{A}$ $\left(\lambda_1^{eig}, \lambda_2^{eig}, \ldots, \lambda_N^{eig} \right)$ are determined by the solution of the *characteristic equation*:

$$\det \left(\boldsymbol{A} - \lambda^{eig} \cdot \boldsymbol{I} \right) = 0 \tag{C.2}$$

C.1.1 Eigenvalues and stability

The eigenvalues that derive from the *characteristic equation* solution may be real or complex. In case of $\boldsymbol{A}$ matrix is real, then the complex eigenvalues always occur in conjugate pairs. On the other hand, in case of $\boldsymbol{A}$ matrix is real and symmetrical, all eigenvalues and eigenvectors will be real.

In dynamic analysis of EPSs, the stability of a system can be determined by the eigenvalues. A real eigenvalue is correlated to a non-oscillatory mode, with a negative and real eigenvalue representing a decaying mode whereas a positive and real eigenvalue representing an aperiodic instability.

A complex eigenvalue always occur in conjugate pairs and each pair corresponds to an oscillatory mode. The real component corresponds to the damping and the imaginary component corresponds to the frequency of oscillation. For the real component in complex eigenvalues, the previous analysis stands.

C.1.2 Eigenvalue sensitivity

Let the N-column vector $\boldsymbol{\phi_i}$ be the right eigenvector of $\boldsymbol{A}$ associated with the eigenvalue λ_i^{eig}, as follows

$$\boldsymbol{A} \cdot \boldsymbol{\phi_i} = \lambda_i^{eig} \cdot \boldsymbol{\phi_i} \tag{C.3}$$

Differentiating with respect to the element of $\boldsymbol{A}$ in the kth row and jth column (a_{kj}):

$$\frac{\partial \boldsymbol{A}}{\partial a_{kj}} \cdot \boldsymbol{\phi_i} + \boldsymbol{A} \cdot \frac{\partial \boldsymbol{\phi_i}}{\partial a_{kj}} = \frac{\partial \lambda_i^{eig}}{\partial a_{kj}} \cdot \boldsymbol{\phi_i} + \lambda_i^{eig} \cdot \frac{\partial \boldsymbol{\phi_i}}{\partial a_{kj}} \tag{C.4}$$

Premultiplying (C.4) by $\boldsymbol{\psi_i}$ results in:

$$\boldsymbol{\psi_i} \cdot \frac{\partial \boldsymbol{A}}{\partial a_{kj}} \cdot \boldsymbol{\phi_i} = \frac{\partial \lambda_i^{eig}}{\partial a_{kj}} \tag{C.5}$$

Considering that all elements of $\frac{\partial \boldsymbol{A}}{\partial a_{kj}}$ are zero, except for element in the kth row and jth column, the sensitivity of the eigenvalue λ_i^{eig} to the element a_{kj} is given by the product of the left eigenvector element and the right eigenvector element as follows:

$$\frac{\partial \lambda_i^{eig}}{\partial a_{kj}} = \boldsymbol{\psi_{ik}} \cdot \boldsymbol{\phi_{ji}} \tag{C.6}$$

C.2   EIGENVECTORS

The column vector $\boldsymbol{\phi_i}$ that is solution for (C.1) is defined as the right eigenvector of matrix $\boldsymbol{A}$ associated with the eigenvalue λ_i^{eig}:

$$\boldsymbol{A} \cdot \boldsymbol{\phi_i} = \lambda_i^{eig} \cdot \boldsymbol{\phi_i} \qquad i = 1, 2, \ldots, N \tag{C.7}$$

where:

$$\boldsymbol{\phi_i} = \begin{bmatrix} \phi_{1i} \\ \phi_{2i} \\ \vdots \\ \phi_{Ni} \end{bmatrix} \tag{C.8}$$

and also, the matrix of right eigenvectors is defined as:

$$\phi = \begin{bmatrix} \boldsymbol{\phi_1} & \boldsymbol{\phi_2} & \cdots & \boldsymbol{\phi_N} \end{bmatrix} \tag{C.9}$$

Similarly to the right eigenvector definition, the left eigenvector is also defined. It is a 1xN row vector that satisfies (C.10), associated with the eigenvalue λ_i^{eig}:

$$\boldsymbol{\psi_i} \cdot \boldsymbol{A} = \boldsymbol{\psi_i} \cdot \lambda_i^{eig} \tag{C.10}$$

where:

$$\boldsymbol{\psi_i} = \begin{bmatrix} \psi_{i1} & \psi_{i2} & \dots & \psi_{iN} \end{bmatrix} \tag{C.11}$$

and also, the matrix of left eigenvectors is defined as

$$\boldsymbol{\psi} = \begin{bmatrix} \boldsymbol{\psi_1} \\ \boldsymbol{\psi_2} \\ \vdots \\ \boldsymbol{\psi_N} \end{bmatrix} \tag{C.12}$$

The product of left and right eigenvectors associated with different eigenvalues are orthogonal:

$$\boldsymbol{\psi_j} \cdot \boldsymbol{\phi_i} = \boldsymbol{0} \tag{C.13}$$

As for the product of left and right eigenvectors associated with the same eigenvalues, it results in a non-zero real or complex constant $\boldsymbol{C_i}$.

$$\boldsymbol{\psi_i} \cdot \boldsymbol{\phi_i} = \boldsymbol{C_i} \tag{C.14}$$

The normalization of left and right eigenvectors are commonly considered for different applications and results in:

$$\boldsymbol{\psi_i} \cdot \boldsymbol{\phi_i} = 1 \tag{C.15}$$

C.3 MODAL MATRICES

Let $\boldsymbol{\Lambda}$ be defined as a NxN diagonal matrix, that has the eigenvalues of $\boldsymbol{A}$ $\left(\lambda_1^{eig}, \lambda_2^{eig}, \dots, \lambda_N^{eig}\right)$ as diagonal terms:

$$\mathbf{\Lambda} = \begin{bmatrix} \lambda_1^{eig} & 0 & \dots & 0 \\ 0 & \lambda_2^{eig} & \dots & 0 \\ \vdots & \vdots & \ddots & \vdots \\ 0 & 0 & \dots & \lambda_N^{eig} \end{bmatrix} \tag{C.16}$$

From Equations (C.7) and (C.15), the following relationship between matrices $\boldsymbol{A}$ and $\mathbf{\Lambda}$, and vectors $\boldsymbol{\phi}$ and $\boldsymbol{\psi}$ can be inferred:

$$\boldsymbol{A} \cdot \boldsymbol{\phi} = \boldsymbol{\phi} \cdot \mathbf{\Lambda} \tag{C.17}$$

$$\boldsymbol{\psi} \cdot \boldsymbol{\phi} = \boldsymbol{I} \tag{C.18}$$

$$\boldsymbol{\psi} = \boldsymbol{\phi}^{-1} \tag{C.19}$$

Based on (C.18), the relationship between matrices $\boldsymbol{A}$ and $\mathbf{\Lambda}$ can be redefined as:

$$\boldsymbol{\psi} \cdot \boldsymbol{A} \cdot \boldsymbol{\phi} = \mathbf{\Lambda} \tag{C.20}$$

C.3.0.1 *Eigenproperties example*

Consider the system of linear equations in (C.21).

$$\boldsymbol{A} \cdot \boldsymbol{x} = \boldsymbol{b} \tag{C.21}$$

where $\boldsymbol{A}$ is a matrix that contains the corresponding linear equations coefficients, $\boldsymbol{x}$ is a vector that contains the corresponding linear equations variables and $\boldsymbol{b}$ is a vector that contains the corresponding linear equations independent terms.

Manipulating the vector of linear equations variables in order to eliminate the linkage between variables results in:

$$\boldsymbol{\phi} \cdot \hat{\boldsymbol{x}} = \boldsymbol{x} \tag{C.22}$$

The same may be considered for the vector of independent terms:

$$\phi \cdot \hat{b} = b \tag{C.23}$$

Replacing Equations (C.22) and (C.23) in (C.21) results in:

$$A \cdot \phi \cdot \hat{x} = \phi \cdot \hat{b} \tag{C.24}$$

which can be simplified, considering the relationship between A and Λ from (C.20), as follows:

$$\psi \cdot A \cdot \phi \cdot \hat{x} = \hat{b} \tag{C.25}$$

$$\Lambda \cdot \hat{x} = \hat{b} \tag{C.26}$$

From (C.25), the linkage between variables in each linear equation of the system of equations is eliminated. This condition improves the analysis for a system of linear equations, and is widely applied in electrical power system studies.

C.3.1 Mode-shape

Based on the aforementioned example, in (C.22) the right eigenvector is characterized for giving the system of equations mode-shape. "The degreee of activity of the state variable x_k in the ith mode is given by the element ϕ_{ik}" (KUNDUR, 1994). Similarly, the left eigenvector is characterized for identifying which combination of the original variables displays only the ith mode.

The mode-shape is, therefore, a graphical visualization of the manitude and angles of the right eigenvector elements ϕ_{ik}. The magnitudes of the elements gives the extents of the activities of the N variables in the ith mode and the angles gives phase displacement of the variables with regard to the mode (KUNDUR, 1994).

C.3.2 Participation factor

The participation factor combines the informations in the left eigenvector ψ with the ones in the right eigenvector ϕ, in order to obtain the relationship between eigenvalues and the vector of variables of the system of equations. The goal is to calculate the participation of a given state k for a given mode i.

$$P = \begin{bmatrix} p_1 & p_2 & \cdots & p_N \end{bmatrix} \tag{C.27}$$

$$
\boldsymbol{p_i} = \begin{bmatrix} p_{1i} \\ p_{2i} \\ \vdots \\ p_{Ni} \end{bmatrix} = \begin{bmatrix} \phi_{1i} \cdot \psi_{i1} \\ \phi_{2i} \cdot \psi_{i2} \\ \vdots \\ \phi_{Ni} \cdot \psi_{iN} \end{bmatrix} \tag{C.28}
$$

The element p_{ki} is named as the participation factor (KUNDUR, 1994; PÉREZ-ARRIAGA; VERGHESE; SCHWEPPE, 1982), which is an dimensionless term. It is a sensibility measurement for the eigenvalue λ_i to the diagonal element a_{kk} of the $\boldsymbol{A}$ matrix, also defined as follows:

$$
p_{ki} = \frac{\partial \lambda_i^{eig}}{\partial a_{kk}} \tag{C.29}
$$

The participation factor indicates the relative participations of the respective states of matrix $\boldsymbol{A}$ in the corresponding modes.